

UNIVERSIDAD DE VALENCIA  
FACULTAD DE FÍSICA



PhD Thesis

**A Silicon Strip Detector for the  
Phase II High Luminosity Upgrade  
of the ATLAS Detector at the  
Large Hadron Collider**

Author:

Carlos García Argos

Supervisors:

Dr. Carlos Lacasta Llácer

Dr. Stephen J. McMahon

Valencia, 2014



# Abstract

ATLAS is a particle physics experiment at the Large Hadron Collider (LHC) that detects proton-proton collisions at a centre of mass energy of 14 TeV. The Semiconductor Tracker is part of the Inner Detector, implemented using silicon microstrip detectors with binary read-out, providing momentum measurement of charged particles with excellent resolution. The operation of the LHC and the ATLAS experiment started in 2010, with ten years of operation expected until major upgrades are needed in the accelerator and the experiments. The ATLAS tracker will need to be completely replaced due to the radiation damage and occupancy of some detector elements and the data links at high luminosities. These upgrades after the first ten years of operation are named the Phase-II Upgrade and involve a re-design of the LHC, resulting in the High Luminosity Large Hadron Collider (HL-LHC).

This thesis presents the work carried out in the testing of the ATLAS Phase-II Upgrade electronic systems in the future strips tracker after 2023, to be installed for operations in the HL-LHC period. The high luminosity and number of interactions per crossing that will happen after the HL-LHC starts require a complete replacement of the ATLAS tracker. The systems that have been defined for the Phase-II Upgrade will be designed to cope with that increased radiation and have the right granularity to maintain the performance with higher pile-up.

In this thesis I present results on single modules and larger structures comprising multiple modules.

The single modules are built using silicon microstrip sensors with four rows of 1280 strips. The read-out of the strips is done using 128 channel chips, glued and bonded on a hybrid circuit that holds 20 chips. Two hybrids are glued to the sensor to read-out all its strips.

In addition to the new sensors and read-out chips, the specifications for the ATLAS Phase-II Upgrade programme require a different powering scheme in the strips tracker than the current ATLAS Semiconductor Tracker. Two approaches have been proposed, which are serial powering and Direct Current to Direct Current (DC-DC) conversion. The decision on which will be used is not final yet, pending the results on efficiency and performance of the tracker using both of them.

Larger structures are constructed by mounting the single modules on a bus tape that carries the signals to one end of the structure, which interfaces with the tracker read-out systems. The bus tape is glued on a structure that provides mechanical support and cooling. All the modules on a structure are read-out through the same interface, aggregating multiple signals in one physical channel. The structures are called staves or stavelets. The latter typically mount four modules on a side of the structure. Two different stavelets have been tested in the context of this thesis, one with serial powering and one with DC-DC conversion. Both are single-sided objects and double-sided objects have been constructed and tested in other institutes.

One full size stave with twelve modules on one side has been constructed. It is powered using DC-DC conversion, and tested at the Rutherford Appleton Laboratory (RAL) as part of the work for this thesis.

In the context of the current ATLAS Semiconductor Tracker studies, I present an analysis of the data taken by the detector from the beginning of operation in 2010 until the first Long Shut-down in 2013. The analysis consists of an energy loss study in the Semiconductor Tracker, a task the detector was not designed to perform.

However, the availability of the Time-over-Threshold of the signals generated by particles traversing the detector elements allows an estimation of the charge deposited by the particles. This calculation of the energy loss is typically used to perform particle identification, a feature that is usually not required from the tracker. In addition, I present a study that proposes the use of this energy loss calculation as a means of tracking radiation damage in the silicon.

# Acknowledgements and Remarks

A lot of other people have contributed in one way or another to this thesis, from the various institutes that participate in the ATLAS Collaboration. In hope of not forgetting too many of them, I would like to thank, in no particular order: Fernando, Ashley, Bruce, Matt, Ingo, Conrad, Tony W., Tony A., Phil, Dave, Sergio G., Sergio D., Pippa, Susanne, Ingrid, Uli, Miguel, Víctor, Todd, Samer, Bart, Ian, Madalina, Takashi and Stephen.

Thanks to the colleagues from IFIC in Valencia, for their help and collaboration: Carlos, Pepe and Ricardo. Special thanks to Carlos for agreeing to supervise this thesis, for his thorough reviews and chats about the various topics in the thesis.

I do not want to miss the opportunity to thank the Science and Technology Facilities Council (STFC) in the United Kingdom for their support, both financial and technical, with the tests done at Rutherford Appleton Laboratory, in close collaboration with Peter Phillips. A special thanks to Peter for his help.

A big thanks to Steve for also agreeing to supervise this work and for his constant support, his kindness and enthusiasm.

A huge thanks to my family and friends for their support and love in the distance.

The author acknowledges the financial support from Spanish grant SEII-2010-00101, IFIC-CSIC and CERN.

This PhD Thesis is written following the spelling recommendations from the Oxford English Dictionary and Fowler's *A Dictionary of Modern English Usage*.

The figures, tables, equations and units are written following the ATLAS Style Guide.

This document was last updated 11th October 2018.



# Contents

<b>Abstract</b>	<b>iii</b>
<b>List of Figures</b>	<b>9</b>
<b>List of Tables</b>	<b>15</b>
<b>1 Introduction</b>	<b>17</b>
1.1 The Large Hadron Collider Accelerator and its Experiments at CERN .	17
1.2 The ATLAS Experiment at the Large Hadron Collider . . . . .	19
1.3 Operating Conditions of the ATLAS Detector . . . . .	21
1.4 Thesis Outline . . . . .	22
<b>2 Tracking in High Energy Physics Experiments</b>	<b>23</b>
2.1 The Role of Trackers . . . . .	23
2.2 Track Reconstruction . . . . .	23
2.2.1 Track Parameterization . . . . .	25
2.2.2 Resolution . . . . .	26
2.2.3 Track Fitting . . . . .	28
2.2.4 Alignment . . . . .	29
2.3 Silicon Trackers . . . . .	31
2.4 The ATLAS Semiconductor Tracker . . . . .	38
2.4.1 Tracking of the Radiation Damage in the SCT . . . . .	40
2.4.2 Noise Performance . . . . .	41
2.4.3 Alignment and Resolution of the Tracker . . . . .	43
<b>3 Upgrades at the LHC</b>	<b>47</b>
3.1 Motivation . . . . .	47
3.1.1 Long Shut-down 1 . . . . .	47
3.1.2 Long Shut-down 2 . . . . .	48
3.1.3 LHC End of Life . . . . .	49
3.2 High Luminosity Large Hadron Collider . . . . .	49
3.2.1 Experiments Upgrades in the HL-LHC . . . . .	51
3.3 Phase-II Upgrade of the ATLAS Inner Tracker . . . . .	52
3.3.1 Tracker Upgrade Overview . . . . .	52
3.3.2 The Strip Detector for the Upgrade . . . . .	54
<b>4 The ATLAS Silicon Strips Tracker Upgrade</b>	<b>61</b>
4.1 Silicon Sensors . . . . .	61
4.1.1 Barrel Sensors . . . . .	62

4.1.2	Endcap Sensors . . . . .	64
4.2	Front-End and Read-Out Electronics . . . . .	66
4.2.1	The ABCn25 Chip . . . . .	66
4.2.2	The ABC130 Chip . . . . .	67
4.2.3	Hybrids . . . . .	68
4.2.4	End of Stave/Petal Card . . . . .	70
4.3	Powering Schemes . . . . .	70
4.3.1	Serial Powering . . . . .	72
4.3.2	DC-DC Conversion . . . . .	74
4.3.3	Advantages of DC-DC and SP . . . . .	76
4.4	Sensor Biasing . . . . .	77
4.5	The Stavelet Concept for the Tracker Barrel . . . . .	79
4.5.1	Silicon Microstrip Modules . . . . .	79
4.5.2	Multi-module Structures . . . . .	80
<b>5</b>	<b>Results and Discussion of the Structures for the Silicon Tracker Upgrade</b>	<b>83</b>
5.1	Tests of Modules and Stavelets . . . . .	83
5.1.1	Infrastructure . . . . .	83
5.1.2	Data Acquisition System for System Tests . . . . .	83
5.1.3	Electronic Equipment . . . . .	86
5.1.4	Cooling Plant . . . . .	87
5.1.5	Performance Tests and Calibration . . . . .	88
5.1.6	Modules and Stavelets . . . . .	90
5.1.7	Tests Description . . . . .	91
5.2	Noise Model . . . . .	92
5.3	Single Module Performance Tests . . . . .	95
5.3.1	Varying Temperature . . . . .	97
5.3.2	High Voltage Scans . . . . .	100
5.3.3	Low Temperature Tests . . . . .	101
5.4	Performance Tests of Four Module Stavelets . . . . .	103
5.4.1	High Voltage Scans . . . . .	103
5.4.2	Hybrid Powering Variations . . . . .	105
5.4.3	High Voltage Multiplexing . . . . .	109
5.4.4	Electromagnetic Interference . . . . .	112
5.4.5	Dual and Single Stavelet Tests . . . . .	116
5.5	DC-DC Powered Stave . . . . .	119
5.5.1	Assembly of the Stave . . . . .	120
5.5.2	Setup at RAL . . . . .	121
5.5.3	Results with Three Modules . . . . .	121
5.5.4	Results with Nine Modules . . . . .	124
5.5.5	Results with Twelve Modules . . . . .	127
5.6	Discussion . . . . .	134
<b>6</b>	<b>Measurement of the Energy Loss and Particle Identification in the ATLAS SCT</b>	<b>137</b>
6.1	Introduction . . . . .	137
6.2	Event and Track Selection . . . . .	138
6.3	$dE/dx$ Reconstruction . . . . .	141



---

6.3.1	SCT Data Acquisition, Hits and Timing . . . . .	143
6.3.2	SCT $dE/dx$ Calculation with the Time-over-Threshold Method . . . . .	144
6.4	Particle Identification . . . . .	145
6.4.1	Particle Identification with 2011-2012 Data . . . . .	147
6.4.2	Efficiency and Mistag Rate . . . . .	153
6.5	Long-term Stability . . . . .	155
6.6	Discussion . . . . .	158
<b>7</b>	<b>Conclusions and Future Work</b>	<b>161</b>
<b>8</b>	<b>Resumen</b>	<b>163</b>
8.1	Introducción . . . . .	163
8.1.1	El experimento ATLAS . . . . .	163
8.1.2	El detector de trazas de semiconductor en ATLAS . . . . .	164
8.2	Detector de bandas de silicio en ATLAS Fase 2 . . . . .	164
8.2.1	Fase 2 del LHC: HL-LHC . . . . .	164
8.2.2	Descripción del detector de bandas . . . . .	165
8.2.3	Sistemas electrónicos . . . . .	166
8.2.4	Prestaciones del módulo con alimentación serie . . . . .	167
8.2.5	Prestaciones de estructuras con múltiples módulos . . . . .	170
8.2.6	Stave de doce módulos con alimentación DC-DC . . . . .	181
8.3	Cálculo del poder de frenada en el SCT . . . . .	183
8.3.1	Introducción . . . . .	184
8.3.2	Selección de eventos y de trazas . . . . .	184
8.3.3	Reconstrucción de $dE/dx$ . . . . .	185
8.3.4	Identificación de partículas . . . . .	186
8.3.5	Estabilidad a largo plazo . . . . .	189
8.4	Conclusiones . . . . .	190
	<b>Acronyms</b>	<b>191</b>
	<b>Bibliography</b>	<b>193</b>

---



# List of Figures

1.1	The CERN Accelerator Complex showing all experiments around the LHC. . . . .	18
1.2	View of the whole ATLAS detector. . . . .	19
1.3	Axial representation of particle detection at the ATLAS sub-detectors. . . . .	20
2.1	Particle track deflection in the transverse plane due to a perpendicular magnetic field. . . . .	24
2.2	Coordinate system in a tracker. . . . .	25
2.3	Illustration of the track parameters in the transverse ( $xy$ ) and longitudinal ( $Rz$ ) planes. . . . .	26
2.4	Measurement of the track curvature. . . . .	27
2.5	Track hits residuals. . . . .	29
2.6	Weak modes of geometrical distortions. . . . .	30
2.7	Basic detector scheme: from radiation absorption in the sensor to digitization of the event. . . . .	31
2.8	Semiconductor band structure. . . . .	32
2.9	A p-n junction under thermal equilibrium. . . . .	32
2.10	Description of the charge collection concept. . . . .	33
2.11	Double sided strip sensor for two dimension positioning. . . . .	36
2.12	SCT barrel module photograph and illustration, showing the sensors with the built-in stereo angle and the electronics. . . . .	38
2.13	SCT endcap module types (outer, middle and inner). . . . .	39
2.14	One of the SCT barrels during insertion into the Inner Detector. . . . .	39
2.15	SCT endcap modules mounted on endcap discs: left has outer and inner modules, right shows middle modules. . . . .	40
2.16	Leakage current evolution in the SCT over time. . . . .	41
2.17	Sample performance measurements on the SCT modules. . . . .	42
2.18	Average input noise per chip for the four SCT barrels. . . . .	43
2.19	Noise occupancy of one front-end chip as a function of the discriminator threshold. . . . .	44
3.1	Possible integrated luminosity evolution for the LHC with the foreseen three long shut-downs superimposed. . . . .	49
3.2	Baseline layout of the Inner Tracker for the ATLAS Phase-II Upgrade. . . . .	53
3.3	Drawing of a barrel stave showing the 13 modules and the End of Stave card. . . . .	55
3.4	Drawing of the arrangement of the staves in barrels. The tilt angle is $10^\circ$ . . . . .	55
3.5	Drawing of an endcap petal showing the 9 modules and the services. . . . .	56
3.6	The arrangement of petals in the endcaps. . . . .	57

3.7	Picture of a functional stavelet showing the 4 modules and the End of Stave card. . . . .	58
3.8	Drawing of a petalet. The modules are unfolded to show both sides of the petalet, the hybrids and services routing. . . . .	59
4.1	Cross sections of the p-in-n, n-in-n and n-in-p detectors used in the studies on their radiation hardness. . . . .	61
4.2	Wafer layout defined in ATLAS12 specifications for the barrel short strips sensor prototypes. . . . .	64
4.3	Sensors on a barrel module: both stereo and axial strips on the same sensor. . . . .	64
4.4	Pictures of wafers with endcap sensors produced by CNM-IMB. . . . .	65
4.5	A drawing that shows the three different petalet sensors, including the size of the petalet. . . . .	66
4.6	Path of the signals from the strip to the End of Stave card. . . . .	66
4.7	Functional blocks diagram and picture of an ABCn25 chip. . . . .	67
4.8	Block diagram of the ABC130. . . . .	68
4.9	A hybrid with 20 ABCn25 chips, with the bonds to the sensor (top and bottom), to the powering (right) and to the BCC board (left) shown. . . . .	69
4.10	A BCC board. . . . .	69
4.11	End of Stave card from a four-module stavelet. . . . .	70
4.12	Picture of a VTRx showing the components of the transceiver package. . . . .	71
4.13	Independent powering of hybrids. . . . .	71
4.14	Serial powering of modules. In this case, each hybrid is at a different voltage reference, so this scheme is called “chain of hybrids”. . . . .	73
4.15	Serial powering with one shunt regulator and shunt transistor external to the load. . . . .	73
4.16	Serial powering board on a serially powered four-modules stavelet. . . . .	74
4.17	Powering of modules with DC-DC conversion. The drawing shows the parallel powering scheme. . . . .	74
4.18	Different versions of the DC-DC converter designed at CERN for the ATLAS and CMS trackers upgrade. . . . .	75
4.19	A tandem DC-DC converter with dual output. . . . .	75
4.20	DC-DC converters mounted on a stavelet. . . . .	76
4.21	SiC based high voltage multiplexer developed at BNL. . . . .	78
4.22	Single modules on a test frame (serially powered) and on a stavelet (DC-DC powered). . . . .	79
4.23	The two stavelets built at RAL and tested at CERN. . . . .	81
5.1	The clean room in Building 180 at CERN. . . . .	83
5.2	HSIO board used in the Strips Upgrade DAQ system. . . . .	84
5.3	The Burst Data window of the new SCTDAQ software. . . . .	85
5.4	Chillers used in the B180 test facility. . . . .	87
5.5	Strobe Delay data for the fit on two adjacent chips. . . . .	88
5.6	Quadratic fit to a response curve. . . . .	89
5.7	DC-DC stavelet (top) and SP stavelet (bottom). . . . .	91
5.8	Result of the noise model for the ABCn25 chip with varying input capacitance. . . . .	94

---

5.9	Result of the noise model for the ABCn25 chip with varying temperature for unbonded channels. . . . .	94
5.10	Result of the noise model for the ABCn25 chip with varying temperature for short strips (2.36 cm). . . . .	95
5.11	Reference noise ( $e^-$ ENC) for the serially powered module. . . . .	96
5.12	Reference gain (mV/fC) for the serially powered module. . . . .	96
5.13	Noise variation with temperature on the SP module. . . . .	98
5.14	Fit of the noise variation with temperature for all chips. . . . .	98
5.15	Noise variation with temperature for an unbonded hybrid. . . . .	99
5.16	Sensor bias voltage scan on the SP module up to 300 V. . . . .	100
5.17	Sensor bias voltage scan on the SP module up to 500 V. . . . .	101
5.18	Input noise ( $e^-$ ENC) with chiller temperature set to $-6^\circ\text{C}$ , three point gain scans centred at 1 fC. . . . .	102
5.19	Input noise ( $e^-$ ENC) with chiller temperature set to $-20^\circ\text{C}$ , three point gain scans centred at 1 fC. . . . .	103
5.20	DC-DC stavelet input noise ( $e^-$ ENC) with sensor bias. . . . .	104
5.21	DC-DC stavelet input noise ( $e^-$ ENC) with sensor bias, first ramping up to 300 V and then ramping down. . . . .	105
5.22	SP stavelet input noise ( $e^-$ ENC) with sensor bias. . . . .	105
5.23	SP stavelet input noise ( $e^-$ ENC) with sensor bias, first ramping up to 300 V and then ramping down. . . . .	106
5.24	DC-DC stavelet input noise ( $e^-$ ENC) with low voltage value. Low voltage from 10 V to 14 V, up and down, 1 V steps. . . . .	107
5.25	DC-DC stavelet Double Trigger Noise variation with low voltage value for 0.5 fC threshold. . . . .	108
5.26	SP stavelet input noise ( $e^-$ ENC) with low voltage value. Input current varied between 9 and 10 A in 0.1 A steps. . . . .	108
5.27	SP stavelet Double Trigger Noise variation with low voltage value for 0.5 fC threshold. . . . .	109
5.28	Noise comparison of high voltage scans on the DC-DC stavelet, using the high voltage multiplexer and using independent biasing, with the chiller temperature set to $6^\circ\text{C}$ . . . . .	110
5.29	Noise comparison of high voltage scans on the DC-DC stavelet, using the high voltage multiplexer and using independent biasing, with the chiller temperature set to $9^\circ\text{C}$ . . . . .	110
5.30	Noise comparison of high voltage scans on the DC-DC stavelet, using the high voltage multiplexer and using independent biasing, with the chiller temperature set to $12^\circ\text{C}$ . . . . .	111
5.31	Noise comparison of high voltage scans on the DC-DC stavelet, using the high voltage multiplexer and using independent biasing, with the chiller temperature set to $15^\circ\text{C}$ . . . . .	111
5.32	Noise comparison of high voltage scans on the serially powered stavelet, using the high voltage multiplexer and using independent biasing. . . . .	112
5.33	Position of the VersatileLink on top of the EoS card for one of the tests. . . . .	113
5.34	Noise measurements for module M3 with the interaction of the VersatileLink. . . . .	114
5.35	Temperatures measured on the stavelet during the noise tests with the interaction of the VersatileLink. . . . .	115

---

5.36	Double Trigger Noise results for 0.5 fC threshold on the DC-DC stavelet with the interaction of the VersatileLink. . . . .	116
5.37	Noise differences on the DC-DC stavelet when operated alone and when operated with the SP stavelet at the same time. . . . .	117
5.38	Noise differences on the DC-DC stavelet when operated alone and when operated with the SP stavelet at the same time. . . . .	118
5.39	Temperatures recorded on the Serially Powered stavelet when operated alone and together with the DC-DC stavelet. . . . .	119
5.40	Signal integrity at the End of Stave buffers for different termination resistors. . . . .	122
5.41	Input noise results of the DC-DC stave with the first three modules. . .	123
5.42	Double Trigger Noise of the DC-DC stave with three modules. . . . .	124
5.43	A picture of the DC-DC stave with nine modules. . . . .	124
5.44	Input noise of the DC-DC stave with nine modules. . . . .	125
5.45	Double Trigger Noise of the DC-DC stave with nine modules. . . . .	126
5.46	Hybrids temperatures on the DC-DC stave hybrids with nine modules. . .	126
5.47	A picture of the DC-DC stave with all the modules on one side modules. .	127
5.48	Hybrids temperatures on the DC-DC stave hybrids with 12 modules. . .	128
5.49	Leakage currents curves for each sensor mounted on the DC-DC stave, measured at 22°C in nitrogen. . . . .	128
5.50	Input noise of the DC-DC stave with twelve modules, compared to the noise with three and nine modules. . . . .	129
5.51	Double Trigger Noise of the DC-DC stave with twelve modules. . . . .	130
5.52	Evolution of the input noise for each module of the DC-DC stave with changing sensor bias. . . . .	130
5.53	Evolution of the input noise for each module of the DC-DC stave with changing input voltage at the converters, from lower to higher. . . . .	132
5.54	Evolution of the input noise for each module of the DC-DC stave with changing input voltage at the converters, from higher to lower. . . . .	132
5.55	Evolution of the double trigger noise with 0.5 fC threshold for each column of the DC-DC stave with changing input voltage at the converters, from lower to higher. . . . .	133
5.56	Evolution of the double trigger noise with 0.5 fC threshold for each column of the DC-DC stave with changing input voltage at the converters, from higher to lower. . . . .	134
6.1	$Rz$ section of ATLAS showing a quarter of the Inner Detector. . . . .	137
6.2	Primary and secondary vertex tracks. . . . .	139
6.3	Pixel $dE/dx$ extracted for data taken in 2011. At low momenta, the proton bands are visible for both positive and negative tracks. . . . .	142
6.4	Functionality of the ABCD3TA chip. . . . .	143
6.5	Time-over-Threshold for two different pulse sizes. . . . .	144
6.6	$dE/dx$ distributions vs $pq$ in 2010. . . . .	146
6.7	Pixel and SCT $dE/dx$ distributions vs $pq$ for the different particle species as tagged by the Pixel ( $P_i^{\text{norm,Pixel}} > 0.9$ ). Data taken in 2011. . . . .	148
6.8	$dE/dx$ distributions for positive pions, kaons and protons at low momenta. .	149
6.9	SCT $dE/dx$ distributions for 2011 data, primary vertex tracks only. . .	150
6.10	SCT $dE/dx$ distributions for 2011 data, secondary vertex tracks only. .	151

6.11	SCT $dE/dx$ distributions for 2012 data, primary vertex tracks only. . .	152
6.12	Proton tagging efficiency in the SCT for 2011 data. . . . .	154
6.13	Proton tagging efficiency in the SCT for 2012 data. . . . .	154
6.14	Time evolution of the proton (positive tracks) mean $dE/dx$ for track momentum in the (500, 550) MeV/ $c$ range, extracting the protons with the geometrical cut and with the Pixel likelihood for 2011-2012. . . . .	156
6.15	Evolution of the proton mean $dE/dx$ with time, showing the effect of the timing misadjustments and the timing scans dates. . . . .	157
6.16	Correlation between the mean time-bin size and the calculated mean proton $dE/dx$ . . . . .	157
6.17	Evolution of the proton mean $dE/dx$ with time, including a correction for the 2010 runs. . . . .	158
8.1	Vista del experimento ATLAS. . . . .	164
8.2	Esquema de un stave de barril con 13 módulos. . . . .	165
8.3	Esquemas alternativos de alimentación de los módulos. . . . .	166
8.4	Ajuste lineal de la variación del ruido con la temperatura para los chips de los dos híbridos. . . . .	168
8.5	Ruido en el módulo serie en función de la polarización del sensor. . . . .	169
8.6	Ruido del módulo serie con refrigerante a $-20^{\circ}\text{C}$ . . . . .	170
8.7	Los dos stavelets construidos en RAL y probados en CERN. . . . .	171
8.8	Ruido del stavelet DC-DC en función del alto voltaje. . . . .	172
8.9	Ruido del stavelet serie en función del alto voltaje. . . . .	172
8.10	Ruido del stavelet DC-DC en función de la tensión de entrada a los convertidores. . . . .	173
8.11	Ruido del stavelet con alimentación serie en función de la corriente de entrada. . . . .	173
8.12	Comparación de la dependencia del ruido en el stavelet DC-DC en función del alto voltaje, con multiplexor y con líneas independientes. . . . .	174
8.13	Comparación de la dependencia del ruido en el stavelet con alimentación serie en función del alto voltaje, con multiplexor y con líneas independientes. . . . .	175
8.14	Ruido ENC medido en el módulo M3, con interferencia del prototipo de VersatileLink. . . . .	176
8.15	Ruido de doble disparo con umbral a 0.5 fC, con interferencia del prototipo de VersatileLink. . . . .	177
8.16	Temperaturas en los híbridos del stavelet serie operado por separado y junto al stavelet DC-DC. . . . .	178
8.17	Diferencias de ruido en el stavelet DC-DC cuando funciona independientemente y cuando funciona junto al stavelet serie. . . . .	179
8.18	Diferencias de ruido en el stavelet serie cuando funciona independientemente y cuando funciona junto al stavelet DC-DC. . . . .	180
8.19	El stave con alimentación DC-DC, con los doce módulos montados. . . . .	181
8.20	Ruido del stave DC-DC con doce módulos. . . . .	182
8.21	Temperaturas medidas en el stave durante las pruebas. . . . .	183
8.22	Ruido de doble disparo en el stave DC-DC con doce módulos. . . . .	183
8.23	$dE/dx$ calculada en el SCT para datos de 2010. . . . .	186

8.24	Distribuciones de $dE/dx$ en el SCT para datos de 2011 y 2012, trazas positivas y vértices primarios. . . . .	187
8.25	Eficiencia de etiquetado de protones en función del corte de verosimilitud $P_p^{\text{norm,SCT}}$ , datos de 2011. . . . .	188
8.26	Eficiencia de etiquetado de protones en función del corte de verosimilitud $P_p^{\text{norm,SCT}}$ , datos de 2012. . . . .	188
8.27	Evolución de la $dE/dx$ media de protones con el tiempo. . . . .	189



# List of Tables

1.1	Annual fluences and ionizing doses for the tracker at the LHC design luminosity. . . . .	21
2.1	Abundance of semiconductor constituents in the Earth's crust. . . . .	34
2.2	Some physical characteristics of semiconductors. . . . .	35
2.3	Track parameter resolution for tracks with $p_T > 30$ GeV/ $c$ from cosmic ray data. . . . .	44
3.1	Design specifications of the LHC and the HL-LHC. . . . .	50
3.2	Number of staves or stubs in each barrel layer of the Strips Tracker for the Upgrade. . . . .	56
3.3	Active radii and $z$ positions of the endcap discs. . . . .	57
3.4	Radiation length estimates for barrel stave and endcap petal. Power ASICs and EoS are not included. . . . .	58
4.1	Summary of ATLAS12 specifications pre-irradiation. . . . .	63
4.2	Comparison of some features of the three powering schemes: Independent Powering (IP), Serial Powering (SP) and DC-DC conversion. . . . .	77
5.1	Characteristics of the sensors on the DC-DC stavelet. . . . .	91
5.2	Characteristics of the sensors on the serially powered stavelet. . . . .	91
5.3	Coolant and hybrid temperatures in the serially powered module. . . . .	97
5.4	Predicted and measured $\Delta ENC/\Delta T$ for SCT Endcap modules. . . . .	99
5.5	Temperatures measured during low temperature testing . . . . .	101
5.6	Voltages measured at the DC-DC converters inputs, as well as the output current of the power supply. . . . .	106
5.7	Characteristics of the sensors on the DC-DC stave. . . . .	127
5.8	Voltages at the DC-DC converter inputs with different settings on the power supplies. . . . .	131
6.1	Datasets used in the $dE/dx$ study. . . . .	141
8.1	Temperaturas del refrigerante y los híbridos. . . . .	168



# Chapter 1

## Introduction

This thesis is focused on silicon strips detectors. In particular, studies of the ATLAS Phase II Upgrade for the High Luminosity Large Hadron Collider (HL-LHC), with special emphasis on the future silicon strips tracker. This upgrade of the ATLAS detector will take place in the early 2020s and poses several challenges due to the harsh conditions that the LHC experiments will have to cope with. This thesis also discusses some work done on the performance studies of the current ATLAS silicon strips tracker.

This introduction chapter gives a brief overview of the current ATLAS detector.

### 1.1 The Large Hadron Collider Accelerator and its Experiments at CERN

The Large Hadron Collider is the hadron accelerator and collider that was installed in the 26.7 kilometres long tunnel that held the CERN Large Electron-Positron Collider (LEP) and its experiments. LEP was decommissioned in 2000 and LHC civil works commenced in 1998, and its installation was finished in 2008.

The layout of the LHC is the same one as that of LEP, with eight straight sections. The two high luminosity insertions are located at opposite sides of the LHC ring, Intersection Points 1 and 5 (IP1 and IP5), where the two large general-purpose experiments, ATLAS and CMS, are placed.

The LHC is capable of accelerating and colliding hadrons, namely protons, and heavy ions. The injection of protons and heavy ions into the LHC is done by the previously existing infrastructure: the Linear Accelerators Linac2 (protons) and Linac3 (heavy ions), Booster, the Proton Synchrotron (PS) and the Super Proton Synchrotron (SPS). They perform the pre-acceleration of the particles that are injected into the LHC ring.

The main design parameters of the LHC for proton-proton (p-p) operation are the maximum proton single-beam energy of 7 TeV, for a 14 TeV maximum centre of mass energy, and the peak luminosity of  $10^{34} \text{ cm}^{-2}\text{s}^{-1}$ , with  $1.15 \times 10^{11}$  protons per bunch, crossing in the experiments every 25 ns. In addition to the p-p collisions, the LHC also collides heavy ions, in particular lead nuclei, at a beam energy of 5.5 TeV and a design luminosity of  $10^{27} \text{ cm}^{-2}\text{s}^{-1}$  [1, 2].

The whole CERN accelerator complex, shown in Figure 1.1, comprises not only the LHC ring, but also the experiments, injectors and other non-LHC experiments. The

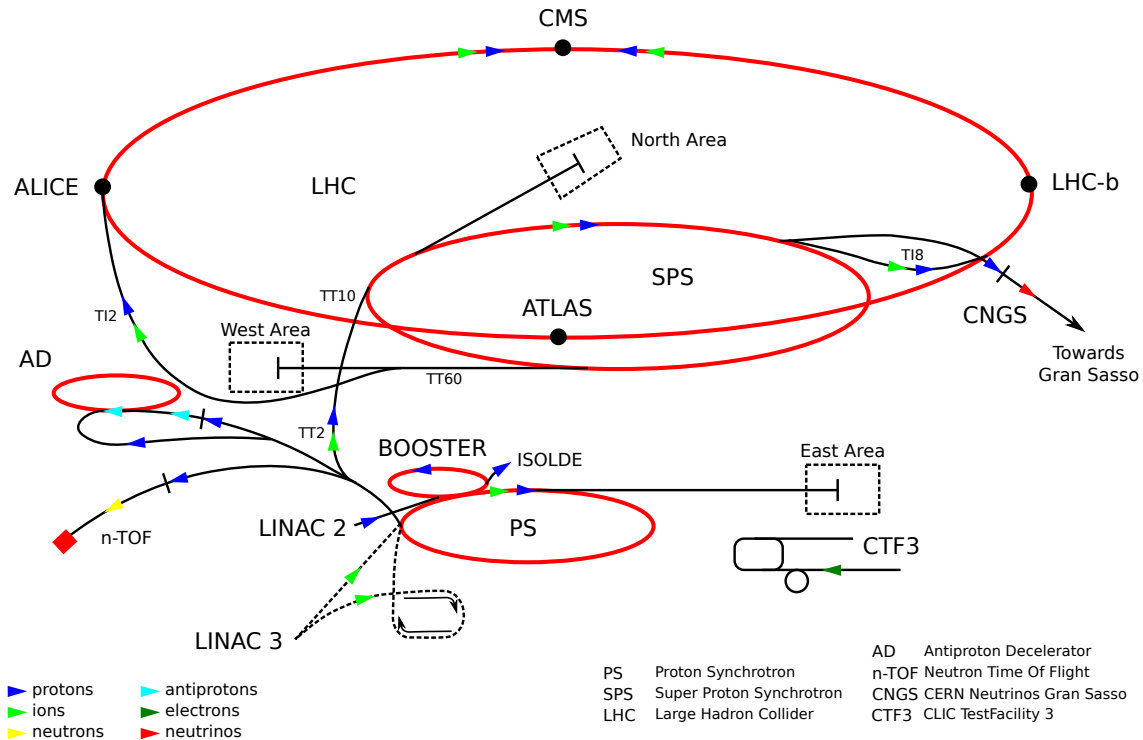


**Figure 1.1: The CERN Accelerator Complex showing all experiments around the LHC.**

six LHC experiments, of which four are depicted in the figure, are:

- *A Large Ion Collider Experiment (ALICE)*: it is a specialized detector to study heavy ion collisions, which at the LHC are lead-lead (Pb-Pb) and proton-lead (p-Pb). The experiment is located at the intersection point IP2.
- *A Toroidal LHC Apparatus (ATLAS)*: it is one of the two large general-purpose experiments at the LHC, located at intersection point IP1. It is used to study a wide range of physics, including the search for the Higgs boson, extra dimensions, super-symmetry and particles that could make up dark matter.
- *Compact Muon Solenoid (CMS)*: it is the other large general-purpose experiment together with ATLAS, located at intersection point IP5.
- *Large Hadron Collider beauty (LHCb)*: located at intersection point IP8, it is a specialized B-physics experiment, that measures the parameters of CP violation in the interactions of b-hadrons (heavy particles containing a bottom quark).
- *Large Hadron Collider forward (LHCf)*: it is a special-purpose experiment for astroparticle physics, designed to study the particles generated in the “forward” region of collisions, those almost directly in line with the colliding proton beams. It shares the interaction point IP1 with ATLAS.
- *TOTAL Elastic and diffractive cross section Measurement (TOTEM)*: it shares intersection point IP5 with CMS and has multiple detectors spread over 440 metres. Its purpose is to measure the structure and effective size of the proton, as well as precisely measure the cross section of proton-proton interactions.

This thesis is focused on the ATLAS silicon tracker and the next section gives a short description of the ATLAS experiment. Further details about the silicon tracker will be part of chapter 2.

## 1.2 The ATLAS Experiment at the Large Hadron Collider

ATLAS is a multi-purpose detector that was designed to detect charged and most neutral particles. The detected particles are the decay products of unstable Standard Model particles, such as the  $Z$  and  $W^\pm$ , the recently observed Higgs boson [3] and other particles from physics beyond the Standard Model.

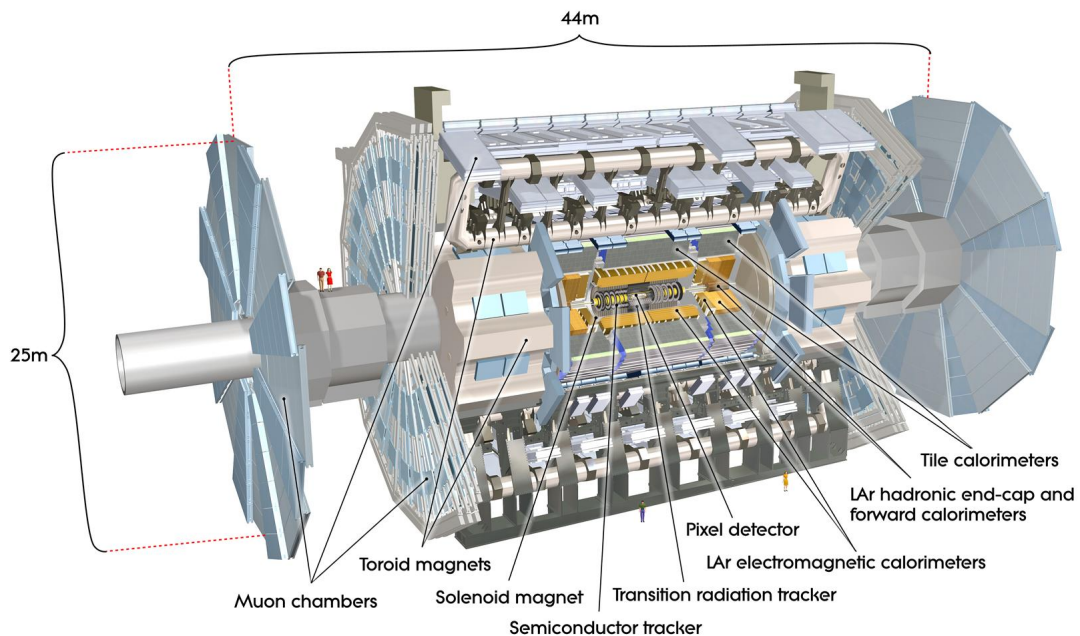


Figure 1.2: View of the whole ATLAS detector.

A schematic representation of the ATLAS detector is shown in Figure 1.2, where the layout of the sub-detectors can be seen. The dimensions are also indicated in the figure. The detector is 44 metres long and 25 metres high, weighting approximately 7000 tonnes [2]. A brief description of its sub-detectors follows.

The first element, surrounding the interaction point, is the Inner Detector, which performs the tracking role, one of the central functions in a particle detector. A discussion on trackers, as well as some additional information about the ATLAS Inner Detector, is part of chapter 2.

It is designed to do robust pattern recognition, excellent momentum resolution and both primary and secondary vertices measurements for charged particles with transverse momentum as low as 0.1 GeV. It covers the pseudorapidity range  $|\eta| < 2.5$ . It is immersed in a 2 tesla magnetic field that bends the trajectory of charged particles, providing the information needed to determine the momenta of the particles.

Three sub-systems form the Inner Detector: a Pixel detector and a Semi-Conductor Tracker (SCT) both implemented using silicon sensors, and a Transition Radiation Tracker (TRT) that uses ionization caused by charged particles in straw tubes filled with gas. The three are surrounded by a solenoid magnet that generates the 2 tesla magnetic field, designed to minimize the material thickness before the calorimeters, in order to have an adequate calorimetry performance. A more detailed description of the Semi-Conductor Tracker is given in chapter 2.

The calorimetry system, surrounding the Inner Detector, is composed of two types of calorimeters. The first one, that surrounds the inner detector, is the electromagnetic calorimeter, dedicated to absorbing and measuring the energy of electrons and photons that leave the tracker. The second layer is the hadronic calorimeter, which is responsible for performing the equivalent task for hadrons. The calorimeters have a large pseudorapidity coverage,  $|\eta| < 4.9$ . The two types are implemented using different technologies and more detailed information is available in [2].

The Muon spectrometer is located at the outer part of the detector and it is designed to detect charged particles that are not absorbed in the calorimeters and to measure their momenta in the  $|\eta| < 2.7$  range. These particles are muons, which are the only detectable particles that are not stopped in the calorimeters, both the muons that originated in the hard interaction and those that are products of decays inside the detector.

The muons trajectories are bent by a set of toroid magnets that can reach up to 4.7 tesla, serving the same purpose as the solenoid in the Inner Detector, that is, bend the particles trajectories to measure their momenta.

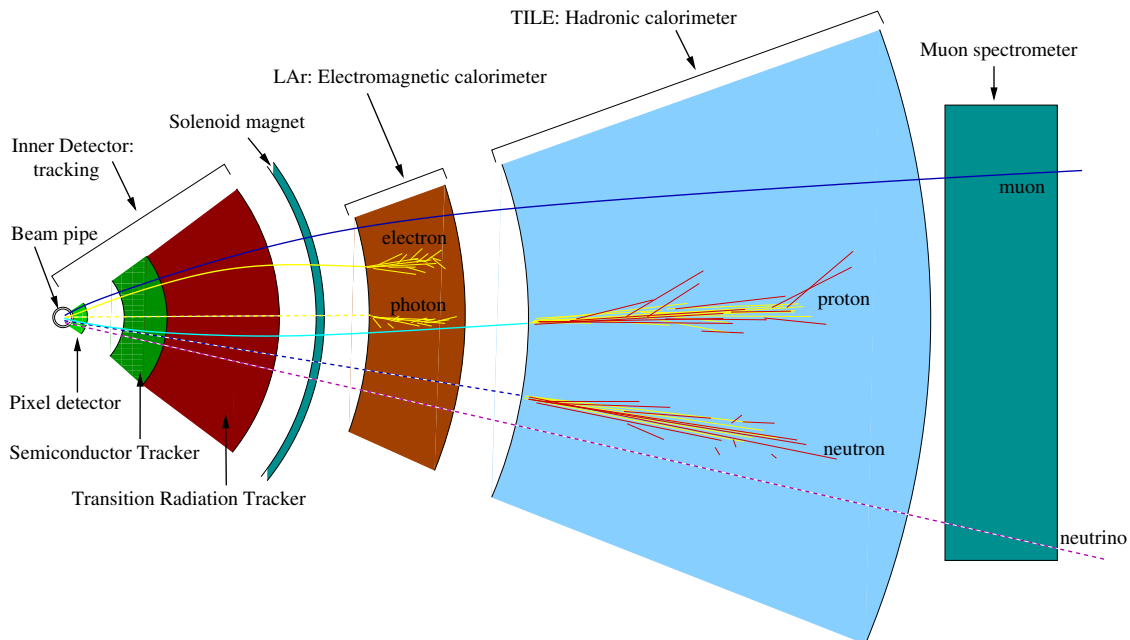


**Figure 1.3: Axial representation of particle detection at the ATLAS sub-detectors (to scale): the dashed lines indicate that the particle is not detected in that section of the experiment.**

Figure 1.3 shows each of the ATLAS layers with some sample particle species and their representative traces in each of the sub-detectors. The dashed lines for a given

particle type means that the particle is not detected in that part of the detector. The trajectories of charged particles such as protons and electrons are bent in the Inner Detector, whereas neutral particles such as neutrons are invisible to it. Photons, electrons, protons and neutrons create showers in their respective calorimeters, while muons go all the way to the muon chambers, and neutrinos cannot be seen by ATLAS because they interact very rarely with matter.

### 1.3 Operating Conditions of the ATLAS Detector

The read-out system of the whole detector has to deal with an enormous amount of data. Although the occupancy is never close to 100%, the available number of channels is still a huge number. The Inner Detector has a total of more than 86 million channels, 80 million in the pixel detector, 6.3 million in the SCT and 351000 in the TRT. The electromagnetic calorimeter has 173304 channels while the hadronic calorimeter has 19008 channels. Last, the muon system has a total of more than 1 million channels. All together, it is more than 87 million channels.

At the LHC design luminosity, the mean number of collisions is expected to be about 23 per bunch crossing. This means that an event will consist of 23 single minimum bias events superimposed, what is called pile-up.

The tracker occupancy increases with the number of interactions per bunch crossing, and the estimated peak values are around 0.1% for the Pixel detector, 1% for the SCT and 40% for the TRT, with a maximum of 30 reconstructed vertices in 2012 [4]. The increase in occupancy of the tracker may eventually cause performance degradation, leading to the impossibility to resolve close-by tracks.

With respect to the radiation environment, in particular of the tracker, the radiation levels are very high in this area. The extreme levels of radiation lead to damage in both the silicon sensors and the electronics. The fluences that the tracker sub-detector will accumulate at the LHC design luminosity are shown in Table 1.1. These levels of radiation cause several problems for the Inner Detector: the silicon sensors are affected, the electronics performance suffers and the particles contribute to background hits. All the materials used in the Inner Detector must be qualified to survive the doses and fluences expected at their locations [5].

Sub-detector	1 MeV equivalent neutron fluence [ $10^{13} \text{ cm}^{-2}/\text{year}$ ]		Ionizing dose [kGy/year]	
	Typical	Maximum	Typical	Maximum
Pixel detector	5	50	30	300
SCT	1.5	2	4	10
TRT	0.7	1	2	6

**Table 1.1: Annual fluences and ionizing doses for the tracker at the LHC design luminosity [5].**

The effects of radiation damage in silicon detectors will be briefly presented in chapter 2.

## 1.4 Thesis Outline

This thesis is structured as follows. Chapter 2 gives an overview of tracking in High Energy Physics experiments, focused on modern semiconductor trackers and with some insight into the ATLAS Semi-Conductor Tracker. The Phase II of the ATLAS Upgrade is presented in chapter 3, with additional specific information on the upgrade of the inner tracker in chapter 4. The results of the tests performed on the strips structures for the upgrade are presented in chapter 5.

Chapter 6 discusses a study of the ATLAS Semiconductor Tracker performance over time, using a method to calculate the  $dE/dx$  in the SCT, as a means to track the radiation damage in the silicon. Finally, chapter 7 is the conclusions chapter that summarizes the results of the tracker upgrade and  $dE/dx$  studies.

A shorter version of the complete thesis has been written in Spanish and included as chapter 8.



# Chapter 2

## Tracking in High Energy Physics Experiments

### 2.1 The Role of Trackers

The main role of a tracker in a High Energy Physics (HEP) experiment, such as those at the LHC, is to measure the trajectory of charged particles, by recording several points along the track. These points are found by the particles “hitting” the tracker at known locations, defined by the position of the tracker components. These hits result in the track coordinates in radius and the longitudinal coordinates. The hits are fitted to a curve and the momentum is measured from the curvature of charged particles in a magnetic field. Tracking is central in the experiments event reconstruction and analysis [6].

Trackers also contribute in the process of particle identification (PID). It is possible in some cases to measure the rate of energy loss,  $dE/dx$ , in the tracker. However, dedicated detectors are normally used for this task and the main contribution from the tracker is matching the tracks with:

- Showers in the calorimeter to identify electrons from their characteristic shower shape.
- Muon chamber track segments, improving the muon momentum measurement.

There are, in general, two types of tracker geometries, depending on the physics. Classical, central-forward-backward trackers (one cylinder barrel and two endcaps) are symmetric about the interaction point and they usually are immersed in a magnetic field that is oriented parallel to the beam direction. This is the case of ATLAS. There are asymmetric trackers like the LHCb tracker, which may not be immersed inside a magnetic field. This chapter is focused on the classical trackers, like the ATLAS Inner Detector.

### 2.2 Track Reconstruction

The process of reconstructing the tracks of an event includes extrapolating the tracks from the hit information, also reconstructing the interaction point for each track. One event in the ATLAS detector involves, in general, one hard interaction, generating

multiple vertices, a primary vertex from the hard interaction and the rest from the secondary interactions.

As an example, for proton-proton collisions at the LHC instantaneous design luminosity of  $10^{34} \text{ cm}^{-2}\text{s}^{-1}$  and  $E_{cm} = 14 \text{ TeV}$  with 25 ns operation, there are approximately 23 hard interactions per crossing on average. Therefore, about that mean number of primary vertices will be reconstructed for each event.

Apart from the primary interactions in the collision point, there are other interactions inside the detector volume. These secondary interactions can be identified by reconstructing their vertices, which are called, accordingly, secondary vertices. They are reconstructed from tracks left by particles that are the decay products of a variety of other particles, such as tau-leptons, strange hadrons, photon conversions and nuclear interactions. Looking at the charged decay products is one way of detecting neutral particles in trackers.

The tracker is immersed in a magnetic field, for which usually strong magnitude and uniform distribution are desired. For instance, the ATLAS Experiment Tracker has a 2 T magnetic field, while the CMS Experiment Tracker has a 4 T one. A stronger magnetic field usually implies a better momentum resolution. However, a strong field requires more material for the magnet, which in turn has a negative impact on the global efficiency of the detector, in particular of the sub-systems that are located outside the magnet.

Charged particles describe a spiral trajectory when they move inside a magnetic field, which projects to a circle in the plane transverse to the magnetic field. The curvature of this circumference is proportional to the transverse momentum:

$$p_T[\text{GeV}/c] \approx 0.3 \times B[\text{T}] \times R[\text{m}] \quad (2.1)$$

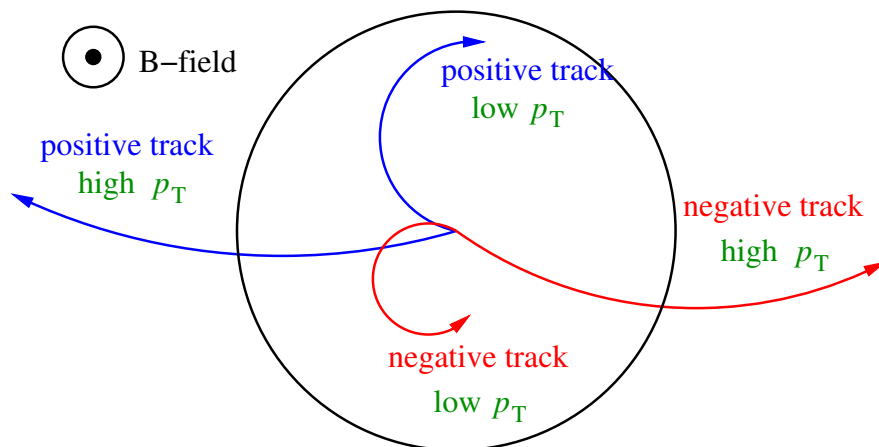


**Figure 2.1: Particle track deflection in the transverse plane due to a perpendicular magnetic field.**

Figure 2.1 shows the effect of the magnetic field in the deflection of the particles, depending on their charges and the magnitude of the transverse momentum. The magnetic field is perpendicular and pointing “outside of the paper”. With such orientation of the magnetic field, the sense of rotation of the tracks is clockwise for positively charged particles and counter-clockwise for negative particles. The radius of the curvature is greater for high momentum and vice-versa.

### 2.2.1 Track Parameterization

The track parameters are described with respect to a given coordinate system. Usually the  $z$  axis is the longitudinal axis, following the beam line, while the  $x$  axis points horizontally to the centre of the accelerator ring (in circular accelerators, like the LHC) and the  $y$  axis points vertically. The coordinate system is depicted in Figure 2.2.

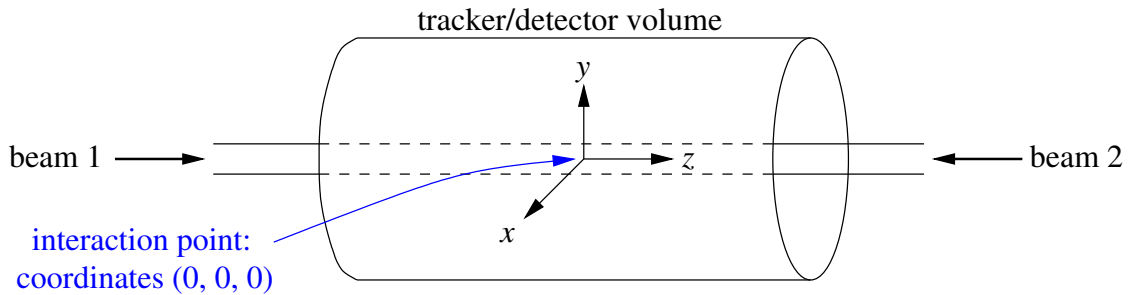


**Figure 2.2: Coordinate system in a tracker.**

With the usual approach of a magnetic field orientation parallel to the  $z$  axis, charged particles describe a circumference in the axial plane. By measuring the curvature perpendicular to the magnetic field, the transverse momentum of the particle can be measured. The parameters that describe a track are also called *perigee parameters* and are depicted in Figure 2.3. Their definitions follow:

- The transverse impact parameter,  $d_0$ , is the distance from the origin of the detector to the track's closest approach (point of closest approach, or PCA, to the  $z$  axis) in the  $xy$  plane. The uncertainty in its resolution depends on the radial position of the active elements, and on the space point precision.
- The longitudinal impact parameter,  $z_0$ , is the distance from the origin of the detector to the track's closest approach in the  $Rz$  plane. Both the longitudinal and transverse impact parameters can be defined with respect to a primary vertex instead of the origin.
- The azimuthal angle ( $xy$  plane) at the point of closest approach,  $\phi$ . It is the angle formed by the  $x$  axis and the line between the origin and the PCA.
- The polar angle,  $\theta$ , is the angle of the track momentum vector with the  $z$  axis.
- The pseudorapidity,  $\eta = -\ln \tan(\theta/2)$ . It is just a different way of expressing the polar angle.
- The transverse momentum,  $p_T = p \sin \theta$ . It is the projection of the momentum vector in the  $xy$  plane.
- The charge,  $q$ , is defined by the sense of rotation of the helix in the  $xy$  plane. Usually the charge over the momentum vector magnitude,  $q/p$ , is used.

These definitions are used in the ATLAS experiment. Other experiments may use different notation or definitions.

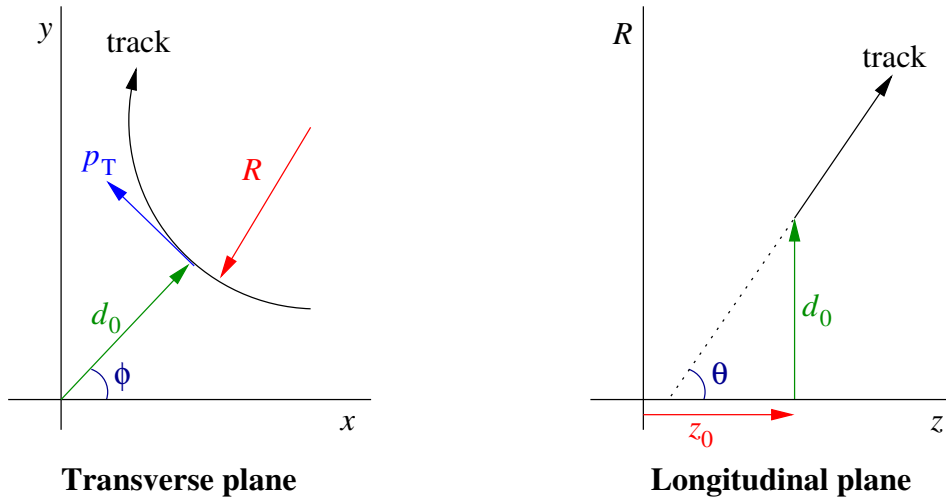


**Figure 2.3:** Illustration of the track parameters in the transverse ( $xy$ ) and longitudinal ( $Rz$ ) planes.

### 2.2.2 Resolution

There are a number of uncertainty sources in the aforementioned parameters, such as the position measurement precision, the precise knowledge of the magnetic field configuration and the contribution that comes from multiple scattering in the tracker material. The uncertainties limit the resolution of the track reconstruction process. The position measurement can be improved through a good alignment of the detector, first during the assembly and after by measuring the actual position of the detector elements over time.

In actual trackers, the magnetic field is not homogeneous. Although the momentum measurement through curvature is still proportional to the magnetic field strength, the field has to be mapped inside the tracker and numerical methods are used to interpolate between points in the field and to integrate the field along the particle trajectory. The parameters are defined locally, depending on the coordinate along the trajectory, yet there is still some bias on the momentum measurement after these adjustments.

One of the most important sources of uncertainty is multiple scattering in the material. When a charged particle traverses a medium, it is deflected by many small angle scatters. Most of these deflections are caused by Coulomb scattering in the nuclei and, for hadrons, the strong interaction is an additional contribution to multiple scattering.

For an incident particle on a layer with thickness  $x/X_0$  radiation lengths, assuming the projected angular distribution is Gaussian, its width is given by the following formula [7].

$$\theta_0 = 13.6 \text{ MeV} \frac{z}{p\beta c} \sqrt{\frac{x}{X_0}} \left( 1 + 0.038 \ln \left( \frac{x}{X_0} \right) \right) \quad (2.2)$$

Where  $p$  is the momentum,  $\beta c$  is the velocity and  $z$  is the charge number of the incident particle. Scattering is lower with high momentum particles.

Minimizing the amount of material is essential in order to reduce multiple scattering and other interactions inside the tracker volume. However, since there are a number

of services inside the tracker, such as supporting structures, cooling, electricity and data input/output, the minimization has a limit. The amount of material is initially calculated from the engineering plans and by knowing all the material properties and position of all the pieces. With this information, the whole detector can be simulated and, for an accurate simulation, the material interactions have to be considered.

With multiple scattering in mind, there are several parameters resolutions to be considered.

The impact parameters resolutions,  $\sigma_{d_0}$  and  $\sigma_{z_0}$ , are driven by local misalignments of the tracker, namely the radii and space point precision of the layers. For the simplified case of only two measurement layers, the resolution on the impact parameter, due to only geometrical uncertainty, is [6, 8]

$$\sigma_{d_0}^2 = \frac{r_2^2 \sigma_1^2 + r_1^2 \sigma_2^2}{(r_2 - r_1)^2} \quad (2.3)$$

Where  $r_i$  are the radii of the two layers and  $\sigma_i$  are the intrinsic measurement errors. In addition, the measurement precision is also degraded by multiple scattering:

$$\sigma_{d_0} = \sqrt{\frac{r_2^2 \sigma_1^2 + r_1^2 \sigma_2^2}{(r_2 - r_1)^2}} \oplus \frac{r}{p \sin^{3/2} \theta} 13.6 \text{ MeV} \sqrt{\frac{x}{X_0}} \quad (2.4)$$

At low momentum, the resolution is driven by multiple scattering in the beam pipe and the first layers of the tracker. For high momentum ( $\gtrsim 10 \text{ GeV}/c$ ), there is an asymptotic limit determined by the intrinsic tracker resolution and misalignments [9].

Figure 2.4 depicts a track with several hits and the curvature radius is calculated from the sagitta,  $s$ , and the distance between planes or path length,  $L$ :

$$R = \frac{L^2}{2s} + \frac{s}{2} \quad (2.5)$$

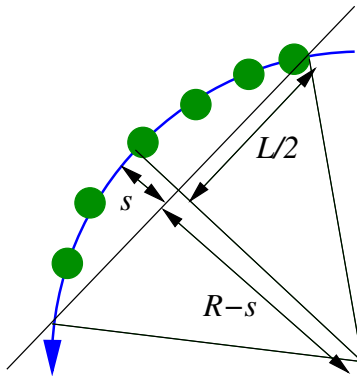


**Figure 2.4: Measurement of the track curvature.**

The relative uncertainty in the transverse momentum is proportional to the transverse momentum itself,  $p_T$ , and the sagitta uncertainty,  $\sigma_s$ . It is also inversely proportional to the magnetic field magnitude and the path length:

$$\frac{\sigma_{p_T}}{p_T} = \frac{8p_T}{0.3BL^2} \sigma_s \quad (2.6)$$

The sagitta uncertainty decreases with increasing number of points, each of them with a resolution  $\sigma_{r\phi}$ :

$$\sigma_s = \sqrt{\frac{A_N}{N+4} \frac{\sigma_{r\phi}}{8}} \quad (2.7)$$

Where  $A_N = 720$  [10] is the statistical factor. The point error  $\sigma_{r\phi}$  has a constant part that comes from the intrinsic resolution and a multiple scattering part. The multiple scattering contribution enters the sagitta uncertainty as

$$\sigma_s \propto \frac{L}{p_T \sin^{1/2} \theta} \sqrt{\frac{L}{X_0}} \quad (2.8)$$

Finally, a precise and reliable reconstruction of the track direction, that is, the angular resolution ( $\theta$  and  $\phi$ ), is an important contribution to the momentum vector determination. Therefore, the angular resolution is vital for the search of decay vertices and for matching the tracker signal with signals coming from other sub-detectors [9].

### 2.2.3 Track Fitting

The pattern recognition provides a series of measurements along a particle trajectory, together with a first estimation of the track parameters. The track fitting is responsible for computing the best possible estimation of those track parameters.

There are two widely used track fitting techniques, which are the global least squares fit and the Kalman filter. They will not be discussed in detail here.

The global least squares fit [11] minimizes the  $\chi^2$  function:

$$\chi^2 = \sum_{i=1}^{N_{\text{hits}}} \left( \frac{\Delta_i}{\sigma_i} \right)^2 + \sum_{i=1}^{N_{\text{layers}}} \left( \frac{\theta_{\text{scat}}^2}{\sigma_{\text{scat}}^2} + \frac{(\sin \theta_{\text{local}})^2 \phi_{\text{scat}}^2}{\sigma_{\text{scat}}^2} \right) \quad (2.9)$$

The first term of the equation is the sum of all detectors hits of the residuals,  $\Delta_i$ , divided by the measurement error,  $\sigma_i$ . The second part of the equation implements the possible changes in the track direction using the scattering angles,  $\phi_{\text{scat}}$  and  $\theta_{\text{scat}}$ .  $\theta_{\text{local}}$  is the angle between the track and the  $Z$  axis at the scattering plane. The factor  $\sin \theta_{\text{local}}$  is needed because  $\phi_{\text{scat}}$  is defined in the  $x-y$  plane. The scattering angles enter the algorithm initialized to zero and the error,  $\sigma_{\text{scat}}$ , is calculated from the traversed material thickness [12, 13].

The other technique is the Kalman filter [14], which actually does least squares fitting, with an iterative process of stepping from one measurement to the next, extrapolating the parameters from the previous step to the next measurement surface to calculate a prediction of the track state at that surface. This method results in a fast algorithm, as it does not require to invert large matrices. The least squares fitting involves the inversion of a  $N \times M$  matrix with  $N$  the number of fit parameters and  $M$  the number of measurements and the number of scattering angles that have been used in the fit [12].

There are three steps in the Kalman filter method: prediction using the track parameters and their covariance matrix in every step, filtering by updating the track parameters with the current hit measurement and smoothing by backwards propagation of the previously filtered points [15].

After the tracks have been fitted, the vertices may be reconstructed, through fitting of the tracks to common points of origin. Constrains such as invariant mass or momentum vector direction may be applied. The fast vertex fitting method, also known as the Billoir algorithm, is described in [16]. It uses the fitted tracks parameters and their errors,  $\Delta q_i = q_i^{\text{measured}} - F(\mathbf{V}, \vec{p}_i)$ , to find the vertex position ( $\mathbf{V}$ ) and momentum vectors of the associated tracks ( $\vec{p}_i$ ) that minimize

$$\chi^2 = \sum_{i=1}^{N_{\text{tracks}}} \Delta q_i^T V_i \Delta q_i \quad (2.10)$$

The algorithm operates with small matrices, what leads to a computational complexity of order  $N_{\text{tracks}}$ , in contrast to the least squares method, which requires  $N_{\text{tracks}}^3$  operations.

Additional information on track fitting and vertex fitting techniques is available in [17].

## 2.2.4 Alignment

The accuracy with which particle tracks can be reconstructed is highly dependant on how well the positions and orientations of the tracker sensors are known. This is, in turn, limited by the precision of the assembly process and the stability of the structures holding the tracker in place.

Usually, the intrinsic resolution of the tracker is better than the precision of the assembly. Additionally, the position of the detector elements may vary over time due to the effect of the magnetic field and other environmental effects, such as temperature variations inside the volume [18]. As a consequence, the alignment has to be surveyed periodically, to account for possible deformations or movement of the elements in the tracker volume, even right after the assembly.

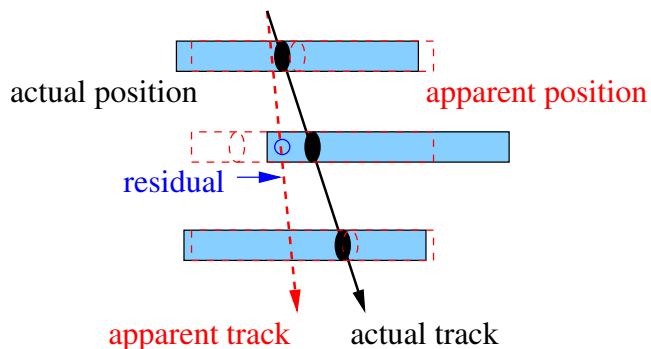


**Figure 2.5: Track hits residuals.**

The basis of the track based alignment algorithms is the minimization of the sum of hit residuals  $r$  from high momentum tracks, which have lower multiple scattering distortion. A residual is defined as the distance between the position of the measurement and the intersection of the fitted track with that module, see Figure 2.5.

The alignment algorithms use six constants for every independent module or structure, resulting in six degrees of freedom of a rigid body: three translations with respect

to the nominal position and three rotations with respect to the nominal axis orientations. Module deformations such as twisting and bending are ignored. The alignment constants can be determined by minimizing the  $\chi^2$  function [9]:

$$\chi^2 = \sum_{\text{tracks}} \vec{r}^T V^{-1} \vec{r} \quad (2.11)$$

Where  $V$  is the track covariance matrix and  $\vec{r}$  is the residuals vector for a given track, which is a function of both the track parameters and the alignment constants.

The use of several types of tracks may be required, depending on the geometrical distortion mode to be constrained. This is because minimization of the residuals might not be sufficient to guarantee a correct alignment. Some global distortions preserve the helical trajectory of the tracks but bias the track parameters, while not affecting the  $\chi^2$ .

These are called weak distortion modes, shown in Figure 2.6, and they represent a great danger to physics results. For instance, elliptical distortion affects the measurement of the vertices masses.

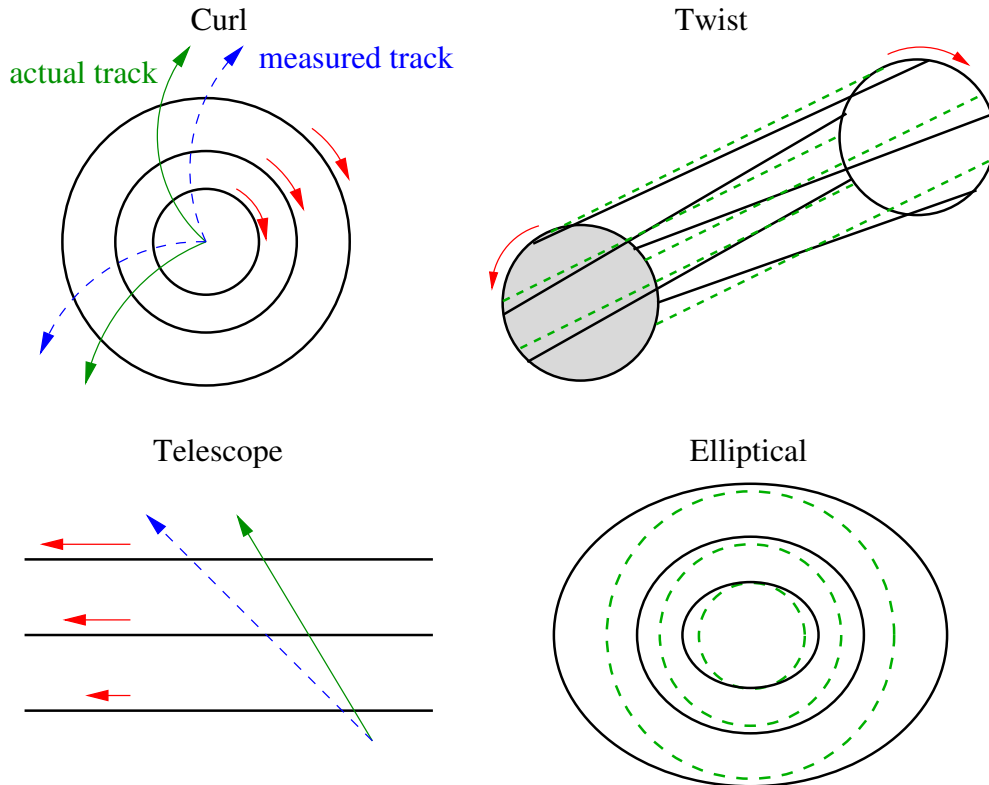


**Figure 2.6:** Weak modes of geometrical distortions [19].

Weak modes are difficult to remove and require different track topologies. Some ways to constrain these weak modes are:

- Cosmic ray tracks provide a continuous helical trajectory across the whole tracker. In addition, a large fraction of cosmic rays cross the tracker far from the beam axis, what provides additional constrains not available with the tracks coming from the interaction point.



- Tracks passing through the overlapping regions of adjacent modules help constrain the circumference of cylindrical arrangements, improving the determination of the average radial position of the modules.
- Reconstruction of the invariant mass of track pairs from  $Z$  and  $J/\Psi$  decays provides sensitivity to systematic correlation between separate detector elements.
- Survey measurements provide additional information.

See [2] and [19] for further details. A brief description of the alignment in the ATLAS tracker is given in section 2.4.3.

## 2.3 Silicon Trackers

### A Short Introduction to Detectors

The principle of operation of a detector is the transfer of part or all of the radiation energy carried by the particles to the detector mass. This energy transfer is a process that converts the radiation energy to some other form of energy that is processable by other means, for instance, electric signals. Charged particles transfer their energy by means of direct collisions with electrons in the atoms of the detector material. The form in which the energy appears after its conversion in the detector is dependent of the detector type and its design [20].

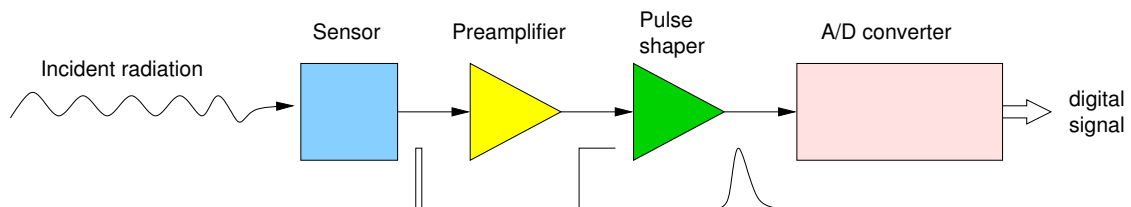


**Figure 2.7: Basic detector scheme: from radiation absorption in the sensor to digitization of the event.**

Semiconductor detectors are based on crystalline semiconductor material and generate electric signals that can be processed with electronic technology. The most frequent semiconductor materials used for charged particle detection are silicon and germanium. Their operation principle is analogous to gas ionization detectors: the creation of electron-hole pairs in the material mass during the passage of ionizing radiation.

The band gap of any material is the energy difference between the valence and the conduction band, as shown in Figure 2.8. In conductors, such as copper, the separation is very small or non-existent, while insulators have a very large gap. Semiconductors have a smaller band gap, a few electronvolts, which is the energy required to create an electron-hole pair. Silicon has a band gap of 1.12 eV, with an ionization energy of 3.6 eV. In comparison, gas detectors have an ionization energy of around 30 eV.

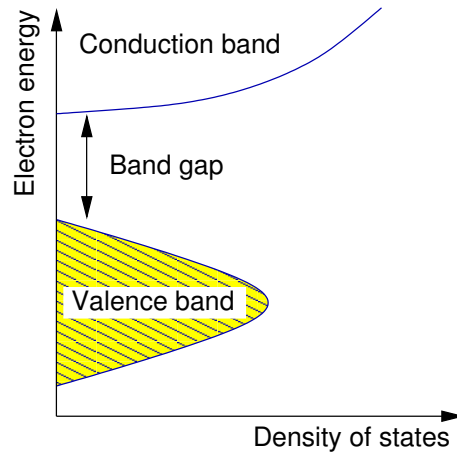


Figure 2.8: Semiconductor band structure.

**How are semiconductors used in particle detection?**

A semiconductor detector is, essentially, a p-n junction. The p and n regions are electrically neutral by themselves, but, when they are part of a p-n junction, thermal diffusion drives holes and electrons across the junction. This leads to a net positive charge in the n region, which in the end results in a built-in potential,  $V_{b-i}$ , as shown in Figure 2.9. In this situation, the Fermi levels of each region,  $E_{F_n}$  and  $E_{F_p}$ , determine the built in potential, as  $V_{b-i} = E_{F_n} - E_{F_p}$ . The diffusion of holes and electrons leads to an area free of mobile carriers, named the “depletion region”. Strictly speaking, the depletion area is not completely empty of mobile carriers, as the diffusion profile is a gradual transition instead of an abrupt one.

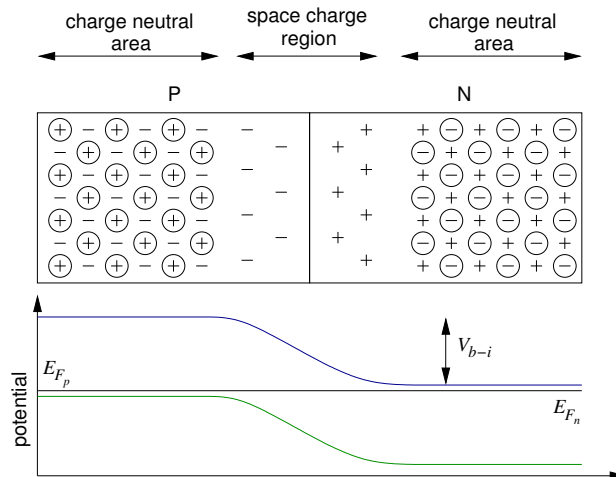


Figure 2.9: A p-n junction under thermal equilibrium.

The number of free carriers in the junction when it is under thermal equilibrium, that is, unbiased, is several orders of magnitude larger than the number of electron-hole pairs that are generated by a Minimum Ionizing Particle (MIP) passing through the silicon. For instance, the carrier concentration in intrinsic silicon is around  $1.45 \times 10^{10} \text{ cm}^{-3}$ . In a volume  $1 \text{ cm} \times 1 \text{ cm} \times 300 \text{ }\mu\text{m}$ , there are  $4.5 \times 10^8$  free carriers, while a

minimum ionizing particle generates  $3.2 \times 10^4$  electron-hole pairs. The signal to noise ratio (SNR) in this case is very low.

However, when the junction is reverse biased, the depletion region widens across the whole p-n junction. When the bias reaches the “depletion voltage”, the complete volume is devoid of free carriers and all the material is sensitive to ionizing particles. In addition, the reverse bias adds an electric field that helps the collection of the generated electron-hole pairs. A minimum ionizing particle traversing the volume will leave some energy behind and create a number of electron-hole pairs proportional to that energy. As a result, the SNR increases significantly.

The electron-hole pairs drift due to the electric field present in the semiconductor junction, inducing an electrical current. The charge collection process is depicted in Figure 2.10 [21]. Because the average energy required to produce an electron-hole pair in semiconductors is an order of magnitude smaller than gas ionization detectors, semiconductor detectors have a greater energy resolution.

The energy may be calculated by integrating the signal current that is induced in the electrodes.

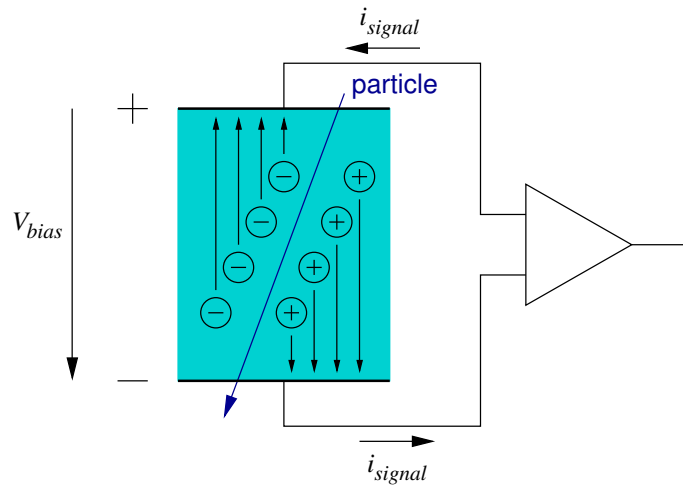


**Figure 2.10:** Description of the charge collection concept.

In order to be able to estimate the energy deposited by the traversing particle, some discretization of the collected charge has to be done. Some detectors aim at measuring not the energy of the particles, but if a particle has gone through, so this information is usually not available as it is not necessary. Thus, there are two options when designing the detector:

- If the goal is to know the path of a particle (tracking) through a volume, then the output of the detector would be “measured some charge above threshold”. The threshold is usually set so noise is minimized and efficiency is maximized. This is called binary read-out.
- If the goal is to know the energy deposited by a particle traversing the volume, then the amount of charge that is generated needs to be measured somehow. The charge generated in the detector volume is proportional to the deposited energy:

$$Q = \frac{E}{E_i} e \quad (2.12)$$

Where  $E$  is the absorbed energy and  $E_i$  is the ionization energy, which for silicon it is  $E_i = 3.6$  eV. An approximation for the ionization energy as a function of the band gap energy is [21]

$$E_i \approx 2.8E_g + 0.6 \text{ eV}$$

The absorbed energy is proportional to the amount of material that the particle traverses, so the thickness of the semiconductor material is also a parameter to be considered for two reasons:

- Thicker material results in higher absorbed energy, what increases the energy resolution. Even if energy resolution is not important, charge collection efficiency is also increased as more electron-hole pairs are generated by minimum ionizing particles for thicker material.
- But low material is needed in order to reduce multiple scattering in the material. Multiple scattering is a major contributor to momentum measurement uncertainty for low momentum, up to several tens of GeV/ $c$  transverse momentum [22].

Apart from the material, the absorbed energy depends on the type of material, which is fixed, and the type of particle: electrons, muons, protons, etc. This is related to the  $dE/dx$  or differential energy loss, described by the Bethe-Bloch formula. This topic is discussed in detail in chapter 6.

### Why Silicon?

There are several advantages of silicon over other semiconductor materials. To begin with, it is very abundant in the Earth's crust [23], orders of magnitude above the other semiconductors' constituents, as can be seen in Table 2.1. Another important advantage of silicon is the fact that it is one of the main materials used in everyday electronic technology. Therefore, the development of the production techniques is well advanced, leading to low production cost, which is always desirable.

Element	Fraction	Element	Fraction	Element	Fraction
<b>Silicon</b>	0.283	Zinc	$7 \times 10^{-5}$	Cadmium	$2 \times 10^{-7}$
Aluminium	0.083	Gallium	$1.5 \times 10^{-5}$	Indium	$10^{-7}$
Phosphorus	0.001	Germanium	$5 \times 10^{-6}$	Mercury	$8 \times 10^{-8}$
Sulfur	$2.6 \times 10^{-4}$	Arsenic	$1.8 \times 10^{-6}$	Selenium	$5 \times 10^{-8}$
Carbon	$2 \times 10^{-4}$	Antimony	$2 \times 10^{-7}$	Tellurium	$1 \times 10^{-9}$

**Table 2.1: Abundance of semiconductor constituents in the Earth's crust.**

Regarding the physical properties of silicon, they are summarized in the following list [24]:

- It has a small band gap,  $E_g = 1.12$  eV, with an ionization energy of  $E_i = 3.6$  eV.
- It has a high specific density, which increases the absorbed energy ( $dE/dx$ ), generating more electron-hole pairs for a minimum ionizing particle.

- Despite that high density, it has a high carrier mobility, which allows fast charge collection, in the order of 10 nanoseconds over hundreds of micrometres of fully depleted silicon.
- It is very pure, with less than 1 part per million impurities and less than 0.1 parts per billion electrically active impurities.
- Its rigidity is appropriate for constructing thin, self-supporting structures.

	Diamond	SiC	GaAs	Ge	Si
Z	6	14/6	31/33	32	14
$E_g$ [eV]	5.5	3.3	1.42	0.66	1.12
$E_i$ [eV]	13	7.6 – 8.4	4.3	2.9	3.6
density [g/cm <sup>3</sup> ]	3.515	3.22	5.32	5.32	2.33
$\mu_e$ [cm <sup>2</sup> /Vs]	1800	800	8500	3900	1450
$\mu_h$ [cm <sup>2</sup> /Vs]	1200	115	400	1900	450

**Table 2.2: Some physical characteristics of semiconductors.**

Some of the physical properties of silicon are compared to other semiconductor materials in Table 2.2. Although silicon does not have the best numbers for all the properties, they are more than adequate for detectors. The facts that the fabrication methods production are well known and that it is very abundant make it the preferred choice so far. However, research on alternatives, such as diamond, silicon carbide (SiC) and other compounds as detectors is a very active research field [25].

### Characteristics of Silicon Trackers

Semiconductor detectors are usually constructed on a substrate which is several centimetres long and wide. Depending on how the p-n junctions are implanted on the substrate, it is possible to have two types of detectors:

1. Pixel detectors are implemented as a matrix of p-n junctions, which are several micrometres long and wide.
2. Strip detectors are made by creating a straight pattern of wide p-n junctions separated by several micrometres.

For pixel detectors, spatial resolution depends only on the separation between the junctions but for strip detectors, a single row of strips will only give good resolution in one direction. In order to have spatial resolution in two directions, it is necessary to use another set of strips with certain subtended angle with respect to the first detector, having a double sided detector as shown in Figure 2.11.

The configuration shown in the figure has problems at high hit densities, because each hit generates an  $x$ - and a  $y$ -coordinate. That leads to  $n$  tracks generating  $n$   $x$ -coordinates and  $n$   $y$ -coordinates, simulating  $n^2$  hits, out of which  $n^2 - n$  are fake. Additional information is needed to eliminate coordinates not consistent with tracks. The area subtended by two sensing strips of length  $L$  in a  $90^\circ$  angle is  $A = L^2$ , which

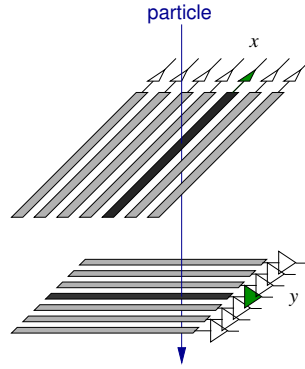


**Figure 2.11: Double sided strip sensor for two dimension positioning.**

provokes that a hit in a given strip may form combinations with hits in all the transverse strips. The solution to this problem is using “small-angle stereo”, where the subtended angle is (much) lower than  $90^\circ$ . Thus, if the subtended angle is  $\alpha$  and the strip pitch is  $p$ , the capture area is

$$A \approx L^2 \tan \alpha + Lp \quad (2.13)$$

The probability of multiple hits within this acceptance area is lower as  $\alpha$  is made smaller, but resolution in the longitudinal coordinate also deteriorates.

Position resolution is the spread of the reconstructed position of the particle hit with respect to the actual position. There are design parameters that influence this resolution. First, the pixel size or strip pitch determines the area sensitive to one particle hit. Once the size has been fixed, the signal to noise ratio (SNR) of the detector has an influence on analogue systems. The SNR is higher if the following conditions are met:

- Low detector capacitance, achieved with small pixels or short strips. The noise is directly proportional to the capacitance at the input of the front-end electronics.
- Low leakage current, which depends on the quality of the bulk material. The noise increases with the square root of the leakage current.
- Large bias resistor, in order to have a good inter-strip isolation and increase the integration time.
- Short and low resistance connection from the detector to the amplifier.

When analogue read-out is used, the position resolution is

$$\sigma_x \approx \frac{p}{1.5 \text{ SNR}} \quad (2.14)$$

For binary read-out with threshold counter, the resolution is estimated as

$$\sigma_x \approx \frac{p}{\sqrt{12}} \quad (2.15)$$

Typical SNR values in the electronics are from 15 to 40.

## Radiation Damage in Silicon

Semiconductors in general, and silicon in particular, are relatively sensitive to radiation damage. The damage is caused by the incident particles colliding with the crystal lattice atoms, causing point defects by “knocking” the atoms out of their normal positions.

The defects in the lattice give rise to discrete trapping levels in the forbidden band gap, that reduce the number of charge carriers in the semiconductor [20]. Effects observed from these defects caused by radiation include [26]:

- Leakage current increase, due to the defects acting as centres that increase the bulk current.
- Energy resolution decrease, as the defects are discrete trapping centres that reduce the number of charge carriers in the semiconductor and, in turn, at the electronics input.
- Reduction of the carrier mobility.
- Increase in the output pulse rise time or charge collection time, as a consequence of the charge trapping and the carrier mobility reduction.
- Actual material change, what is called “type inversion”: n type silicon turns into p type silicon. This happens because the radiation removes the donors and creates acceptors in their place. Type inversion occurs after a fluence of around  $10^{13} \text{ n}_{\text{eq}}\text{cm}^{-2}$  [27].

The leakage current increase can be estimated as [28]:

$$\Delta I = \alpha \Phi V \quad (2.16)$$

Where  $V$  is the volume of the silicon,  $\Phi$  is the radiation fluence and  $\alpha$  is the damage constant, which depends on the radiation type and its energy.

Heavy charged particles, protons and neutrons, can cause a large recoil energy to the silicon bulk, creating “clusters” of damage, apart from some isolated single defects. These clusters generate charge traps and leakage current increase. Lightly ionizing particles, such as electrons and minimum ionizing particles, cause primarily single defects.

Refer to [20, 26] for additional information on the damage constants.

This model is used to compare with the monitoring of the leakage current of the silicon detectors. An example of such monitoring during the first three years of operation is shown in section 2.4.1 for the ATLAS Semiconductor Tracker.

In addition to the radiation damage defects described above, heavy charged particles and fast neutrons produce vacancy clusters that are not entirely stable at room temperature. They “decay” or migrate to smaller vacancy aggregates, what is called annealing.

This effect was discovered after irradiating detectors, when the observed damage to the detector started decreasing with time, depending on what temperature the detector was kept at during the waiting period [24, 29].

Although this effect might be naively interpreted as a reduction in the radiation generated defects in the silicon and true annealing (the crystal becoming perfect again) actually exists, in many cases the defects may just be transformed into other stable defects [24].

## 2.4 The ATLAS Semiconductor Tracker

The Semi-Conductor Tracker (SCT) in the ATLAS Inner Detector covers the radial range from 299 to 514 mm, and  $z$  range up to  $\pm 2720.2$  mm, with four barrel layers and nine endcap discs to each side of the barrel.

There are 4088 modules in the SCT, split in 2112 modules in the barrel layers and 988 on each of the two endcaps. The micro-strip silicon modules for the SCT are of six different types, one on the barrel and five different types on the endcaps.

The barrel modules are all rectangular, with 768 read-out strips that have a  $80\ \mu\text{m}$  pitch. The modules are double sided, with the active strips of the two sides forming a  $40\ \text{mrad}$  stereo angle that provides the two-dimensional resolution. Each side holds two sensors with 768 strips, 6 cm long, which are daisy chained together with wirebonds in order to get 12 cm long active strips on each module.

The endcap discs layout makes the geometry of the sensors more complicated. The modules have a trapezoidal shape, with an interstrip angle that varies between  $161$  and  $207\ \mu\text{rad}$  and a strip pitch that varies from  $56.9$  to  $94.2\ \mu\text{m}$ . There are five sensor types, named W12, W21, W22, W31 and W32. All of them also have 768 strips, to comply with the read-out hybrid assembly that comprises the twelve ABCD3TA chips [30] (ABC stands for “ATLAS Binary Chip”). The hybrid is folded around the module so each side is read-out by six chips.

All sensors are p-in-n with a thickness of  $285 \pm 15\ \mu\text{m}$ , supplied by Hamamatsu Photonics and CiS. In principle, all the sensors were meant to be fabricated on  $\langle 111 \rangle$  silicon due to availability of supply [31], but 93 modules, 2.3% of the total, have sensors with  $\langle 100 \rangle$  silicon. The different crystal lattice structure has a small but measurable effect on the carrier mobility [32]. This difference also has an effect on the noise performance of the modules [33].

The sensors are glued back-to-back and the electronics mounted on a hybrid are glued and wirebonded to build the modules. The assembly includes the mounting frame, cooling, powering and data input/output.

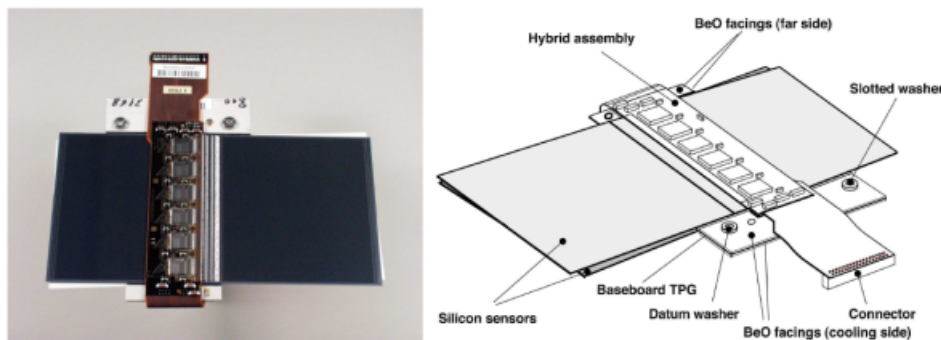


**Figure 2.12: SCT barrel module photograph and illustration, showing the sensors with the built-in stereo angle and the electronics.**

A barrel module is shown in Figure 2.12, both a photo of a fully assembled module and a drawing showing its components: the two silicon sensors, the hybrid, facings for the assembly and the connector for the electronics.

Three of the endcap module types are shown in Figure 2.13. The outer module is composed of W31 (top) and W32 (bottom) sensors, the middle module is composed of



W22 (top) and W21 (bottom) sensors and the inner module has only W12 sensors. A fourth type that is not shown is the short-middle, which only has W22 sensors [34].



**Figure 2.13:** SCT endcap module types (outer, middle and inner).

The strips read-out is made through the twelve chips mounted on each hybrid. This chip is the ABCD3TA [30], with 128 channels, performing the following functions:

- Charge integration.
- Pulse shaping.
- Discrimination.
- Compression and transmission of the data.
- Configuration of the thresholds and read-out modes.

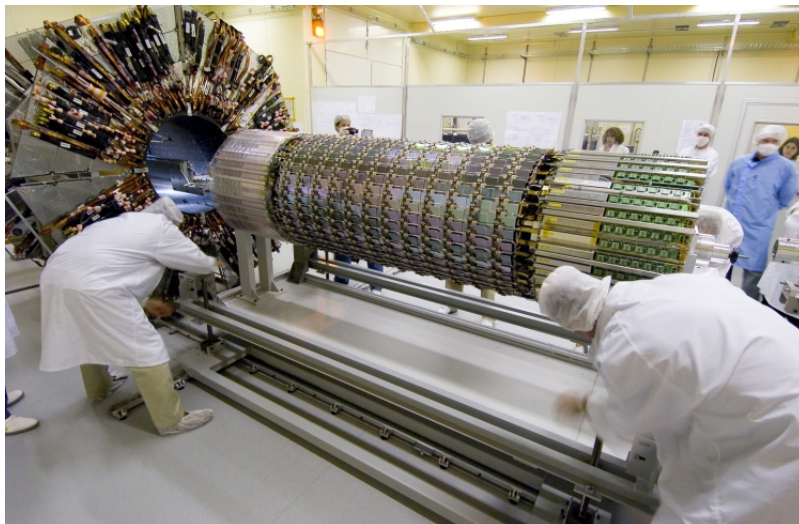


**Figure 2.14:** One of the SCT barrels during insertion into the Inner Detector.

The four SCT barrel layers are numbered from 3 to 6, continuing the Inner Detector layer numbering, from the three Pixel layers (numbered from 0 to 2). The two endcaps have nine discs, numbered from 1 to 9, and the two endcap sides are named “Endcap A” and “Endcap C”.

Figure 2.14 shows one of the SCT barrels during the insertion in the Inner Detector.

Figure 2.15 shows two sides of an endcap disc, one of the sides is populated by outer and inner modules and the other side by middle modules.

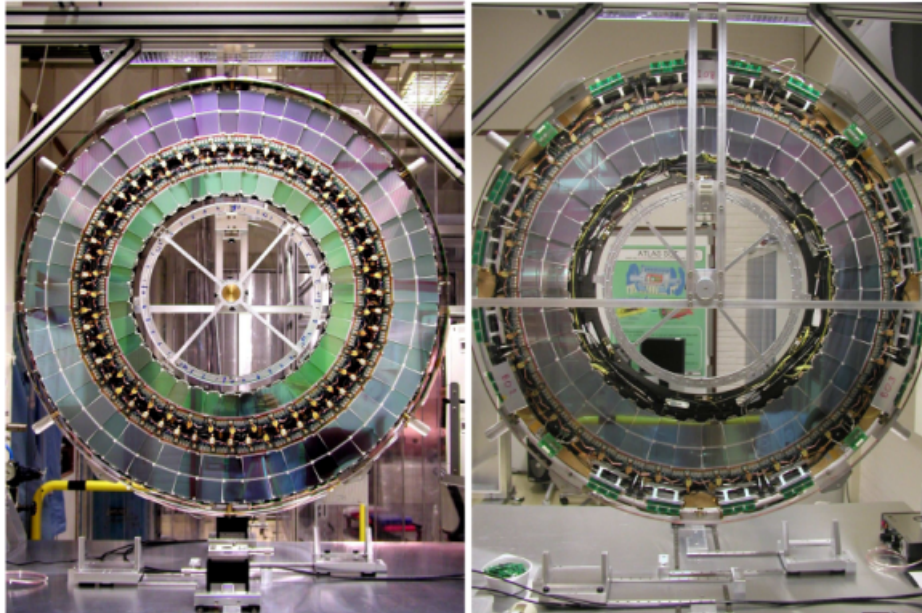


**Figure 2.15: SCT endcap modules mounted on endcap discs: left has outer and inner modules, right shows middle modules.**

The SCT sensors are required to operate stably up to 500 V bias and to have less than one percent bad read-out strips, before and after a neutron equivalent fluence of  $F_{\text{neq}} = 2 \times 10^{14} \text{ cm}^{-2}$ .

### 2.4.1 Tracking of the Radiation Damage in the SCT

The model for the leakage current increase with the radiation damage that was described before is compared against the actual monitored leakage current of the SCT modules.

Figure 2.16 shows the evolution of the leakage current for the four barrel layers, both the measurements and the prediction from the model [35]. The temperature profile of the sensors is also plotted, as well as the integrated luminosity. The data ranges from mid-2010 up to the beginning of 2013.

The plot shows the leakage current density in  $\mu\text{A}/\text{cm}^3$ , normalized to  $0^\circ\text{C}$ .

The temperature dependence of the leakage current follows the following scaling formula [36]:

$$\frac{I_{\text{ref}}}{I_T} = \left(\frac{T_{\text{ref}}}{T}\right)^2 \exp\left(-\frac{E_{\text{gen}}}{2k_B} \left(\frac{1}{T_{\text{ref}}} - \frac{1}{T}\right)\right) \quad (2.17)$$

Where  $T_{\text{ref}}$  is a reference temperature at which the leakage current is known,  $E_{\text{gen}} = 1.21 \text{ eV}$  is the effective generation energy in silicon and  $k_B$  is the Boltzman constant.

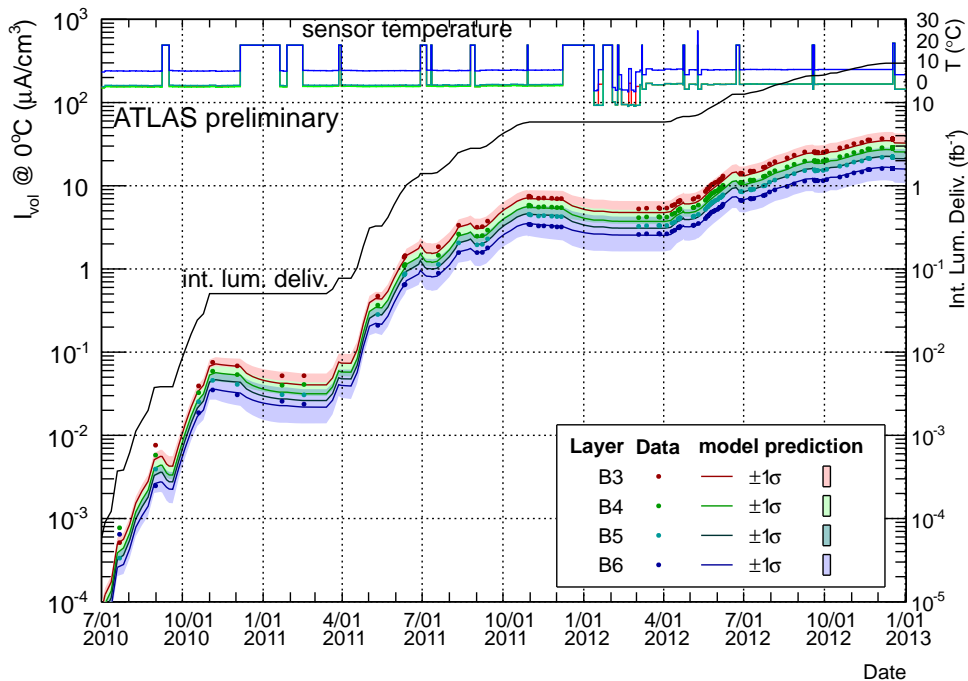


Figure 2.16: Leakage current evolution in the SCT over time [35].

## 2.4.2 Noise Performance

The performance of the silicon modules in terms of noise is usually measured through two main parameters, which are not independent: Equivalent Noise Charge (ENC) and Noise Occupancy (NO). This section only refers to the SCT sub-detector, however, the same performance measurements are applicable to the Pixel detector [9].

The Equivalent Noise Charge is defined as the number of electrons that have to be collected from the sensor in order to create a signal equivalent to the noise of the sensor.  $N$ -point gain scans are used to measure this noise, being usually  $N = 3$ . In this kind of scan a known, calibrated charge is injected for each point to the chip front-end and the discriminator threshold is varied. The occupancy of the strips decreases as the threshold is raised.

The voltage at the input of the discriminator is measured over a certain number of triggers. The noise is assumed to be Gaussian, therefore the voltage at the discriminator is fitted to a Gaussian distribution, with the mean and sigma values corresponding to the  $V_{t50}$  (named the 50% threshold) and the output noise ( $\sigma$ ).

This 50% threshold is plotted against the injected charge, leading to a response curve, of which the slope is called the gain ( $G$ ), usually measured in mV/fC. The calibration circuit of the ABCD3TA chip of the SCT modules is capable of injecting charges between 0.5 fC and 16 fC.

The aforementioned sigma of the distribution is the output noise, typically measured in mV. The input noise is the result of dividing this output noise by the gain and, since  $1 \text{ fC} \approx 6242 e^-$ ,

$$e^- \text{ENC} = 6242 [\text{fC}/e^-] \frac{\sigma [\text{mV}]}{G [\text{mV}/\text{fC}]} \quad (2.18)$$

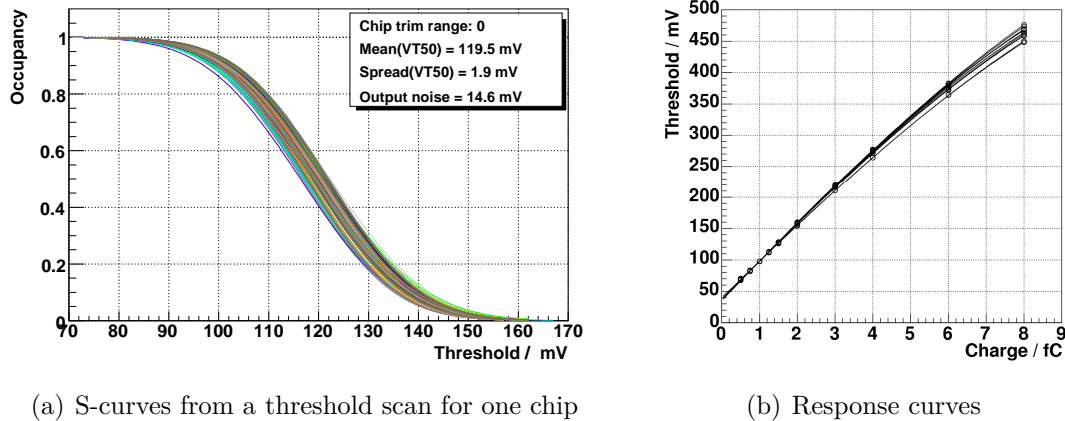


**Figure 2.17: Sample performance measurements on the SCT modules.**

When injecting a known charge, plots like those shown in Figure 2.17(a) are generated. This picture shows the s-curves from the threshold scan done on one chip. The vertical axis is the occupancy and the horizontal axis is the threshold setting. The output noise is the standard deviation of the threshold from the 50% occupancy and the  $V_{t50}$  is the threshold at which the occupancy is 50%. With  $N$  (at least 3) of these s-curves, the response curve can be plotted and the gain of the chip is calculated, leading to the input noise calculation as shown above. The plot in the figure was taken from [37].

In the SCT chip, the ABCD3TA, the gain has an average value of 55 mV/fC. The Noise Occupancy in the SCT is defined as the number of hits per event for an equivalent threshold setting of 1 fC. The ENC requirement of the SCT before irradiation is 1500 electrons r.m.s. and 1800 electrons r.m.s. for an irradiated module.

With the goal of keeping the noise in the SCT very low, the threshold is set at a level that suppresses the noise. However, a too high threshold will have a negative impact on the hit efficiency. The requirement for the SCT system is comes from a compromise between noise occupancy and efficiency, and it was established that the noise occupancy has to be below  $5 \times 10^{-4}$  hits per event, while maintaining 99% efficiency [9].

The noise occupancy is measured without an injected charge, as opposed to the equivalent noise charge.

As was mentioned before, by fitting the  $N$  points to a response curve, such as that shown in Figure 2.4.2, which is a 10 point gain scan. The slope is the gain of the chip and the intersection with the vertical axis (zero charge) is called the “offset”. The plot corresponds to the 12 chips on one whole SCT module [38]. When  $N = 3$ , specially in the low injected charge region, between 0.5 and 2.5 fC, the curve is well fitted to a straight line.

The noise is dependent on a number of parameters from both the sensor and the chip, such as:

- The amplifier input capacitance.
- The chip temperature.
- The sensor temperature.
- The sensor leakage current.

A complete noise model was developed to study the noise of the SCT modules, considering these contributions and how they enter the equation [39].

Before installation, the SCT barrels were tested and characterized in terms of noise, both ENC and NO. Figure 2.18 shows the noise distributions for each of the four barrels, tested “warm”, contrary to the usual operation temperature of  $-7^{\circ}\text{C}$ .

The values shown in the plot are conforming to the requirements, since the noise at the operation temperature will be about  $150 e^{-}\text{ENC}$  lower, accounting for a noise variation of  $d\text{ENC}/dT \approx 5 e^{-}\text{ENC}/\text{K}$  [38].

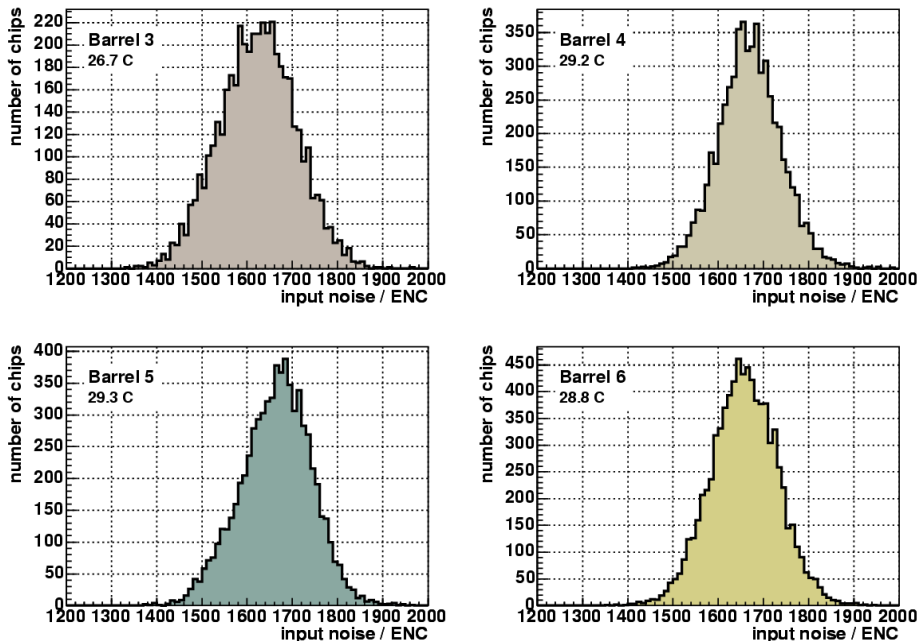


Figure 2.18: Average input noise per chip for the four SCT barrels.

Figure 2.19 represents the natural logarithm of the average noise occupancy in one chip, as a function of the threshold squared. This test is done by means of threshold scans without charge injection and the linear fit of the shown plot allows an estimation of the input noise of the modules.

The full description of the functional testing of the SCT barrels is available in [40]. The three-point gain test was performed with injected charges 1.5, 2.0 and 2.5 fC.

The concept of ENC and noise occupancy will be discussed again in chapters 4 and 7, in the context of the tracker upgrade modules performance.

### 2.4.3 Alignment and Resolution of the Tracker

The alignment of the Inner Detector takes place at four levels, using the widely extended residual minimization technique mentioned in section 2.2.4:

- Level 0 is the global alignment, in which large structures are aligned with respect to the entire pixel detector.
- Level 1 is part of the local alignment of the sub-detectors. The pixel barrels were split into upper and lower halves plus the two endcaps, while the SCT was split into the four barrel layers plus the two endcaps.

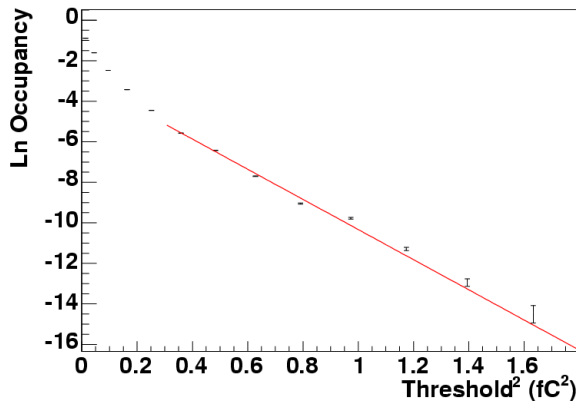


**Figure 2.19:** Noise occupancy of one front-end chip as a function of the discriminator threshold.

- Level 2 is the next step, in which the pixel and the SCT are aligned stave-by-stave. The SCT “staves” are not actual staves, but groups of 12 modules in a row, which are considered rigid bodies.
- Last, level 3 is the alignment at the module level. Although the pixel modules are assembled in staves and these were surveyed after the assembly took place, the deformation of the staves is expected to be larger than the survey errors.

Each level introduces additional degrees of freedom, but not all alignment parameters are used at every step. Also, the expected sizes of the corrections at each stage are smaller [9].

The goal is that the pixel modules must be aligned with a precision of 7  $\mu\text{m}$  and the SCT modules with a precision of 12  $\mu\text{m}$  in the  $R\phi$  direction. Both pixel and SCT barrel modules require an alignment precision of several tens of micrometres in the  $z$  direction, while the endcap modules require this precision in the  $R$  direction.

Parameter	Asymptotic resolution from cosmic ray data 2008
$d_0$ [ $\mu\text{m}$ ]	$22.1 \pm 0.9$
$z_0$ [ $\mu\text{m}$ ]	$112 \pm 4$
$\phi_0$ [mrad]	$0.147 \pm 0.006$
$\theta$ [mrad]	$0.88 \pm 0.03$
$q/p$ [ $(\text{GeV}/c)^{-1}$ ]	$(4.83 \pm 0.16) \times 10^{-4}$

**Table 2.3:** Track parameter resolution for tracks with  $p_T > 30$   $\text{GeV}/c$  from cosmic ray data.

In addition to the minimization of residuals using tracks in the detector, a Frequency Scanning Interferometry system is installed in the SCT to monitor variations in the shape of the detector. Refer to [41] for further details on the FSI system.

The resolution of the track parameters in the Inner Detector were predicted using cosmic ray data. Since particles originating from cosmic ray showers mostly traverse the detector from top to bottom, it is only possible to assess the resolution for the

barrel layers. The resolution of the parameters excluding multiple scattering can be measured by taking tracks with  $p_T > 30 \text{ GeV}/c$ . These are shown in Table 2.3, taken from [9].

The momentum resolution is key in physic analyses. For the Inner Detector, the  $q/p$  resolution is flat in the pseudorapidity range  $|\eta| < 1$ , although it degrades at high transverse momentum,  $p_T \gtrsim 10 \text{ GeV}/c$  [9].





# Chapter 3

## Upgrades at the LHC

### 3.1 Motivation

The Large Hadron Collider operations began in 2010, with an outstanding performance until early 2013. First, during 2010 and 2011 at a centre of mass energy of  $\sqrt{s} = 7$  TeV and after, in 2012, at  $\sqrt{s} = 8$  TeV. During this period, it has delivered a total integrated luminosity close to  $26 \text{ fb}^{-1}$ , allowing the two general purpose experiments, ATLAS and CMS, to record an integrated luminosity of around  $25 \text{ fb}^{-1}$  [42].

Two planned shut-downs will be used to increase the performance of the machine and to reach its design luminosity and collision energy of  $\sqrt{s} = 14$  TeV. In addition, the four experiments will perform consolidation work to enhance their performance and to fix possible problems appeared during operation. These are called the first long shut-down, LS1, taking place during 2013 and 2014, and the second long shut-down, LS2, which will take place during 2018. The two are part of the Phase-0 Upgrade and Phase-I Upgrade, respectively.

After these two shut-downs, the next step involves a full replacement of the accelerator and major updates to the experiments.

This chapter briefly describes LS1 and LS2, and gives a longer overview of the major upgrade of the ATLAS experiment at the LHC.

#### 3.1.1 Long Shut-down 1

After the first long shut-down, LS1, from 2013 to 2014, the centre of mass energy will be increased to  $\sqrt{s} = 13\text{-}14$  TeV, the number of bunches per beam will increase from 1380 to 2808 and the bunch spacing will be reduced from 50 to 25 ns. With these modifications, the instantaneous luminosity will reach  $10^{34} \text{ cm}^{-2}\text{s}^{-1}$  from 2015. The expected integrated luminosity delivered until the next shut-down will be around  $100 \text{ fb}^{-1}$  [43].

In order to achieve this goal, consolidation works are taking place during LS1 on the splices at the magnets interconnections [44].

Some experiments will also perform upgrade works of some of their sub-systems during LS1.

In the case of ATLAS [43], a new pixel layer, called Insertable B-Layer (IBL), is going to be installed in the pixel detector. It will be placed between the existing first pixel layer and the beam pipe, at a radius of 33 mm. As a consequence, the beam pipe is also replaced with a smaller radius one: from 39 mm down to 23.5 mm [45].

New front-end electronics, optical transceivers and read-out systems have also been developed for the IBL.

In addition to the new layer, the pixel detector will deploy new service quarter panels. The initial motivation for it was to move the optical transmitters away from the inaccessible parts of the pixel detector and it finally received some extra improvements for the whole sub-system [46]. These new service panels have been designed to take services out of the pixel volume, thus reducing material.

The SCT will see a rearrangement of the read-out drivers with an increase from 90 to 128 RODs to cope with the pile-up increase after the shut-down. The expansion could allow a  $\langle\mu\rangle$  up to 80 at a level 1 trigger rate of 100 kHz, compared to the SCT design target of  $\langle\mu\rangle = 23$ . In addition, all the off-detector optical transmitters will be replaced with a new solution [47]. These transmitters are used to send the Timing, Trigger and Control (TTC) signals to the SCT modules and the original devices have experienced low reliability [48].

The cooling plant for the pixel and the SCT will be modified to an evaporative cooling system and the IBL will use CO<sub>2</sub> based cooling.

On the calorimeters, all low voltage power supplies will be changed.

### 3.1.2 Long Shut-down 2

A second long shut-down will take place in 2018 to do upgrades to the collimators and injectors, preparing some systems for the high luminosity LHC [49]. After these upgrades, the LHC will pursue the goal of attaining twice its design instantaneous luminosity, reaching  $2.2 \times 10^{34} \text{ cm}^{-2}\text{s}^{-1}$ . This will allow the LHC to deliver between 300 and 400 fb<sup>-1</sup> in its whole operations period, ending in the early 2020s [43].

To achieve this goal, there will be an injector upgrade, integrating the new Linear accelerator, Linac4 [50], into the injector chain, also increasing the energy of the PS Booster and upgrading the collider collimators [51].

On the experiments side, the upgrades planned so far for LS2 are the following:

- ATLAS will upgrade its muon system, with the introduction of a New Small Wheel (NSW). The Level 1 trigger will also be improved, both in the muon spectrometer and the electromagnetic and forward calorimeters [51]. One of the requisites for this upgrade phase is that they have to be fully compatible with the physics programme of the Phase-II upgrades after the third long shut-down.
- CMS will completely replace its pixel system [52] and upgrade the Level 1 trigger system [53, 54].
- LHCb will replace the Vertex Locator (VELO) and the silicon strips tracker, and upgrade the read-out system to support a flexible Level-0 trigger. These upgrades will cover the operations beyond the third long shut-down [55].
- ALICE will install a new silicon tracker around a very small beampipe. Also, the Time Projection Chamber (TPC) will be upgraded as well as the electronics for the other sub-detectors, and a minimum bias trigger will be implemented [56].

Depending upon the performance and issues that could arise during operation in the 2015-2018 period, other updates may be needed.

### 3.1.3 LHC End of Life

The expected integrated luminosity delivered by the current Large Hadron Collider is around 300 to 400  $\text{fb}^{-1}$  through the ten years of operation that will end in 2022. By that time, the LHC will be facing the degradation of its components due to the accumulated radiation damage [44] and also parts of the experiments will need replacing.

Figure 3.1 shows the expected integrated luminosity of the LHC until the third long shut-down (LS3), when the LHC replacement will be deployed. This replacement of the accelerator is described in the following section.

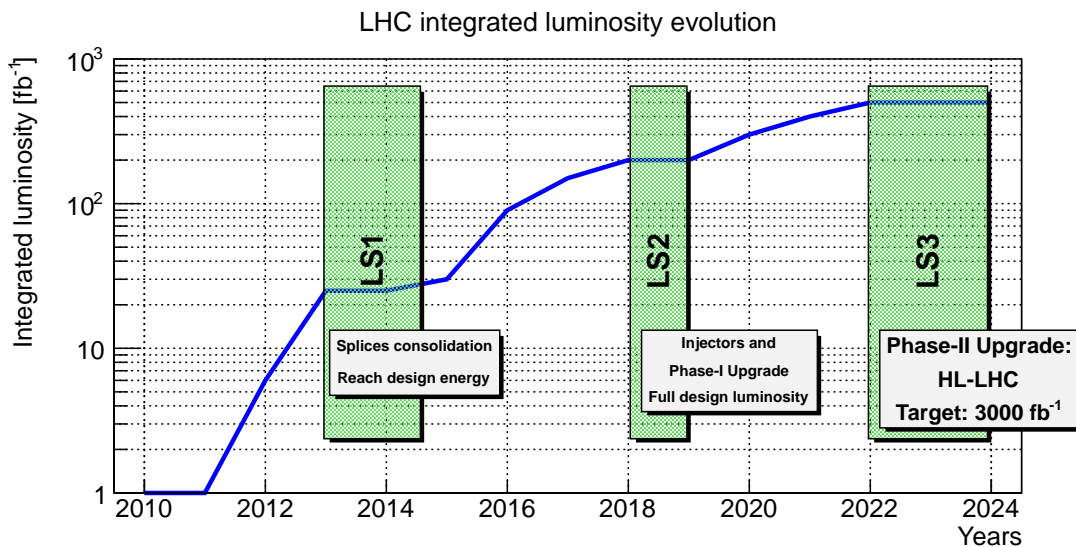


Figure 3.1: Possible integrated luminosity evolution for the LHC with the foreseen three long shut-downs superimposed [44].

## 3.2 High Luminosity Large Hadron Collider

The LHC evolution beyond LS3 is called High Luminosity Large Hadron Collider (HL-LHC). The design goal for integrated luminosity over its lifetime is over 2500  $\text{fb}^{-1}$ , up to 3000  $\text{fb}^{-1}$ , with peak luminosity increasing five times with respect to the LHC design, while maintaining the 14 TeV centre of mass energy. With this goal, the whole LHC+HL-LHC programme is expected to deliver over 3000  $\text{fb}^{-1}$ .

If the current LHC is not upgraded to a HL-LHC after LS3, maintaining the original design luminosity, the total integrated luminosity that can be expected after another ten years of operation would be around 1000  $\text{fb}^{-1}$  [57]. In any case, the current LHC inner triplets have to be replaced after 400  $\text{fb}^{-1}$  integrated luminosity.

The work for the HL-LHC and the various experiments upgrades has already begun. Specification and design of the diverse components is well advanced for some of the systems. Another topic that is being treated are the simulations to define the physics cases.

After the discovery of the Standard Model Higgs boson, made by ATLAS and CMS in the LHC [3], the case study for a High Luminosity Large Hadron Collider (HL-LHC) is easier to define and quantify. The Standard Model predicts, for a Higgs boson mass

around  $125 \text{ GeV}/c^2$ , that all the decay final states are accessible for exploration with the whole LHC programme, given a high enough integrated luminosity.

For instance, the detection and measurement of the decays  $H \rightarrow \mu^+\mu^-$  and  $H \rightarrow Z\gamma$  require an integrated luminosity of the order of  $3000 \text{ fb}^{-1}$ , which justifies the need for a major upgrade of the accelerator.

The extra amount of data will also allow better precision measurement of the Higgs couplings, with precisions between 5% and 30%. For instance, the full luminosity should allow studying Higgs self-coupling in channels  $HH \rightarrow \tau\tau bb$  and  $HH \rightarrow \gamma\gamma bb$  [58]. This factor of ten increase in the luminosity is beyond the design specifications of the LHC and its experiments.

In addition to the characterization of the Standard Model Higgs boson decay modes, there are other scenarios of physics Beyond the Standard Model (BSM), such as supersymmetric partners of quarks and gluons with mass greater than  $1.5 \text{ TeV}/c^2$ .

Another example is the new  $Z'$  gauge bosons that would imply the existence of new weak interactions, which requires at least  $300 \text{ fb}^{-1}$  but needs the full HL-LHC luminosity if its mass is above  $2.5 \text{ TeV}/c^2$ .

Table 3.1 shows a brief comparison between the design specifications of the HL-LHC and those of the LHC [1, 44].

Parameter	LHC	HL-LHC
Peak luminosity [ $\text{cm}^{-2}\text{s}^{-1}$ ]	$10^{34}$	$5 \times 10^{34}$
Maximum integrated yearly luminosity [ $\text{fb}^{-1}$ ]	40	> 250
Beam energy [TeV]	7	7
Dipole magnetic field [T]	8.3	8.3
Bunches per beam	2808	2808
Bunch spacing [ns]	25	25
Protons per bunch	$1.15 \times 10^{11}$	$2 \times 10^{11}$
Average pile-up	27	140
$\beta^*$ at the IP [cm]	55	15

**Table 3.1: Design specifications of the LHC and the HL-LHC.**

In this context of increasing luminosity and pile-up, the upgrade of the experiments is mandatory. The current detectors elements will have accumulated an amount of radiation that will render them unsuitable for further use.

In particular, the inner tracking systems of the two general purpose experiments, ATLAS and CMS, will have reached their end of lifetime. Therefore, they need to be replaced for the future HL-LHC and they will also need to meet new requirements:

- Improved radiation hardness, due to the much higher luminosity and fluence.
- Higher granularity (especially in the tracker) due to the increased pile-up and track density.
- Reduction of material for better  $p_T$  resolution, and adequate pattern recognition with the higher occupancy.
- Additional trigger level for a higher rate of at least 500 kHz.

These requirements call for a new design of the trackers in the experiments and will also need an upgrade of the electronics for the data acquisition of the other sub-detectors.

### 3.2.1 Experiments Upgrades in the HL-LHC

The four experiments in the LHC, ALICE, ATLAS, CMS and LHCb, will need some upgrades after the LHC end of life. For the first three experiments, these upgrades are needed in order to cope with the much higher luminosity and pile-up that the HL-LHC will deliver. The upgrades in LHCb are aimed at triggering at 40 MHz. Also, some of the components, specifically the trackers, will have to be replaced due to the radiation damage incurred in the first ten years of operation of the LHC.

The two general purpose experiments, ATLAS and CMS, will need similar upgrades during LS3. These are summarized in the list below [54, 58]:

- Full replacement of the trackers. The pixel detectors will have accumulated their maximum design fluence and the whole tracker will not be able to withstand both the fluence in the HL-LHC and the occupancy. In the case of ATLAS, the SCT and TRT parts will be replaced by an all-silicon tracker.
- A completely new trigger system is required for the new conditions in the HL-LHC, with higher particle density in the detectors. An additional trigger level, called Level-0, is expected to work at a rate of at least 500 kHz. This is at least a fivefold increase from the current Level-1 trigger rate of 100 kHz.
- The Trigger and Data Acquisition (TDAQ) systems will need an upgrade for the new rates in the HL-LHC.
- Electronics replacements will be needed in various parts of the calorimeters and muon spectrometers.

The greatest challenge for both experiments is the tracker upgrade. The two trackers will be silicon based and have to be designed to cope with a very high radiation environment and very high pile-up. There will be layout changes and a big increase in the number of channels.

The ALICE requirements for the HL-LHC are summarized in the following list [59]:

- A new inner tracker system to improve the impact parameter resolution, getting closer to the interaction point, reducing the amount of material and the pixels size. Fast removal and insertion will be needed for modules replacement during yearly shut-downs.
- Upgrade of the read-out systems of the TPC, Transition Radiation Detector (TRD), Time of Flight detector (TOF), calorimeters and muon detectors, to cope with the higher trigger rates.

For LHCb, the systems that need an upgrade for the 40 MHz rate are [55]:

- The VELO and the silicon strips tracker will need a complete replacement.

- The read-out systems for the tracker straw tubes and the Hybrid Photon Detectors (HPD) will be replaced.
- Also, the present read-out system at a maximum data rate of 1 MHz will be upgraded to support a flexible Level-0 trigger, reading out all detectors at a 40 MHz rate.
- In the case of LHCb, the upgrade deployment will take place during LS2 instead of LS3.

The next section and chapters focus solely on the ATLAS Tracker Upgrade. At first, I will describe part of the Phase-II Upgrade of the ATLAS Pixel Detector, but the main topic of this thesis is the Strips Tracker Upgrade.

## 3.3 Phase-II Upgrade of the ATLAS Inner Tracker

### 3.3.1 Tracker Upgrade Overview

The current ATLAS Inner Detector consists of three layers with three detector types: A pixel detector in the innermost layers, a semiconductor tracker (SCT) and a transition radiation tracker (TRT) at larger radii. The silicon pixel layers provide high-resolution tracking, as does the semiconductor tracker built with silicon microstrip sensors. After the first long shut-down, a fourth pixel layer will be installed closer to the interaction point.

The pixel detector was designed to cope with a 1 MeV neutron equivalent fluence of  $10^{15} \text{ cm}^{-2}$ , which corresponds to an integrated luminosity of  $400 \text{ fb}^{-1}$ . The SCT can operate up to a 1 MeV neutron equivalent fluence of  $2 \times 10^{14} \text{ cm}^{-2}$ .

After the ten years of expected lifetime, the pixel sub-detector will have accumulated a 1 MeV neutron equivalent fluence of around  $8 \times 10^{14} \text{ cm}^{-2}$ , while the SCT is expected to be well below its design requirement. However, its maximum attainable fluence is much lower than the requirement for the luminosity beyond 2022 [2, 58].

In addition to the radiation damage, the sub-systems were designed to accommodate up to 23 pile-up events. In the first place, the front-end electronics of both the pixel detector and the SCT cannot cope with the HL-LHC pile-up without a degradation in their efficiency. In addition, the track density with that pile-up will also be so high that the TRT would be close to 100% occupancy and both the pixel and the SCT would be unable to resolve close-by particles.

The bandwidth of the optical links that read-out the data from the tracker would also reach saturation in such high pile-up scenario.

As a consequence, after ten years of operation, it will be necessary to replace the inner tracker with a new one. The innermost layers will be implemented with pixel sensors and the outer layers will be all silicon strips. All the details can be found in the Letter of Intent (LoI) for the Phase-II Upgrade of the ATLAS Experiment [58].

The current ATLAS pixel detector has 80 million channels spread over three barrel layers and three discs on each endcap side. The extra layer that was inserted during LS1 in the pixel detector, called Insertable B-Layer (IBL), contributes with an extra 12 million channels [45]. The pixel detector after the Phase II upgrade will have 638 million channels, with four barrel layers and six discs for each endcap. The sensors for the pixel upgrade will be smaller than the sensors in the current detector.

Also, the current ATLAS SCT has 6.3 million channels with four barrel layers and nine discs on each endcap. The TRT has 351000 channels. The new ATLAS Strips Tracker will be all-silicon, with 74 million channels spread over five barrel layers plus a stub layer and seven endcap discs on each side.

The barrel strips will have different lengths depending on the occupancy of the region in which they are. The shorter strips will be used in areas with higher track density.

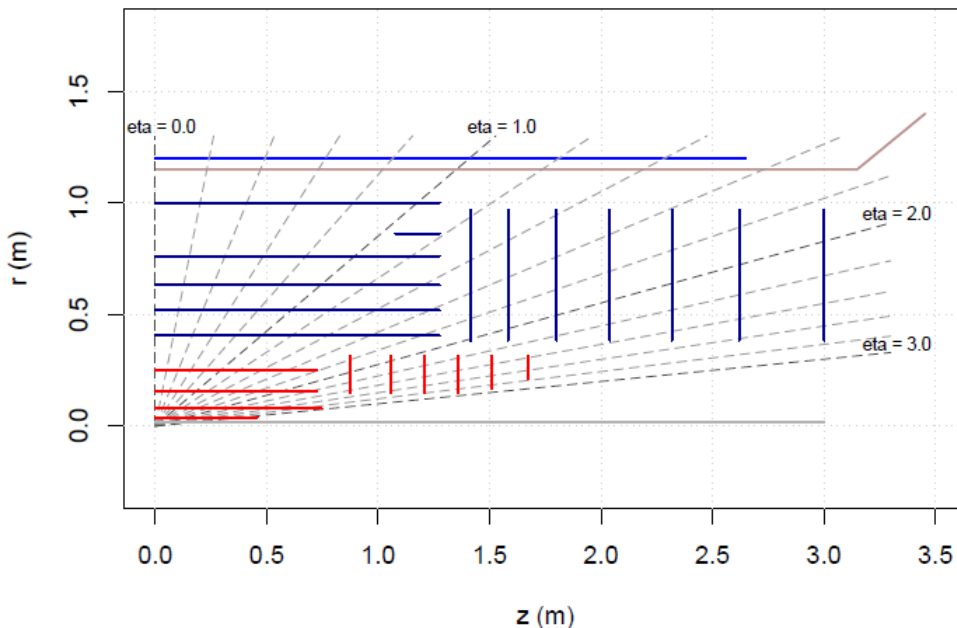


**Figure 3.2: Baseline layout of the Inner Tracker for the ATLAS Phase-II Upgrade [58].**

In addition to increasing the capacity of the system, there are other requirements to be met. For instance, modularity allows easy replacement of damaged layers. As an example, it would permit the removal of the first two pixel layers without removing the beam pipe and also the whole pixel detector without disturbing the strips tracker.

The removability requirement effectively separates the pixel and strip detector envelopes, which needs a Pixel Support Tube (PST) and routing all pixel services within its own envelope.

The new layout of the Inner Tracker has been defined. There is a baseline layout, shown in Figure 3.2, that has four pixel barrel layers with six endcap layers on each side. The strip detector has five barrel layers and an additional “stub” that maintains hermeticity at the barrel-forward boundary. Finally, seven strips discs compose the endcaps on each side.

The beam pipe is assumed to be 33 mm radius and the innermost layer of the pixel detector will be at a radius of 39 mm [58].

This layout was conceived following the requirement of having at least 14 hits in the tracker, with a minimum of four hits in the pixel detector, up to  $|\eta| < 2.5$  [60].

The total coverage of the pixel detector is close to  $|\eta| < 3.0$  and the whole inner tracker covers up to  $|\eta| < 2.5$ . The last pixel barrel layer will be placed at a radius of 250 mm and the maximum length in  $z$  of each barrel is 747 mm. The pixel barrel will

be composed of staves, holding between 22 and 36 modules.

The pixel endcaps will cover radial distances between 150.1 mm and 315 mm with  $z$  positions between 877 mm and 1675 mm.

The strips barrel will be surrounding the pixel barrel, with a maximum radius of around one metre and length of the active area up to 1.25 m. The endcap regions start around  $z = 1.4$  m and end at around 3 m, covering radii ranges between 405 mm and 1000 mm. Further details on the strip detector can be checked in the following section and in the next chapter.

Other alternative layouts have been defined. They are briefly described below, refer to [58] for more detailed information.

- The conical layout is based on a bent stave in the pixel layers, reducing the material in the forward region.
- Five pixel barrel layers, what allows a more robust pattern recognition and better two-particle separation in high  $p_T$  jets.
- In the alpine layout, pixel modules at high  $\eta$  are placed with increasing inclination angle. This layout removes the need for endcap discs and reduces the total silicon area in the pixel from 8.2 m<sup>2</sup> to 4.6 m<sup>2</sup>.

Although these are the proposals included in the Letter of Intent, the layout is not complete yet. For instance, the “stub” in the strips detector lacks of modularity.

The next section is focused on the strip detector and further details about the pixel detector and the other sub-systems upgrades can be found in the Phase-II Letter of Intent [58].

### 3.3.2 The Strip Detector for the Upgrade

The strip detector for the ATLAS Phase-II Upgrade will have one barrel region covering a radius of 1 m and a length of 1.3 m to each side of the interaction point. The endcaps cover the length up to 3 m. The pseudorapidity range coverage of the strip detector is  $|\eta| < 2.5$ .

For the barrel, a layout with six layers that include five full length cylinders surrounding the pixel detector along the beam line is conceived. The fifth barrel layer will be a short “stub” that covers the acceptance loss between the endcap and the barrel on each side, as shown in Figure 3.2.

The “stave” is the basic mechanical element of the barrel. A drawing is shown in Figure 3.3, it consists of a stave core that provides support for the detectors, powering, read-out electronics and cooling services.

The detectors are modules made from a silicon microstrip sensor, with two hybrids holding the read-out chips glued on top of the sensor, and wire-bonded to the strips. The sensors and the electronics will be described in the next chapter.

Each stave consists of two sides for double dimension position resolution and each side holds 13 modules, for a total of 26 modules in a double sided stave. The End of Stave (EoS) card holds the interface to the stave modules, including the read-out electronics and the optical transceivers. The total length of a stave including the End of Stave card is around 1.3 m and its width is around 12 cm.

The short stub in the fifth layer is expected to have two modules on each side of the core, for a total of four modules per stub.



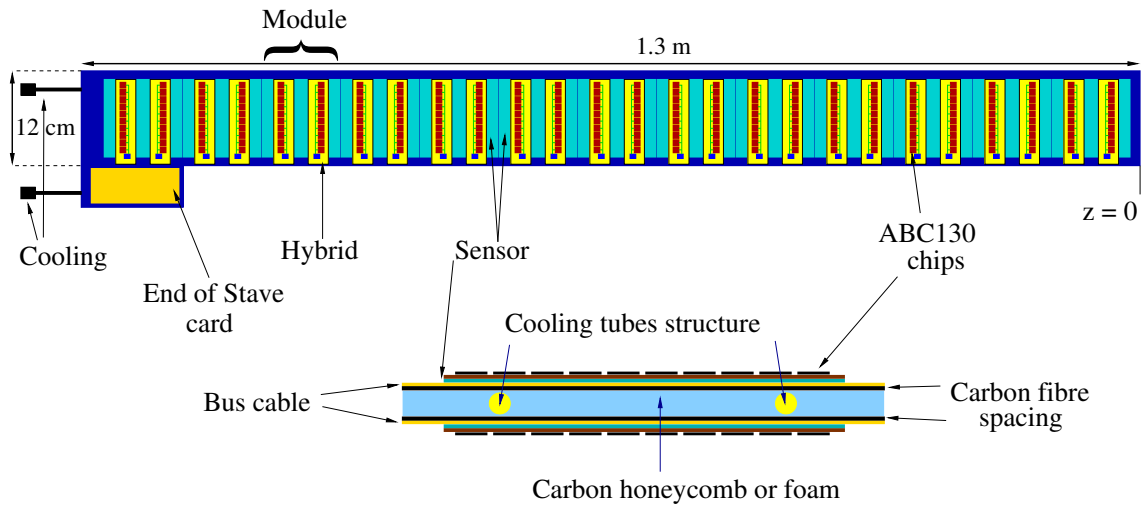


**Figure 3.3:** Drawing of a barrel stave showing the 13 modules and the End of Stave card. The drawing does not reflect the actual device arrangement.

The barrel will be composed of 472 full length staves, with 236 staves to each side of  $z = 0$ . The fifth layer will hold 64 staves on each side of  $z = 0$ . The first three layers have modules with 23.82 mm long strips (“short strips”) and the three outer layers (the two outer cylinders and the stub layer) have modules with 47.755 mm long strips (“long strips”).

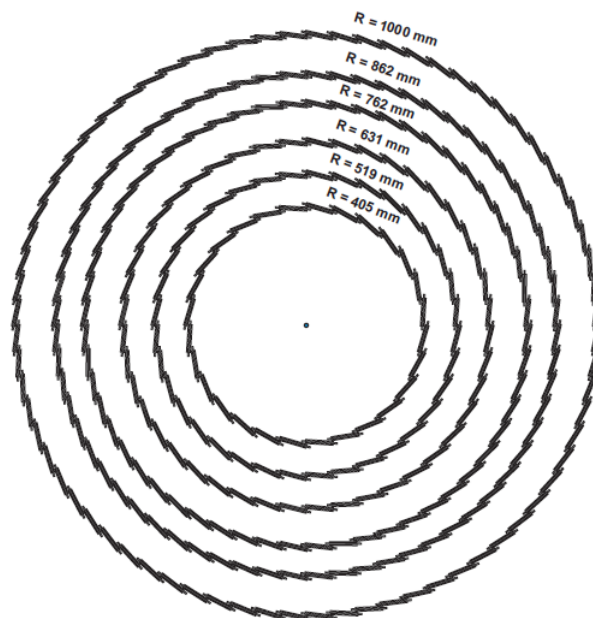


**Figure 3.4:** Drawing of the arrangement of the staves in barrels. The tilt angle is  $10^\circ$ .

The total number of modules is 12272 for full length stave layers while the stub layer will have 512 modules. That gives a total of 12784 modules in the whole barrel.

Figure 3.4 shows the arrangement of the staves in the six barrel layers in the axial

plane, including the tilt angle, which is specified to be at least 10 degrees.

The barrel staves are arranged in a way that each layer is completely hermetic for 1 GeV/ $c$  tracks. The rotation direction is chosen to minimize the charge spread among strips due to the Lorentz angle.

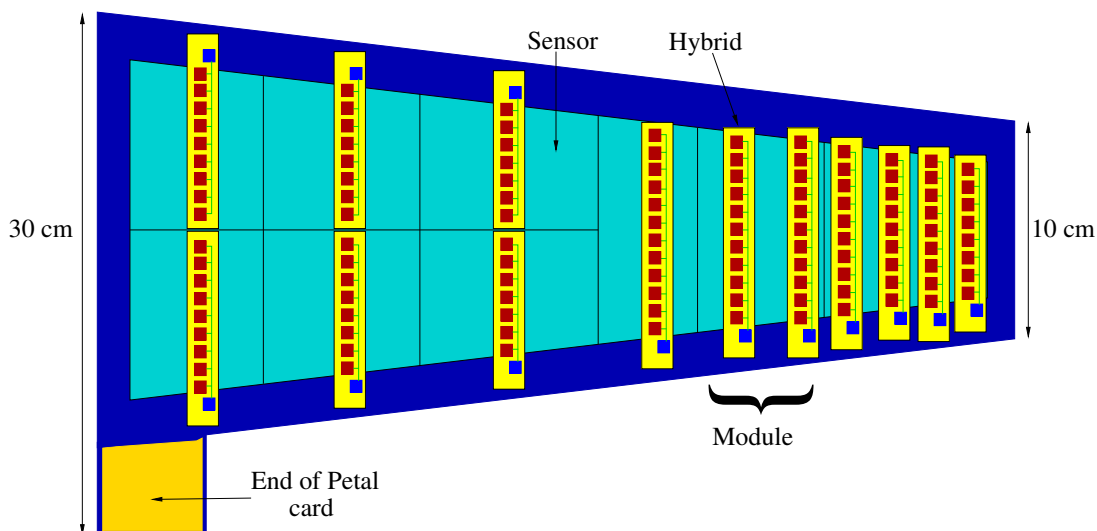
The total number of staves in one cylinder has been chosen to be a multiple of four. This allows simplifying the services routing and the design of structure supports.

Table 3.2 shows the number of staves that compose each barrel layer of the strip detector in the Phase-II Upgrade [58, 60], the radii where they are located and the active silicon length. The layers numbering on this table do not represent the actual numbering of the tracker layers.

Layer	Radius	Number of staves	Active length ( $z > 0$ )
1	405 mm	28	1275 mm
2	519 mm	36	1275 mm
3	631 mm	44	1275 mm
4	762 mm	56	1275 mm
5 (stub)	862 mm	64 stubs	196 mm
6	1000 mm	72	1275 mm

**Table 3.2:** Number of staves or stubs in each barrel layer of the Strips Tracker for the Upgrade.

On the endcaps, the basic element is called “petal”, analogous to the staff, with a wedge shape that allows a disc to be built with full cover and reduced overlap. The current geometry of the petal foresees a structure 63 cm high, with a minimum width of around 10 cm and a maximum width of around 30 cm. A drawing showing the geometry and elements of one side of the petal can be seen in Figure 3.5.



**Figure 3.5:** Drawing of an endcap petal showing the 9 modules and the services. The drawing does not reflect the actual device arrangement.

Each endcap disc is made from 32 identical petals. The petals have nine modules

on each side, covering six rings, requiring a total of six sensor types, with different geometries, and 14 hybrid variations.

Since every petal has 18 modules and there are seven discs on each endcap side, every disc has 576 modules and the total module count for the endcaps is 8064. The number is comparable to the barrel, with the added complexity of having different types of modules. Both the high number of total modules for the barrel and endcap structures and the variety of modules affect the production and quality assurance planning [61].

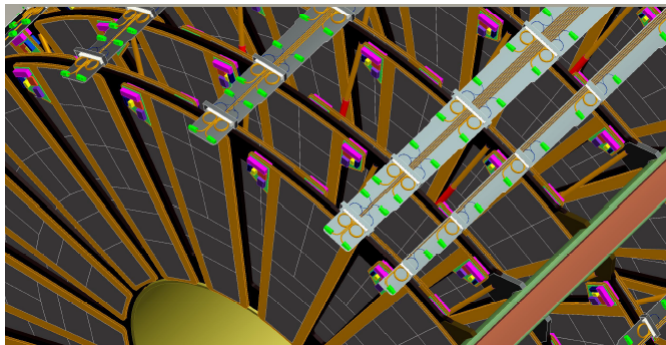


**Figure 3.6:** The arrangement of petals in the endcaps.

The petals are arranged in endcap discs that are hermetic for  $1 \text{ GeV}/c$ , with an overlap such that a petal covers an angle slightly greater than  $\pi/16$ . The layout for the discs is shown in Figure 3.6, with a “castellated” arrangement.

Table 3.3 summarizes the geometrical characteristics of the endcap discs. The greater inner radius of the last disc, implemented by removing the bottom module, is motivated by the integrated non-ionizing radiation [62].

Disc	Inner radius	Outer radius	$z$ position
1	385 mm	970	1415 mm
2	385 mm	970	1582 mm
3	385 mm	970	1800 mm
4	385 mm	970	2040 mm
5	385 mm	970	2320 mm
6	385 mm	970	2620 mm
7	471 mm	970	3000 mm

**Table 3.3:** Active radii and  $z$  positions of the endcap discs [62].

Table 3.4 shows estimate values for the radiation length of the various elements and the total sum of both a short-strips stave and a petal. The numbers are based on the current prototyping with extrapolation to the use of lower mass components.

For comparison, the current SCT radiation lengths without the mechanical supports are  $2.48\%X_0$  for the barrel and  $3.28\%X_0$  for the endcaps. This material reduction is one of the goals for the Phase II, in order to improve the resolution and performance of the tracking, and is obtained thanks to the greater degree of mechanical support, power and services sharing in these new structures.

Although there is yet no material budget specified, the preliminary performance simulation studies were done under the following assumptions for the detector materials and support structures:

- The inner pixel layers have a radiation length  $< 1.5\% X_0$  per layer.
- The outer pixel layers have a radiation length  $< 2.0\% X_0$  per layer.
- The inner short strips layers have a radiation length  $< 2.5\% X_0$  per layer.
- The outer long strips layers have a radiation length  $< 2.0\% X_0$  per layer.

Barrel		Endcap	
Element	$\%X_0$	Element	$\%X_0$
Stave core	0.55	Petal core	0.47
Bus cable	0.30	Bus cable	0.03
Modules	1.07	Modules	1.04
Module adhesive	0.06	Module adhesive	0.06
Total	1.98	Total	1.60

**Table 3.4: Radiation length estimates for barrel stave and endcap petal. Power ASICs and EoS are not included [58].**

In both the stave and petal cases, the basic unit is a module. For the barrel staves, all modules in a stave are of one type, whereas for the endcaps, different rings of the petal need different modules. Therefore, the petal construction and testing involve many different kinds of sub-structures.

The ATLAS Strips Upgrade project comprises the design, construction and testing of the silicon modules that will be used at the new detector. Single modules are mounted into the structures, the staves and petals. Therefore, not only individual modules have to be tested, but also the larger structures that include multiple modules.

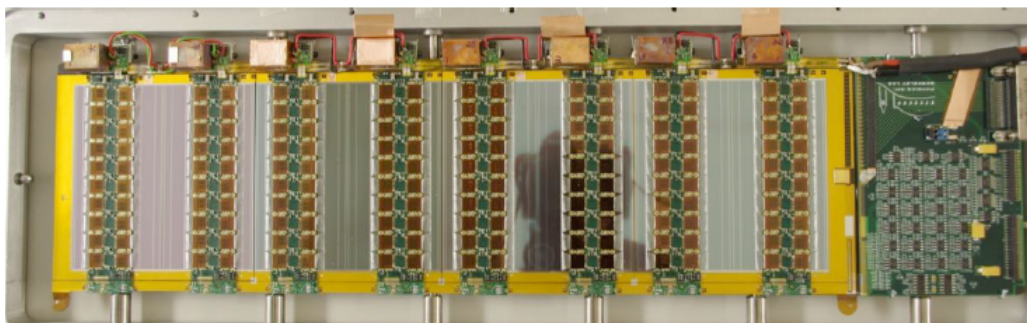


**Figure 3.7: Picture of a functional stavelet showing the 4 modules and the End of Stave card.**

While the complete barrel staves and endcap petals will integrate 26 and 18 modules, respectively, smaller structures have been prototyped as proof of concept. In the

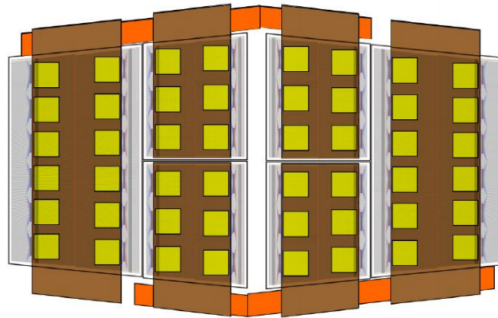


**Figure 3.8: Drawing of a petalet. The modules are unfolded to show both sides of the petalet, the hybrids and services routing.**

case of the barrel, this structure is named “stavelet” and is based on four single sided modules.

For the endcap structures, the proof of concept structure is called the “petalet”. It is based on the first and fifth rings, with three modules on each side, for a total of six modules.

Figure 3.7 shows one of the actual stavelets that was built at Rutherford Appleton Laboratory (RAL) and is currently at CERN, undergoing tests. Some of the tests done on this and other stavelet will be discussed in the following chapters of this thesis.

One of the proposed petalet layouts is shown in Figure 3.8 [63]. The drawing shows an unfolded petalet, where the six modules can be seen, as well as the services routing on the sides of the modules. The first petalet prototypes are expected to be built during the first quarter of 2014.

These proofs of concept are aimed at providing insight with respect to the feasibility of the design as well as to check the performance evolution as more modules are added to the structure and the differences between powering schemes. This topic will be discussed in the next chapter.

The staves and petals concepts for barrel and endcaps of the strips tracker upgrade are considered baseline. They are not, however, the only project that has been working in the conception of the new strips tracker for ATLAS.

As an alternative to the stave concept, the so called “supermodules” have been considered. These supermodules are an evolution of the current SCT design, trying to maintain some of its merits, such as mechanical and thermal stability, and true stereo space-point reconstruction. For further details, refer to [62].

The next chapter discusses in detail the strips tracker upgrade, focused on the staves and petals structures and their constituents. The description includes an overview of the sensors, electronics, powering and the various testing structures for both the barrel and the endcap.



# Chapter 4

## The ATLAS Silicon Strips Tracker Upgrade

The ATLAS Phase-II Upgrade has been presented in the previous chapter together with the Inner Tracker and some details of the strip detector. In this chapter we will focus on the strips detector in greater detail, from the electronics and system points of view.

### 4.1 Silicon Sensors

The proposed baseline sensors for the new strips detector are n-type implants in p-type float-zone silicon substrate. The sensors have a thickness of  $320 \pm 15 \mu\text{m}$ , which could be reduced with additional costs [58].

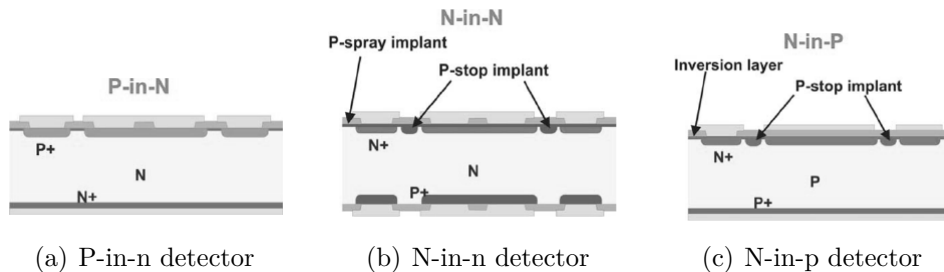


**Figure 4.1: Cross sections of the p-in-n, n-in-n and n-in-p detectors used in radiation hardness studies. The n-in-n detector shows P-spray and P-stop implants and back side processing. The n-in-p detector shows P-stop implants [64].**

The choice of n-in-p technology was made after studying the radiation hardness and complexity of different types of combinations [64]:

- P-type implants in n-type substrate. It is the usual choice for radiation detectors in pixel and microstrips sensors because it is a simple technology due to the lower number of masks required for their processing, and therefore has lower cost. The fluence limit of this technology is about  $3 \times 10^{14}$  protons/cm<sup>2</sup>, which is an order of magnitude lower than the expected fluence on the strips tracker in the HL-LHC. An example of this technology is shown in Figure 4.1(a).

- N-type implants in n-type substrate. These detectors are expected to withstand fluences of up to  $10^{15}$  protons/cm<sup>2</sup>. However, this technology is the most complex of the three: it requires ten mask levels and double sided processing. A cross section showing this type of technology with P-stop and P-spray implants can be seen in Figure 4.1(b)
- N-type implants in p-type substrate. This technology is more radiation hard, due to the fact that the bulk is already p-type, so no type inversion occurs. On the negative side, these detectors are more complex than their p-type implants in n-type substrate counterpart. They need extra insulation, which achieved by different techniques: blank surface implants (named P-spray) or P-type junctions (named P-stop). A sample of the n-in-p technology is shown in Figure 4.1(c), where P-stop implants are included.

The fluence in the inner layers of the strips detector in the HL-LHC is expected to be about  $1.2 \times 10^{15}$  1 MeV neutron-equivalent for the full operation period. For the outer layers the expectation is around  $5 \times 10^{14}$  1 MeV  $n_{eq}/\text{cm}^2$ . These numbers include a safety factor of 2 [65].

The choice of n-type implants in p-type substrate was made after considering the fact that the n-type bulk becomes p-type after a 1 MeV neutron-equivalent fluence of  $10^{13}$  cm<sup>-2</sup>. This means that the SCT approach for the sensors is not suitable for the HL-LHC upgrade. Even considering the higher radiation hardness of the n-in-n technology, it is a double sided process, more complex than n-in-p and there are less foundries available. These difficulties lead to higher production costs and the n-in-n technology is harder to handle and test [66].

### 4.1.1 Barrel Sensors

The barrel sensors have an area of  $97.54 \times 97.54$  mm<sup>2</sup> with 1280 active strips plus two guard strips across the sensor, with a strip pitch of 74.5 μm. The size of the sensor was chosen so they can be laid out on 6 inch (150 mm) diameter wafers [67].

The wafer also includes 24 miniature sensors,  $10 \times 10$  mm<sup>2</sup>, surrounding the main sensor, which are used to study radiation hardness properties of the different isolation techniques. The initial testing of the n-in-p structures for the ATLAS Upgrade began with the ATLAS07 specification [68], with results on the radiation hardness [69] and charge collection efficiency comparison of different substrates [70].

There are two sensor variations, as it was mentioned in the previous chapter, there will be short strips and long strips, depending on the track density of the regions where the sensors are located. The short strips have a length of 23.82 mm, which results in four rows of strips in the sensor. The long strips are 47.755 mm, therefore a sensor accommodates two rows of long strips [58].

Complete details about the sensors specifications and manufacturing process can be found in the two specification documents that have been written so far. These are the technical specifications for the ATLAS07 [68] and the ATLAS12A/ATLAS12M [71] sensors.

A number of ATLAS07 sensors have been fabricated following these specifications and have been tested under various conditions. The baseline material is float-zone (FZ) p-type silicon. The read-out is AC coupled and the biasing of the strips is implemented with poly-silicon resistors.



As mentioned above, the strip pitch in these sensors is  $74.5 \mu\text{m}$ , whereas the read-out implant strips are  $16 \mu\text{m}$  wide highly doped n-type implants and the read-out strips are  $22 \mu\text{m}$  aluminium depositions over the n-implant strips [71].

Some of the specifications for pre-irradiated sensors in the ATLAS12 specification are summarized in Table 4.1.

Parameter	ATLAS12 specification
Thickness	$310 \pm 25 \mu\text{m}$
Crystal orientation	$< 100 >$
Outer dimension	$97.54 \times 97.54 \text{ mm}^2$
Strip segments	4
Strip segment length	23.86 mm
Strip pitch	$74.5 \mu\text{m}$
Strip implant width	$16 \mu\text{m}$
Strip read-out width	$22 \mu\text{m}$
Depletion voltage	$< 300 \text{ V}$
Maximum operating voltage	600 V
Leakage current (normalized to $20^\circ\text{C}$ )	$< 2 \mu\text{A}/\text{cm}^2$ at 600 V
Maximum fluence	$1.2 \times 10^{15} \text{ 1 MeV n}_{\text{eq}}/\text{cm}^2$

**Table 4.1: Summary of ATLAS12 specifications pre-irradiation [71].**

The layout of the wafers for the ATLAS12 specification is shown in Figure 4.2, which corresponds to the axial-stereo sensor, two strips rows have an axial orientation, that is, parallel to the sensor edge. The other two rows have a  $40 \text{ mrad}$  stereo angle. The various P-stop isolation structures that have been implemented for testing are also shown, together with the Punch-Through Protection (PTP) function [71, 72].

ATLAS12 describes different sensor types, being the most relevant the ATLAS12A, with all strips axial (A = axial), and ATLAS12M, with two rows of strips axial and the other two rows having a  $40 \text{ mrad}$  stereo angle [71] (M = mixed). Since ATLAS12A has been chosen as the baseline, the stereo angle in the detector will be achieved by rotating the sensors.

This is the overall description of the barrel sensors. The exact mask is yet to be defined, including the Punch-Through Protection and the isolation structures.

The batches that have been produced so far include higher quality (Float-Zone 1, FZ1) or Grade A sensors as well as lower quality (Float-Zone 2, FZ2) or Grade B sensors. The main difference between them is that FZ1 sensors have a leakage current around two orders of magnitude lower than FZ2 sensors. The isolation structure used on the main sensor is equivalent to the Zone 3 shown in Figure 4.2. An example of the ATLAS07 sensors can be seen in Figure 4.3, which shows the two types of strips: axial and stereo.

More details about the batches of the ATLAS07 sensors can be found in [67]. The devices that have been tested at CERN for the barrel structures, that is, modules and stavelets, all use ATLAS07 sensors. There are some differences between the ATLAS07 and ATLAS12 sensors, mainly on the PTP structures and the existence of all axial strips sensors.

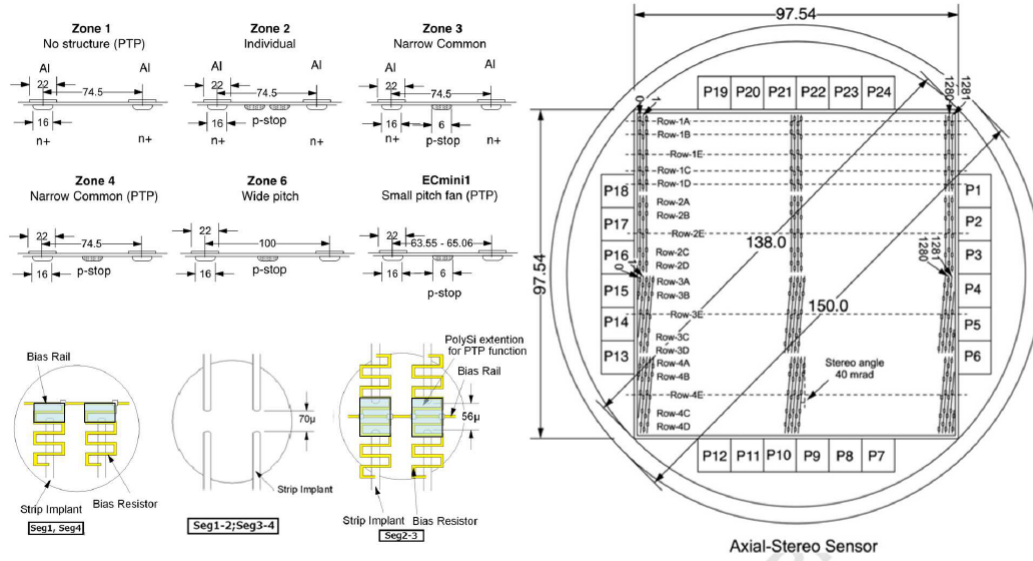


Figure 4.2: Wafer layout defined in ATLAS12 specifications for the barrel short strips sensor prototypes [72]. On the left, top to bottom are the P-stop isolation and the PTP structures. On the right, the wafer mask for an ATLAS12M sensor. Measures of the wafer drawing are in millimetres, measures of the PTP and isolation schemes are in micrometres.

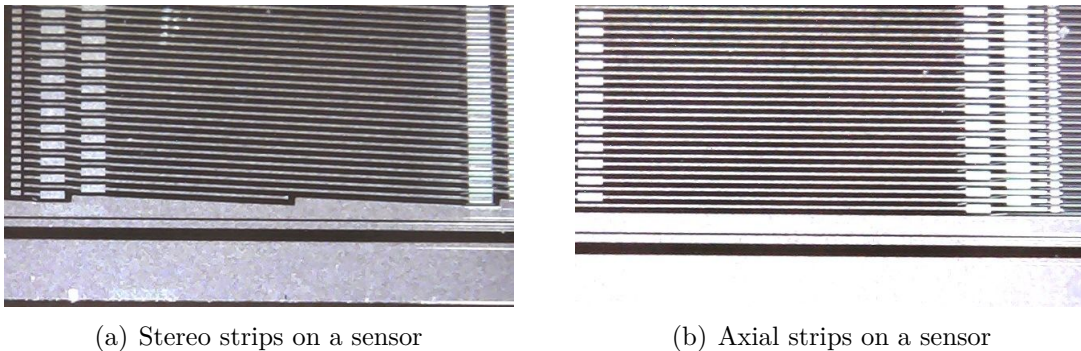


Figure 4.3: Sensors on a barrel module: both stereo and axial strips on the same sensor.

### 4.1.2 Endcap Sensors

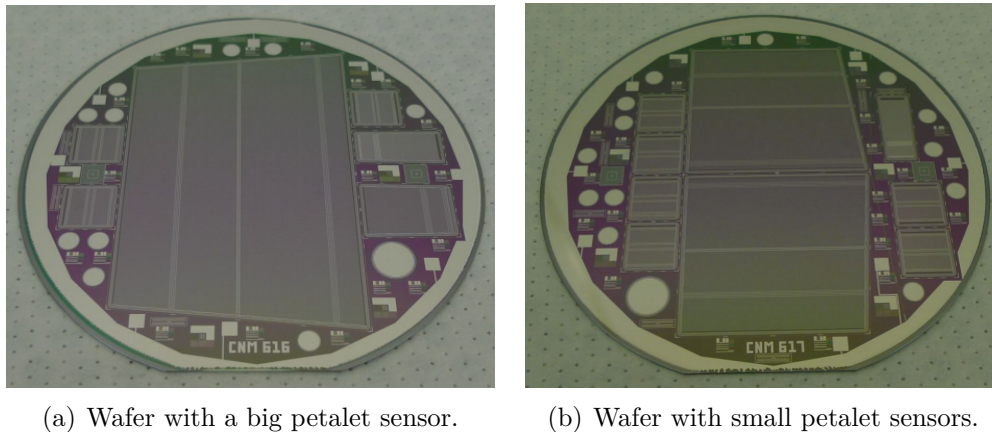
The endcap sensors that will be used to build the petals need radial strips, pointing at the beam line, for accurate measurement of the  $r\phi$  coordinate. To achieve this, the sensors have a wedge shape and there need to be several sensor shapes [73]. The size of the sensors need to be such that all shapes can be fabricated on 6 inch wafers.

In the endcap petals, the stereo angle of 40 mrad is achieved by rotating the strips within the sensors by 20 mrad. Each side of the petal points slightly away from the beam line, but the angle bisector of the two sides points at the beam line.

The sensors are, like in the barrel, n-in-p type and the specifications are the same, except for the wedge shape and the different geometries.

The petal sensors will be divided in pairs of strips rows, due to the ABC130 chip,

which is designed to read-out two rows of strips. The inner ring has shorter strips to accommodate the higher hit occupancy. This ring has sensors with four pairs of rows and hence will hold four read-out hybrids. The second ring has two pairs of strips and two read-out hybrids. The four outer rings have one pair of strips and hence one read-out hybrid for each module.



(a) Wafer with a big petalet sensor.

(b) Wafer with small petalet sensors.

**Figure 4.4: Pictures of wafers with endcap sensors produced by CNM-IMB [74].**

The strip pitch at the bond-pad region is made as close to the barrel sensors strip pitch as possible, that is,  $74.5 \mu\text{m}$ . This requirement constrains the number of chips on a hybrid for each of the rings [58].

Some prototypes of the endcap petal sensors have been produced already. These are the three types that are needed for the petalet proof-of-concept and are fabricated by Centro Nacional de Microelectrónica-Instituto de Microelectrónica de Barcelona (CNM-IMB), a research centre owned by the Spanish National Research Council (Consejo Superior de Investigaciones Científicas, CSIC). Figure 4.4 shows two wafers of the three sensor types used in the petalet [74].

The small sensors that have been fabricated by CNM-IMB have a depletion voltage of  $68.2 \pm 7.63 \text{ V}$ . The big sensors have a depletion voltage of  $70.33 \pm 9.45 \text{ V}$ . These are the measurements performed by CNM before cutting the sensors from the wafers. The measurements have been repeated by the institutes receiving the sensors after cutting and they are consistent with the values obtained by CNM [75].

The big sensors are also called “bottom sensors” and the small sensors are the “top right” and “top left” sensors, depending on their position in the petalet. Figure 4.5 shows a drawing of the three sensors of the petalet. All types of sensors in the petalet have one pair of rows. The petalet is designed for the ABCn25 chip and each sensor will be read-out with one hybrid holding two columns of chips, as in the barrel modules.

The petalet is conceived as the small petal that helps understanding the whole model and the issues that are specific to the endcap region. This is done with a combination of the elements at the innermost radius and elements from the region where the petal elements are split in two separate sensors.

A plan for a full sized petal with the ABCn25 has not been considered. The ABC130 chip will be used to build the first full sized petal.

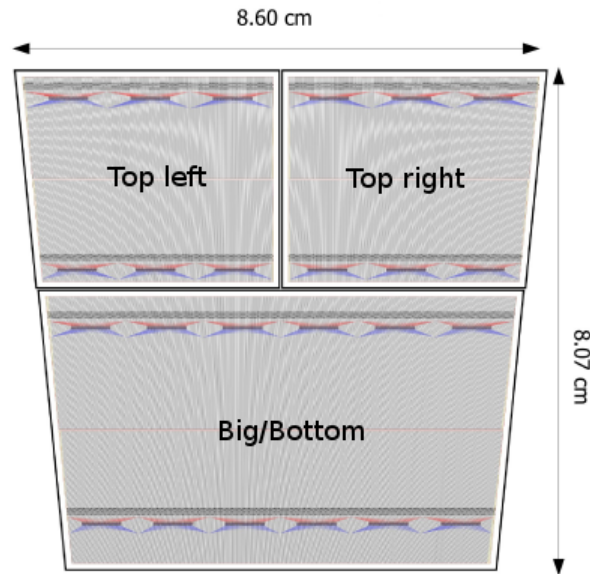


Figure 4.5: A drawing that shows the three different petalet sensors, including the size of the petalet.

## 4.2 Front-End and Read-Out Electronics

The front-end electronics collect the charge on the strips and compare it with the configured threshold. The read-out electronics then process all of the hit strips in the event and send the signals outside the detector through the appropriate path, in a series of stages. This signal path is represented in Figure 4.6.

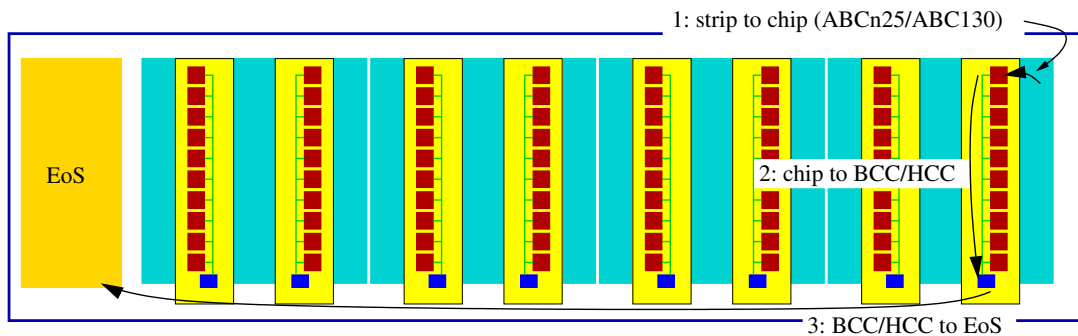


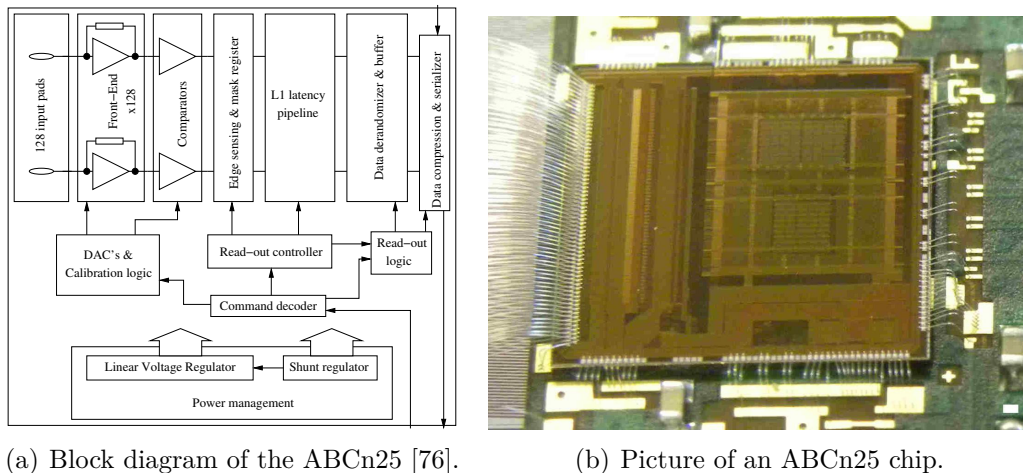
Figure 4.6: Path of the signals from the strip to the End of Stave card.

First, the collected charge on the strip is processed at the chip, which has a link with another chip that aggregates the signals from the front-end chips and this other chip has, in turn, another link with the read-out electronics.

### 4.2.1 The ABCn25 Chip

A front-end electronics chip for the strips detector have been prototyped on 250 nm technology, the chip is named ABCn250 or ABCn25, with 128 channels. It is a binary read-out chip that only provides hit information and no charge information. A drawing

of the block diagram for this chip is shown in Figure 4.7(a). It is very similar to the present SCT chip as the functionality required is the same [30].



(a) Block diagram of the ABCn25 [76].

(b) Picture of an ABCn25 chip.

**Figure 4.7: Functional blocks diagram and picture of an ABCn25 chip. The picture shows the 128 input pads to the left of the chip, the rest of the bond-pads are for addressing and data reception and transmission.**

A picture of one of the chips mounted on a hybrid is shown in Figure 4.7(b). The wire-bonds to the left of the chip connect the 128 strips to the ASIC inputs. They are divided in two sets of 64 channels, one with short bonds and the most visible ones are the long bonds.

The chip is implemented with IBM 250 nm CMOS technology. The design of the final read-out chip is foreseen to be based on 130 nm technology. Some of the relevant features of the ABCn25 chip are [76]:

- Analogue gain of 100 mV/fC with an integral non linearity lower than 3% for input charges in the range  $(-10, +10)$  fC.
- Equivalent Noise Charge lower than  $800 e^-$  for a detector capacitance up to 5 pF.
- Each channel has an internal calibration capacitor at their input to allow the injection of test charges up to 16 fC with 0.0625 fC/step, using an 8-bit calibration DAC.

There were technical and economical reasons to do an initial implementation of the ABCn chip in 250 nm technology instead of the final 130 nm. The designers were able to re-use some of the functional blocks that were designed for the SCT, so the design could be finished in a relatively short time, saving initial chip design costs.

The power consumption of the ABCn25 chip is split between the digital and the analogue part. The analogue function requires 40 mA while the digital blocks require 90 mA at  $V_{dd} = 2.5$  V [77].

## 4.2.2 The ABC130 Chip

The design of the ABC130 was finished in 2013 [77] and the first produced units arrived by the end of 2013. The detector prototypes that have been tested within the scope of this thesis are based on the ABCn25 chip.

One of the reasons to embrace the 130 nm technology for the ATLAS Upgrade binary read-out chip is the additional radiation hardness with respect to 250 nm technology [78].

The main difference from the ABCn25 is that the ABC130 has 256 read-out channels on a single chip. One chip reads out two rows of strips on a sensor, instead of just one.

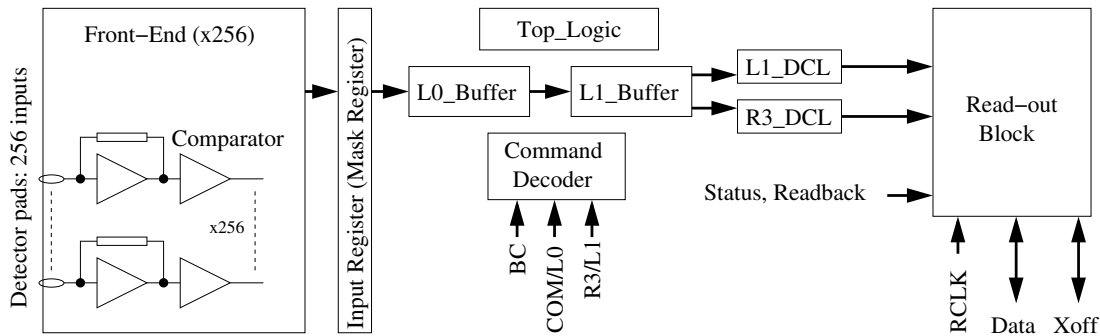


Figure 4.8: Block diagram of the ABC130 [79].

Figure 4.8 shows a functional block diagram of the ABC130 chip [79], where the blocks are different from the ABCn25 chip.

Some of the most important features that differ from the previous chips are the following:

- External supply voltage of 1.3 V, down from 2.5 V.
- Data flow controlled by three trigger types: L0, R3 and L1
- Read-out clock up to 160 Mbps.
- Bi-directional read-out to allow the system to operate if one chip fails.

Performance optimization of the ABC130 is done for short strips. The post-irradiation noise for a load capacitance of 5 pF is specified to be below  $650 e^-$ . This load corresponds to the maximum capacitance of a 47.755 mm long strip.

The gain at the discriminator input is specified to be 95 mV/fC for nominal bias current, with a linearity better than 15% up to 8 fC.

For the calibration signals, the on-chip capacitor is 60 fF. The 8-bit DAC provides an amplitude step of 0.586 mV in the 0-150 mV range, giving a charge step of 0.035 fC in a charge range from 0 to 9 fC.

Regarding the power consumption of the chip, the estimation for the analogue part is 160  $\mu$ W per channel for short strips and 300  $\mu$ W per channel for long strips. These numbers assume an analogue voltage of 1.2 V with 34 mA drawn current for the 256 channels in case of short strips. The current almost doubles for long strips [77].

### 4.2.3 Hybrids

For the ABCn25 based hybrids, part of the Stave09 programme, the hybrids are kapton flex circuits,  $24 \times 107.35 \text{ mm}^2$  in size. The kapton circuits hold the passive components and the chips to read-out the silicon strips.

These hybrids also include a Buffer Control Chip (BCC) that allows the multiplexing of the signals to and from the chips on one hybrid to the read-out system.

The ABCn25 chips are connected in a chain, in a way that if a chip fails, the rest of the chips in the chain are also lost. The chain direction can be changed by swapping the master and end chips.

The ABCn25 based hybrids for the barrel contain 20 chips each. This means that a fully populated hybrid requires a current of around 4 A at 2.5 V [77].

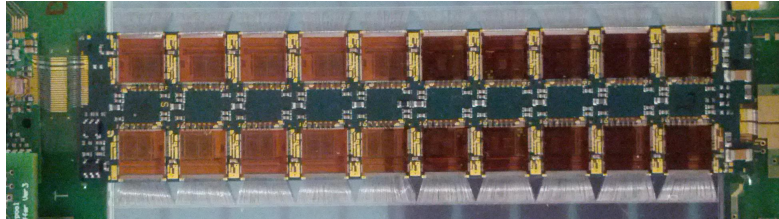


**Figure 4.9: A hybrid with 20 ABCn25 chips, with the bonds to the sensor (top and bottom), to the powering (right) and to the BCC board (left) shown.**

Figure 4.9 shows a picture of a barrel hybrid, with the 20 chips wirebonded. Figure 4.10 shows a BCC chip on a module test frame with the wirebonds to the hybrid on the bottom part of the picture.

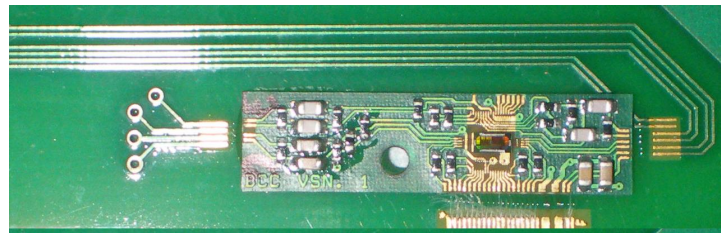


**Figure 4.10: A BCC board.**

The hybrids for the ABC130 chips follow the same philosophy and are built using kapton flex circuits but of smaller size,  $16 \times 97.54 \text{ mm}^2$ , just covering the length of a sensor. Also, the layout has been redesigned to accommodate the different number of chips, 10 instead of 20, because each chip reads out 256 strips. In addition, instead of having a Buffer Control Chip to aggregate and send the signals to and from the hybrid, the chip has been redesigned in a 130 nm process and named Hybrid Control Chip (HCC). The BCC is placed on a board separate from the hybrid and connected through wirebonds, whereas the HCC is placed on the hybrid.

A limited level of redundancy is added in the read-out chain at the hybrid level. The ABC130 chip allows data transmission in both directions, forming two possible data loops towards the HCC. This means that, unlike what happens with an ABCn25 hybrid, failure of one chip only means losing that one chip, instead of all the chips in the chain from the faulty chip.

The barrel hybrids for the ABC130 hold 10 chips each. This hybrid requires, based on the current consumption of the chip, 1.51 W in the case of short strips. There is a significant reduction power of the power consumption compared to the ABCn25 based hybrids.

#### 4.2.4 End of Stave/Petal Card

The interface between the Hybrid Control Chips and the off-detector read-out systems is done through the End of Stave (EoS) and End of Petal (EoP) cards. These contain a controller, a DCS dedicated chip and interfaces for optical communication with the off-detector system.

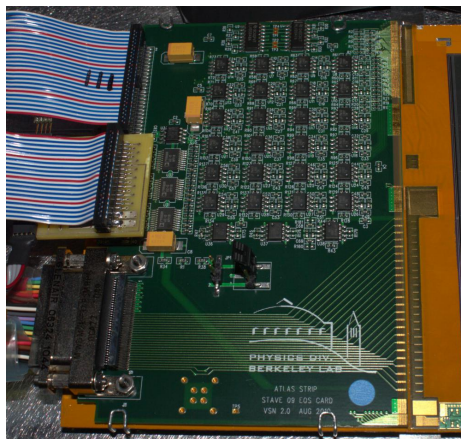


**Figure 4.11: End of Stave card from a four-module stavelet.**

Figure 4.11 shows the End of Stave card used on a four-module stavelet, with only electrical interfaces. This board is designed to support up to 12 modules on a stave, by having the 48 streams that are needed to read-out the 24 BCCs (two streams per chip, one per column of chips). The two flat cables transmit the data to and from the BCCs, as well as the temperature sensors read-out and the power for the LVDS buffers on End of Stave card. The bottom connector is used on this EoS card to connect the high voltage to bias the sensors. On the right side the card is connected to the bus tape using wire-bonds.

The optical interface to be used in the final stave design is implemented using the GigaBit Transceiver (GBT), a radiation tolerant chip that allows bi-directional optical transmission for data read-out, trigger, timing, control and monitoring links. The point to point link speed is specified to be 5 Gbps. Both multi-mode and single-mode transmission are being considered, using 850 nm and 1310 nm wavelengths, respectively.

The GBT chip is part of the Versatile Link transceiver (VTRx), which is designed to use optical fibres with standard LC connectors on an SFP-like package. The commercial Small-Form factor Pluggable (SFP) packages have a metallic case which is, in principle, unsuitable for operation in the HL-LHC environment. An option is to remove the case and design a custom connector latch with non metallic materials [80]. A picture of one of the transceiver prototypes is shown in Figure 4.12.

### 4.3 Powering Schemes

The power delivery in the current silicon detectors at the LHC is made independently for each detector element. In the case of the ATLAS SCT, each module is powered with its own line, which means this sub-system uses 4088 independent power supplies, one for each module, what involves a set of cables in order to supply power to the hybrids, power to the read-out and trigger, timing and control signals, and sensor bias [81].



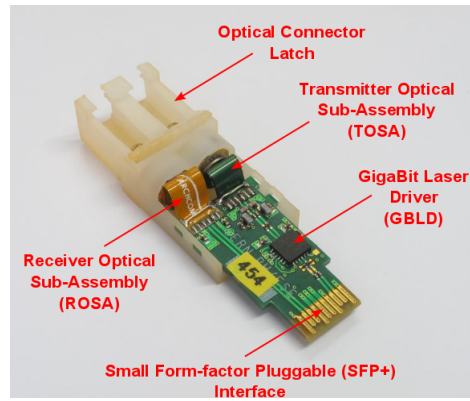


Figure 4.12: Picture of a VTRx showing the components of the transceiver package [80].

Since the power supplies have to be placed at a safe distance from the irradiated area, the power lines in the current ATLAS detector are in the order of 100 m long. An immediate consequence is that the cable resistance causes heating and waste of power in the cables. Between fifty and eighty percent of the low voltage power supplies output power is lost in the cables.

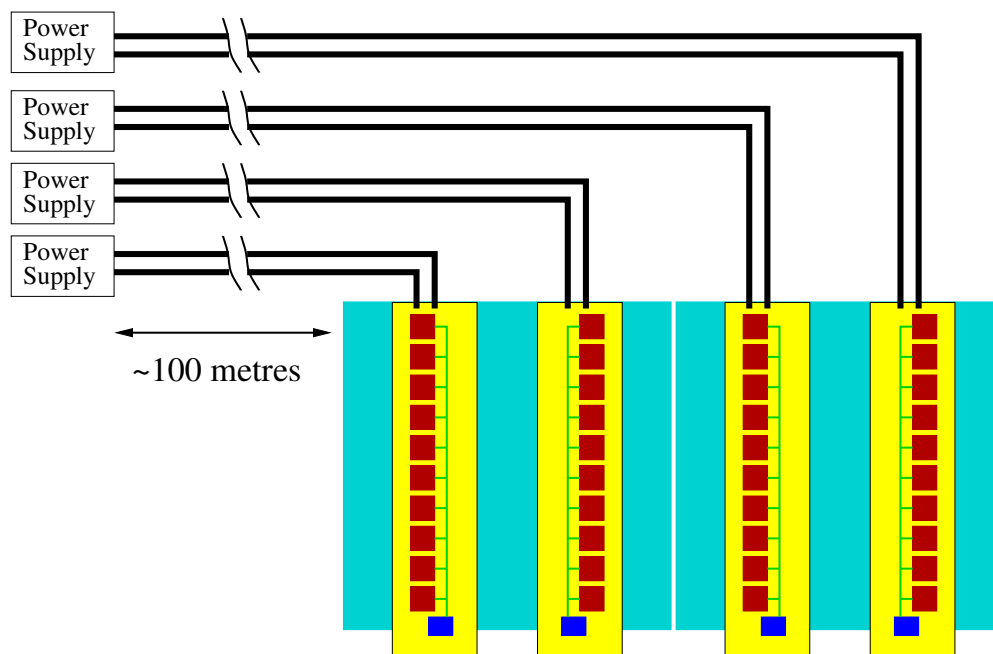


Figure 4.13: Independent powering of hybrids.

This approach is shown in Figure 4.13, where each module has two hybrids, independently powered by separate cables and power supplies. This power distribution model is not suitable for the electronics in the HL-LHC trackers. The power calculation for a short strips stave with 26 hybrids holding 10 ABC130 chips each yields 78.5 W per stave and 37 kW for the whole tracker barrel [77].

The petal consumes around 30 W in its current design, leading to a power consumption of the endcaps of around 13 kW for all the 448 petals. The current SCT,

with a consumption of 3.1 mW per channel, has a total power consumption of 19.5 kW, including both the barrel and the endcaps.

Considering this great increase in power consumption, due to the much higher number of read-out channels, the following problems have to be considered for the high luminosity upgrade [82]:

- More power lines would be needed in an independent powering scheme, leading to an equivalent increase in material.
- That increased volume of cables also causes lack of space in the tracker volume.
- Very low power efficiency, more heating and wasted power.

The current space allocated for the services on the LHC experiments turned out to be barely sufficient for the trackers. In an upgrade scenario, there is absolutely no room to route more cables. Additionally, a requirement for the HL-LHC trackers is that they should not be more massive than the current ones, to avoid degrading the resolution.

Several alternative proposals for the power distribution have been made. The solution is aimed at reducing the current on the long power distribution cables. In order to achieve this, the two techniques under study are:

- Serial powering of modules is an innovative and elegant solution that relies on a constant current provided to the hybrids.
- DC-DC conversion is a more traditional approach, in which power transmission takes place at a high constant voltage, with low current, then a conversion to a lower voltage and higher current is done local to the tracker.

A brief description of these two approaches follows.

### 4.3.1 Serial Powering

In the serial powering (SP) scheme, a constant current is fed to a series of elements. A local shunt regulator circuitry provides the voltage to each element. In this context, an element can be either a module or a hybrid.

The voltage across the chain of elements (e.g. modules) is  $n$  times the element voltage and the reference potential of each module is different. These different reference levels require an AC coupling or optical decoupling of the digital control and data signals [82].

Between 10 and 20 modules would be chained in series, leading to a great reduction in the number of power cables, as such that less cables would be required in the HL-LHC trackers than in the current LHC trackers.

A sample of the serial powering technique is shown in Figure 4.14, with two modules, each with two hybrids, powered with constant current.

The voltage is regulated locally on each hybrid, by means of a shunt regulator. The current overhead to keep the right voltage on each hybrid can be low if all hybrids are electrically similar, drawing about the same current. Otherwise, the hybrid with the highest consumption sets the current draw on every hybrid of the chain, which can lead to efficiency losses when power consumption is uneven.

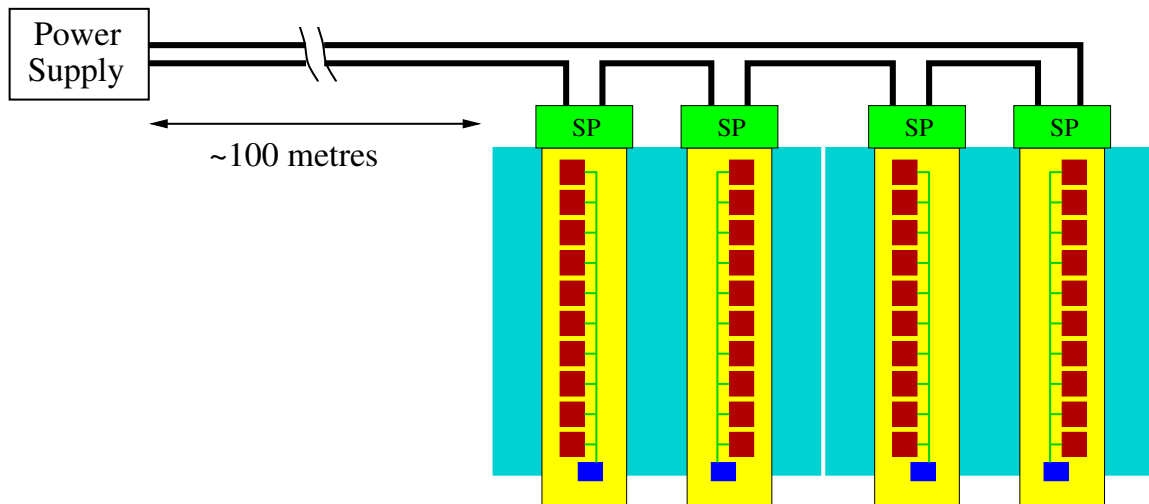


Figure 4.14: Serial powering of modules. In this case, each hybrid is at a different voltage reference, so this scheme is called “chain of hybrids”.

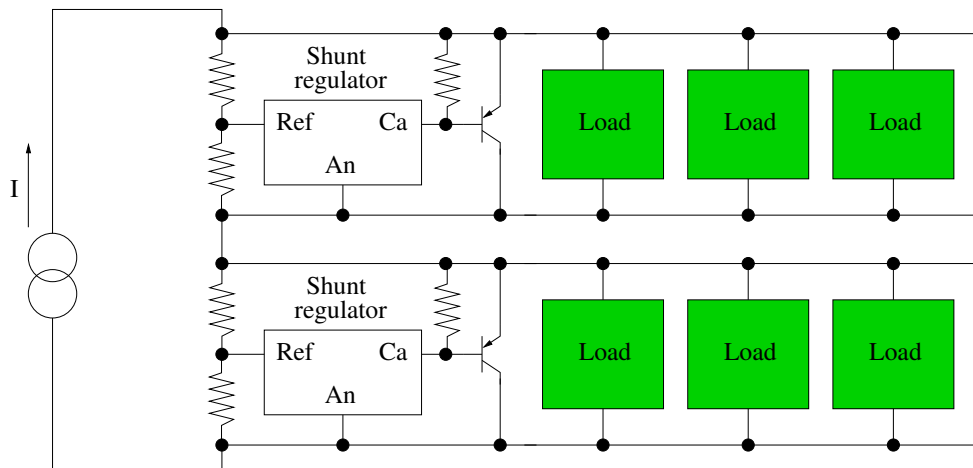


Figure 4.15: Serial powering with one shunt regulator and shunt transistor external to the load.

An example of such an implementation is shown in Figure 4.15, which depicts one of the alternatives to power two modules. Other options are having one shunt regulator and one shunt transistor per load unit (chip) or having one shunt regulator for a group of chips and one shunt transistor in each chip [83].

A preliminary study of this powering scheme was performed using ATLAS SCT barrel hybrids [84], with promising results. Currently, there is a wide community studying the performance of serial powering using the Phase-II Upgrade modules and hybrids. Several devices implementing serial powering have been constructed.

There are single modules as well as stavelets, the latter either chaining modules or hybrids. The chain of modules means that both hybrids on a module have the same reference voltage, while the chain of hybrids implementation forces all hybrids to have different reference voltages.

Figure 4.16 shows a serial powering board used in one of the serially powered stavelets, assembled at RAL. The powering configuration of this stavelet is a chain of mo-

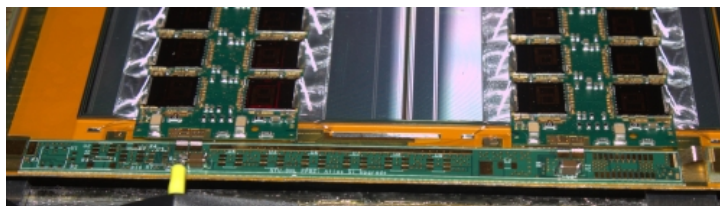


**Figure 4.16:** Serial powering board on a serially powered four-modules stavelet.

dules.

Some test results performed on serially powered devices, in the scope of this thesis, will be presented in chapter 5. The devices will be described later in this chapter.

### 4.3.2 DC-DC Conversion

The use of local DC-DC conversion is, *a priori*, a more natural approach than serial powering. Both independent powering and parallel powering can be utilized with DC-DC conversion, without completely losing the advantage of cable material reduction.

A popular DC-DC architecture is the buck converter, which uses an inductor as the energy storage unit, switching transistors, a switch control unit and a filtering capacitor. The efficiency of this architecture is high and it has the capability of delivering high current to the device [82].

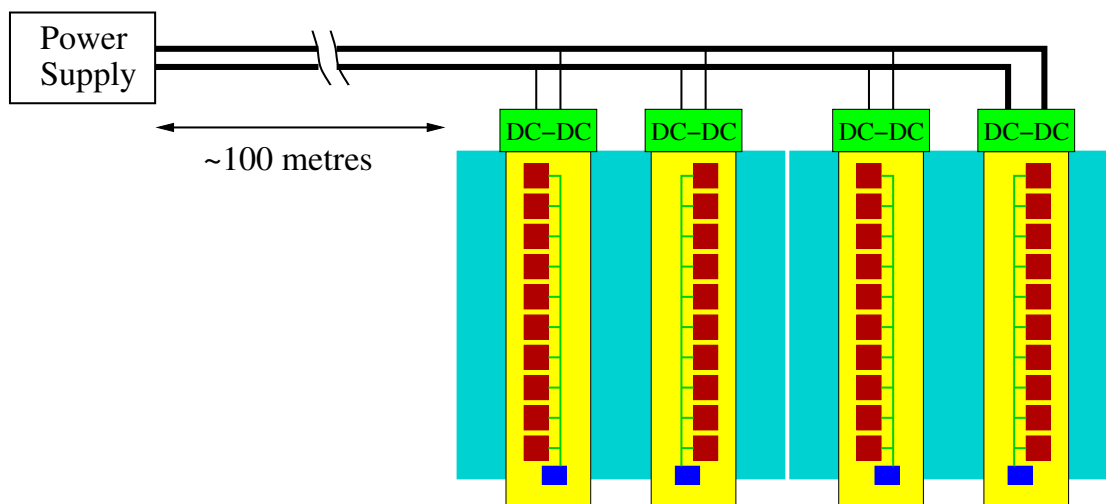


**Figure 4.17:** Powering of modules with DC-DC conversion. The drawing shows the parallel powering scheme.

A sample scheme of this approach is shown in Figure 4.17, where two modules, each with two hybrids, are powered by a higher voltage supply that gets converted down at the hybrids.

One of the challenges for DC-DC converters in the HL-LHC trackers is to minimize the material, through miniaturization of the device. In addition, the converters have to cope with an extremely high radiation environment and operate in a strong magnetic field. As a reminder, the ATLAS solenoid magnet is 2 T and the CMS magnet is 4 T.

This last detail limits the implementation of the inductor to an air core version, not allowing the use of ferromagnetic cores, in order to avoid saturation. As a result, the size of the inductor increases for a target inductance value.

A low noise and low mass DC-DC converter has been developed at CERN and is now the baseline for the DC-DC powering schemes in the Strips Tracker Phase-II Upgrade community [85]. Three versions of the converter modules that have been designed are shown in Figure 4.18.

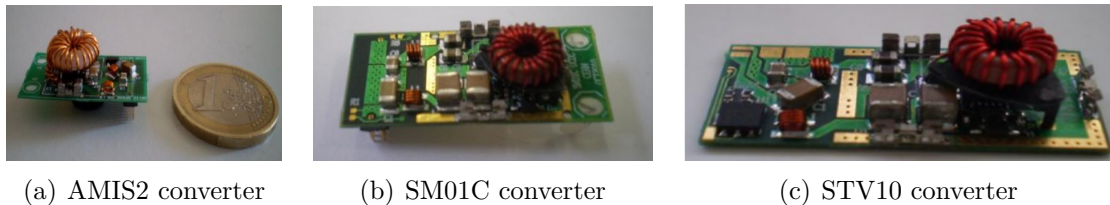


**Figure 4.18: Different versions of the DC-DC converter designed at CERN for the ATLAS and CMS trackers upgrade [85].**

The AMIS2 converter [86] is designed for the 130 nm CMOS chips, providing up to 3 A with an output voltage between 1.2 and 5 V, and a peak efficiency of 80%. The input voltage range is 7 to 10 volts. This converter cannot deliver enough current to the ABCn25 based hybrids, as these require about 5 A peak current.

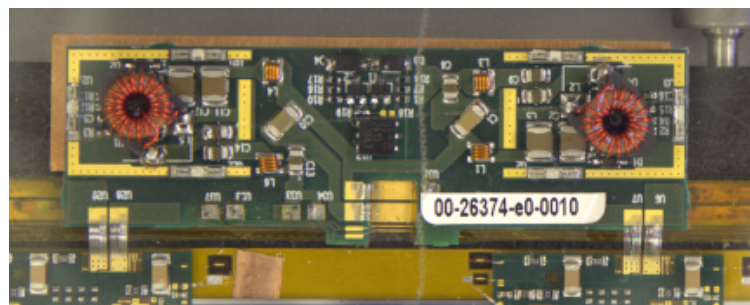


**Figure 4.19: A tandem DC-DC converter with dual output.**

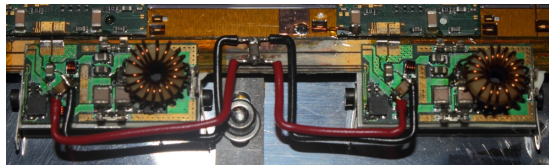
The other two converters, SM01C and STV10, were designed to meet this requirement. The first, SM01C, is a pluggable converter, whereas the STV10 is a connectorless, wirebondable module [85]. The STV10 is the power module used in the construction of the stavelets and petalets.

With respect to the noise performance, the AMIS2 is designed to be suitable for the High Luminosity LHC tracker front-ends. The two designs of DC-DC converters for ABCn25 chips have slightly higher noise than the AMIS2.

For stavelets with DC-DC converters, a common connection from the bus tape to the converters input is needed for the two converters of a module, in order to have good noise performance [87]. This requirement leads to the design of the so-called “tandem” converter, which consists of two DC-DC converters placed on the same board and with a common reference plane.

The tandem converter has a single power input and two outputs, placed at the locations of the hybrids in a module. A re-manufacture was done by partially splitting

the ground plane and this converter has been used for the first full length stave with DC-DC powering and using the ABCn25 chip. One of these converters is shown in Figure 4.19.



(a) DC-DC converters with their shields removed.



(b) DC-DC converters with the shields covering the coils.

**Figure 4.20: DC-DC converters mounted on a stavelet.**

One of the difficulties in using DC-DC converters is the big inductor, which generates interferences to the read-out electronics and forces the use of shields to attenuate the emitted electromagnetic field. The shields are made of a plastic box that is covered with a copper paint layer. This shield increases the amount of material that the DC-DC converter adds to the tracker.

In addition, due to the high power that has to be switched, the converter needs to dissipate some of it, generating a lot of heat. This heat needs to be extracted, increasing the cooling system requirements.

Figure 4.20 shows two converters on a stavelet, powering one hybrid each. The first image shows the converter without the EMI shield covering the big coil. The switching ASIC is located underneath the coil.

The star point implemented with wire for the two converters of one module can be seen in the centre of the pictures.

### 4.3.3 Advantages of DC-DC and SP

Each of the two techniques presented here have their own advantages and disadvantages. The two have clear advantages over independent powering. The different solutions are described next.

The main advantages of the serial powering approach with respect to DC-DC conversion are lower mass and potentially higher efficiency with increasing number of modules [84]. The geometry of the DC-DC converters is also more difficult to accommodate into the tracker volume due to the reduced clearances caused by the shield around the coil.

However, while this is true for the barrel staves, as was described in section 3.3.2, the endcap hybrids have different number of chips for different rings. Due to this difference, the power requirements differ for each hybrid on the endcaps. As a result, the use of serial powering in the endcap would require adding power dumps in the hybrids with lower power consumption, leading to waste of power and a greatly reduced efficiency.

The consequence is that the endcap petals are forced to use DC-DC conversion in order to obtain an adequate power efficiency.

In the case of the barrel, all hybrids in a stave hold the same number of chips. Therefore, there are no efficiency losses unless there is a change in the power consumption of a hybrid, such as a disconnected chip.

In addition, serially powered modules and stavelets tend to show more susceptibility to external noise and are harder to protect from common mode and differential mode noise pickup.

Both DC-DC conversion and serial powering techniques lead to reduced number of power supplies and rack space in comparison to an independent powering scheme. Also, as we have already discussed, the gain in efficiency leads to much less wasted power and cable material inside the detector.

With respect to a possible disadvantage of using either DC-DC conversion or serial powering, in both cases the number of lost modules in case of failure of a power line is high. However, the number of connections that may fail is greatly reduced, compared to a more robust, independent powering scheme. In addition, the savings of these two powering schemes can be exploited to engineer robust module connections [88].

Attribute	IP	SP	DC-DC
Power efficiency	10 – 20%	60 – 80%	60 – 80%
Local regulator efficiency	N/A	$\approx 90\%$	$> 80\%$
Number of power cables	4 per hybrid	$2n$ reduction	$2n$ reduction
Protection	Yes	Yes	Not known yet

**Table 4.2: Comparison of some features of the three powering schemes: Independent Powering (IP), Serial Powering (SP) and DC-DC conversion.**

Some features of the various powering schemes, namely independent powering, serial powering and DC-DC conversion, are shown in Table 4.2 [82]. The protection features are conceived in order to address the event of a connection failure or an over-current or over-voltage situation.

In the independent powering case, the protection mechanism is the simplest that can be conceived, that is separate cables for each hybrid. In the serial powering approach there are over-current protection mechanisms and redundant regulators protecting the devices.

## 4.4 Sensor Biasing

The biasing of the sensors, in the case of the barrel, is done at the whole module level. This means that the four short strips rows are biased using the same high voltage line. When scaling the numbers to full staves and the barrel cylinders, this leads to over 12000 high voltage (HV) lines, only for the strips tracker barrel.

The endcap discs have a total of 8064 sensors, summing up to more than 20000 high voltage lines for the whole microstrips tracker.

Independent high voltage lines for each sensor would be the natural approach, as it permits disabling individual modules (for instance, in case of malfunction) without disturbing the rest, as well as individual leakage current measurement.

However, the amount of cable material needed for this is very high, to allow for these two particular features. A means to reduce the number of cables is being studied, by using a technique that is called “high voltage multiplexing”.

In this approach, the high voltage lines for all the modules on a stave, or the modules on one stave side are multiplexed at the stave, feeding the staves with only two high voltage cables, reducing the total number of lines by a factor of 13.

As indicated in Table 4.1, the maximum operating voltage for the strips sensors is around 600 V. Therefore, the key factor in the high voltage multiplexing approach is to find a radiation hard switch rated above 500 V. In addition, a desirable feature is to allow measuring the leakage current on each sensor individually.



**Figure 4.21: SiC based high voltage multiplexer developed at BNL.**

A four channel multiplexer based on silicon carbide (SiC) field-effect transistors (FET) has been developed and tested on four-module stavelets. There is no performance degradation of the modules and the only disadvantage is the lack of individual leakage current sensing for this particular prototype.

The SiC transistors switch each of the four channels, which allows the individual disconnection of HV channels. A picture of this multiplexer is shown in Figure 4.21. Results of the tests with this device on a DC-DC powered and a serially powered stavelet are presented in chapter 5.

The investigation on radiation hard, high voltage devices that can be used to multiplex up to 13 lines, corresponding to one side of a full length, 130 nm based stave, is ongoing. The existing MOSFET and bipolar transistors that can operate above 500 V are not as radiation hard as required. Materials such as silicon carbide (SiC) and gallium nitride (GaN) are the main candidates for implementing these multiplexers [58]. These materials have a wider band-gap what gives them a greater intrinsic radiation hardness [89].

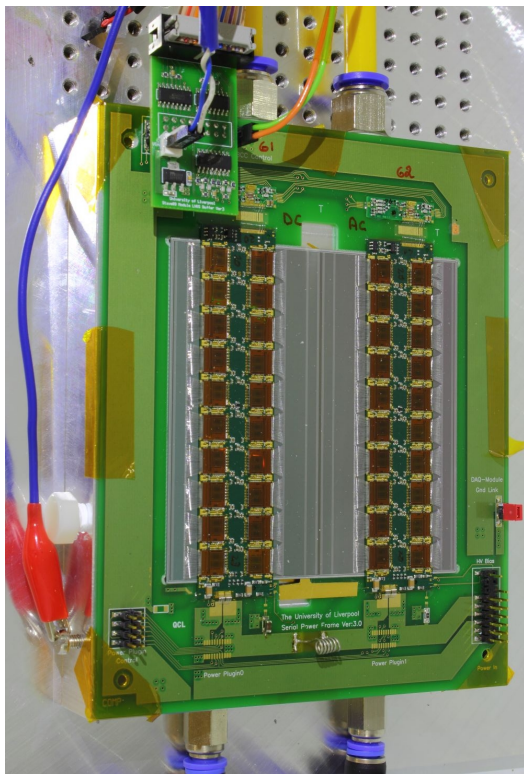


## 4.5 The Stavelet Concept for the Tracker Barrel

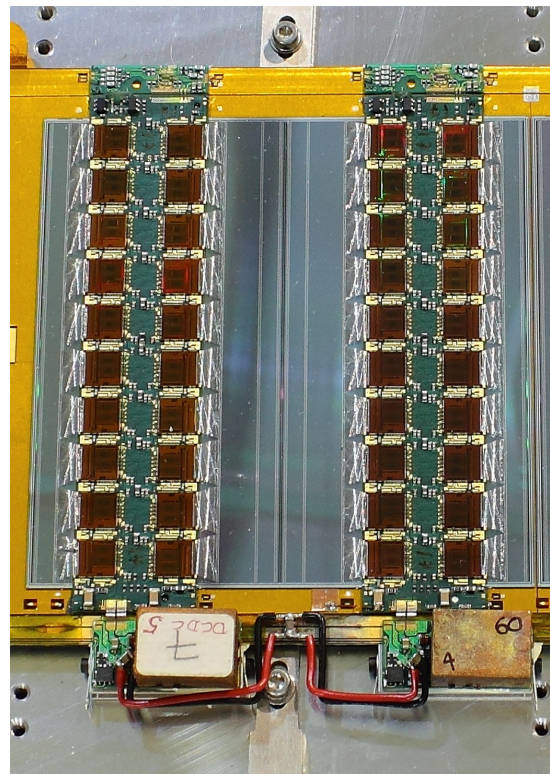
The stavelet proof-of-concept of the tracker stave is a multi-module structure, holding four individual modules in its first incarnation. The initial stavelets were single sided, others have been assembled with two sides [90]. Both DC-DC conversion and serially powered modules and stavelets (with chain of hybrids and chain of modules) have been built and tested.

### 4.5.1 Silicon Microstrip Modules

The stavelets tested at CERN are single sided and consist of four individual silicon modules. Each module has a short strips silicon sensor, with integrated electronics for the read-out and control of the module. The sensors and the individual electronic components have been described earlier in this chapter.



(a) A single module attached to its frame. The picture shows the two hybrids, the sensor, serial powering line on the bottom and the BCC boards on the top of the module. The module is placed on an aluminium cooling plate.



(b) A single DC-DC module on the stavelet. The DC-DC converters are at the bottom, the BCC boards are on the top and the module is mounted on a bus tape that routes the powering and signal lines.

**Figure 4.22: Single modules on a test frame (serially powered) and on a stavelet (DC-DC powered).**

Figure 4.22(a) shows a single module, mounted on a test frame that interfaces with the power, sensor bias and DAQ system. The two hybrids with 20 read-out ABCn25 chips are shown, the BCC boards are on the top of the picture, the powering and sensor

bias come from the bottom right and the Low Voltage Differential Signalling (LVDS) come from the top left.

The powering scheme is implemented on the test frame, the picture shows a serially powered module on such test frame. Also, the BCC is mounted on the test frame due to the lack of space on the hybrid.

The picture shows the yellow cooling pipes on the top, the vacuum connectors on the bottom, the LVDS buffer board at the top left side of the module and the powering connector at the bottom right (without the board connected to the module). The module jig can be seen from the perspective on the left hand side of the module.

Figure 4.22(b) shows a DC-DC powered module mounted on a stavelet. The DC-DC converters power one hybrid each and they are connected in a star configuration.

All the modules constructed to date use the ABCn25 ASICs, with 128 channels each. Each hybrid contains 20 chips that are arranged in two columns, and the read-out from the BCC is done for each column (called “chip column”).

The single modules on a test frame are usually tested using an aluminium block to cool down the electronics, with a vacuum pump pulling down the module, in order to have a good thermal contact between the cooling block and the module.

The connection to the read-out system, the HSIO board, is done by means of a 16-pin IDC ribbon cable to a Low-Voltage Differential Signal (LVDS) buffer board, that is in turn plugged to the module test frame.

The low voltage and sensor bias power are connected via two connectors (Molex for low voltage and LEMO for high voltage) that are plugged into a PCB on the test frame.

Typically, the power for the hybrids is provided by a custom current source [91] in the case of serially powered modules, which is capable of providing up to 6 A. A serially powered module is usually powered with 5 A and the voltage drop is around 6 V. Alternatively, a commercial DC power supply may be used, set to limit the current around 5 A.

To power DC-DC modules, a commercial DC power supply is normally used, capable of providing 10 V and around 3 A.

For the sensor bias, there are prototypes of the SCT high voltage cards available, that work on a VME crate. These cards are compatible with the requirements of the sensors. At CERN, this is typically used with stavelets. When testing single modules, a commercial high voltage unit is normally used.

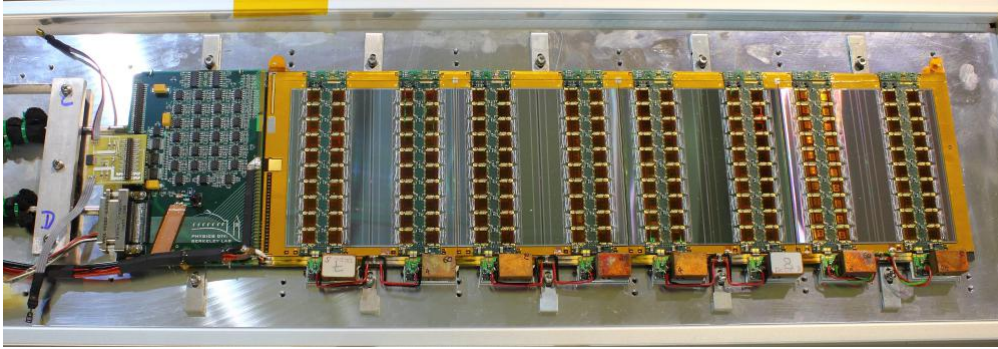
## 4.5.2 Multi-module Structures

Several multi-module prototypes of these short strips modules have been designed and constructed, consisting of 4 modules in a single sided structure. These prototypes were conceived in order to assess the potential problems and challenges that appear when multiple modules are powered and read-out together.

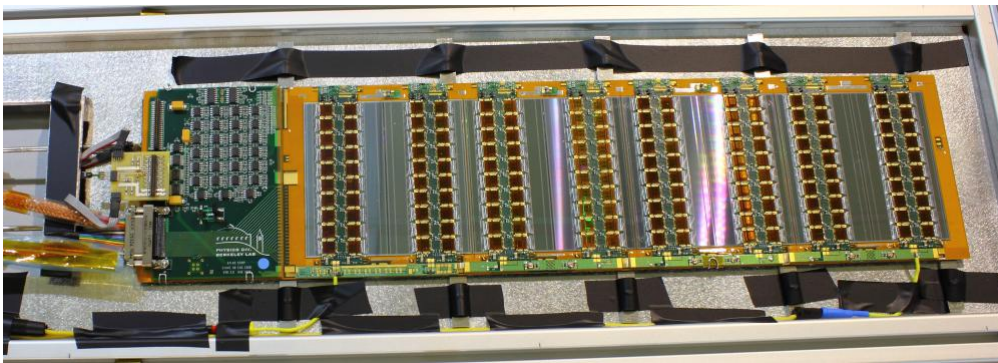
Such multi-module structure is called “stavelet” in the case of barrel modules, and is currently being used as the proof of concept of the stave design.

The stavelet consists of a low mass carbon composite core, that provides mechanical support and cooling, the latter through the embedded aluminium cooling pipes.

The modules are mounted on the stavelet using precision mechanical tools and attached to the core with glue [90]. The structure of the stavelet can be seen in both



(a) DC-DC powered stavelet.



(b) Serially powered stavelet.

**Figure 4.23:** The two stavelets built at RAL and tested at CERN. Both pictures show the four modules, the end of stave card to the left, as well as the cooling pipes. The powering is placed at the bottom side of the modules.

pictures of Figure 4.23, with the 4 sensors and the EoS card. Each of the sensors has the hybrids on top of it, holding the 20 ABCn25 chips.

Figure 4.23(a) shows a DC-DC powered stavelet, and the DC-DC converters with the EMC shield covering the coils can be seen at the bottom of the picture. The left side of the picture shows the End of Stave card and cooling pipes. The stavelet is mounted on an aluminium plate with a Bosch profile attached for transportation. Figure 4.23(b) shows the serially powered stavelet in a similar manner. Instead of DC-DC converters, the bottom side of the picture shows the serial power regulation.

Power and LVDS control signals are routed along the stavelet on a bus tape that has a copper trace layer under an aluminium shield [92]. The high voltage lines are routed independently for each module. Other stavelet implementations use a shieldless tape [90].

The tapes for the DC-DC and the SP stavelets are slightly different, as in the SP stavelet it has a segmented serial power chain along one of the edges. In the DC-DC stavelet, that edge has simple parallel lines.

In addition, the width of the DC-DC stavelet is increased in order to add mechanical support for the DC-DC converters. The increase is achieved by means of aluminium pieces glued to the stavelet edge, what also adds a cooling path to the converters [92].

Other features are equal between the two stavelets, such as the AC-coupled interface of the BCC board with the End of Stave card, which is unnecessary for the DC-DC

stavelet. The EoS card is the same design for both. However, in the DC-DC stavelet, the power traces cannot cope with the current needed. Therefore, they have been bypassed using thick copper [92].

The DC-DC stavelet is typically powered using a commercial DC power supply. The voltage is normally set so the voltage sense at the converters inputs is very close to 10 V, accounting for the losses in the cables and the traces. The current drawn when all eight hybrids are powered is around 10 A.

The Serially Powered stavelet, as it follows the chain of modules scheme, is powered by a commercial DC power supply, set to work in current limit mode, with the current limit set between 9 A and 10 A. The typical current setting is 9.5 A, with a typical voltage drop around 12 V.

Sensors on a stavelet are normally biased using SCT high voltage cards as described in the previous section. These cards can deliver up to 500 V. They require a low pass filter in order to reduce noise on the lines. Also, a high voltage multiplexer like the one described in Section 4.4 is typically used in the tests.

The following chapter describes the tests and results performed on various devices that were tested at CERN, in a facility in Building 180. These devices are a serially powered single module, a serially powered stavelet and a DC-DC powered stavelet. A DC-DC powered full length stave with 12 modules on one side was also tested at Rutherford Appleton Laboratory (RAL).

# Chapter 5

## Results and Discussion of the Structures for the Silicon Tracker Upgrade

### 5.1 Tests of Modules and Stavelets

#### 5.1.1 Infrastructure

The test facility at CERN is located in Building 180 (B180), which was initially put in place in 2010. After summer 2011, it has been regularly used for the Strips Tracker Upgrade projects: staves and supermodules.

This facility includes a clean room that is used for regular testing and assembly of strips and pixels projects, and a bunker area outside the clean room. The clean room is shown in Figure 5.1.



**Figure 5.1: The clean room in Building 180 at CERN.**

The clean room is equipped with compressed air lines. A gowning room is placed before the main entrance and there is an equipment entry area that is used to bring in and take out big equipment and furniture.

#### 5.1.2 Data Acquisition System for System Tests

The Data Acquisition (DAQ) system used for the tests of modules and stavelets consists of the read-out board, the firmware running on it, and the software running on a

computer that controls the whole system.

### The HSIO Board

The ATLAS Strips Upgrade project is currently using an updated version of SCTDAQ software for detector hardware development. The legacy VME based system used in the current SCT cannot scale to read-out larger objects like stavelets. For this reason, the next generation of read-out hardware/firmware is being developed using an FPGA based board called the HSIO (High-Speed I/O) board, designed at SLAC. A picture of the HSIO board is shown in Figure 5.2.

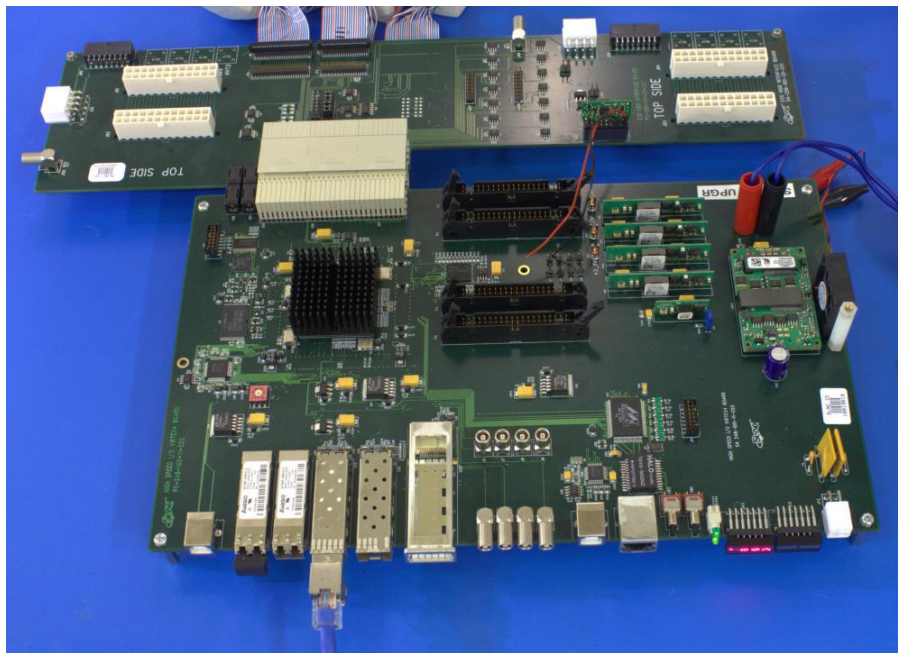


Figure 5.2: HSIO board used in the Strips Upgrade DAQ system.

The HSIO is a stand-alone unit with a Virtex-4 FPGA and many interface options. It has a variety of standard network connections, such as copper and optical Gigabit Ethernet, making Ethernet the preferred communications protocol.

The HSIO board is connected to an interface board that allows the connection of single sided modules and stavelets.

In order to communicate with a computer, the currently supported interfaces are the 100 Mbps Ethernet connection as well as the 1 Gbps copper connections through an SFP connector that is plugged into the HSIO board. The firmware version used for the tests described in the next chapter use a direct communication over Ethernet, not relying on any higher layer protocols.

### SCTDAQ Software for the Upgrade

The SCTDAQ software used in the prototype tests for the Upgrade is based on the SCTDAQ software that was used for the system tests of the current SCT. It has been modified to support the new HSIO system and to handle multiple modules.

Figure 5.3 shows the Burst Data window of the SCTDAQ software as seen with up to four visible modules. The drawing on the top depicts the structure of a four module

stavelet, which permits the visual identification of the conditions of each module: bias voltage and leakage current, temperatures of the hybrids, low voltage power status and temperature/humidity sensors at the pipes.

The four pads on the bottom show the hit occupancy for every strip on the module, with one pad for each hybrid column (1280 strips per pad). There is a tab for each module configured in the software.

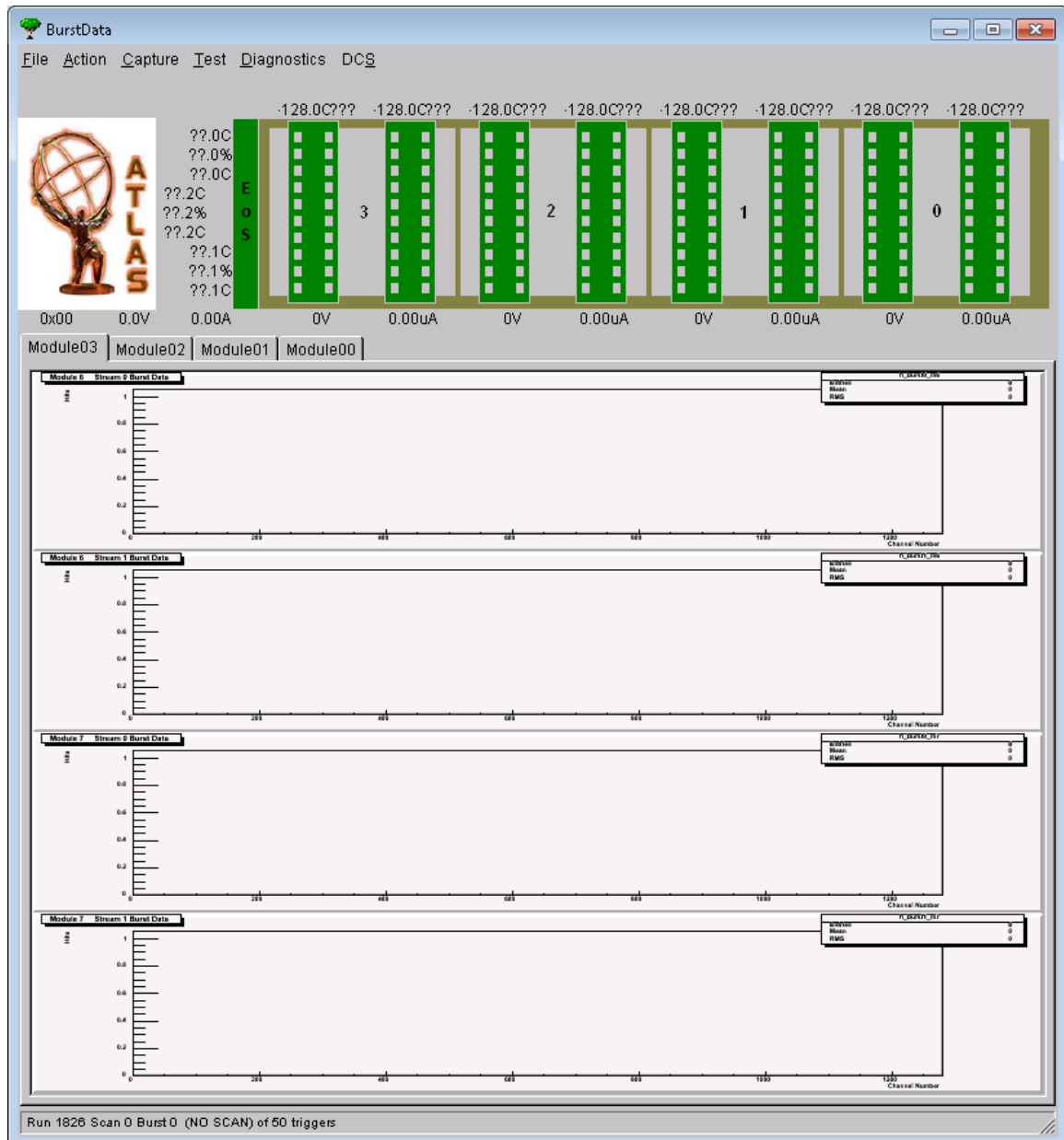


Figure 5.3: The Burst Data window of the new SCTDAQ software.

The software runs on either Windows or Linux computers, in a ROOT environment [93]. It consists of compiled libraries supporting the various interfaces with the devices and a set of ROOT macros that use these libraries to implement the tests. The supported devices range from VME crates to commercial power supplies.

Configuration files and ROOT macros are used to control the power supplies or VME crates in use, modules connected to the HSIO and parameters of the modules.

Results of the tests are saved to raw ROOT files, which are usually processed and the final output are text files and, for some tests, plots saved in PostScript or PDF files. The environmental variables, such as hybrids temperatures and sensors leakage currents are also recorded.

The ROOT macros enable flexible configuration and setup of tests. Automation is possible and frequently used for long term tests, scans and varying parameters of the tests. Interlocks are used to power off the hybrids in case of a cooling failure, thus preventing the destruction of the devices when running unattended tests.

It is possible to include support for additional devices by means of a National Instruments VISA driver that is included in the software, for equipment supporting this system. Other devices that require a specific driver may also be supported with an extra effort.

### 5.1.3 Electronic Equipment

The testing facility is equipped with the necessary material to run tests on upgrade modules and staves, and to do minor repairs, modifications and adjustments.

Two computers control the two HSIO systems that are available. One of the HSIO boards is used with single modules, either in the clean room or in the radiation zone. The second HSIO is normally used to test stavelets.

Several commercial and non-commercial power supplies are available in the room. A Keithley 2410 source meter is used to bias the sensors, controlled through its GPIB or RS-232 interfaces. A variety of TTI power supplies are used to power the HSIO and the modules or stavelets, also controlled through a GPIB interface. A custom current source used to power hybrids on the chain of hybrids configuration of a serially powered module or stavelet [94] can be controlled through USB. Last, a VME crate holding SCTHV boards which are the pre-production series for the SCT high voltage have four channels and are used to bias the sensors on stavelets [95].

The chance of damaging the modules is minimized by means of an interlock system developed at the University of Cambridge [96] that monitors the temperature of the devices. In case of failure of the cooling plant, the power to the modules is interrupted. This way, unattended, long term tests can be safely performed.

An optical table, assembled in the University of Freiburg, is used to hold an X-Y motion stage, covered by a light-tight enclosure built at CERN. Inside the enclosure, modules and stavelets can be placed to be tested in a dark environment. The motion stage can be used to map the electromagnetic field of a DC-DC stavelet, inject electromagnetic noise on a stavelet at different positions and inject charge on the strips with a laser.

#### Single module DAQ stand

This setup uses an HSIO board, powered by a linear power supply set to 12 V, and a Huber chiller with a 20% glycol-water mix. A Julabo chiller has also been used to test single modules. This chiller uses an oil based coolant which can be cooled below  $-20^{\circ}\text{C}$ . Low temperature tests down to  $-20^{\circ}\text{C}$  have been performed on a single module.

A vacuum pump is used to hold the module in the aluminium block, in order to have a good thermal contact between the module and the coolant. In addition, an interlock monitors NTC temperature sensors on the hybrids. If the temperature goes above the set threshold (usually around  $40^{\circ}\text{C}$ ), the hybrid power is turned off. This



may happen in the event of a cooling failure or a vacuum problem that causes the module to lose thermal contact with the cooling block.

The single modules are tested inside a small freezer that is used to keep the light from falling on the biased silicon sensor.

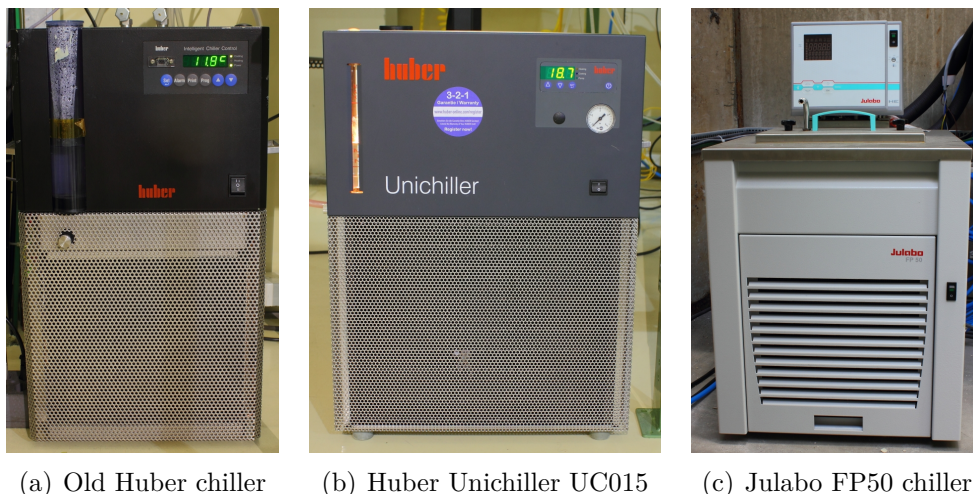
A compressed air line is available and can be connected to the freezer in order to keep the relative humidity in the freezer low, thus avoiding condensation when testing the module at low temperatures.

### Stavelets DAQ stand

This setup is similar to the single module DAQ system. However, some pieces are slightly different:

- A VME crate with two pre-production SCTHV cards controlled from the computer, via a PCI-VME card. These cards have four output channels each, which permit the biasing of up to eight modules without multiplexing.
- There is no extra power supply to power any LVDS buffer board. The stavelet has the LVDS buffers on the End of Stave card, powered through the HSIO.
- Dual channel power supply to provide power to two stavelets at the same time.
- The interlock monitors the inlet and outlet pipes of the stavelets. Small increases in the temperature of either is interpreted as a cooling failure.

### 5.1.4 Cooling Plant



(a) Old Huber chiller      (b) Huber Unichiller UC015      (c) Julabo FP50 chiller

**Figure 5.4: Chillers used in the B180 test facility.**

There are three chillers at the testing facility. Two of them are inside the clean room, they both are Huber chillers with a water-glycol mix at a 20% glycol concentration. The single module setup uses an old version of the Unichiller 007-MPC and the stavelets setup has a Unichiller UC015.

The third chiller is located in the radiation bunker, it is a Julabo FP50 running with an oil-based coolant. It has been operated at  $-20^{\circ}\text{C}$  with a single module in the clean room. The three chillers are shown in Figure 5.4.

The typical temperature setting of the chillers in the clean room is  $12^{\circ}\text{C}$ . The temperature and humidity are monitored using SHT71 sensors in order to avoid going below the dew point, thus avoiding condensation.

Lower temperature settings are used for some tests and, for these tests, dry air is flushed into the modules or stavelets enclosures to prevent condensation.

### 5.1.5 Performance Tests and Calibration

This section describes the typical performance tests and calibration functions that are performed on the modules and stavelets. The tests are typical for describing the silicon microstrips devices performance, and they are the same as the ones performed on the SCT modules.

The calibration functions are normally performed before the tests, in order to have adequate timing and response variability for all the channels.

#### Strobe Delay

The Strobe Delay (SD) test is one of the calibrations that have to be done before testing the modules. It varies the phase of the charge injection relative to the Level 1 Accept (L1A) command. An optimal setting of the SD for each chip is important for the accuracy of the threshold calibration. The test consists in scanning the timing while injecting a charge. To achieve 100% hit efficiency when the timing is correct, while at the same time minimizing noise, the injected charge is 4 fC and the threshold is set to 2 fC [97].

The delay of the strobe (with respect to the clock phase) can be tuned for individual chips within a range of around 50 ns, controlled by a 6-bit SD register (1 DAC step  $\approx 0.8$  ns). Other SD ranges are possible, for which 1 DAC step is equal to 1 or 1.3 ns respectively. The SD is actually recorded in an 8-bit register but only the first 6 bits of this are used, resulting in a delay range of 0 to 63 [98].

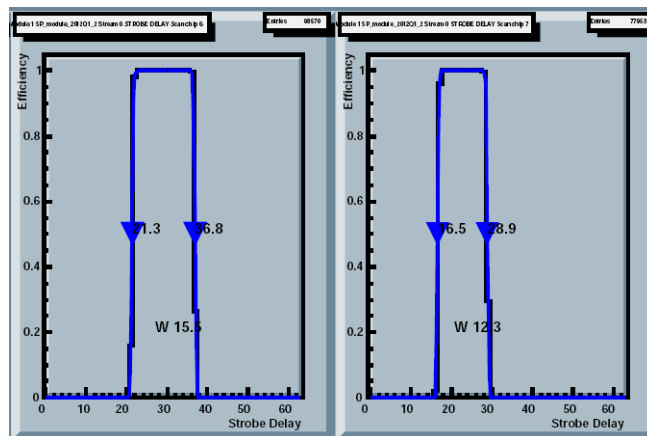


Figure 5.5: Strobe Delay data for the fit on two adjacent chips.

The SD test does a scan of the SD setting, from 0 to 63, sending 200 triggers at each SD value. The resulting average hit efficiency for all channels of a single chip as a function of the SD setting then looks as shown in Figure 5.5, where the efficiency for two adjacent chips is shown. The resulting SD settings are calculated taking the SD value that is at the 25% of the working range, defined as the interval between rise and fall times of the curve

### Trim Range

The channel trims are always set to minimize the variations of the response between channels. An untrimmed hybrid is spotted when the offset shows big variations from chip to chip and within the same chip as well.

The trim range scan injects a 1 fC charge for all events and does threshold scans for different trim DAC settings. The test ultimately generates optimal Trim Range settings that can be applied to each of the channels.

The analysis involves determining how many channels are trimmable for each trim range setting. Then the trim range setting that maximizes the number of trimmable channels is chosen [97].

### Three Point Gain and Response Curve

The 3-point gain test consists in performing threshold scans at three different injected charges [97]. There are two typical 3-point gain scans, one with a central injected charge of 1 fC and another one that injects charges around 2 fC. They correspond to a fairly linear region of the response curve and the injected charges are  $\{0.52, 1.0, 1.48\}$  fC and  $\{1.5, 2.0, 2.5\}$  fC, respectively.

The purpose of this test is to verify the analogue performance of the modules. The performance is measured with respect to the Equivalent Noise Charge ( $e^-$  ENC), which is measured in electrons ( $e^-$ ). This  $e^-$  ENC value is the result of dividing the output noise by the gain and converting the input noise in fC to electrons ( $1 \text{ fC} \approx 6242 e^-$ ).

The output noise, which is measured in mV, is the variance of the distribution of the threshold for a particular injected charge. The gain, measured in mV/fC, is calculated from a linear fit of the three threshold scan points [97].

The extrapolated offset is obtained from the linear fit and its spread is an indicator of the trimming uniformity.

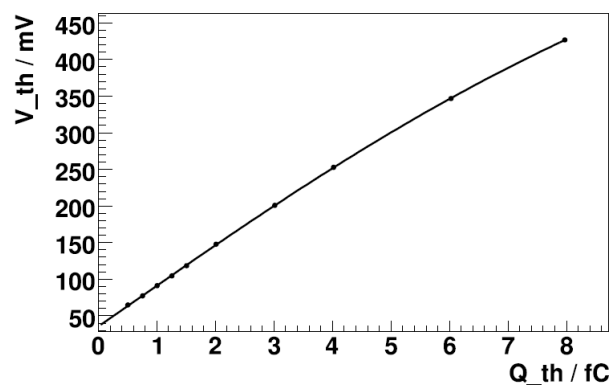


Figure 5.6: Quadratic fit to a response curve.

The response curve is an extension of the three point gain test to 10 scan points, where the injected charges are set to 0.5, 0.75, 1.0, 1.25, 1.5, 2, 3, 4, 6 and 8 fC. In the current SCT, this test is used to get a more precise measurement of the gain and offsets that can be used to update the configuration [97]. A quadratic fit to a response curve can be seen in Figure 5.6. This plot shows the non-linearity of the pre-amplifier in the chips as the input signal increases.

### Double Trigger Noise

The goal of the Double Trigger Noise (DTN) test is to assess the module susceptibility to electrical and optical pickup during the read-out [97].

The test is performed by sending two L1A triggers to the modules, separated by a specified number of 40MHz clock periods. The first event of each pair is discarded, leaving the second event to be recorded. The spacing of the two triggers is varied from 120 to 160 clock periods, to determine the occupancy of the modules at various points during the read-out cycle.

A trigger spacing of 132 is of particular interest as this is equal to the depth of the read-out pipeline: the second event records the occupancy of the module as the read-out cycle of the first event starts [40].

The typical DTN test is done with three different thresholds: 0.5 fC, 0.75 fC and 1 fC. Usually healthy modules and DAQ setups show no hits for 0.75 fC and 1 fC thresholds and a rather low number of hits for the 0.5 fC threshold.

### 5.1.6 Modules and Stavelets

Currently, there are three devices available for testing in the B180 facility: a serially powered single module, a DC-DC powered stavelet and a serially powered stavelet.

The serially powered (SP) module arrived at the beginning of 2012 from the University of Liverpool.

The DC-DC powered stavelet arrived at the beginning of 2012 from the Rutherford Appleton Laboratory (RAL), where it was assembled. The serially powered stavelet arrived at the beginning of 2013 from RAL.

A DC-DC powered stave with twelve modules on one side was assembled at RAL and has been tested there in the context of this thesis work.

The results presented in this chapter refer to these four devices.

A picture of the serially powered module can be seen in Figure 4.22(a), and pictures of the two stavelets are shown in Figure 4.23. Both stavelets are shown together in Figure 5.7, with the four modules on the left side of the picture, the End of Stave card around the centre of the picture and the services (powering, cooling and bias) on the right side.

All three have ABCn25 based hybrids using BCC boards. The sensors are from the ATLAS07 production batches, which means they all have two rows of axial strips and two rows of strips with a stereo angle of 40 mrad. The SP module has a FZ2 sensor, while the two stavelets have a mixture of FZ1 and FZ2 sensors.

The four modules mounted on the DC-DC stavelet come from the University of Liverpool. The characteristic parameters of the sensors are summarized in Table 5.1. The parameters were measured before the module assembly, in a clean room at 22°C. Both the leakage current and the capacitance are measured for the whole sensors, that is, for 5120 strips. The sensor of module LIV-M14, a FZ1 sensor, has insufficient

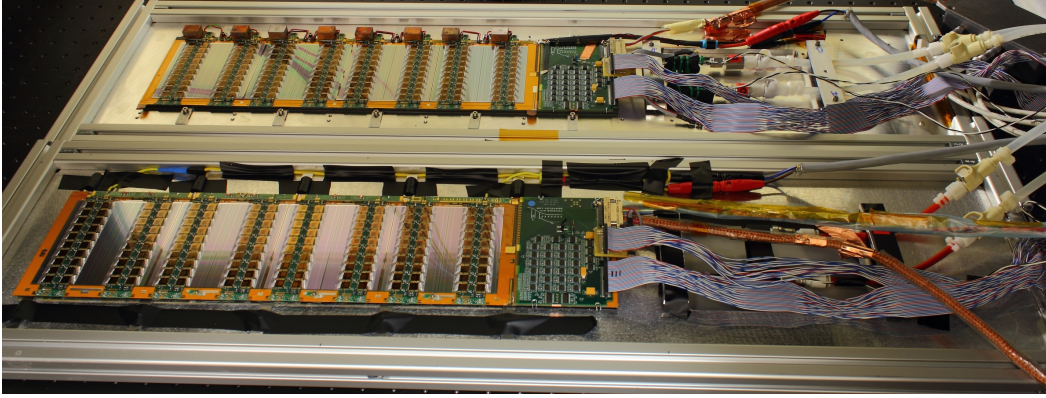


Figure 5.7: DC-DC stavelet (top) and SP stavelet (bottom).

oxide in the guard rings, leading to transients in the leakage current above 300 V bias voltage [99].

Module	Type	Isolation	$V_{\text{dep}}$	$C@250 \text{ V}$	$I_{\text{leak}}@250 \text{ V}$
0 (LIV-M16)	FZ2	P-stop, $10^{13} \text{ cm}^{-3}$	145 V	2.63 nF	10.0 $\mu\text{A}$
1 (LIV-M14)	FZ1	P-stop, $4 \times 10^{12} \text{ cm}^{-3}$	240 V	2.95 nF	0.24 $\mu\text{A}$
2 (LIV-M15)	FZ2	P-stop, $10^{13} \text{ cm}^{-3}$	130 V	2.63 nF	9.29 $\mu\text{A}$
3 (LIV-M17)	FZ2	P-spray, $2 \times 10^{13} \text{ cm}^{-3}$	130 V	2.63 nF	6.62 $\mu\text{A}$

Table 5.1: Characteristics of the sensors on the DC-DC stavelet: wafer type, isolation structures of the strips and concentration dose, depletion voltage, capacitance with 250 V bias and leakage current with 250 V bias.

The modules used to assemble the serially powered stavelet came from both the University of Liverpool and the University of Cambridge. The summary of the parameters for these sensors is shown in Table 5.2.

Module	Type	Isolation	$V_{\text{dep}}$	$C@250 \text{ V}$	$I_{\text{leak}}@250 \text{ V}$
0 (CAM-M2)	FZ1	P-stop, $4 \times 10^{12} \text{ cm}^{-3}$	202 V	unknown	0.31 $\mu\text{A}$
1 (LIV-M21)	FZ2	P-spray, $2 \times 10^{12} \text{ cm}^{-3}$	140 V	2.61 nF	6.63 $\mu\text{A}$
2 (LIV-M12)	FZ2	P-spray, $2 \times 10^{12} \text{ cm}^{-3}$	110 V	2.63 nF	16 $\mu\text{A}$
3 (CAM-M4)	FZ1	P-spray, $4 \times 10^{12} \text{ cm}^{-3}$	202 V	unknown	0.78 $\mu\text{A}$

Table 5.2: Characteristics of the sensors on the serially powered stavelet: wafer type, isolation structures of the strips and concentration dose, depletion voltage, capacitance with 250 V bias and leakage current with 250 V bias.

### 5.1.7 Tests Description

The performance tests were done under controlled and measured conditions. Various conditions were applied to the modules and stavelets, such as different coolant tempera-

tures, sensor bias, hybrid power parameters and external electromagnetic interference.

For some of the tests, multiple measurements were done at each setting, in order to ensure temporal stability of the tests conditions. In these cases, the average is calculated as well as the deviation, represented as error bars in the plots. There usually is a small variation of the measured noise values between consecutive tests under the same conditions.

The typical performance test is the three point gain test, centred at 1 fC. It is used for parameter scans and long term stability tests, through the automation allowed by the SCTDAQ software. For some of the tests, a Double Trigger Noise (DTN) test is also run. Both tests were described in the previous chapter.

Every time a noise measurement is started for a particular test, a SD is run in order to always have the optimal timing between the charge injection and the read-out. This is particularly important when the coolant temperature is changed, because the optimal SD settings are dependent on the temperature.

## 5.2 Noise Model

A noise model for the SCT modules, using the ABCD3TA chip, had already been developed [39, 100]. The main difference between the ABCD3TA and the ABCn25 chips is the input to the front-end chip, which changes from a bipolar transistor to a MOSFET. The noise models differ for both.

Using the EKV model for the MOSFET transistors, another noise model was developed for the first precursor of the ABCn25, which uses the same chip architecture and a similar fabrication process. This model, presented in [101], is applied to the current ABCn25 chip which is used in the modules and stavelets tested.

$$\text{ENC}_{\text{Id}} = \frac{e^3}{12\sqrt{3}} \sqrt{\frac{4k_B T_{\text{chip}} n \gamma}{g_m}} \frac{C}{\sqrt{t_{\text{peak}}}} \frac{1}{q} \quad (5.1)$$

The Gate-Induced Current (GIC) noise component is

$$\text{ENC}_{\text{GIC}} = \frac{e^3 \sqrt{2}}{9\sqrt{15}} \sqrt{\frac{k_B T_{\text{chip}} \gamma}{n g_m}} \frac{C_{\text{OX}}}{\sqrt{t_{\text{peak}}}} \frac{1}{q} \quad (5.2)$$

The noise from the feedback transistor is

$$\text{ENC}_{\text{If}} = \frac{e^3 \sqrt{2}}{9\sqrt{3}} \sqrt{\frac{K_a}{W L}} \frac{C}{\sqrt{C_{\text{OX}}}} \frac{1}{q} \quad (5.3)$$

The correlation term is

$$\text{ENC}_{\text{corr}} = \frac{e^3}{18} \sqrt{\frac{k_B T_{\text{chip}} \gamma}{g_m}} \frac{\sqrt{C_{\text{OX}} C}}{\sqrt{t_{\text{peak}}}} \frac{1}{q} \quad (5.4)$$

The flicker noise due to each feedback transistor is

$$\text{ENC}_{\text{thermal}} = \frac{e^3}{18} \sqrt{\frac{5}{3}} \sqrt{k_B T_{\text{chip}} n \gamma g_m^f t_{\text{peak}}} \frac{1}{q} \quad (5.5)$$

Last, the noise due to the leakage current of the sensor is

$$\text{ENC}_{\text{leak}} = \frac{e^3}{18} \sqrt{\frac{5}{3}} \sqrt{k_B T_{\text{chip}} n \gamma g_m^f t_{\text{peak}} \frac{1}{q}} \quad (5.6)$$

And the total noise is the sum in quadrature of those terms:

$$\text{ENC}^2 = \text{ENC}_{\text{Id}}^2 + \text{ENC}_{\text{GIC}}^2 + \text{ENC}_{\text{If}}^2 + \text{ENC}_{\text{corr}}^2 + \text{ENC}_{\text{thermal}}^2 + \text{ENC}_{\text{leak}}^2 \quad (5.7)$$

Where:

- $e$  is the Napier constant.
- $k_B$  is the Boltzman constant.
- $T_{\text{chip}}$  is the chip temperature.
- $W$  and  $L$  are the width and length of the transistor channel,  $W = 320 \mu\text{m}$  and  $L = 0.5 \mu\text{m}$ .
- $n = 1.45$  is the slope factor, technology dependant.
- $\gamma$  is a parameter of the MOSFET that depends on the working mode. Typically  $\gamma = 2/3$  for the working range.
- $C$  is the total capacitance at the input of the pre-amplifier.
- $q$  is the electron charge.
- $g_m$  is the transconductance of the input transistor, and  $g_m^f$  is the transconductance of the transistor used as feedback resistor.
- $t_{\text{peak}}$  is the peaking time, which for the ABCn25 is 22 ns.
- $C_{\text{OX}}$  is the gate oxide capacitance:

$$C_{\text{OX}} = WL \frac{\epsilon_r \epsilon_0}{t_{\text{OX}}}$$

With  $t_{\text{OX}}$  the effective gate oxide thickness and

$$C_{\text{OXU}} = \frac{\epsilon_r \epsilon_0}{t_{\text{OX}}}$$

is the gate oxide capacitance per unit area.

- $K_a$  is a technology dependant parameter, equal to  $6 \times 10^{-27}$  for NMOS and  $10^{-27} \text{ C/m}^2$  for PMOS.

Using the following values for the parameters of the final design of the chip:

Parameter	Value
$t_{\text{OX}}$	6 nm
$I_d^f$	0.8 $\mu\text{A}$
$I_d$	140 $\mu\text{A}$ (nominal)
$C_a$	0.1 pF
$C_f$	0.14 pF
$C_{\text{str}}$	1.5 pF

The total capacitance is:

$$C = C_a + C_f + C_{str} + C_{sensor}$$

Where the sensor capacitance depends mostly on the strip length. It is in the order of 2.6 pF for short strips (2.36 cm) and 5 pF for long strips (4.78 cm), in fully depleted sensors.

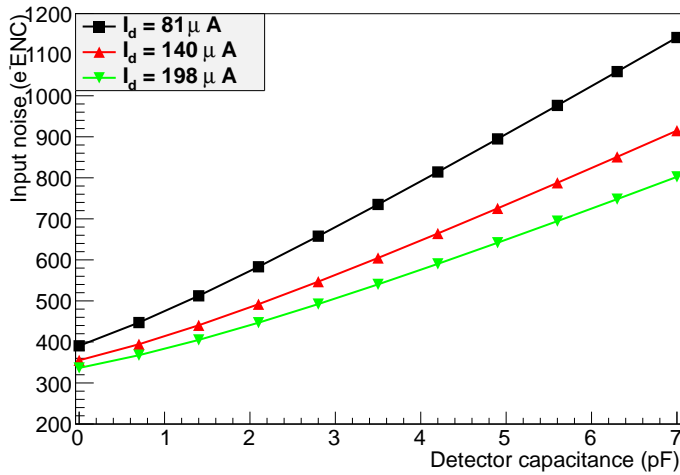


**Figure 5.8:** Result of the noise model for the ABCn25 chip with varying input capacitance.

Figure 5.8 shows the noise evolution with detector capacitance, as calculated from the model, with three different bias currents for the pre-amplifier stage. This is the same result as the one shown in [76], confirming the validity of the model above.

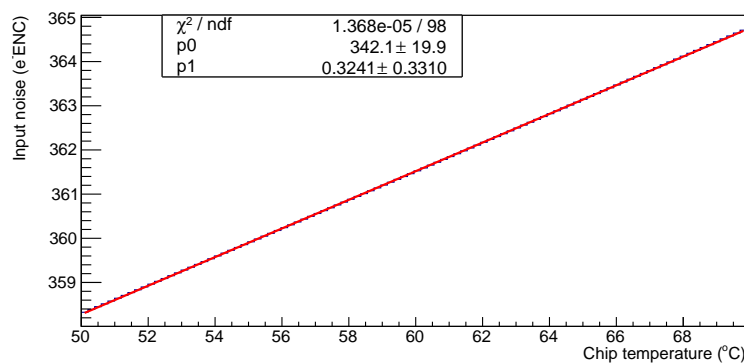


**Figure 5.9:** Result of the noise model for the ABCn25 chip with varying temperature for unbonded channels.

The model was also used with varying temperature values, to extract the temperature dependence of the noise. This dependence is highly dependant on the values of the parameters used, such as the bias current, which is nominally 140  $\mu A$  and this is the value used for the model.



Figure 5.9 shows the noise plot with changing temperature for unbonded channels, together with the fit result. The variation of the noise with temperature is

$$\overline{\Delta\text{ENC}/\Delta T}_{\text{unbonded}} = 0.3241 \pm 0.3310 e^{-\text{ENC}/\text{K}} \quad (5.8)$$

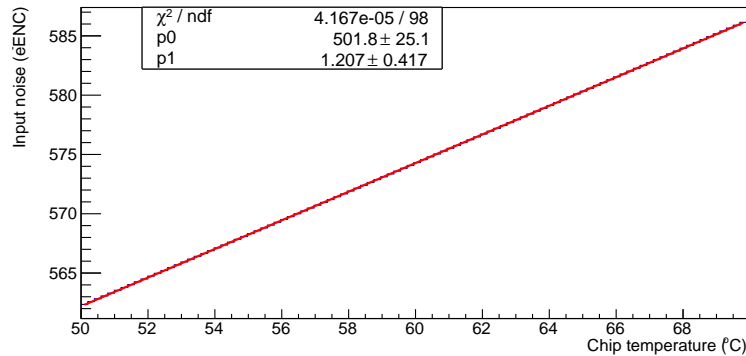


**Figure 5.10: Result of the noise model for the ABCn25 chip with varying temperature for short strips (2.36 cm).**

Figure 5.10 shows the same plot for short strips, 2.36 cm long, with a total capacitance around 2.82 pF. The result, in this case, is

$$\overline{\Delta\text{ENC}/\Delta T}_{\text{shortstrip}} = 1.207 \pm 0.417 e^{-\text{ENC}/\text{K}} \quad (5.9)$$

The capacitance value of 2.82 pF was chosen because it is the measured value for the serially powered module that has been tested. A comparison between the model and experimental data is shown in section 5.3.1.

## 5.3 Single Module Performance Tests

The single module tested at CERN uses serial powering in a chain of hybrids configuration. It has a FZ2 sensor with a leakage current in the order of 50  $\mu\text{A}$  at 200 V and 20°C. The module was assembled at the University of Liverpool and arrived at CERN in January 2012.

The first measurements performed on this module were three point gain tests to have the reference noise for this module. The chiller temperature was set to 12°C, the serial powering current was set to 5 A and the sensor bias to 200 V.

Figure 5.11 shows the input noise, measured in electrons, for the channels of each column of chips of the module. Figure 5.12 shows the gain (measured in mV per fC) plot for all the channels.

The values shown on each plot are the average values for each column. All results in the next sections are presented as average values for the chips, columns or whole modules.

Some of the channels show high noise or very low noise. Usually noise around 400  $e^{-\text{ENC}}$  means the channel is unbonded and zero noise means the channel is masked or dead on the chip. Those kinds of defects are normally masked when the trim range test is performed.

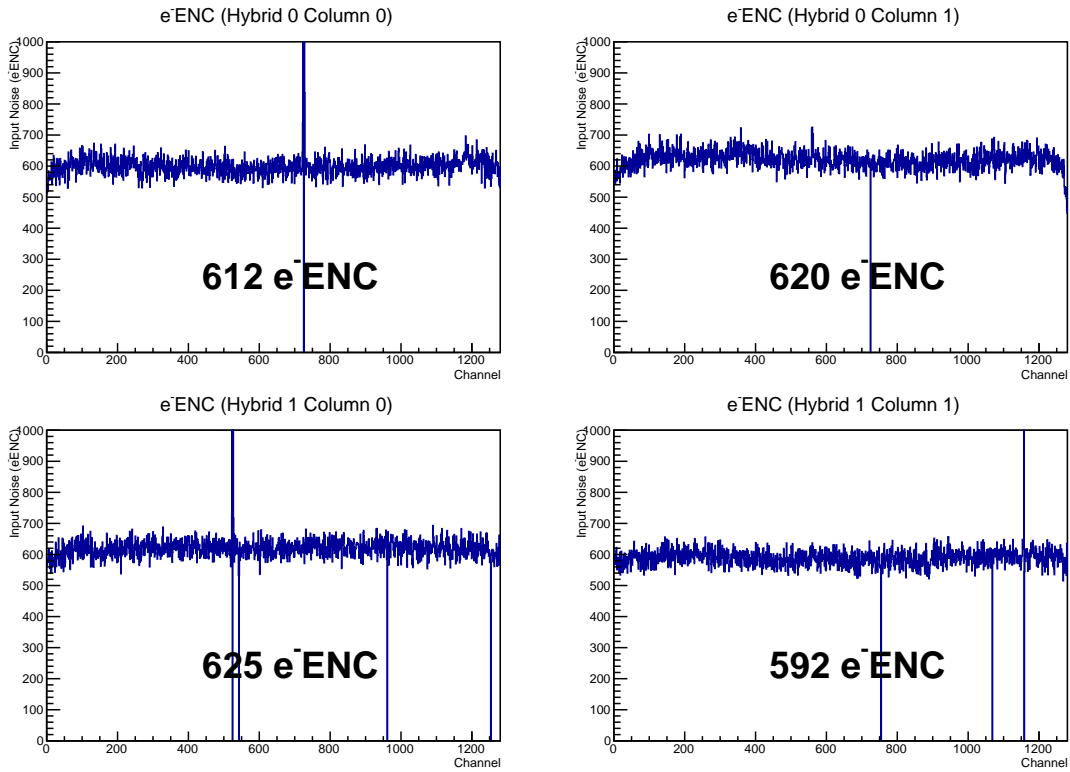


Figure 5.11: Reference noise ( $e^-ENC$ ) for the serially powered module.

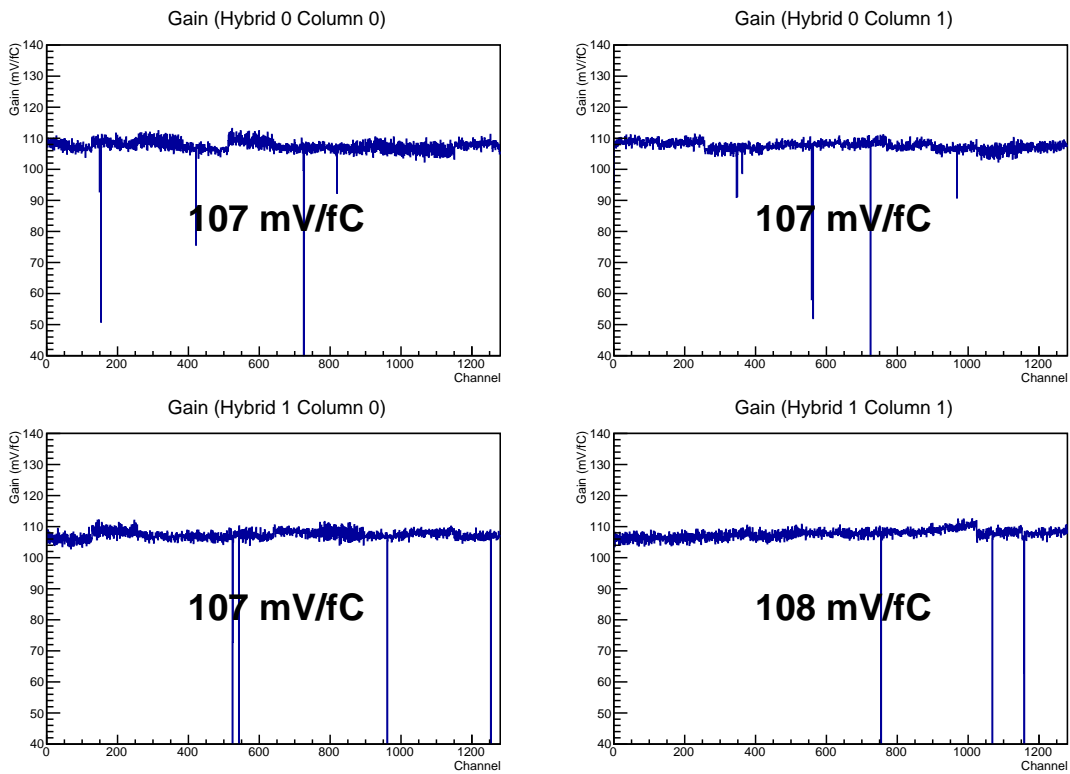


Figure 5.12: Reference gain ( $mV/fC$ ) for the serially powered module.

The results presented in the following sections are all with the correct trim range settings for the single module and the two stavelets.

### 5.3.1 Varying Temperature

This test is conceived as a means of extracting the variation of the module noise with temperature. The chiller is set to different temperature settings, then the noise is measured several times with three point gain tests. By using at least three different temperature settings and fitting to a linear function, it is possible to extract the noise change rate with temperature.

The temperature of the coolant,  $T_{\text{chiller}}$ , was set at various values, the temperature of one of the hybrids was monitored and noise measurements were repeated. The sensor bias was set to 150 V for all the noise measurements.

The temperature settings and measured hybrid temperature correspondence are shown in Table 5.3 (temperatures are in Celsius). The temperature difference between both is not constant due to the effect of the dry air flowing inside the module enclosure and the fact that the coolant is heated slightly in the pipe due to the temperature in the room.

$T_{\text{chiller}} [^{\circ}\text{C}]$	-6	0	6	12	18	24
$T_{\text{hybrid}} [^{\circ}\text{C}]$	11.6	16.0	19.7	25.9	30.8	35.7

**Table 5.3: Coolant and hybrid temperatures in the serially powered module.**

The temperature of the room during these tests was constant at about  $24^{\circ}\text{C}$ , and the relative humidity is around 40%. The humidity in the module enclosure was kept low with a dry air flow, which is at room temperature. As a consequence, the temperature inside the enclosure does not entirely follow the temperature variations of the coolant.

Measurements of the temperature inside the freezer and on the cooling pipes at the enclosure boundaries confirm that the dry air flow increases the temperature of the air inside the freezer, causing a different noise change with temperature for lower temperature settings than expected. In this case, convection has a greater effect in the heat transfer when the temperature difference between the air and the coolant is so high.

This has the effect of the temperature measured on the hybrids not having the same relation with the temperature on the chips. This effect is presented in more detail below, where the very low temperature tests are described.

Because of that effect, the lower temperature settings for this test did not entirely follow the trend of the upper part of the interval, in terms of noise. Therefore, the lower temperature settings were discarded for the study and the only settings that were used are  $T_{\text{chiller}} = \{12, 18, 24\}^{\circ}\text{C}$ .

Figure 5.13 shows the noise behaviour with the measured hybrid temperature. Each subplot corresponds to a chip column and each line shows the noise evolution on each chip.

The slope is very similar for most of the chips and for both columns on the same hybrid. Possible differences can be attributed to small temperature variations among chips and to the noise estimation for each individual channel.

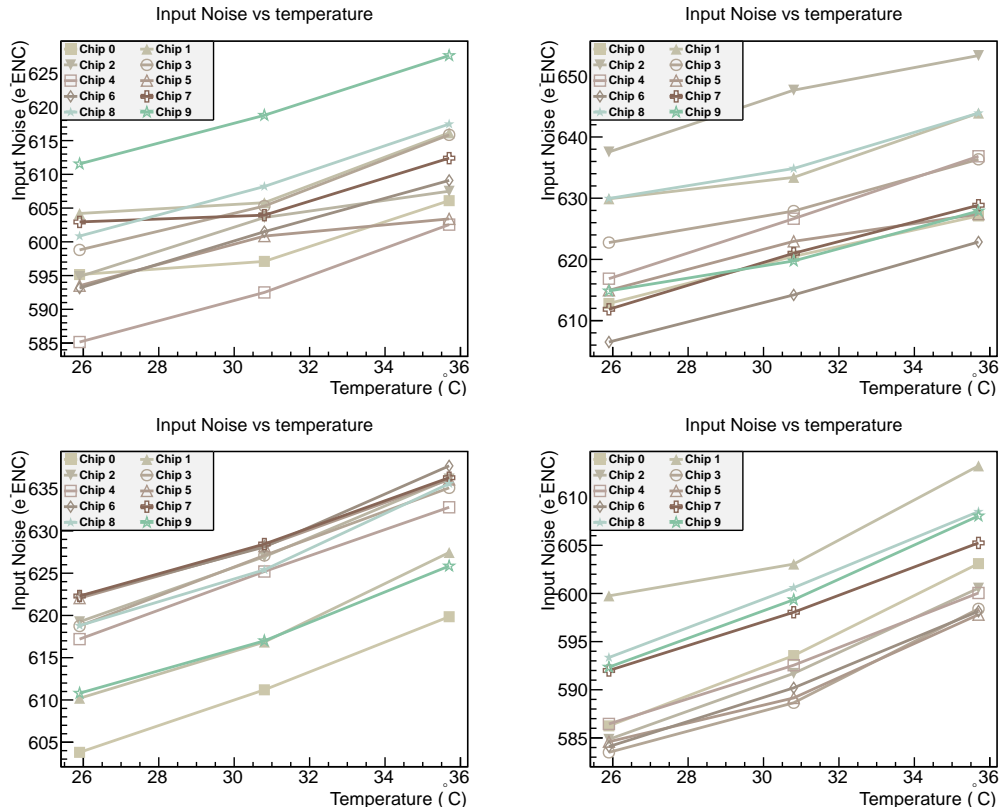


Figure 5.13: Noise variation with temperature on the SP module.

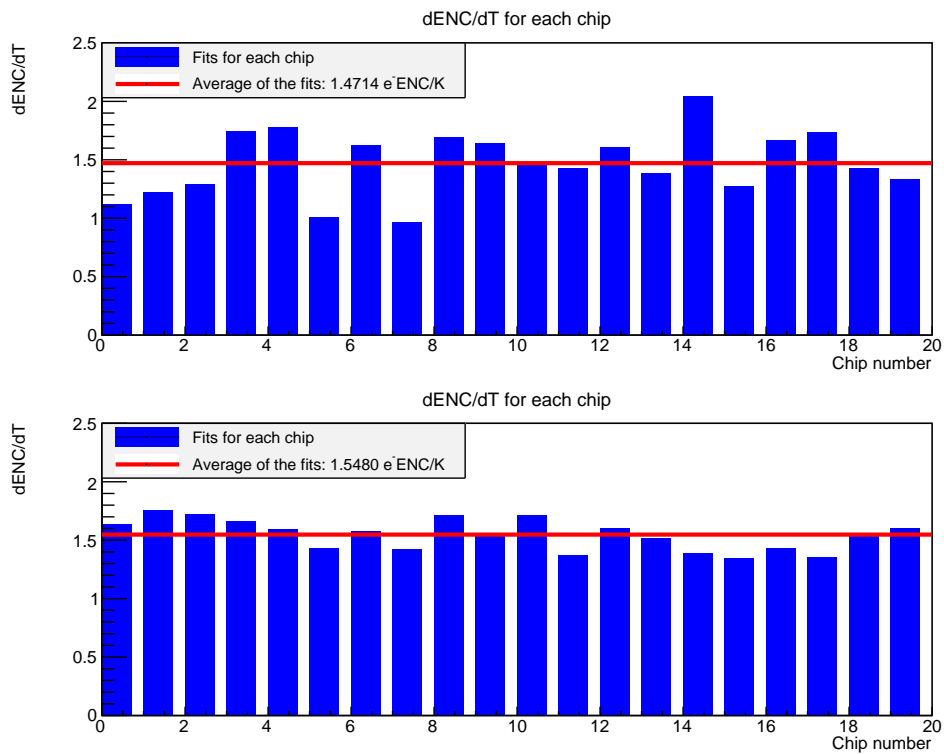


Figure 5.14: Fit of the noise variation with temperature for all chips.

Figure 5.14 shows the slopes for each of the 20 chips in both hybrids. The average values and spreads for both hybrids are:

$$\overline{\Delta\text{ENC}/\Delta T}_{\text{Hybrid 0}} = 1.4714 \pm 0.28 e^{-}\text{ENC}/\text{K} \quad (5.10)$$

$$\overline{\Delta\text{ENC}/\Delta T}_{\text{Hybrid 1}} = 1.5480 \pm 0.13 e^{-}\text{ENC}/\text{K} \quad (5.11)$$

Module type	Model	Measured
Outers	$4.06 \pm 0.18 e^{-}\text{ENC}/\text{K}$	$5.77 \pm 0.27 e^{-}\text{ENC}/\text{K}$
Middles	$3.89 \pm 0.17 e^{-}\text{ENC}/\text{K}$	$4.85 \pm 0.28 e^{-}\text{ENC}/\text{K}$
Inners	$2.84 \pm 0.10 e^{-}\text{ENC}/\text{K}$	$3.86 \pm 0.21 e^{-}\text{ENC}/\text{K}$

**Table 5.4: Predicted and measured  $\Delta\text{ENC}/\Delta T$  for SCT Endcap modules.**

As a comparison, the temperature dependence predicted and measured for the current SCT modules in [39] are shown in Table 5.4 (only endcaps). The results of the tests performed on the upgrade module show a temperature dependence of around  $1.5 e^{-}\text{ENC}/\text{K}$ . In comparison, the dependence of the current SCT endcap modules was measured between  $3.86$  and  $5.77 e^{-}\text{ENC}/\text{K}$ .

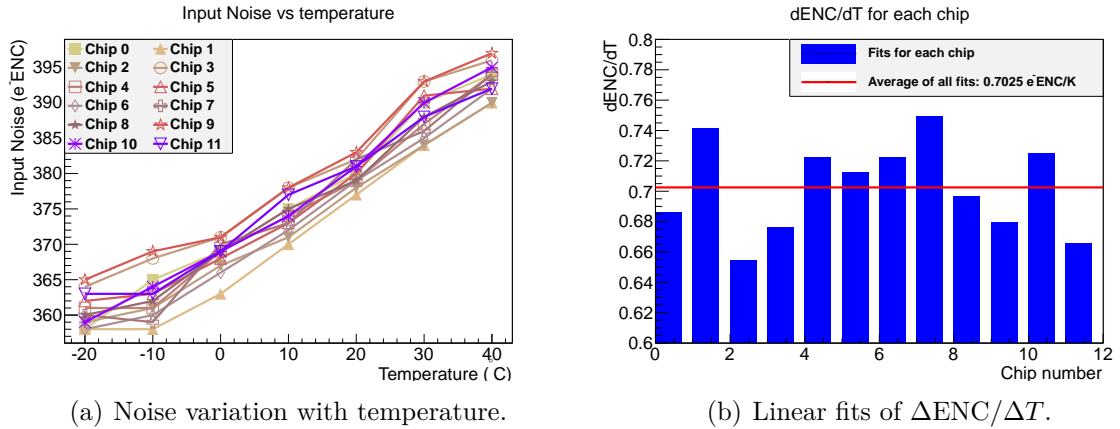


**Figure 5.15: Noise variation with temperature for an unbonded hybrid.**

The noise variation with temperature of a hybrid that was not bonded to a sensor was also studied in the University of Freiburg [102]. The hybrid tested was one of the first Petalet hybrids, with 12 ABCn25 chips on it (2 columns with 6 chips each).

Figure 5.15(a) shows the result of this test and Figure 5.15(b) shows the result of the linear fits for each chip and the average of all the fits for the unbonded hybrid.

The first temperature point ( $-20^{\circ}\text{C}$ ) was ignored for the fit, as it does not entirely follow the expected linear trend of noise variation with temperature.

The linear fit for the rest of the data sets the chip contribution to the noise variation with temperature at

$$\overline{\Delta\text{ENC}/\Delta T}_{\text{Unbonded Hybrid}} = 0.7025 \pm 0.0306 e^{-}\text{ENC}/\text{K} \quad (5.12)$$

This means that about half of the noise increase with temperature on a module is due to the chips, when no sensor is bonded to them.

The model presented in section 5.2 gave a much lower value of the  $\Delta\text{ENC}/\Delta T$  for the unbonded hybrid, less than half of the experimental result. However, the error on the model was quite large. For the bonded chips, the model gave a value approximately 25% lower than the experimental result.

The results obtained for the model used the parameters values shown in section 5.2. Small variations in some of these values may lead to relevant changes in the results. For instance, the bias current of the front-end circuitry is nominally 140  $\mu\text{A}$ , but it has a great influence in the evolution of the noise with temperature.

The differences were also observed between the SCT noise model and the measured results, as shown in Table 5.4.

### 5.3.2 High Voltage Scans

The change in sensor bias voltage effects the depletion depth of the p-n junction, when it is lower than the full depletion voltage. Noise decreases as the bias voltage is increased.

The leakage current increases and usually reaches a semi-plateau after full depletion. If the bias voltage is further increased, the sensor can reach breakdown and the leakage current increases again dramatically.

The sensors used to build the modules for the upgrade programme are specified to withstand up to 1000 V. The voltage on the modules is limited by the hybrid circuitry to 500 V, but the sensors are usually measured up to 1000 V before assembling the modules.

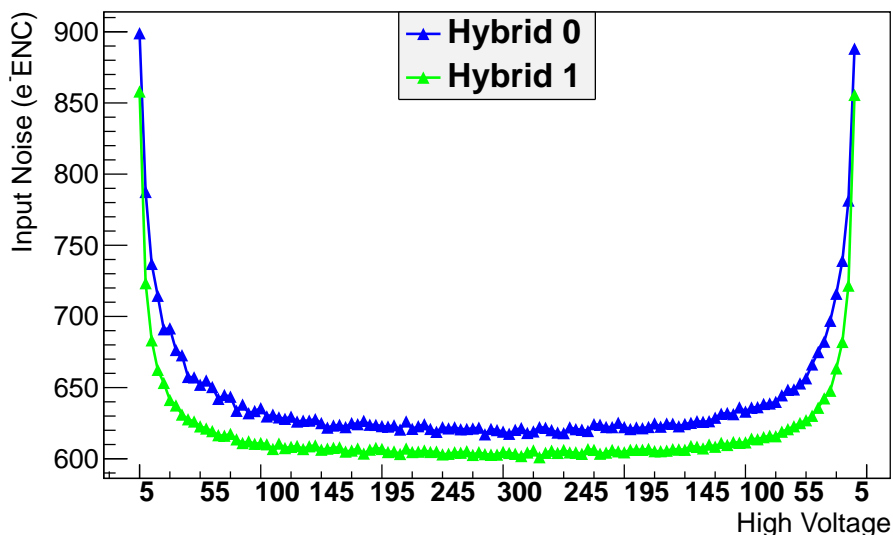


Figure 5.16: Sensor bias voltage scan on the SP module up to 300 V.

Tests with varying bias voltage were run with the serially powered module. First the voltage was ramped up and then it was ramped down, measuring the noise at every bias level.

Figure 5.16 shows the results of a high voltage scan, first ramping up from 5 V to 300 V and then down from 300 V to 5 V, in steps of 5 V. The results are shown

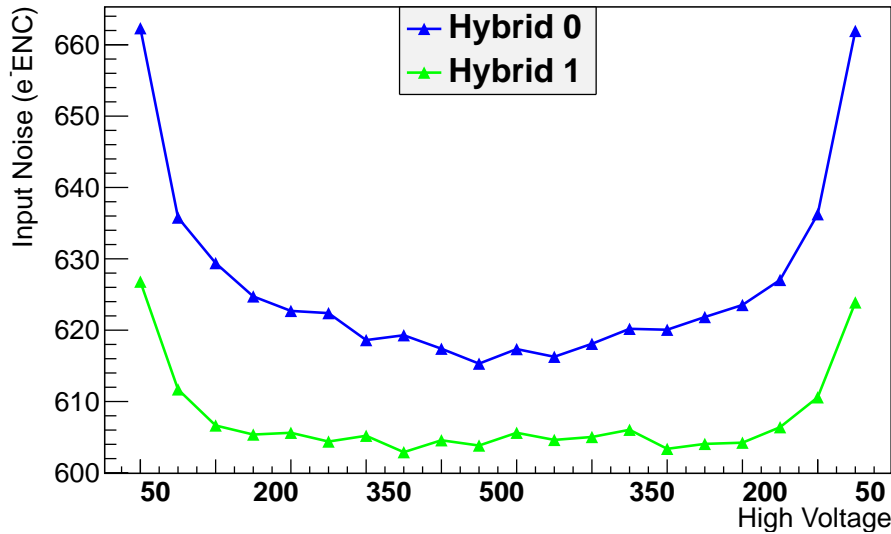


Figure 5.17: Sensor bias voltage scan on the SP module up to 500 V.

averaged for the two hybrids in the module. The noise was calculated using three point gain scans centred at 1 fC. The coolant temperature was set to 12°C.

An additional test with the maximum bias voltage supported by the hybrid was done, ramping up to 500 V, from 50 and with 50 V steps. Figure 5.17 shows the results for this test.

There have been reports of higher noise for the second time the bias voltage is set to some value after ramping up to higher voltages [103]. This module does not show that behaviour, while the temperature was very stable throughout the whole test.

### 5.3.3 Low Temperature Tests

In order to test if the electronic components are capable of operating at very low temperatures, some tests were run below  $-10^{\circ}\text{C}$ . In order to avoid condensation and ice, dry air was flushed into the freezer where the module is tested. The pipes of the chiller were covered with insulating foam to avoid ice on them. The sensor was biased at 200 V.

$T_{\text{chiller}} [^{\circ}\text{C}]$	$T_{\text{pipe}}$	$T_{\text{hybrid}}$	$T_{\text{freezer}}$	$T_{\text{hybrid}} - T_{\text{pipe}}$	$T_{\text{freezer}} - T_{\text{pipe}}$
12	13.4	25.9	18.1	12.5	4.7
-6	-1.5	12.1	14.5	13.6	16.0
-12	-5.8	7.6	10.4	13.4	16.2
-20	-11.7	2.5	8.5	14.2	20.2

Table 5.5: Temperatures measured during low temperature testing: chiller setting, temperature at the input pipe to the freezer, temperature on the hybrid, temperature inside the freezer enclosure and temperature differences between the pipe and the hybrid as well as the freezer.

The disadvantage of using a normal dry air supply is the temperature of the air, which is typically around  $24^{\circ}\text{C}$ , which creates a temperature difference between the sensor and the air. This does not affect the low temperature behaviour of the electronics, but it influences the measurement of noise with varying temperature.

Table 5.5 shows the different temperatures measured for various chiller settings. The temperature was measured on the inlet pipe, next to the freezer using a commercial NTC. The temperature on the hybrid is measured with an NTC that is part of the hybrid circuitry, with the hybrid powered on. The temperature inside the freezer was measured using a SHT71 temperature and humidity sensor.

The temperature difference between the pipe and the hybrid is quite constant while the temperature difference between the air in the freezer and the pipe is greater for lower temperatures. As it was stated above, this is caused by the dry air that is flushed into the freezer at room temperature.

The noise results for  $12^{\circ}\text{C}$  on the chiller were shown in Figure 5.11. Results with lower temperature settings are shown next.

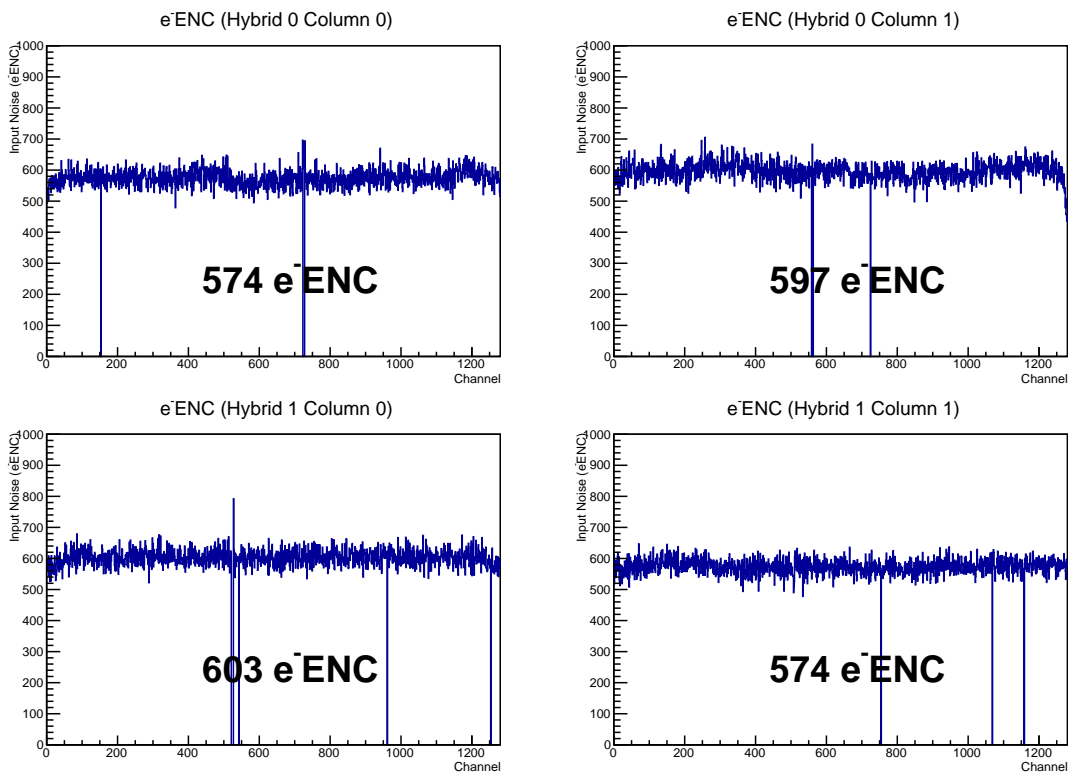


**Figure 5.18:** Input noise ( $e^-ENC$ ) with chiller temperature set to  $-6^{\circ}\text{C}$ , three point gain scans centred at  $1\text{ fC}$ .

Figure 5.18 shows the input noise for a temperature setting of  $-6^{\circ}\text{C}$ . The temperature on the hybrid is shown in Table 5.5.

Figure 5.19 shows the input noise when the temperature was set to  $-20^{\circ}\text{C}$ . All columns show lower noise than the previous plot and all the channels were working correctly, except for those that were not previous to this test. There are some channels in hybrid 0, column 1, between channel numbers 589 and 593 that show up dead in Figure 5.18, but look fine in Figure 5.19. After reviewing the noise history of those channels, it was found out that they are inefficient in the chip and sometimes are masked



by the software but were not during the test at  $-20^{\circ}\text{C}$ . Despite the inefficiency, the input noise result is consistent with the overall column noise, making them appear as normal healthy channels.

The temperature difference of the hybrids between the  $-6^{\circ}\text{C}$  and the  $-20^{\circ}\text{C}$  settings is  $9.6^{\circ}\text{C}$ . Assuming a  $1.55 e^{-}\text{ENC}/\text{K}$  variation, as measured above, a noise difference of  $14.88 e^{-}\text{ENC}$  is expected. The variation observed lies between 16 and  $25 e^{-}\text{ENC}$ , which is consistent with the expectation.

The conclusion of this test is that the system works correctly when operating at much lower temperatures than the typical testing temperature of  $12^{\circ}\text{C}$ . The hybrid has been operated at a temperature below  $3^{\circ}\text{C}$  and the LVDS drivers at a temperature below  $9^{\circ}\text{C}$ .

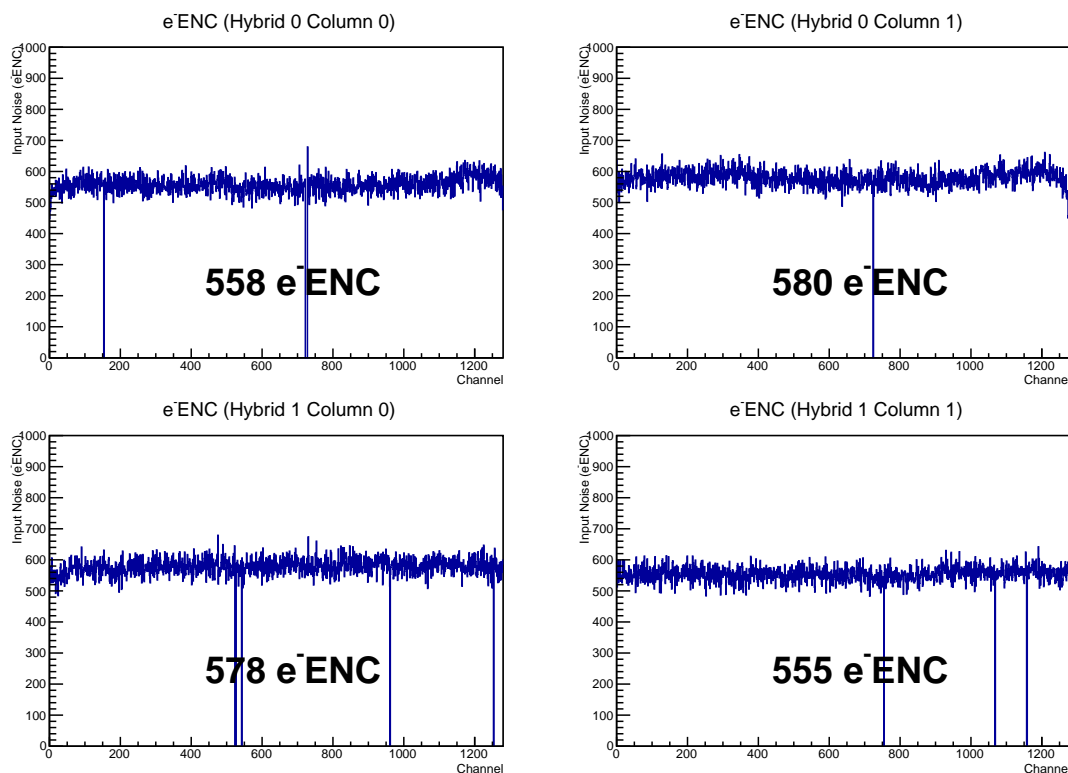


Figure 5.19: Input noise ( $e^{-}\text{ENC}$ ) with chiller temperature set to  $-20^{\circ}\text{C}$ , three point gain scans centred at 1 fC.

## 5.4 Performance Tests of Four Module Stavelets

### 5.4.1 High Voltage Scans

The behaviour of the modules when changing the bias voltage in the sensors was also studied for the four module stavelets. The different types of sensors used to build the stavelets present small differences in their behaviour when changing the sensors bias.

Figure 5.20 shows the noise results with varying bias voltage of the sensors. The scan consisted in running three point gain tests centred at 1 fC, and the chiller temperature was set to  $12^{\circ}\text{C}$ . The voltage set to power the DC-DC converters was calibrated to

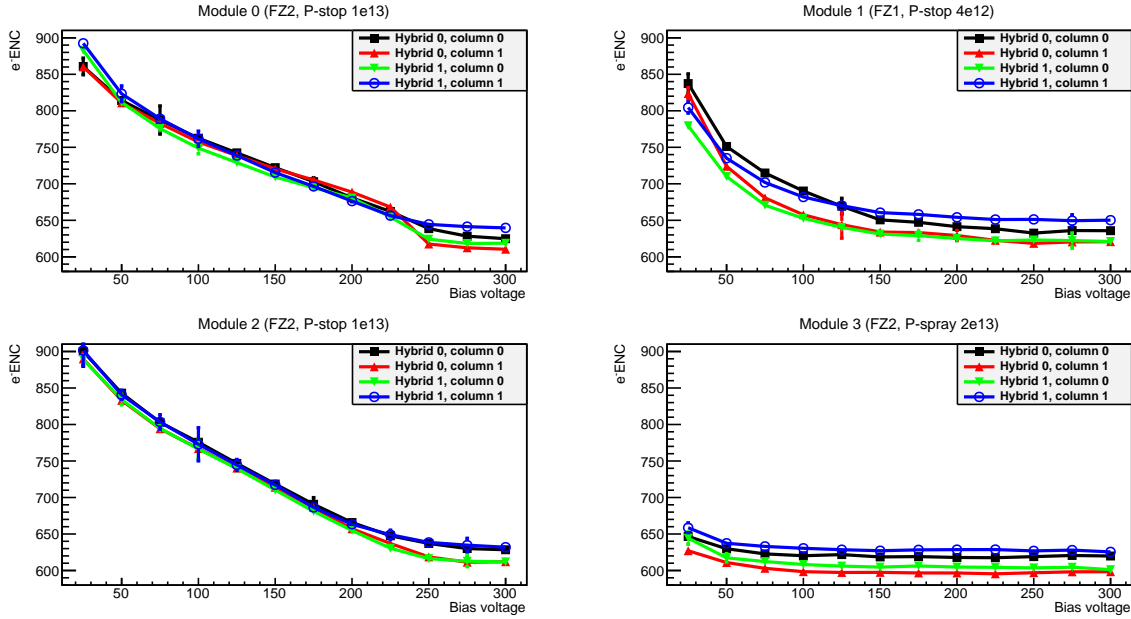


**Figure 5.20:** DC-DC stavelet input noise ( $e^-$  ENC) with sensor bias.

measure 10 V in the sense wires. The voltage on the power supply was 10.3 V. At the time of these tests and with the wires used, the voltage drop up to the DC-DC converters was around 300 mV.

The bias voltage was modified from 25 V to 300 V, in 25 V steps. Two three point gain scans were used to measured the noise, the points show the average value. The errors bars are the calculated deviations at each point.

The noise results show a noise comparable to the estimated values for the fully depleted sensors. The isolation structure for module 3 (P-spray) seems to give the sensor a very low noise from very low bias. Also, the stronger P-stop isolation on modules 0 and 2 seems to lower the noise with voltage later than the weaker P-stop in module 1.

Figure 5.21 shows the results of a test similar to that shown in Figure 5.16, with a ramp up of the sensor bias voltage first and then ramp down. For modules 0, 1 and 2, the effect described in the single module section is now present: the noise for the same values of bias voltage is higher after passing through a higher voltage.

The plots show the timeline of the whole test for each chip column, one module for each graph [99]. The same high voltage scans were done with the serially powered stavelet.

Figure 5.22 shows the noise evolution of the serially powered stavelet with the bias voltage. Like in the DC-DC stavelet, the noise on modules with P-spray sensors starts at a much lower value with low bias voltage than the one P-stop sensor.

The tests were repeated with the SP stavelet, ramping up the bias voltage and also ramping down. The result is shown in Figure 5.23. Some modules present the same behaviour as modules 0 and 2 on the DC-DC stavelet, where the noise is higher after biasing at a lower voltage than a previous setting while ramping down.

Module 0 has a P-stop isolation structure, but with a lower dose than modules 0, 1 and 2 on the DC-DC stavelet. The noise increase exists but it is less than for the DC-DC modules. Modules 1, 2 and 3 are P-spray with different doses. Module 3 is the

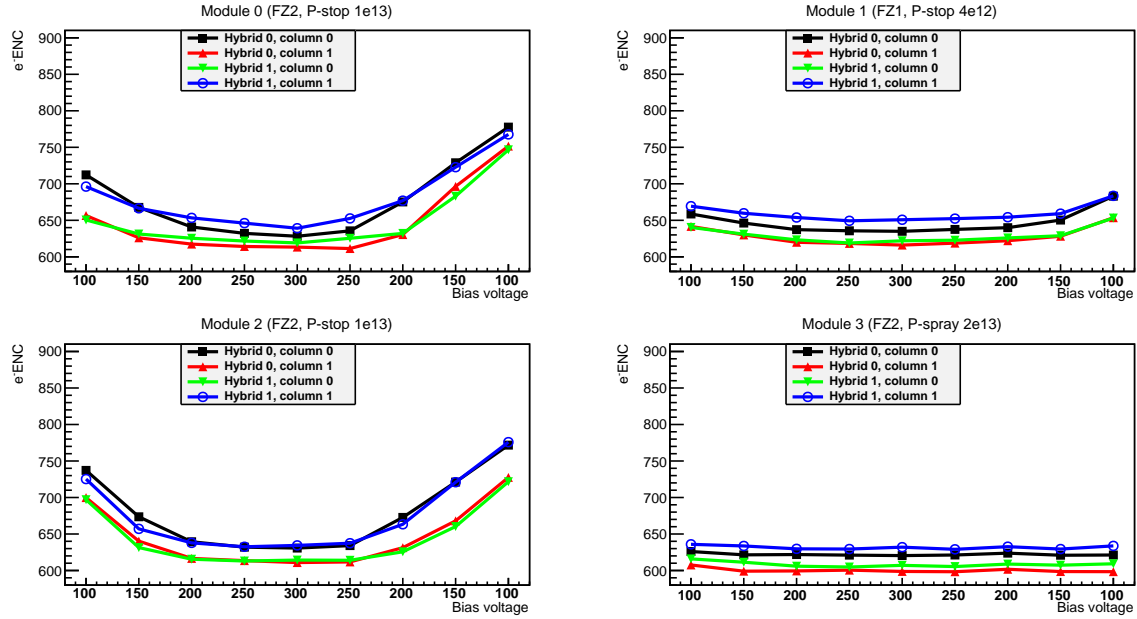


Figure 5.21: DC-DC stavelet input noise ( $e^-ENC$ ) with sensor bias, first ramping up to 300 V and then ramping down.

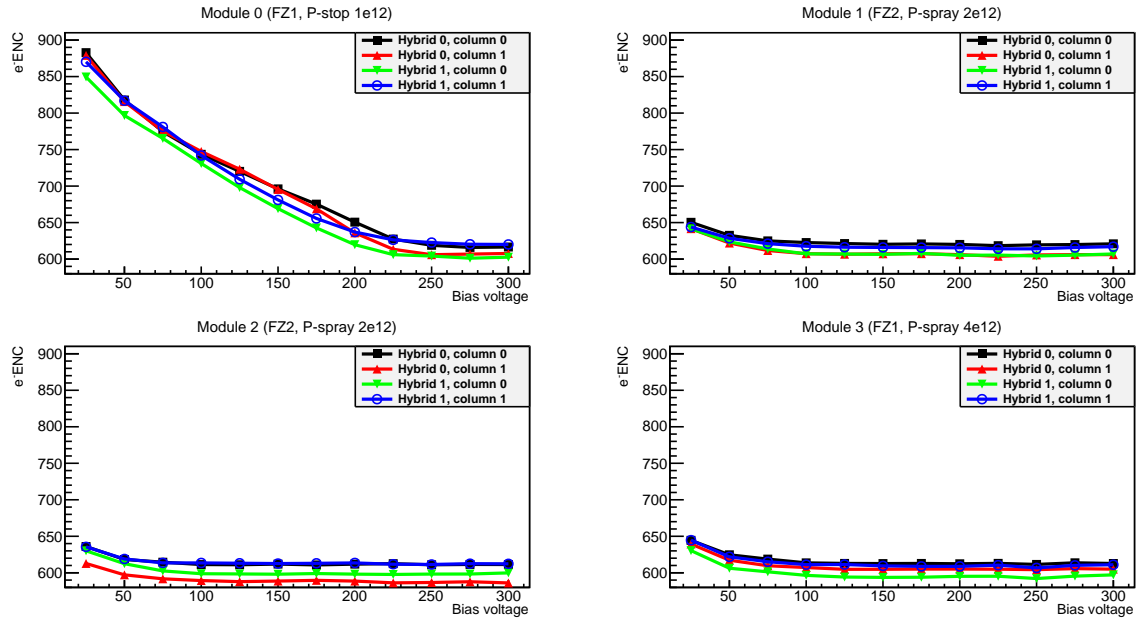
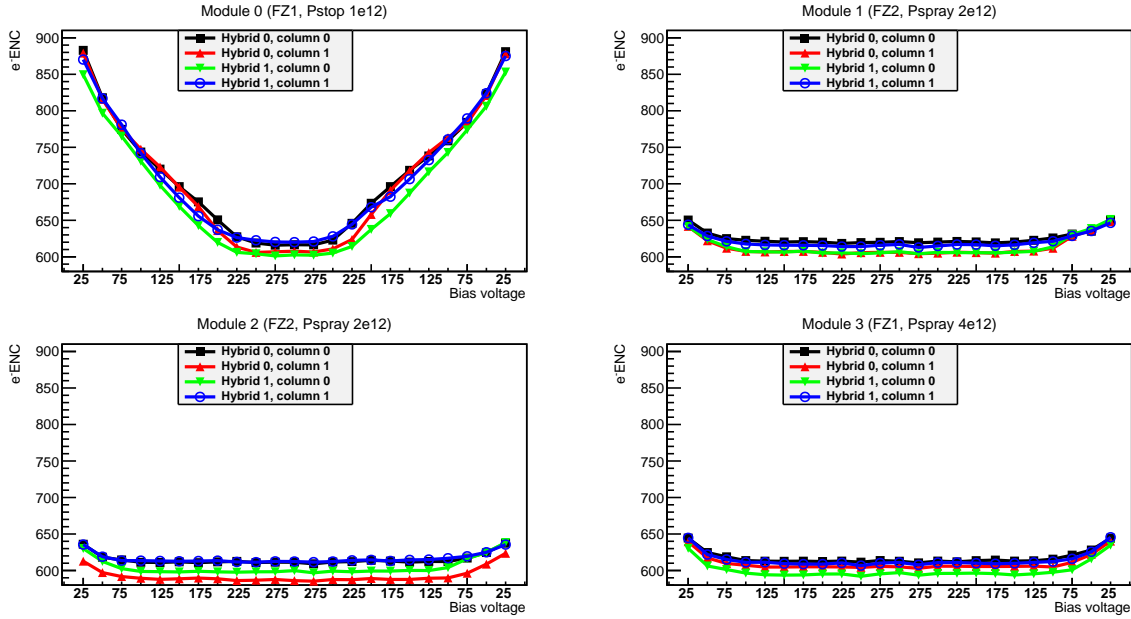


Figure 5.22: SP stavelet input noise ( $e^-ENC$ ) with sensor bias.

one with highest dose and it does not show a clear noise increase when going down in voltage, whereas modules 1 and 2 show a small noise increase in most of the columns..

## 5.4.2 Hybrid Powering Variations

Both power distribution mechanisms, serial powering and DC-DC, admit a certain range of input current and voltage. A study on how these variations affect the noise



**Figure 5.23:** SP stavelet input noise ( $e^-ENC$ ) with sensor bias, first ramping up to 300 V and then ramping down.

was done with both stavelets.

On the one side, the efficiency of the DC-DC converters varies with the input voltage. The converters are operational for  $V_{in}$  between 7 and 15 V. The tests on the stavelet were performed in the range from 10.5 to 14.5 V.

The “sweet spot” for the DC-DC converters is  $V_{in} = 10$  V, voltage at which the conducted noise is the lowest. Due to the high current, this figure is normally quoted as the voltage at the sense wires that are directly connected to the converters and not the voltage set at the power supply.

There is a typical voltage drop around 500 mV on the setup at CERN at the time of the hybrid powering tests. In order to have a voltage around 10 V at the converters inputs, the output of the power supply is set to 10.5 V. The voltages at the input of the converters were measured for power supply settings of 10.5 V and 14.5 V. These are shown in Table 5.6. The drop on the bus tape is 220 mV for higher currents and 170 mV for lower currents. The current shown is the current drawn from the power supply after configuring the chips, without any tests running.

$V_{PSU}[V]$	$I_{PSU}[A]$	$V_{M3}[V]$	$V_{M2}[V]$	$V_{M1}[V]$	$V_{M0}[V]$
10.5	9.96	9.96	9.85	9.78	9.74
14.5	7.41	14.04	13.97	13.91	13.87

**Table 5.6:** Voltages measured at the DC-DC converters inputs, as well as the output current of the power supply.

In the DC-DC stavelet tests, the voltage is referenced to the approximate measurement on the sense wires, always accounting for a voltage drop on the wires around 500 mV.

The output voltage of the serial power regulator varies slightly with the input current. The serially powered stavelet is typically run with an input current of 9.5 A. The stavelet has been tested also with input currents of 9 A and 10 A. An increase in the current also increases the voltage across the hybrid, resulting in a higher hybrid temperature.

The different low voltage powering tests were performed with a sensor bias voltage of 250 V and a chiller temperature setting of 12°C. The DC-DC stavelet tests consisted in varying the input voltage to the converters from 10 V to 14 V, in steps of 1 V. Ten three point gain tests centred at 1 fC were performed at each low voltage level.

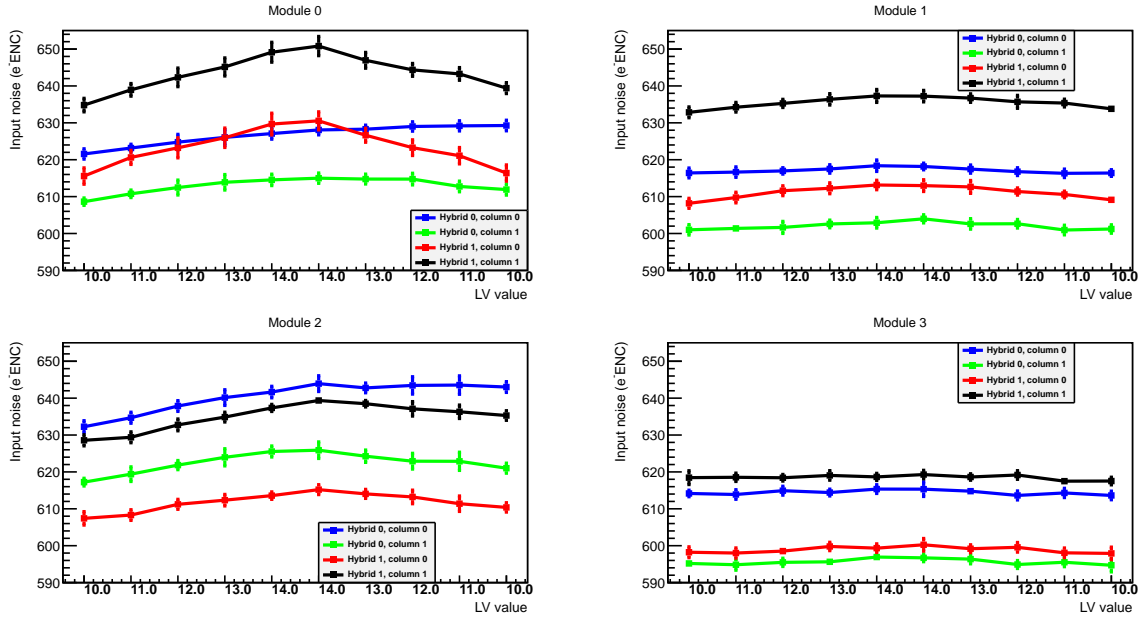


**Figure 5.24: DC-DC stavelet input noise ( $e^-ENC$ ) with low voltage value. Low voltage from 10 V to 14 V, up and down, 1 V steps.**

Figure 5.24 shows the noise evolution of the DC-DC stavelet when the low voltage value is changed between 10 and 14 V. Each line represents one chip column. The points on the plots show the average value of the noise and the error bars represent the deviation from the average. The noise evolution is uneven for the four modules. It is essentially due to a higher noise on the converters when they operate at higher input voltage. However, modules 1 and 3 seem to be immune to this effect.

The noise trend is very clear on the second hybrid of module 0, whereas the first hybrid shows a mixed behaviour, with one of the columns always increasing noise. The behaviour of module 2 is also mixed, with some increase up to 14 V supply voltage, but for one of the hybrids the noise does not decrease when the voltage is reduced back to 10 V.

Some of the shields leave a small gap between the shield and the converter board. However, additional tests with a bigger gap on module 3 show it does not cause the additional noise when increasing the hybrid powering voltage.

The temperatures of the hybrids were stable during the whole test, with variations around 0.1°C for the hybrids closest to the EoS card and smaller than 0.5°C for the hybrids further away from the EoS card.

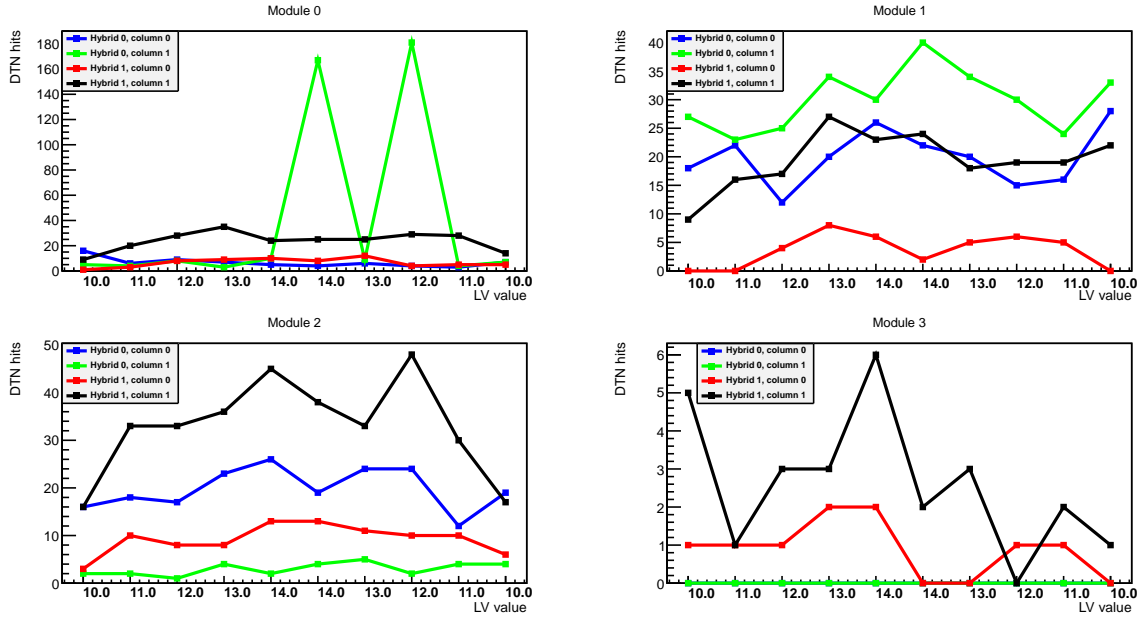


Figure 5.25: DC-DC stavelet Double Trigger Noise variation with low voltage value for 0.5 fC threshold.

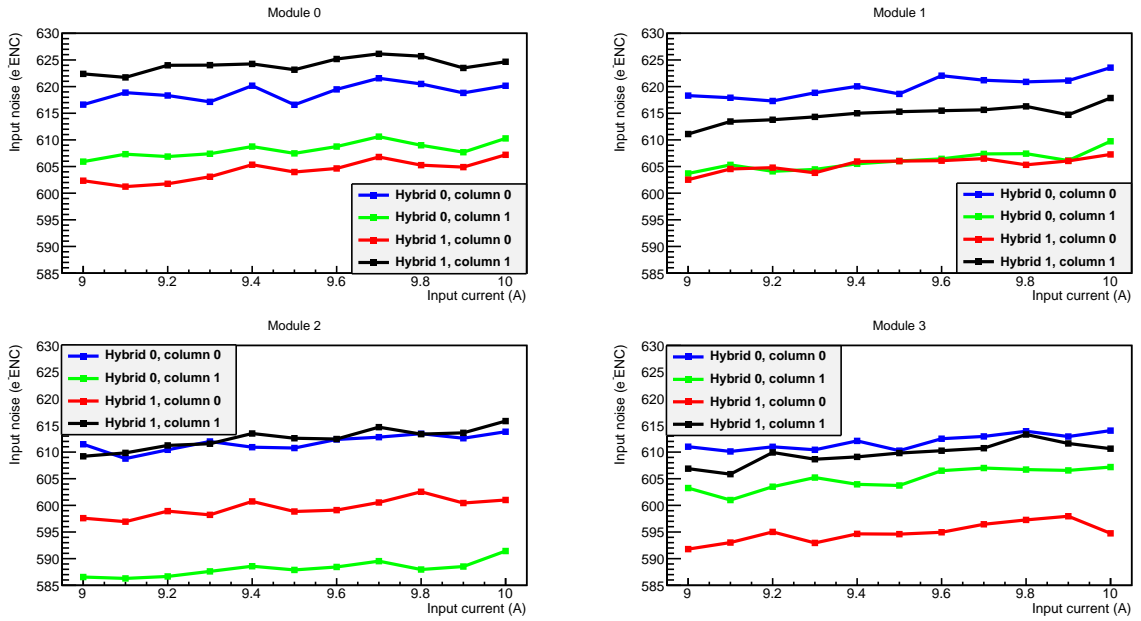


Figure 5.26: SP stavelet input noise ( $e^-ENC$ ) with low voltage value. Input current varied between 9 and 10 A in 0.1 A steps.

In addition, Figure 5.25 shows the Double Trigger Noise variation with the low voltage setting for the 0.5 fC threshold. The plots show a very random variation of the number of hits with different measurements, leading to the conclusion that the variation of the voltage input to the DC-DC converters does not affect the noise pick-up on the stavelet.

The equivalent test on the serially powered stavelet was done varying the input

current from 9 A to 10 A and running three point gain tests. The results are shown in Figure 5.26, with the expected noise increase when increasing the current, due to the higher temperature on the hybrids.

One three point gain test was done at every current value. The hybrids temperature increased between 2.4 and 2.9°C, from the minimum current to the maximum current setting. This variation would account for a noise difference between 3.7 and 4.5  $e^-ENC$ , which is observed in the results.

The same Double Trigger Noise measurement as with the DC-DC stavelet was done for the serially powered stavelet when changing the input current. Figure 5.27 shows the results, the first module has one column that is out of scale (hybrid 1, column 1). This is because it has a very large number of hits, greater than 10000, but with the same behaviour as all the others. As before, this is the Double Trigger Noise test with a threshold of 0.5 fC that allows seeing actual variations of the pick-up. The trend shown in the plots is random and it cannot be attributed to any additional noise pick-up caused by the variations of the input current.

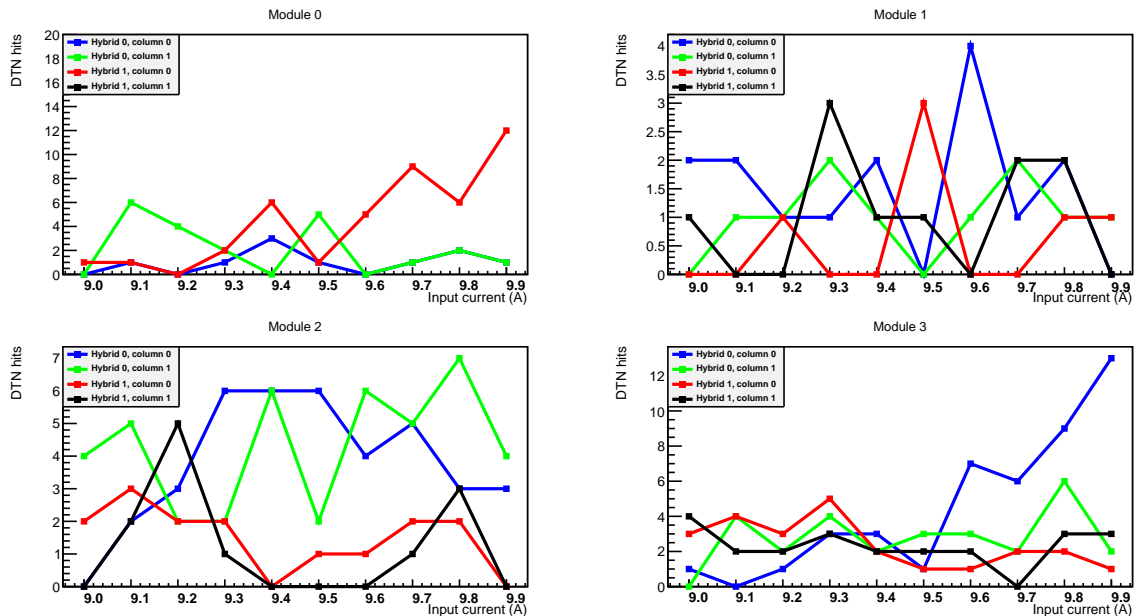


Figure 5.27: SP stavelet Double Trigger Noise variation with low voltage value for 0.5 fC threshold.

### 5.4.3 High Voltage Multiplexing

The high voltage multiplexer presented in section 4.4 is also available for testing. A comparison of high voltage scans with the multiplexer and using the default single high voltage lines follows.

Figures 5.28, 5.29, 5.30 and 5.31 show the results of the high voltage scans on the DC-DC stavelet with different temperature settings.

The bias voltages for both configurations and every temperature setting were chosen from the ranges with sensor over-depletion and under-depletion voltages. These values are  $V_{\text{bias}} = \{10, 25, 50, 75, 100, 125, 150, 200, 250, 275\}$ .

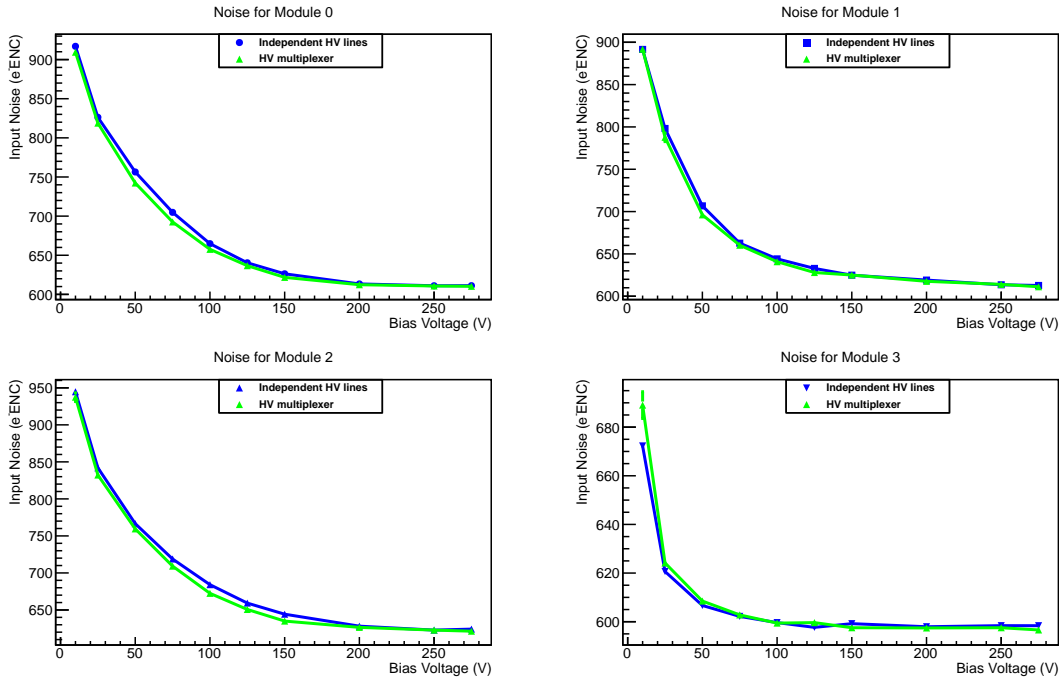


Figure 5.28: Noise comparison of high voltage scans on the DC-DC stavelet, using the high voltage multiplexer and using independent biasing, with the chiller temperature set to 6°C.

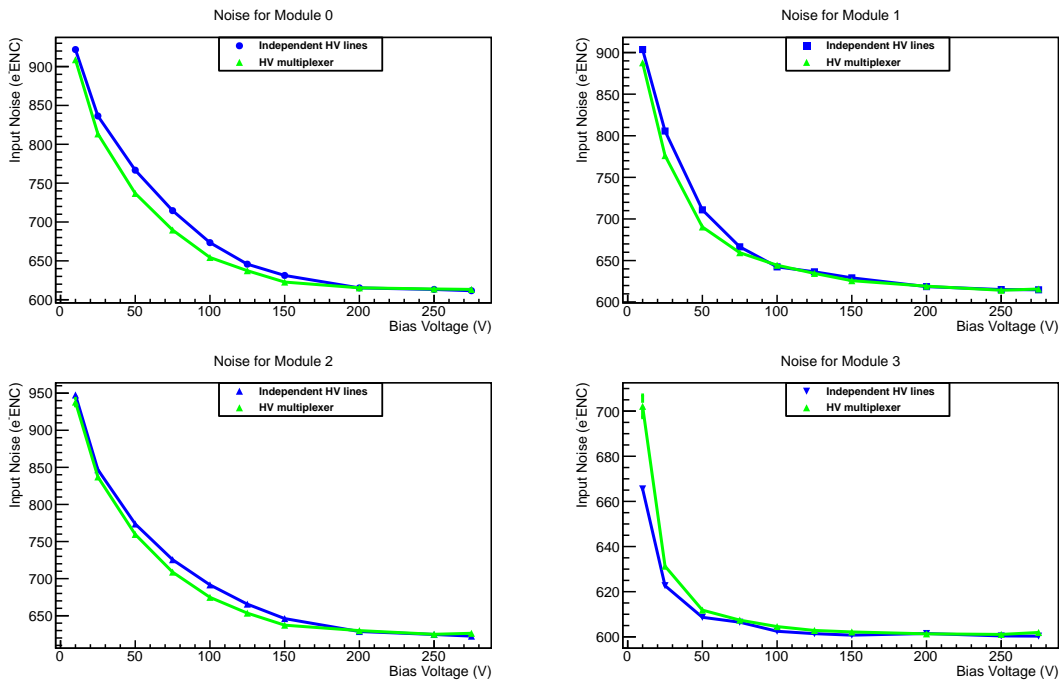


Figure 5.29: Noise comparison of high voltage scans on the DC-DC stavelet, using the high voltage multiplexer and using independent biasing, with the chiller temperature set to 9°C.



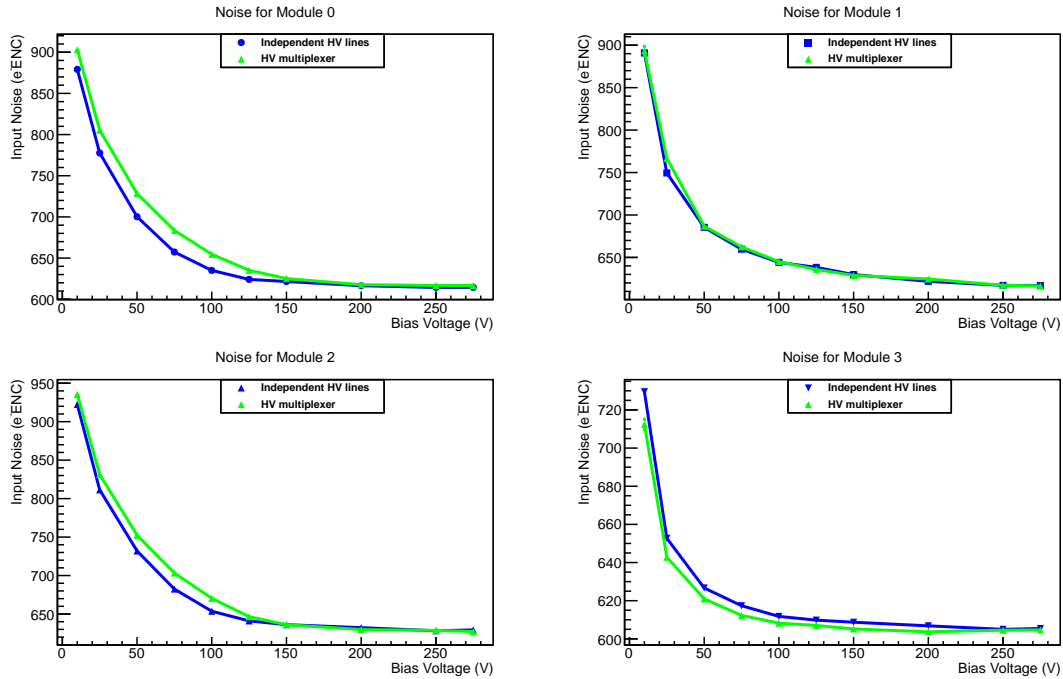


Figure 5.30: Noise comparison of high voltage scans on the DC-DC stavelet, using the high voltage multiplexer and using independent biasing, with the chiller temperature set to 12°C.

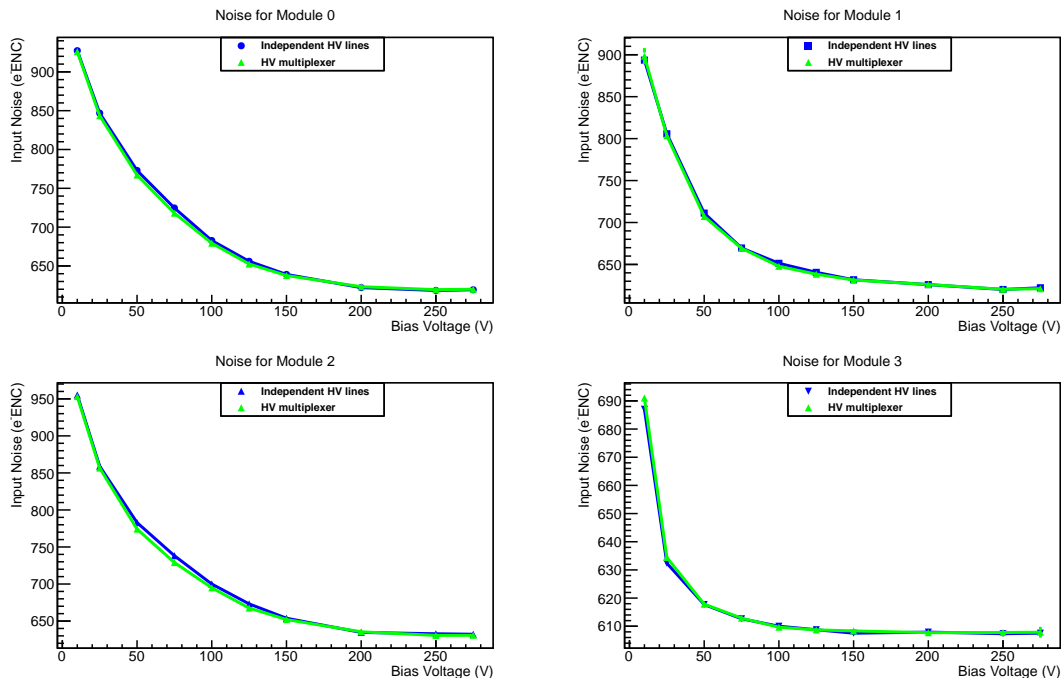
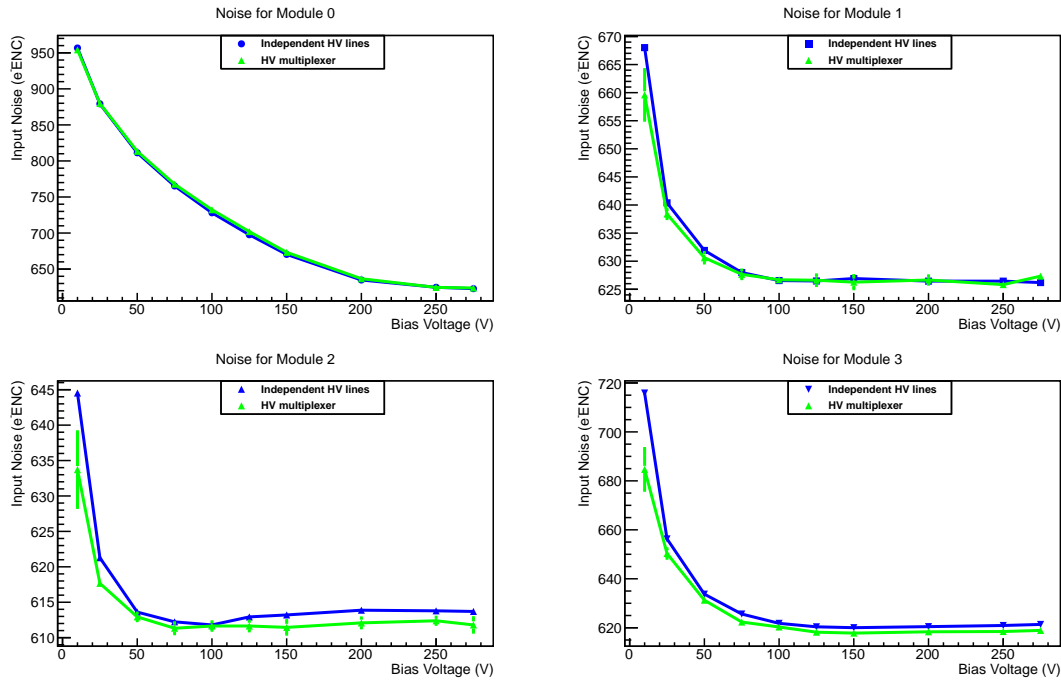


Figure 5.31: Noise comparison of high voltage scans on the DC-DC stavelet, using the high voltage multiplexer and using independent biasing, with the chiller temperature set to 15°C.



**Figure 5.32:** Noise comparison of high voltage scans on the serially powered stavelet, using the high voltage multiplexer and using independent biasing.

The values shown are the average for every module. The error bars represent the noise difference among the three measurements for each bias voltage value. They are not visible for most values due to the small noise differences at each bias voltage setting, being consecutive measurements.

The tests consisted in running high voltage scans, with three point gain tests at each bias voltage, and three repetitions each. The chiller temperature was set to different values to check that the behaviour was consistent for all of them. The low voltage powering of the hybrids was set to 10.5 V, measuring 10 V on the sense wires of the converters.

The results show that multiplexing the high voltage lines has no impact on the noise of the stavelet modules, regardless of the powering scheme used on the stavelets and the temperature setting of the cooling. The small differences are not relevant as they are of different signs for various tests and disappear when the sensor is over-depleted.

Figure 5.32 show the same comparison for the serially powered stavelet. The results reflect a noise variation under  $5 e^-ENC$  for over-depleted sensors. Only one test was done with this stavelet, at  $12^\circ C$  chiller setting and the hybrids temperatures were equal during both tests within  $0.3^\circ C$ .

## 5.4.4 Electromagnetic Interference

### Description of the Electromagnetic Aggressor

A study of the electromagnetic interference was done with the DC-DC stavelet and a VersatileLink prototype. The VersatileLink project is described in [80]. It is a joint ATLAS, CMS and CERN project to develop a high speed fibre-optic transceiver suitable for use in high radiation environments, such as the Phase II Upgrade of the

LHC. The device connects to two fibres using a modified low-mass SFP+ package with standard LC fibre connectors and couples to qualified, commercially available, radiation hard optical fibres.

High speed signals have the potential to broadcast by capacitive and inductive coupling or by electromagnetic transmission to other parts of the detector. We suspected that the silicon strip read-out chips, being of limited bandwidth, would be insensitive to signals transmitting at 4.8 Gbps, but this was the first test of this type performed with the VersatileLink prototype.

The situation is more complex than just a high frequency emission, due to the fact that typical high speed multiplexers frame the data they send in bigger groups of bits called frames, that repeat at a lower frequency, in this case 40 MHz. The current plan for the transmitter includes protocols that randomize the data in a given frame, meaning that even with data packets which are quite uniform, the actual bits sent by the line driver to the VL will have a more random appearance and put more signal power into higher frequencies [104].

### Test Description

The tests performed consisted in measuring the input noise using three point gain tests centred at 1 fC, and Double Trigger Noise tests, putting the VersatileLink prototype at different locations with respect to the DC-DC stavelet. The locations were chosen as both potential locations for the final device (near the EoS card) and also locations with potentially high noise injection on the stavelet [103, 105].



**Figure 5.33: Position of the VersatileLink on top of the EoS card for one of the tests.**

An example of one of such locations is shown in Figure 5.33, with the VersatileLink prototype lying on top of the EoS card. This position is close to the electrical signals coming from the modules, as well as the place at which the VersatileLink device would be located.

The cables used to power the VersatileLink were kept parallel to the cables used to power and read-out the stavelet, in a similar arrangement that would be a realistic scenario, but with data cables that would not be present. This way, the testing conditions are worse than they would be in the actual detector.

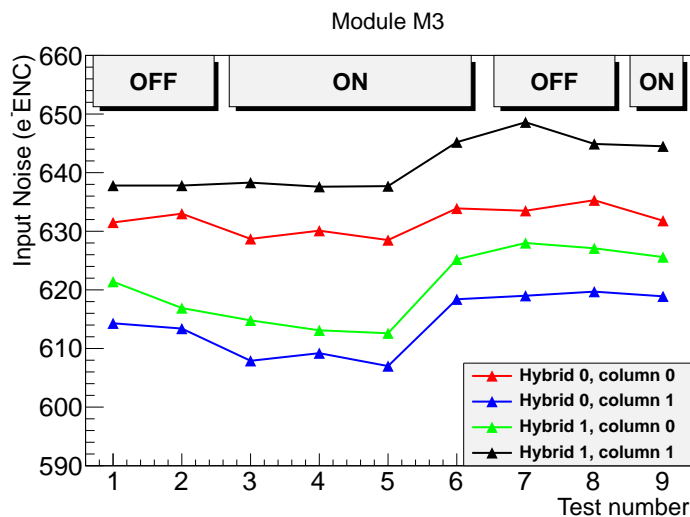
The VersatileLink prototype is connected to a Bit Error Rate Tester (BERT), which generates a Pseudo-Random Bit Stream (PRBS), simulating the data transfer to and from a stave, at a rate of 4.8 Gbps.

The parameters of the tests were:

- Sensor bias: 250 V.
- Low voltage: 10.3 V (10 V on the sense wires).
- $T_{\text{chiller}} = 12^{\circ}\text{C}$ .

There was no light leak test performed with this prototype, due to the working wavelength of 1310 nm, to which silicon detectors are insensitive. This case is different to the current SCT modules that use 850 nm lasers, which can generate signals on the silicon strips [40].

## Tests Results



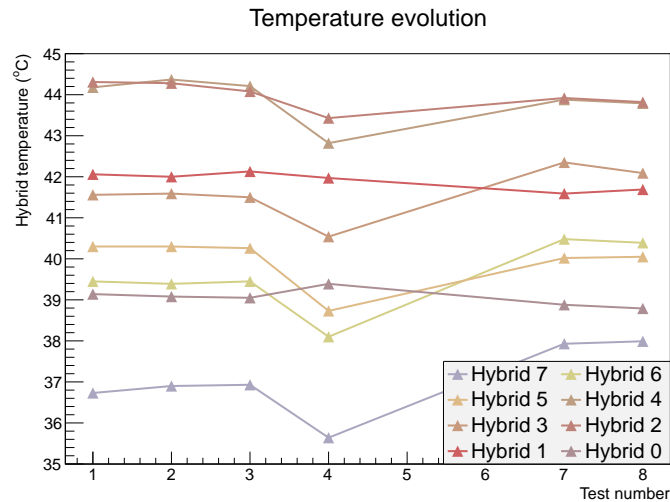
**Figure 5.34: Noise measurements for module M3 with the interaction of the VersatileLink.**

Figure 5.34 shows the noise results for module M3 of the stavelet. The values are the average for each chip column (10 chips). The plot also shows the status (ON/OFF) of the VersatileLink prototype for each test.

The noise reference was established in tests number 1 and 2, and the small noise increase observed is consistent with the temperature increase also observed on the stavelet during the tests, as shown in Figure 5.35. The temperature increase was due to the only available chiller at the time of the tests, which was not working properly and could not sustain the cooling power for prolonged periods.

The test involved placing the prototype in different positions and orientations, as well as turning it off before the last measurement. The fact that it was turned off during tests number 7 and 8 confirms the noise increase was not caused by the VersatileLink.

The tests were done in the following sequence:



**Figure 5.35: Temperatures measured on the stavelet during the noise tests with the interaction of the VersatileLink.**

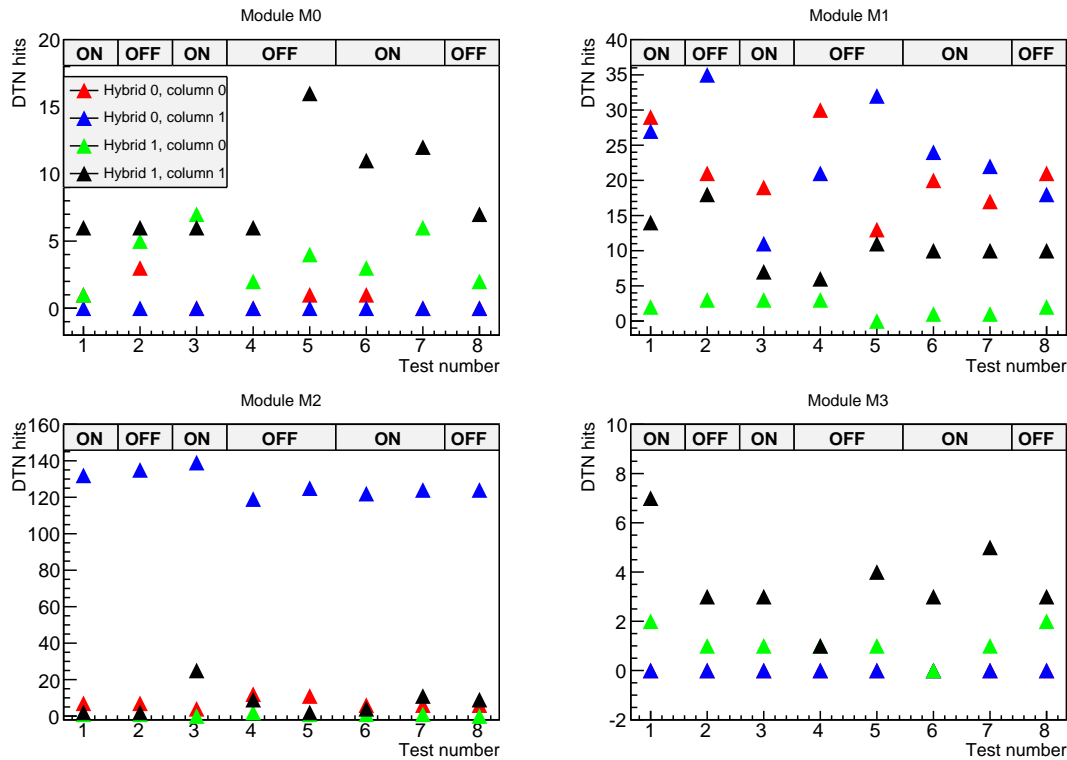
- Tests 1 and 2: VersatileLink prototype turned off. Reference noise measurements.
- Test 3: VersatileLink placed close to the EoS card, turned on. The power cables were routed along the stavelet.
- Test 4: VersatileLink placed close to the EoS card, turned on. The power cables were folded back, following the same path as the optical fibres, which is the realistic configuration.
- Test 5: VersatileLink placed above the EoS card, turned on.
- Test 6: VersatileLink placed above a group of ABCn25 chips in module M3, turned on.
- Tests 7 and 8: VersatileLink turned off to get back a reference noise measurement.
- Test 9: VersatileLink placed above a group of ABCn25 chips in module M3, turned on.

Figure 5.36 shows the Double Trigger Noise results for another test performed. Only the 0.5 fC threshold is presented here, in order to be able to observe variations that might come unnoticed with the other higher thresholds. The variations are consistent with random noise and big variations from one test to another were not observed.

Both 1 fC and 0.75 fC thresholds for all these Double Trigger Noise tests resulted in zero hits for all columns (except for one that sometimes shows a few hits).

The tests labelling is different from the ENC tests. In the DTN case, the tests sequence is the following:

1. VersatileLink on top of module M3, turned on.
2. VersatileLink on top of module M3, turned off.
3. VersatileLink on top of EoS card, turned on.



**Figure 5.36: Double Trigger Noise results for 0.5 fC threshold on the DC-DC stavelet with the interaction of the VersatileLink.**

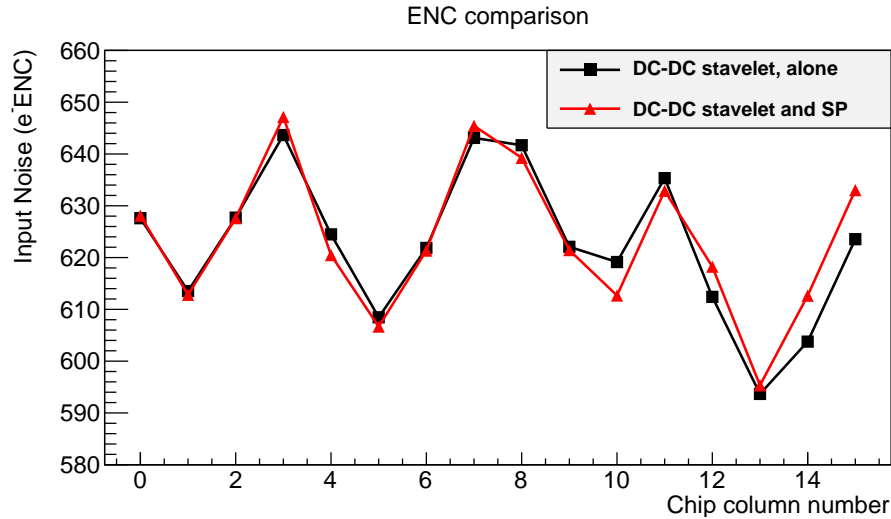
4. VersatileLink on top of EoS card, turned off.
5. VersatileLink on top of EoS card, turned off.
6. VersatileLink on top of EoS card, turned on.
7. VersatileLink on top of EoS card, rotated 90°, turned on.
8. VersatileLink on top of EoS card, turned off.

One of the first prototype Versatile Link (VL) transceivers was used to test the ITk stavelet for immunity to the signals that the VL generates. Several tests were performed with different locations of the VL relative to the stavelet and the noise was compared to the cases where the VL was not powered on. All noise variations seen were consistent with temperature fluctuations of the system. There was no indication that the VL contributed to increase the noise on the ABCn25 based system.

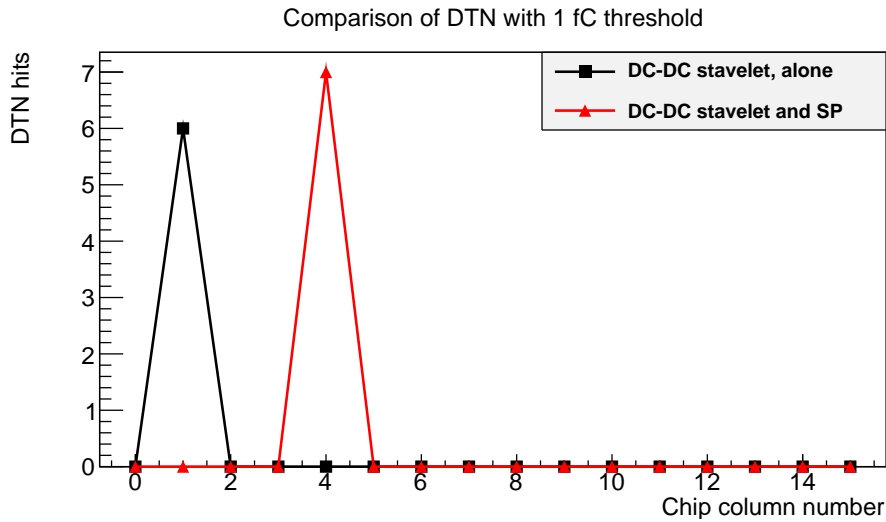
### 5.4.5 Dual and Single Stavelet Tests

The two stavelets, DC-DC and serially powered, have been tested separately and together with the same DAQ, powering and cooling systems. This section presents the results of the tests done with two stavelets running at the same time.

The goal of this type of test is to assess if there is any kind of interference between two near-by stavelets. In particular, I was interested in studying the possible noise increase in one stavelet caused by DC-DC converters placed close to the adjacent



(a) Noise comparison on the DC-DC stavelet alone and together with the SP stavelet.



(b) Double Trigger Noise comparison on the DC-DC stavelet alone and together with the SP stavelet.

**Figure 5.37: Noise differences on the DC-DC stavelet when operated alone and when operated with the SP stavelet at the same time.**

stavelet. Also, the common read-out using the same HSIO board and adjacent power lines, both hybrid power and sensor bias, could have an influence in the noise pick-up on the modules.

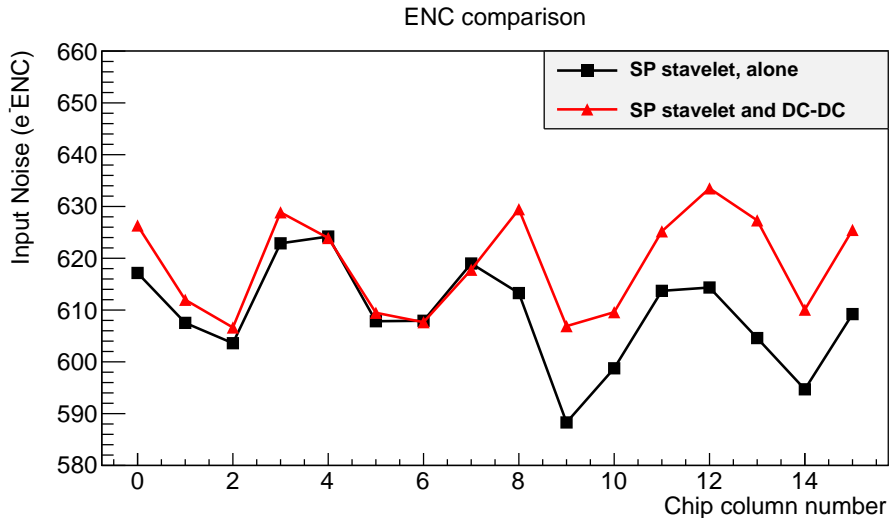
One of the stavelets is biased using independent high voltage lines, whereas the other is biased using the high voltage multiplexer. The results presented in Figures 5.28 through 5.32 show that there is no difference between both biasing methods.

The cooling of the two stavelets when operating together was initially done by connecting the serially powered stavelet in series with the DC-DC powered stavelet. The DC-DC stavelet was first in the cooling path, meaning it ran at the same temperature as if it were operated alone. The SP stavelet ran at higher temperature than it did when operated separately.

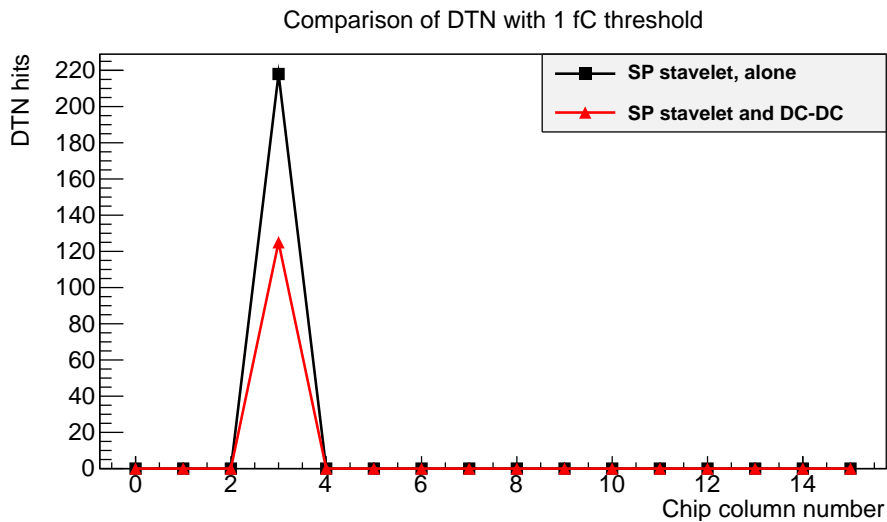
Figure 5.37 shows the input noise results and the Double Trigger Noise results for

the DC-DC stavelet, when running separately and when operated together with the serially powered stavelet. The chiller temperature was set to 12°C in both cases and the sensor bias was 250 V. The stavelet sensor bias was done through independent high voltage lines.

The input noise results are presented per chip column, showing the average noise value for each group of 10 chips and the total number of hits for the Double Trigger Noise plots.



(a) Noise comparison on the serially powered stavelet alone and together with the DC-DC stavelet.



(b) Double Trigger Noise comparison on the serially powered stavelet alone and together with the DC-DC stavelet.

**Figure 5.38: Noise differences on the DC-DC stavelet when operated alone and when operated with the SP stavelet at the same time.**

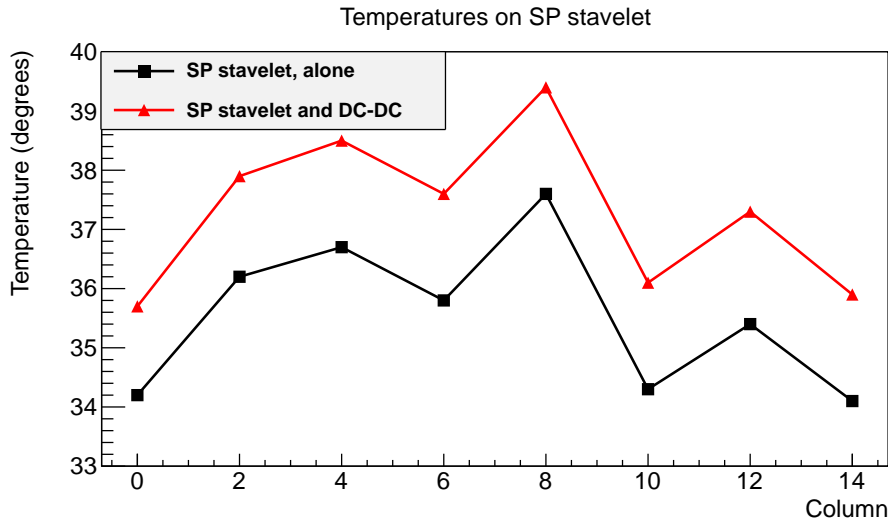
The noise was measured by doing three point gain tests centred at 1 fC. The plots show that there is no increase in the noise when operating both stavelets at the same time and the Double Trigger Noise is not affected either.

Figure 5.38 shows the input noise results and the Double Trigger Noise results for the serially powered stavelet, again when running alone and when operated together



with the serially powered stavelet. The chiller temperature was set to 12°C in both cases and the sensor bias was 250 V. The stavelet bias was done through the high voltage multiplexer in both cases. Results shown before in Figure 5.32 confirm the noise is not affected by the use of high voltage multiplexing.

The first tests resulted in a noise increase by around 70  $e^-$  ENC in some modules of the serially powered stavelet, which was eliminated after using better twisted cables. The cables on the hybrids power supplies are twisted and using a common mode choke in order to get rid of the common mode noise, which the serially powered stavelet is more affected by than the DC-DC stavelet.



**Figure 5.39:** Temperatures recorded on the Serially Powered stavelet when operated alone and together with the DC-DC stavelet.

Considering the temperature increase on the serially powered stavelet due to the cooling configuration, these plots show that there is no increase in the noise caused by operation of both stavelets at the same time. The temperatures on each column in both cases are shown in Figure 5.39. There is a global increase of the hybrids temperatures between 1.5 and 2°C.

As observed in the DC-DC stavelet, running both stavelets at the same time does not have an effect on the Double Trigger Noise hits.

The Double Trigger Noise on the serially powered stavelet shows column 3 is very noisy. However, all the other columns are clean at 1 fC threshold, as expected. The noise on column 3 of this stavelet is related to the use of non-blind vias and the hits appear only at specific locations.

These results show that there is no negative influence originating in the simultaneous read-out of the two stavelets.

## 5.5 DC-DC Powered Stave

The first full length stave was assembled at Rutherford Appleton Laboratory (RAL) by the end of 2013. The Stave-250 is a 12-module stave with DC-DC powering. The denomination “250” comes from the use of the ABCn25 chip.

Initially, only one of the sides has been populated with modules. After its finalization, a serially powered stave is started to be assembled. When complete, the decision to populate the second side of the two staves will be taken based on their performance.

The results obtained with this stave are presented in this section.

### 5.5.1 Assembly of the Stave

The modules are glued on a 1.2 metre long bus tape that is mounted on the stave core. The bus tape routes the signals and power to the hybrids, as well as the sensors bias.

The core is made of thermally conductive carbon foam in a honeycomb layout. It provides support and cooling for the 24 modules that can be mounted on the stave, one on each side. Titanium cooling pipes are embedded in the core, providing the cooling to the whole stave volume.

All the modules used in the assembly of the stave are Grade A, with FZ1 sensors. They come from multiple assembly sites:

- University of Cambridge, United Kingdom (CAM).
- The University of Liverpool, United Kingdom (LIV).
- University of California, Santa Cruz, United States (UCSC).
- University of Freiburg, Germany (FREI).

The DC-DC converters used in the Stave-250 are a re-manufacture of the CERN tandem converter, which has a dual output conceived to power two hybrids on one module with a single board. The main motivation to build this kind of converter was to have a star point for common referencing of the two hybrids on a module, which for single converters is done with wire. By using a common board, the star point is implemented together with the two converters on a single printed circuit board.

The modification consists of a partially split ground plane, which originally was a solid ground plane for both converters and the splitting decreased the noise when tested on a module of a stavelet [106].

In addition, the board includes a 1-Wire chip that is used to turn on and off each of the power outputs individually. This converter was initially described in section 4.3.2.

The modules are glued down on the stave bus tape using a vacuum jig that picks up the module and the vacuum is released when the module is in place. This is done to avoid tension on concave modules, so the module returns to its shape, being pressed down with the vacuum cups.

SE4445 glue was used to glue the modules, curing overnight at room temperature. After the modules, the BCC boards and the DC-DC converters are also glued down and when cured, the wire-bonding is done.

The converters for the first three modules were stuck to the ceramics using Araldite Rapid glue and then glued to the stave using double sided tape. This procedure proved to provide poor thermal contact for the converters, and was changed for the rest of the modules. The remaining nine converters used SE4445 and run cooler than the first three.

Assembly commenced from the end farthest from the End of Stave board. Initially one module was glued down and, after checking the procedure was correct, two more

modules were mounted, together with the DC-DC converters and BCC boards. Next, they were wire-bonded and the stave with three modules was tested.

After the first results, six more modules were assembled and the stave was tested with nine modules. Last, the final three modules were mounted and the results on a full single-sided stave were obtained.

### 5.5.2 Setup at RAL

The setup available at RAL is similar to the one at CERN. There are three TTI power supplies with dual outputs and a VME crate with three SCSHV preproduction boards, for a total of 12 high voltage channels. These boards are controlled through the SCTDAQ software in the same way as in the setup at CERN [95].

Powering of the hybrids was split in three segments, with three different lines on the bus tape, that can withstand the high total current needed for the twelve modules. The total output power when all modules are powered on is around 300 W. All the power supplies are controlled via USB using the SCTDAQ software.

A Neslab Thermoflex 1400 chiller with tap water is used to cool down the stave. The temperature is set to 13°C, in order to avoid going below the dew point, which is typically around 10°C in the lab at RAL. A nitrogen supply is available to run the tests in dry conditions and to ensure there is no condensation if the chiller is run at lower temperature.

In addition, there is a blow-off CO<sub>2</sub> cooling system designed to cool down the stave down to around -30°C. It will be used in some of the tests in the future.

### 5.5.3 Results with Three Modules

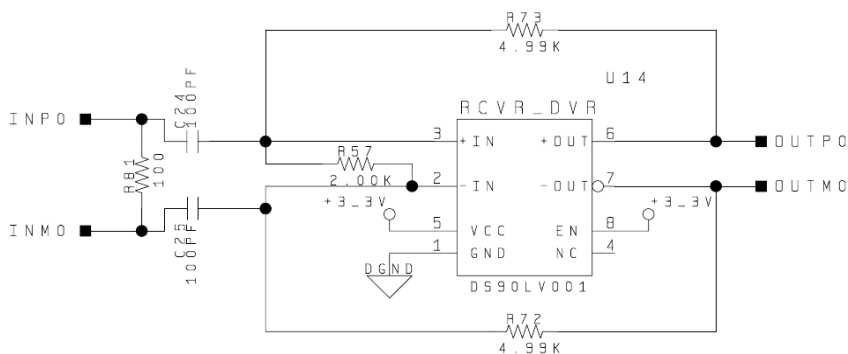
The first tests on the stave were done after three modules were placed and bonded on the stave. These three modules are:

- Two modules from University of Cambridge: CAM-M5 (module 0) and CAM-M6 (module 1).
- One module from University of California, Santa Cruz: UCSC-M4 (module 2).

The first tests consisted in measuring the temperatures of the DC-DC converters when powering up the hybrids. Initially, the coils were shielded with a copper coated plastic case. This type of shield does not have a good heat transfer and that caused a measured temperature on the coil of 140°C.

This high temperature could cause the destruction of the converter, so reducing it was a requirement before proceeding with further tests. In a first iteration, the shield was replaced with a tinned copper one, but the temperature was still around 140°C. After filling the shield with thermal pad, in contact with the coil, the temperature finally decreased to around 60°C.

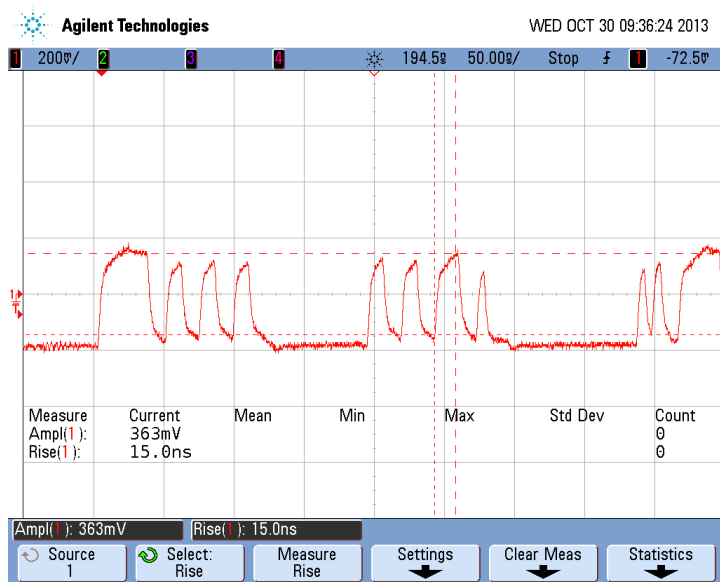
Initially, the communication with the modules was not stable and some streams would have a lot of errors when trying to talk to the hybrids. Since the stave bus tape is a longer one than the stavelets bus tape, a study of the signals was done to assess the signal integrity. The critical point is on the End of Stave card, right at the buffers for the BCC signals.



(a) Circuit diagram of the buffers at the EoS.



(b) Signal for hybrid 1 with 100  $\Omega$  termination.



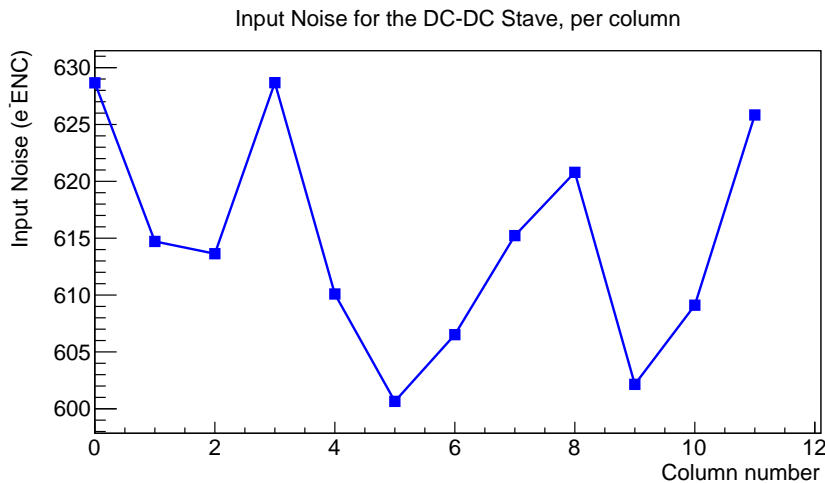
(c) Signal for hybrid 1 with 56  $\Omega$  termination.

Figure 5.40: Signal integrity at the End of Stave buffers for different termination resistors.

Figure 5.40 show the analysis of the signals at the termination resistor of the buffers (see Figure 5.40(a)) on the End of Stave card. The  $100\ \Omega$  termination resistor that is typically used in LVDS signal transmission and used on the End of Stave card results in reflections that causes a badly formed signal, resulting in errors in the reception at the HSIO.

The signal at the  $100\ \Omega$  termination resistor is shown in Figure 5.40(b), showing that the fast signals cannot reach their levels, as opposed to the signal at the  $56\ \Omega$  resistor, shown in Figure 5.40(c), with a lower signal amplitude but with well defined levels.

The capacitive load difference of the long bus tape, combined with the limited drive current of the BCC chips, are responsible for this signal integrity problem. However, the drawback of reducing the value of the termination resistors is a reduction in the signals amplitude. In some cases, the signal levels might be too low even though the reflections are eliminated.



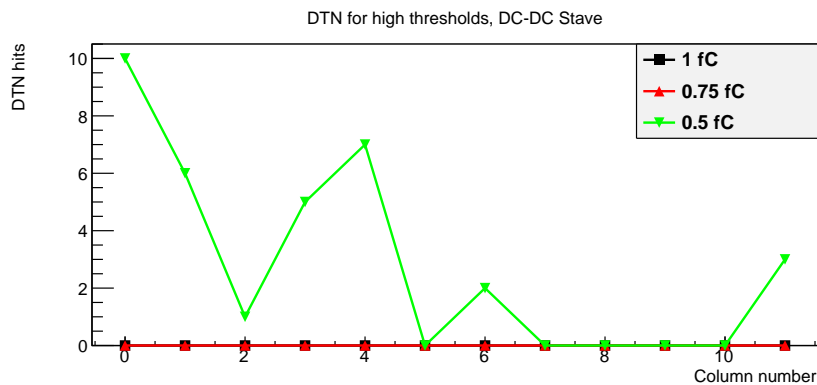
**Figure 5.41: Input noise results of the DC-DC stave with the first three modules.**

The noise results for the stave with three modules are shown in Figure 5.41. The three modules have very good noise results and the values are consistent with the results for the individual modules. The X axis represents the chip columns (3 modules, 6 hybrids, 2 columns per hybrid results in 12 columns). All columns have average noise values between  $600$  and  $630\ e^-ENC$ .

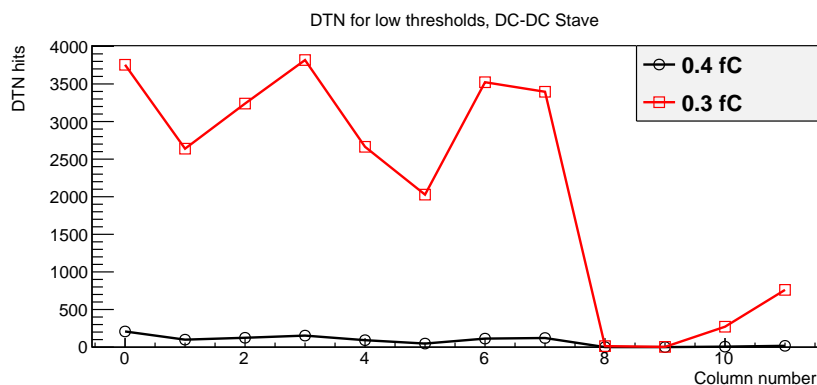
In order to be able to run the input noise tests, the threshold scans had to be started from  $50\ mV$ , instead of the typical  $0\ mV$ . Some hybrids were still problematic from the signal integrity point of view and generating errors at low thresholds. By starting at a higher threshold, these errors were eliminated and the initial threshold was set well below the  $V_{t50}$  so the noise measurements were not affected.

The Double Trigger Noise results are show in Figure 5.42. The counts with  $1$  and  $0.75\ fC$  thresholds are clean on all modules, while the count at  $0.5\ fC$  threshold is not very high, being most of them due to some bad channels. The counts at lower thresholds are as high as it would be expected. The spikes appear in some channels that show noisy behaviour at lower thresholds.

The bad channels are identified by looking at the Double Trigger Noise plots generated by SCTDAQ, and spotting the channels that have hits at most of the BCO



(a) DTN on the Stave 250 with three modules for high thresholds.



(b) DTN on the Stave 250 with three modules for low thresholds.

**Figure 5.42: Double Trigger Noise of the DC-DC stave with three modules.**

delay settings. In some of the modules there is at least one bad channel that could be masked to remove the Double Trigger Noise extra hits.

### 5.5.4 Results with Nine Modules

A picture of the stave with nine modules mounted is shown in Figure 5.43. The nine modules are mounted from the far end of the stave, shown at the left, and the End of Stave card is located at the right side of the picture.

**Figure 5.43: A picture of the DC-DC stave with nine modules.**

The six modules mounted after the first three are the following:

- Four from University of Cambridge: CAM-M9 as module 3, CAM-M10 as module 4, CAM-M11 as module 5 and CAM-M3 as module 8.

- Two from The University of Liverpool: LIV-M31 as module 6 and LIV-M32 as module 7.

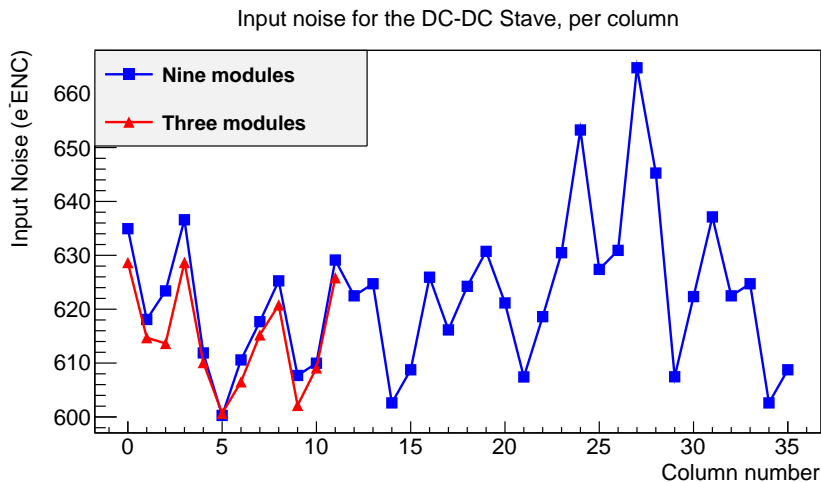


Figure 5.44: Input noise of the DC-DC stave with nine modules.

Figure 5.44 shows the results for the input noise of the nine modules on the stave. The noise values are consistent with the values measured on the individual modules and they are all reasonable values. The results for the first three modules are included in the plot for comparison. They do not show a great difference with respect to the values shown in Figure 5.41. The differences are consistent with the temperature increase due to the next modules increased heat. The inner columns have a noise between 600 and 631  $e^-ENC$ , while the outer columns show a noise between 609 and 665  $e^-ENC$ .

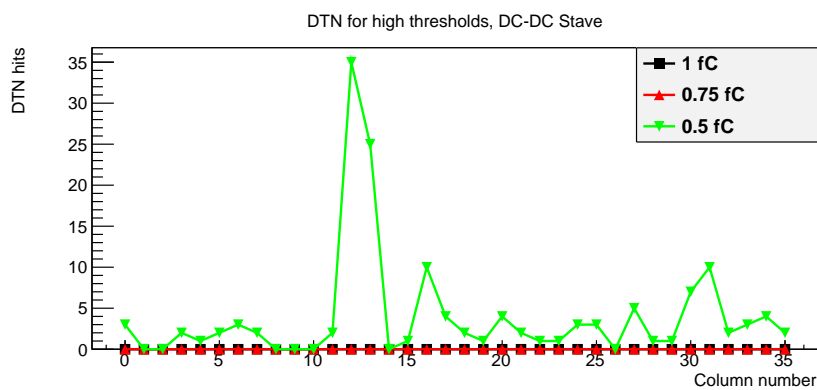
The modules that present highest noise are LIV-M31 and LIV-M32, which are columns 24 to 31. These two modules have shield-less hybrids, which were designed without the bottom shield layer. However, the cause for the higher noise figures is not in the lack of shield, but it is related to it. The flatness of the hybrids is not as good as other shielded hybrids, which results in a different hybrid to sensors glue thickness, which effects the noise.

With the exception of those two modules, the noise on the stave with nine modules is between 600 and 640  $e^-ENC$ .

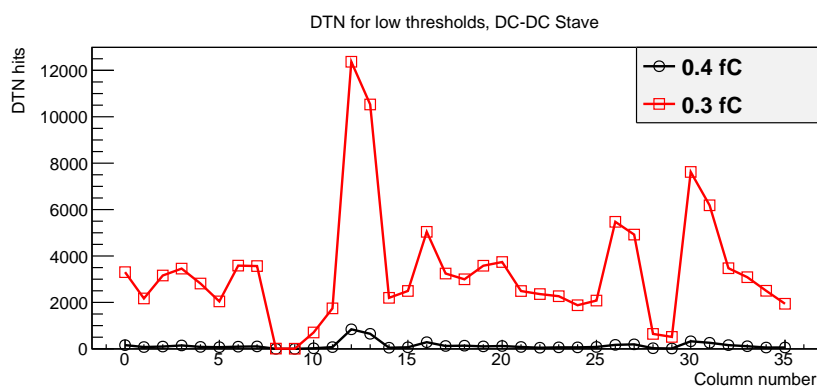
Figure 5.45 shows the Double Trigger Noise results on the stave with nine modules. As indicated in the results on three modules, the X axis represent the chip columns (9 modules, 18 hybrids: 36 columns). The higher threshold Double Trigger Noise results show no hits for the 1 fC and 0.75 fC thresholds, while some hits appear on the 0.5 fC. The spikes appear in some channels that show noisy behaviour at lower thresholds.

These results show that the stave with nine modules worked very well, with good noise results and very low noise pick-up. The temperatures plotted in Figure 5.46 were measured on the stave hybrids while being tested, both with three modules and with nine modules. The first three modules show a temperature increase between 1.6 and 5.5°C. These increased temperatures give consistence to the small noise increase of the first three modules.

Results on the DC-DC Stave with nine modules were first presented at the ATLAS Upgrade Week of November 2013 [107]. Additional results, such as the DC-DC converters and the bus tape temperatures are shown in the talk.



(a) DTN on the Stave 250 with nine modules for high thresholds.



(b) DTN on the Stave 250 with nine modules for low thresholds.

Figure 5.45: Double Trigger Noise of the DC-DC stave with nine modules.

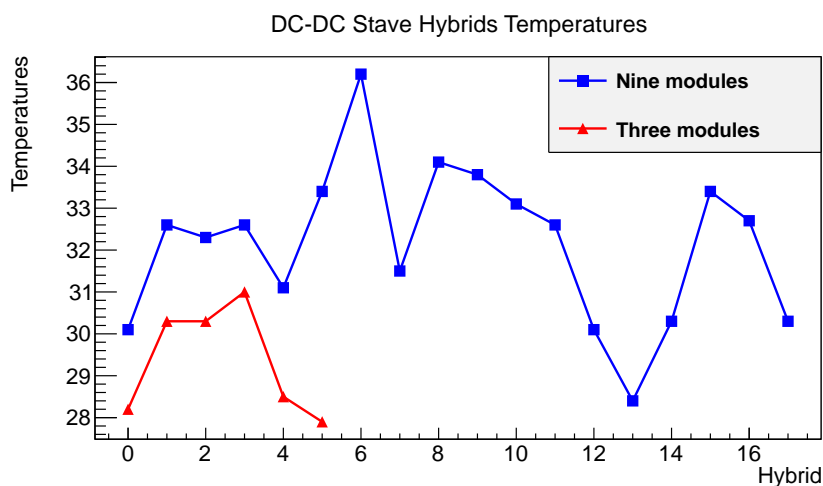


Figure 5.46: Hybrids temperatures on the DC-DC stave hybrids with nine modules.



### 5.5.5 Results with Twelve Modules

The last three modules that were mounted on the DC-DC stave were the following:

- Three from University of Freiburg in Germany: FREI-M9 as module 9, FREI-M11 as module 10 and FREI-M6 as module 11.

The same procedure for modules glueing as for the first nine was followed. The DC-DC converters and the BCC boards were glued as for the previous six modules. Testing conditions were the same as for the previous results.

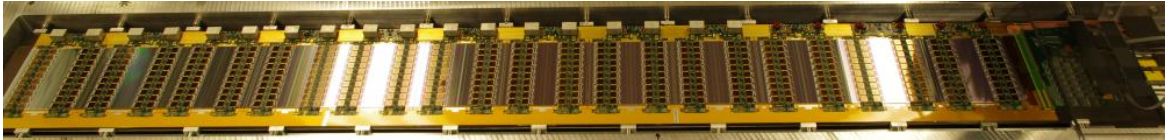


**Figure 5.47: A picture of the DC-DC stave with all the modules on one side modules.**

Figure 5.47 shows a picture of one side of the complete stave, with the twelve modules, before bonding the DC-DC converters and BCC boards. The tests described next include repeating the same tests that were shown above for three and nine modules, as well as a low voltage scan and a high voltage scan.

Module	Isolation	$V_{\text{dep}}$	$C@250\text{ V}$	$I_{\text{leak}}@250\text{ V}$
0 (CAM-M5)	P-stop, $4 \times 10^{12}\text{ cm}^{-3}$	190 V	2.63 nF	0.23 $\mu\text{A}$
1 (CAM-M6)	P-stop, $4 \times 10^{12}\text{ cm}^{-3}$	240 V	2.95 nF	0.27 $\mu\text{A}$
2 (UCSC-M4)	P-stop, $4 \times 10^{12}\text{ cm}^{-3}$	unknown	unknown	0.27 $\mu\text{A}$
3 (CAM-M9)	P-stop, $4 \times 10^{12}\text{ cm}^{-3}$	190 V	3.28 nF	0.27 $\mu\text{A}$
4 (CAM-M10)	P-stop, $4 \times 10^{12}\text{ cm}^{-3}$	200 V	3.29 nF	0.21 $\mu\text{A}$
5 (CAM-M11)	P-stop, $4 \times 10^{12}\text{ cm}^{-3}$	180 V	3.28 nF	0.21 $\mu\text{A}$
6 (LIV-M31)	P-stop, $4 \times 10^{12}\text{ cm}^{-3}$	250 V	2.93 nF	0.38 $\mu\text{A}$
7 (LIV-M32)	P-stop, $4 \times 10^{12}\text{ cm}^{-3}$	190 V	2.92 nF	0.17 $\mu\text{A}$
8 (CAM-M3)	P-stop, $4 \times 10^{12}\text{ cm}^{-3}$	unknown	unknown	0.25 $\mu\text{A}$
9 (FREI-M9)	P-stop, $4 \times 10^{12}\text{ cm}^{-3}$	unknown	unknown	0.20 $\mu\text{A}$
10 (FREI-M11)	P-stop, $4 \times 10^{12}\text{ cm}^{-3}$	250 V	unknown	0.30 $\mu\text{A}$
11 (FREI-M6)	P-stop, $4 \times 10^{12}\text{ cm}^{-3}$	190 V	unknown	0.20 $\mu\text{A}$

**Table 5.7: Characteristics of the sensors on the DC-DC stave: isolation structures of the strips and concentration dose, depletion voltage, capacitance with 250 V bias and leakage current with 250 V bias.**

The input noise and Double Trigger Noise tests were repeated for comparison, biasing the sensors with 250 V. Nitrogen was flushed into the stave enclosure and the chiller temperature was set to 13°C.

The hybrids temperatures were also recorded for the 24 hybrids on the stavelet while in operation. Figure 5.48 shows the temperatures of all the hybrids and the comparison with the first three and nine modules temperatures.

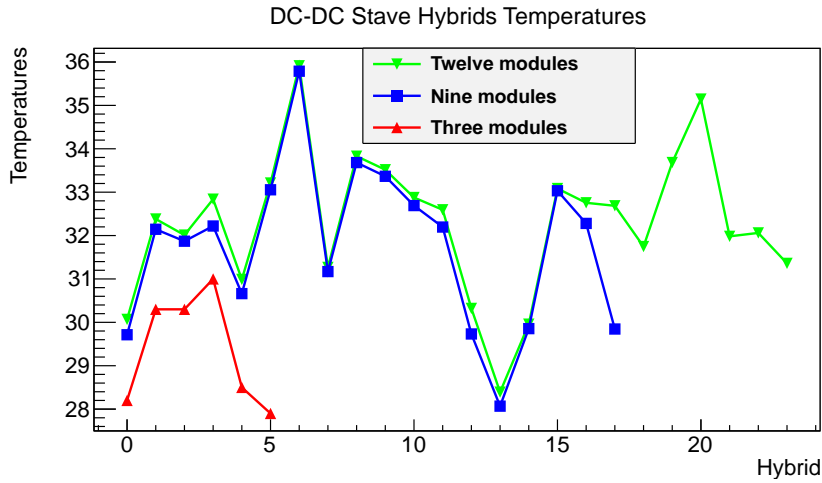


Figure 5.48: Hybrids temperatures on the DC-DC stave hybrids with 12 modules.

The tests with 3 and 9 modules were done in October 2013, while the tests with twelve modules were done in January 2014. The very small difference between nine and twelve modules can be explained due to the temperature difference during those dates. The nitrogen supply was between 7 and 15°C colder in January than in late October. Therefore, despite the increase in heat load coming from the last three modules, the temperature increase is much lower than in the comparison between three and nine modules.

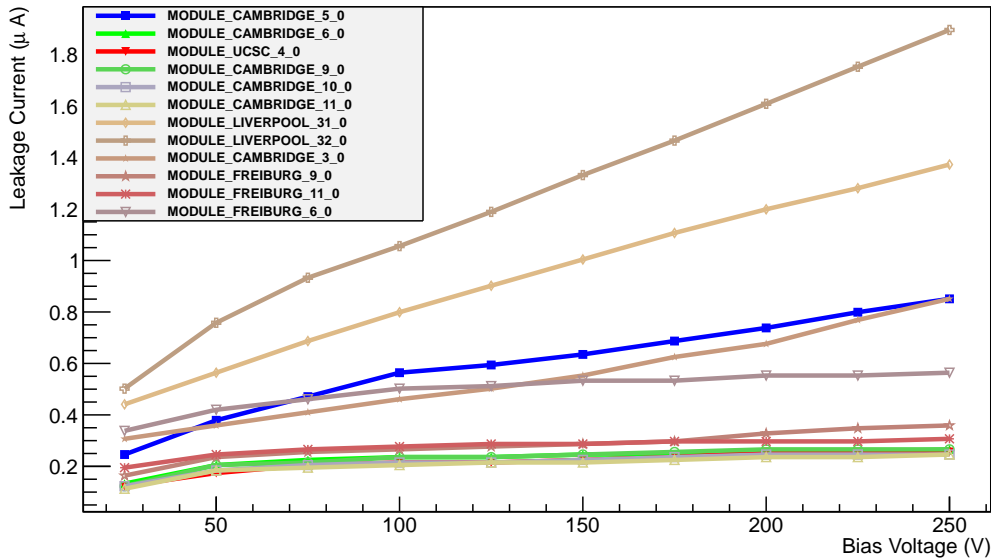
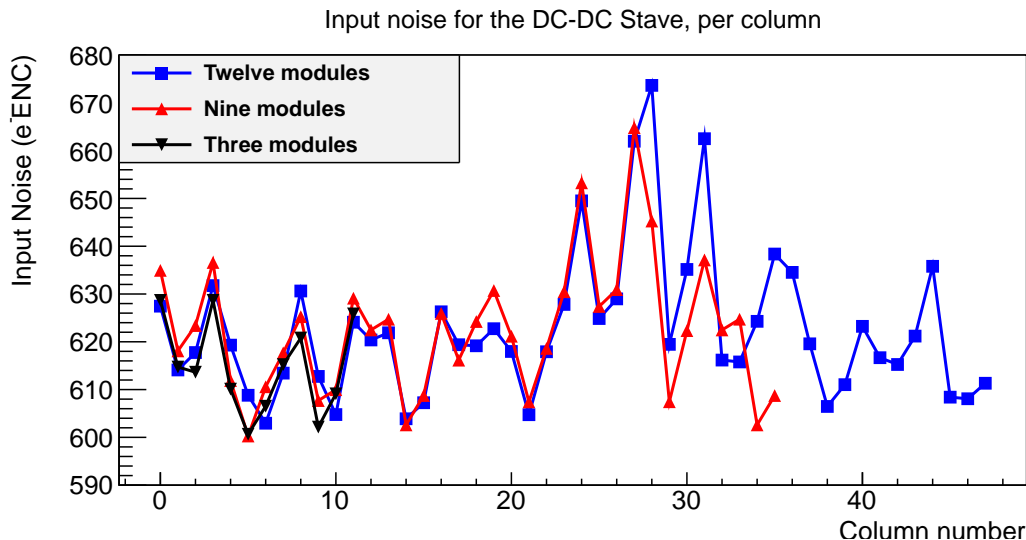


Figure 5.49: Leakage currents curves for each sensor mounted on the DC-DC stave, measured at 22°C in nitrogen.

The leakage currents were measured, performing an I/V scan using SCTDAQ. The results are shown in Figure 5.49. All sensors present leakage current values consistent

with the values presented in Table 5.7, and they show the stave assembly process did not have a negative impact on the sensors. The curves were measured with the stave inside a light-tight enclosure, with a nitrogen flow into the enclosure. The temperature of the sensors was 22°C and the voltage ramp was done in steps of 25 V, waiting for 10 seconds between measuring the current and increasing the voltage.



**Figure 5.50: Input noise of the DC-DC stave with twelve modules, compared to the noise with three and nine modules.**

Figure 5.50 shows the noise results of the stave with one complete side. The results with three and nine modules are also plotted for the corresponding columns. There are no variations on the noise that differ from the expected increase due to the higher operating temperature of the hybrids that are further away in the cooling path.

Figure 5.51 shows the Double Trigger Noise results on the stave with twelve modules. As before, the X axis represents the chip columns (12 modules, 24 hybrids: 48 columns). The higher threshold Double Trigger Noise results show no hits for the 1 fC and 0.75 fC thresholds, while some hits appear on the 0.5 fC.

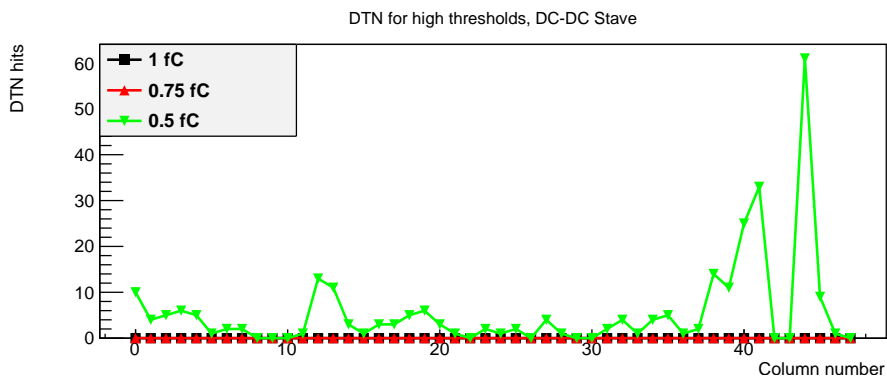
These results show that the single-sided stave with DC-DC conversion has a very good performance. The noise of the modules is not influenced by the common read-out through a long bus. The Double Trigger Noise test also demonstrates that the bus does not have a negative effect on the read-out system.

The only drawback of the long bus tape is the signal integrity for distant hybrids, which can be solved by an adequate choice of termination resistors.

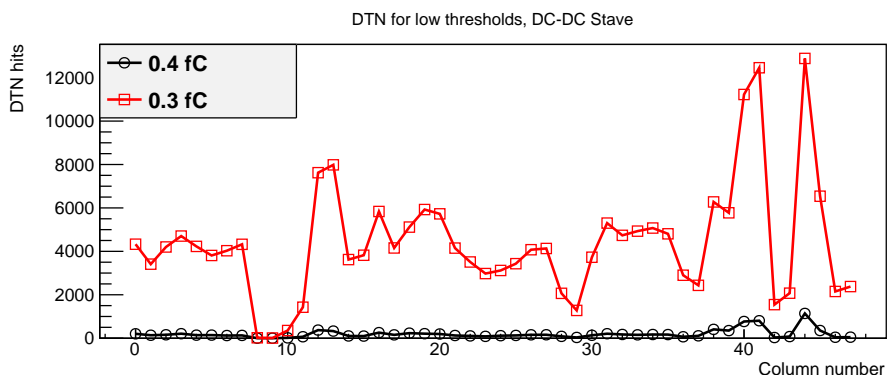
## High Voltage Scan

After the first side of the stave was finalized, high voltage and low voltage scans were performed, in the same way they were done for the stavelets.

Figure 5.52 shows the input noise evolution on each of the modules when the sensor bias was scanned in the set  $V_{\text{bias}} = \{10, 25, 50, 75, 100, 125, 150, 200, 250, 275\}$ . The scan was performed in both directions, first ramping up and then ramping down the voltage. The noise shown in the plot is the average for each of the modules.



(a) DTN on the Stave 250 with twelve modules for high thresholds.



(b) DTN on the Stave 250 with twelve modules for low thresholds.

Figure 5.51: Double Trigger Noise of the DC-DC stave with twelve modules.

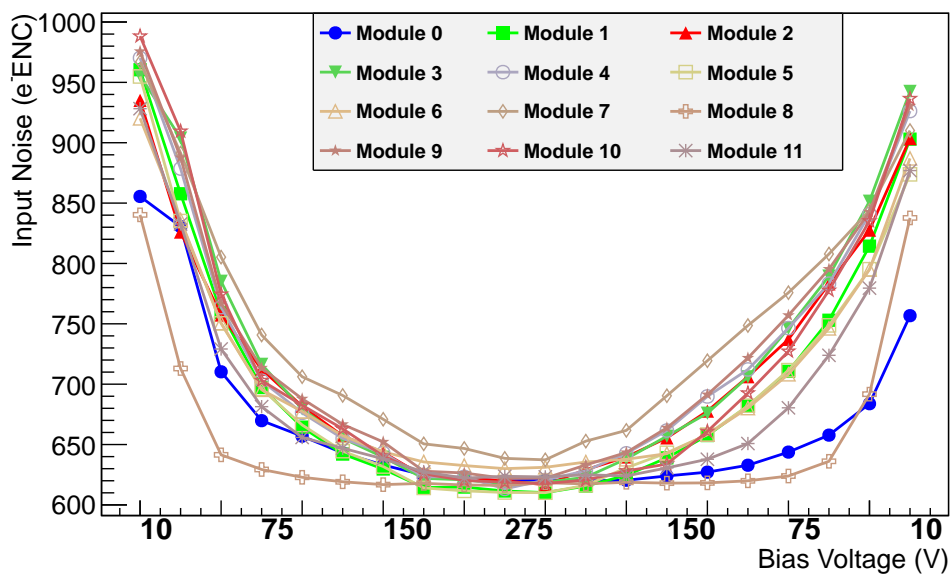


Figure 5.52: Evolution of the input noise for each module of the DC-DC stave with changing sensor bias.

The first observation is the different behaviour of the stave modules with respect to the stavelets modules. The way down of the bias voltage presents lower noise than the way up, contrary to what has been observed previously.

Due to the fact that the stave sensors were left unbiased for long periods of time, this may be attributed to the capacitance stabilization with time. The capacitance of the strips when they are biased decreases with time, at a slow rate with time when they are kept in nitrogen.

### Hybrid Powering Variations

The low voltage power supplies on the stave were programmed to perform noise measurements when the input voltage to the DC-DC converters was changed. Due to the long bus tape, the voltage drop along the stave is higher than on the stavelet. This is shown in Table 5.8 for the power supplies settings used in the low voltage scans. The three segments are separated in the table for clarity.

Since the current draw changes for the different voltage output values on the power supplies, the voltage drop along the cables and the bus tape is not constant. For instance, the voltage drop from M0 to M11 at 10.5 V setting is 740 mV while the drop at 13.5 V is 540 mV.

Voltage on the PSU:	10.5 V	11.0 V	11.5 V	12.0 V	12.5 V	13.0 V	13.5 V
Module	Voltage at the DC-DC converter input (V)						
M0	9.04	9.64	10.22	10.78	11.34	11.89	12.44
M1	9.08	9.67	10.24	10.81	11.36	11.92	12.47
M2	9.14	9.73	10.30	10.86	11.42	11.97	12.51
M3	9.25	9.83	10.40	10.95	11.50	12.05	12.59
M4	9.23	9.81	10.38	10.93	11.49	12.04	12.58
M5	9.26	9.84	10.40	10.96	11.51	12.06	12.60
M6	9.32	9.90	10.46	11.01	11.57	12.11	12.65
M7	9.44	10.01	10.57	11.12	11.66	12.20	12.74
M8	9.58	10.14	10.68	11.22	11.76	12.30	12.83
M9	9.61	10.17	10.71	11.25	11.79	12.31	12.85
M10	9.68	10.23	10.77	11.30	11.84	12.37	12.90
M11	9.78	10.33	10.86	11.39	11.92	12.45	12.98

**Table 5.8: Voltages at the DC-DC converter inputs with different settings on the power supplies. M0 is the module at the far end of the stave, whereas M11 is the module closest to the End of Stave card.**

The voltage on the power supplies was varied in the range 10.5 to 13.5 V, with 0.5 V steps. One three point gain scan was run at each setting, both increasing and decreasing the voltage. Due to the high voltage drop for the long bus tape, the results presented here are referenced to the voltage at the input of the DC-DC converters instead of the power supply setting.

Figure 5.53 shows the results for increasing hybrid voltage. Each plot contains the four lines of the modules included in each power section.

Figure 5.54 shows the decreasing voltage results. The results are compatible with the ones obtained with the DC-DC powered stavelet, which showed a noise increase

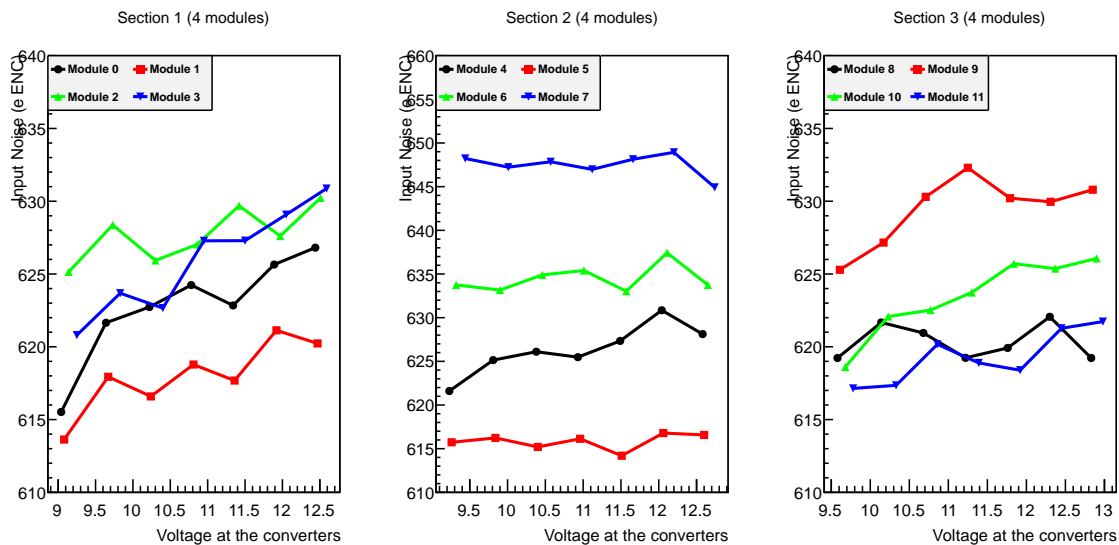


Figure 5.53: Evolution of the input noise for each module of the DC-DC stave with changing input voltage at the converters, from lower to higher.

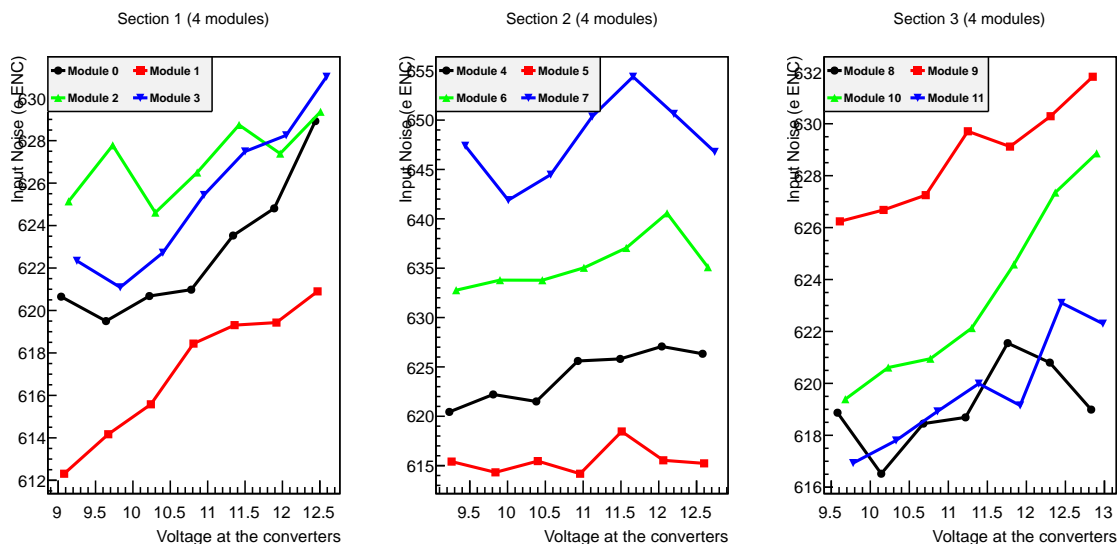
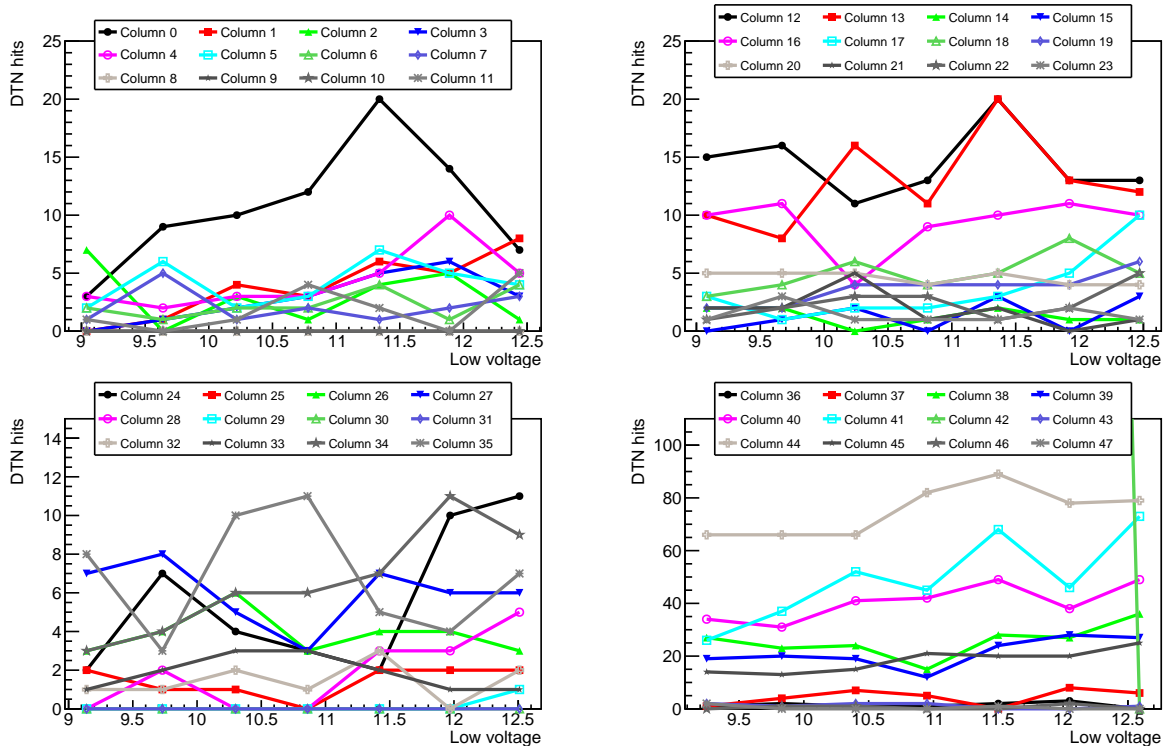


Figure 5.54: Evolution of the input noise for each module of the DC-DC stave with changing input voltage at the converters, from higher to lower.

when the voltage at the converters was set far away from the 10 V “sweet spot” of the current version of the converters.

Some of the modules do not show a clear noise increase, while others do. This does not seem to be related to the sensor strip isolation type, as most of the modules are of the same type and the results for them are mixed.



**Figure 5.55: Evolution of the double trigger noise with 0.5 fC threshold for each column of the DC-DC stave with changing input voltage at the converters, from lower to higher.**

Double Trigger Noise tests were also performed while changing the low voltage values. Figure 5.55 shows the results for every column with increasing low voltage, with a charge threshold of 0.5 fC, in order to have some hits that would allow seeing any trend. All columns show no evidence of noise dependence with the low voltage setting of the power supplies.

As was done with the ENC plots, the horizontal axis represents the voltages at the input of the converters for each module, instead of the setting at the power supplies.

The zoom on the bottom right plot hides column 42 for the most part. This is due to very high noise counts at the beginning of the run, caused by some noisy channels that were eventually masked later in the run.

The Double Trigger Noise results are plotted for each column, in groups of 12 columns (3 modules) per subplot.

Figure 5.56 shows the plots with decreasing low voltage, and we arrive to the same conclusion with respect to the noise dependence. In these plots, which correspond to the same run as the previous, the noisy channels of column 42 were still masked, so the hits values are more realistic.

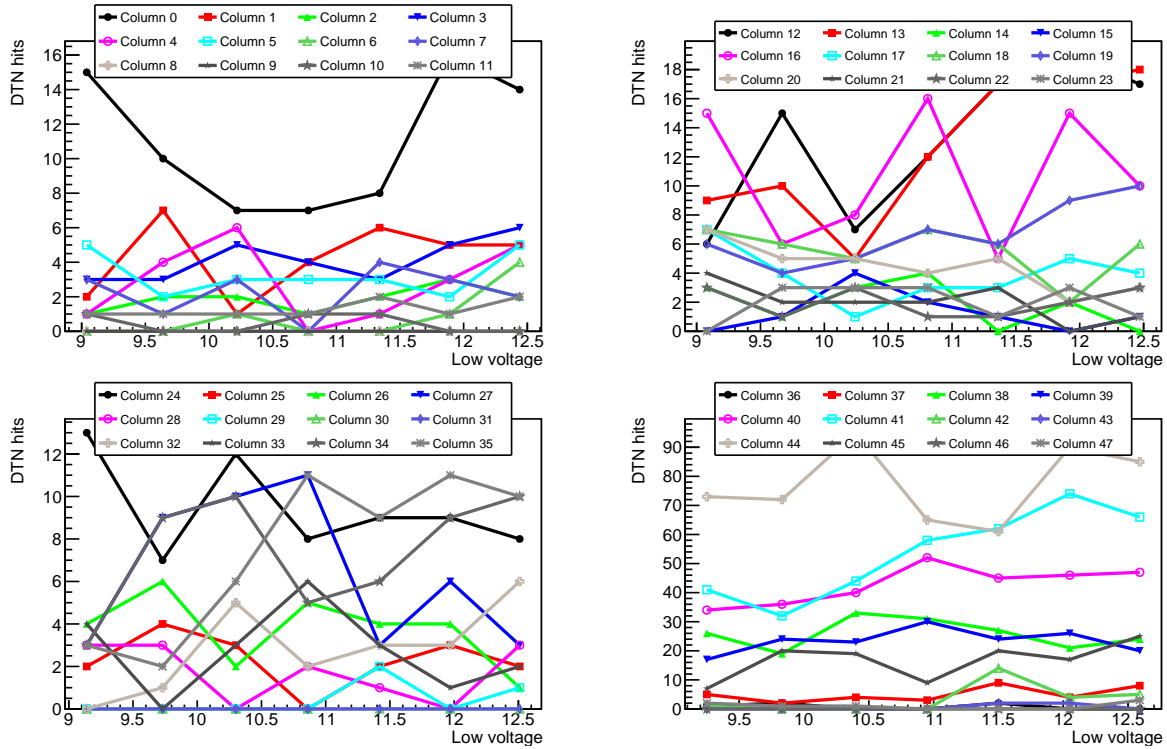


Figure 5.56: Evolution of the double trigger noise with 0.5 fC threshold for each column of the DC-DC stave with changing input voltage at the converters, from higher to lower.

## 5.6 Discussion

This chapter has presented the series of tests that have been done with the upgrade modules and stavelets in the context of this thesis.

The devices produced so far are based on the ABCn25 chip and use a Buffer Control Chip (BCC) to multiplex the data coming from the two data links on the hybrids. Powering of the hybrids is done with DC-DC conversion or Serial Powering.

A serially powered module was available for these tests, together with a DC-DC powered stavelet and another stavelet with serial powering, both holding four modules each. The tests were done in a testing facility in Building 180 at CERN.

Performance of the single module was presented in section 5.3, with extensive measurements done varying the ambient and operational conditions. Cooling temperature variation was used to extract the noise variation with temperature, which was found to be around  $1.5 e^-ENC/K$ .

Noise evolution with the sensor bias was also analysed in detail, with measurements at multiple bias voltages and in both the increasing voltage direction and the decreasing voltage direction.

Last, low temperature tests were done with a dedicated chiller that is capable of operating below  $-30^\circ\text{C}$ . The minimum temperature setting used for these tests was  $-20^\circ\text{C}$  and the electronics worked correctly, with a hybrid temperature of  $2.5^\circ\text{C}$  and ambient temperature around the module of  $8.5^\circ\text{C}$ .

In addition, the two stavelets have been tested intensively. Sensor bias scans, varying the hybrid powering input parameters (voltage or current), using high voltage



multiplexing and trying to interfere using an electromagnetic aggressor. The results on the electromagnetic interference tests, presented in this chapter were done using a prototype of the optical link that will be used to read-out the staves.

The high voltage scan tests show the expected decreasing noise results when the sensor bias voltage is increased, as the sensors become depleted and plateau after over-depletion.

In addition, using a four-way multiplexer designed and built at LBNL to bias the stavelets instead of individual high voltage lines resulted in no difference on the noise measurements of both stavelets. The motivation for the use of multiplexing in the high voltage lines is the reduction of cables to bias the sensors, lowering the material budget by a factor of 13. The results shown in this chapter prove that there is no noise increase with any of the two powering schemes.

The hybrid powering variation shows some performance loss in two of the modules for the DC-DC conversion case. On the serially powered stavelet, there is a noise increase in line with the temperature increase that appears when the input current is higher.

An optical link prototype, which has been proposed to be used in the End of Stave card to read-out the staves, was used as the electromagnetic aggressor on the DC-DC stavelet. There was no evidence of electromagnetic interference that could result in a performance decrease of the stavelet or the whole DAQ system.

The two stavelets were tested both separately and together on the same DAQ setup. The results presented in this chapter show that there is no performance loss resulting from the simultaneous operation. The extra noise observed on the serially powered stavelet is consistent with the temperature increase and the DC-DC stavelet shows no increase in noise. The Double Trigger Noise test does not show any additional noise pick-up on any of the two stavelets.

The stavelet concept has been escalated to a full-sized object, the stave. One such object has been constructed at the time of writing this chapter, a one-sided, DC-DC powered stave with twelve modules. The results of the initial tests of this stave have been presented. The noise performance of the single-sided stave is good and a serially powered stave, in chain of modules configuration, is in construction. The performance differences between the two will drive the decision of building a double-sided object.



# Chapter 6

## Measurement of the Energy Loss and Particle Identification in the ATLAS SCT

### 6.1 Introduction

The Pixel detector and the Semi-Conductor Tracker (SCT), the innermost parts of the ATLAS Inner Tracker, were briefly introduced in chapter 1. They are both based on silicon detectors and are designed for precise charged particle tracking, vertex separation, and precise momentum resolution [2].

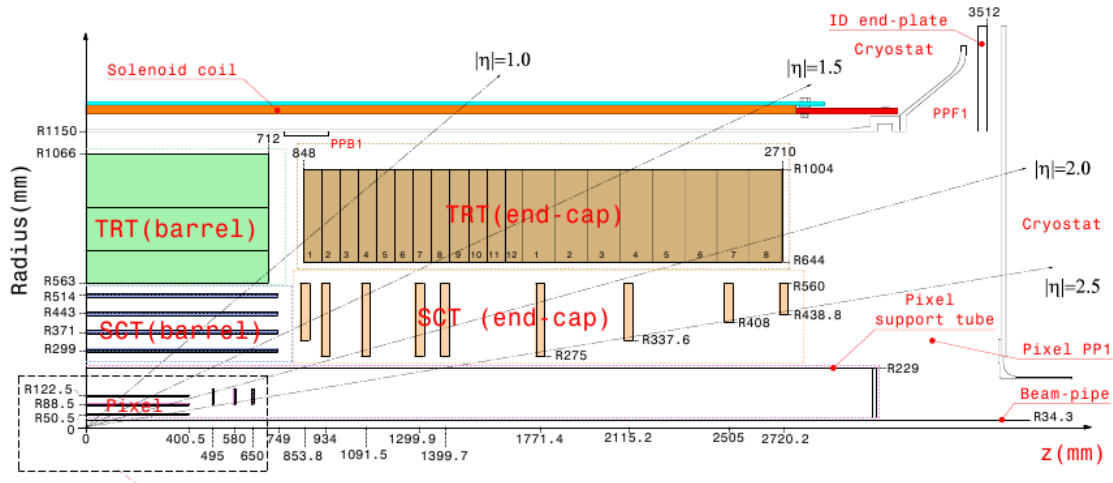


Figure 6.1:  $Rz$  section of ATLAS showing a quarter of the Inner Detector.

However, the SCT and Pixel sub-detectors were not designed to do energy measurements. A way to overcome this limitation is the Time-over-Threshold (ToT) method. It consists in counting the number of cycles of the 40 MHz clock that the charge signal is above the configured threshold. These cycles, 25 ns long, are named time-bins.

The charge collected in each pixel or strip is approximated by counting these time-bins with an 8-bit dynamic range in case of the Pixel detector. In the SCT, a 3-bit dynamic range, together with information about the number of hit strips is stored.

In the Pixel modules, sixteen front-end (FE) electronics chips are connected to each of the sensors through bump bonding. Each of the FE-I3 chips contains 2880 pixel cells of  $50 \times 400 \mu\text{m}^2$  size, in an  $18 \times 160$  matrix [108].

Each cell of the FE-I3 chip has an analogue block, with an amplifier followed by a comparator that has a programmable threshold. The digital read-out transfers the hit pixel address together with the leading edge and the trailing edge timestamps to the buffers of the chip. In these buffers, the Time-over-Threshold is calculated, by subtracting the trailing from the leading edge stamps.

Eight bits are used for the ToT calculation, which allows for a charge measurement of up to 255 ToT counts. A typical Minimum Ionizing Particle (MIP) crossing the sensor at normal incidence will give a ToT count of 30 [109].

The SCT modules have two sides with six ABCD3TA chips each that read-out the sensors strips. There is also a comparator with a programmable threshold which is currently set to  $1 \text{ fC} \approx 6242 e^-$ , for high efficiency and low noise.

For every trigger, the SCT read-out extracts three time intervals from the chip pipeline. The three intervals sequence is checked against a pattern that is determined by the configuration of the SCT read-out.

The data taken in 2010 used a “hit” pattern, which matches hits in any of the three time-bins. Data taken in 2011 and 2012 used a “level” pattern, which matches a hit in the central position. These two patterns are also known as the read-out modes XXX and X1X. In the XXX mode, only a single or consecutive ones are allowed, that is, patterns “000” and “101” are forbidden.

The specific cluster energy loss  $dE/dx$  ( $\text{MeVg}^{-1}\text{cm}^{-2}$ ) is linearly correlated to the cluster charge.  $dE/dx$  can be calculated with the ToT method, counting the number of time intervals which the signal was above the threshold, for every strip in a cluster.

The Pixel  $dE/dx$  calculation exploits the 8 bits resolution of its ToT counter and uses a lower threshold ( $3.5 ke^-$ ) than the SCT. The time-bin information on the SCT uses only 3 bits, what makes the Pixel calculation more precise [109].

The datasets used for this analysis consist of SCT Ntuples, where the Pixel track  $dE/dx$  is provided. With the data contained in these Ntuples, it is possible to reconstruct the SCT track  $dE/dx$  from ToT and number of strips, and compare it with the Pixel value.

The following sections present the study performed on SCT calculations of energy loss,  $dE/dx$ . First, the datasets corresponding to the 2010-2012 running periods are listed. Then, details of how the Time-over-Threshold method is used to calculate the ionization energy  $dE/dx$  are described, with path correction, normalization and comparison with the results from the Pixel.

Next, efficiency and mistag rates of the particle identification process are presented. An application of the  $dE/dx$  calculation in tracking radiation damage is discussed in section 6.5.

Part of the work discussed in this chapter has been included as part of an overview of the SCT performance during the first run of the LHC in [35].

## 6.2 Event and Track Selection

The study used proton-proton collision data taken during 2010 and 2011 with 7 TeV centre-of-mass energy and during 2012 with 8 TeV centre-of-mass energy.

The selected SCT tracks were classified according to the location of the hits. Barrel tracks are those in which all hits associated with the track are located only in the barrel layers, no hits in endcap modules. Endcap tracks are those tracks that had some hits in the endcaps.

Apart from the hits locations, tracks can be classified according to the origin of the particles:

- Primary Vertex (PV): coming from the hard interaction, the tracks have a small transversal distance to the point of closest approach,  $d_0$  (less than 2 mm).

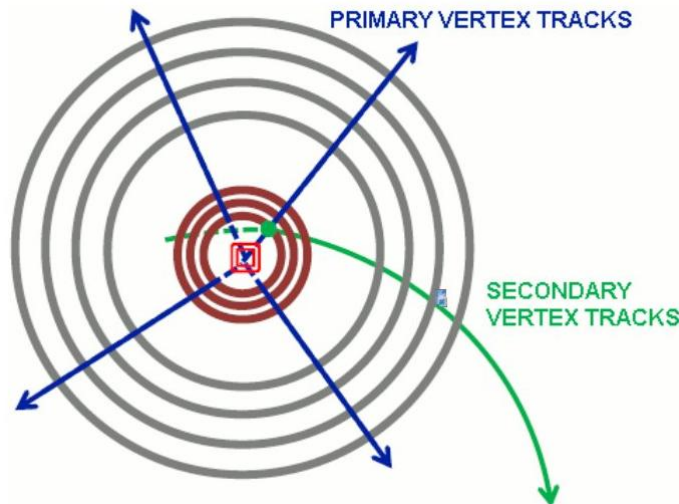


**Figure 6.2: Primary and secondary vertex tracks.**

- Secondary Vertex (SV): apart from the primary vertex, and with the exception of gas processes (interactions with residual gas molecules), no more interactions are expected before the first material layer, which is the beam pipe wall. These processes are rich in protons and deuterons, because they are taking place in material. They have a larger transversal distance,  $d_0 > 2$  mm.

See Figure 6.2 for a schematic description of both primary and secondary vertices.

- Gas interactions: downstream, inside the beam pipe.
- Noise.

The analysis is focused on tracks originating in primary and secondary vertices. Both primary vertex and secondary vertex tracks require a longitudinal impact parameter cut of  $|z_0| < 100$  mm, to be inside the beam spot and to avoid gas interactions.

The datasets come from SCT Ntuples and for each dataset only events with the SCT in “Ready” state are analysed. For every event, a first selection cut requires that they meet the following requirements:

- There has to be at least one primary vertex reconstructed in the event.
- The primary vertex must have at least 4 tracks associated to it.
- At least one of the tracks in the event must have:

- Transverse momentum  $p_T > 500$  MeV/ $c$ .
- At least 6 SCT hits.
- At least 1 Pixel hit.
- Transverse impact parameter  $|d_0| < 1.5$  mm. At least one of the tracks has to be inside the beam spot.
- The longitudinal impact parameter and the polar angle have to be such that  $|z_0 \sin \theta| < 1.5$  mm. This requisite complements the previous one, in the  $Rz$  plane.  
Tracks with low  $d_0$  but large  $z_0$  that have a large polar angle are rejected with this restriction. See Figure 2.3 for the representation of the parameters.

When these conditions are fulfilled, we can say the event originates in a proton-proton interaction.

Then, for each event, tracks selected for  $dE/dx$  calculation have to meet the following requirements:

- At least 8 good SCT hits on track, in order to have a well measured track.
- Transverse momentum has to be at least  $p_T > 100$  MeV/ $c$ . The transverse momentum resolution is better with increasing momentum, but we do not want to miss low momentum tracks.
- The momentum of the track has to be lower than 2500 MeV/ $c$ . The energy loss was calculated up to this momentum, but there is not enough resolution to perform particle identification after  $\approx 800$  MeV/ $c$ .

There is no lower momentum cut as the reconstruction already applies one, 100 MeV/ $c$  for 2010 and 400 MeV/ $c$  for 2011 and 2012 data.

- Longitudinal impact parameter  $|z_0| < 100$  mm. These constrains on the impact parameters select tracks in the interaction region and also not originating in gas interactions.
- For Pixel “true” particles, at least two good Pixel hits.

The goal of these cuts is to study only tracks that are well measured, with enough hits in the SCT and the Pixel detector. In addition, the tracks are originated in the beam spot, and both primary and secondary vertex tracks are analysed.

The total recorded luminosity of the dataset is  $1.76 \text{ fb}^{-1}$ . The number of recorded events is around 11 million, summing the minimum bias and the express streams that were used in each of the periods. The minimum bias streams were generated for the SCT Ntuples before April 2011. After that date, only express streams were available for the SCT. The express stream is normally used for calibration and data quality, whereas minimum bias streams are used for physics. The analysis performed in this thesis does not require information from the minimum bias streams.

The read-out modes have been explained above: 2010 data were taken in XXX mode, whereas 2011 and 2012 data were taken in XIX mode. The first records hits in any time interval combination of the three selected for a trigger, while the second requires that there is one hit in the central time-bin.

Run number	Date	Stream type	Read-out mode	Luminosity
152345	3/4/2010	Minimum bias	XXX	0.01871 nb <sup>-1</sup>
156682	5/6/2010	Minimum bias	XXX	1.407 nb <sup>-1</sup>
159224	18/7/2010	Minimum bias	XXX	69.16 nb <sup>-1</sup>
165591	22/9/2010	Minimum bias	XXX	168.9 nb <sup>-1</sup>
167661	25/10/2010	Minimum bias	XXX	1464 nb <sup>-1</sup>
179710	14/4/2011	Express	X1X	6792 nb <sup>-1</sup>
183407	12/6/2011	Express	X1X	$4.262 \times 10^4$ nb <sup>-1</sup>
183462	14/6/2011	Express	X1X	$4.693 \times 10^4$ nb <sup>-1</sup>
186673	2/8/2011	Express	X1X	$3.726 \times 10^4$ nb <sup>-1</sup>
186729	3/8/2011	Express	X1X	$9.078 \times 10^4$ nb <sup>-1</sup>
190236	1/10/2011	Express	X1X	$1.037 \times 10^5$ nb <sup>-1</sup>
191933	30/10/2011	Express	X1X	197.7 nb <sup>-1</sup>
201190	12/4/2012	Express	X1X	$4.726 \times 10^4$ nb <sup>-1</sup>
204265	3/6/2012	Express	X1X	$2.373 \times 10^5$ nb <sup>-1</sup>
204564	7/6/2012	Express	X1X	$2.014 \times 10^5$ nb <sup>-1</sup>
204763	9/6/2012	Express	X1X	$1.999 \times 10^5$ nb <sup>-1</sup>
205016	15/6/2012	Express	X1X	$1.041 \times 10^5$ nb <sup>-1</sup>
205017	15/6/2012	Express	X1X	$7.403 \times 10^4$ nb <sup>-1</sup>
205071	16/6/2012	Express	X1X	$2.357 \times 10^5$ nb <sup>-1</sup>
209736	3/9/2012	Express	X1X	$1.331 \times 10^5$ nb <sup>-1</sup>
214086	6/11/2012	Express	X1X	$1.98 \times 10^5$ nb <sup>-1</sup>

**Table 6.1: Datasets used in the  $dE/dx$  study.**

The data sets were selected in order to have a good representation of the whole running period, with some spacing in time. The SCT Ntuples were not available for all the recorded runs, although there were enough to cover most of the first LHC run period.

### 6.3 $dE/dx$ Reconstruction

A particle passing through matter interacts with electrons and nuclei [7]. For charged particles which are not highly relativistic, thus applicable in this study case, the main electromagnetic contribution to the energy loss is ionization.

The mean energy loss  $dE/dx$  due to ionization, as a function of  $\beta$ , is given by the Bethe-Bloch formula [20]:

$$-dE/dx = 2\pi N_a r_e^2 m_e c^2 \rho D \frac{Z}{A} \left[ \log \left( \frac{2m_e \gamma^2 v^2 W_{\max}}{I^2} \right) - 2\beta^2 - \delta - 2\frac{C}{Z} \right] \quad (6.1)$$

The units are MeV cm<sup>2</sup> g<sup>-1</sup> and some of the variables definitions are:

- $\beta$  is the projectile velocity in units of  $c$ .
- $D$  is a material constant.

- $Z$  is the atomic number of the medium and  $A$  is its atomic mass [ $\text{g mol}^{-1}$ ].
- $\rho$  is the mass density of the medium [ $\text{g cm}^{-3}$ ].
- $\delta$ ,  $C$  and  $\nu$  are the density, shell and higher order corrections.
- $I$  is the mean excitation energy [ $\text{eV}$ ].
- $W_{\text{max}}$  is the maximum energy transfer in a single collision.

Measurements of energy loss can be used to identify particles if a simultaneous measurement of momentum is available. In this analysis the goal is to identify protons, kaons and pions.

Pixel provides their  $dE/dx$  measurements using the Time-over-Threshold method with 8 bits precision. These  $dE/dx$  values calculated with the Pixel ToT information, available in the SCT Ntuples, are used to compare with the ToT approximations for the SCT.

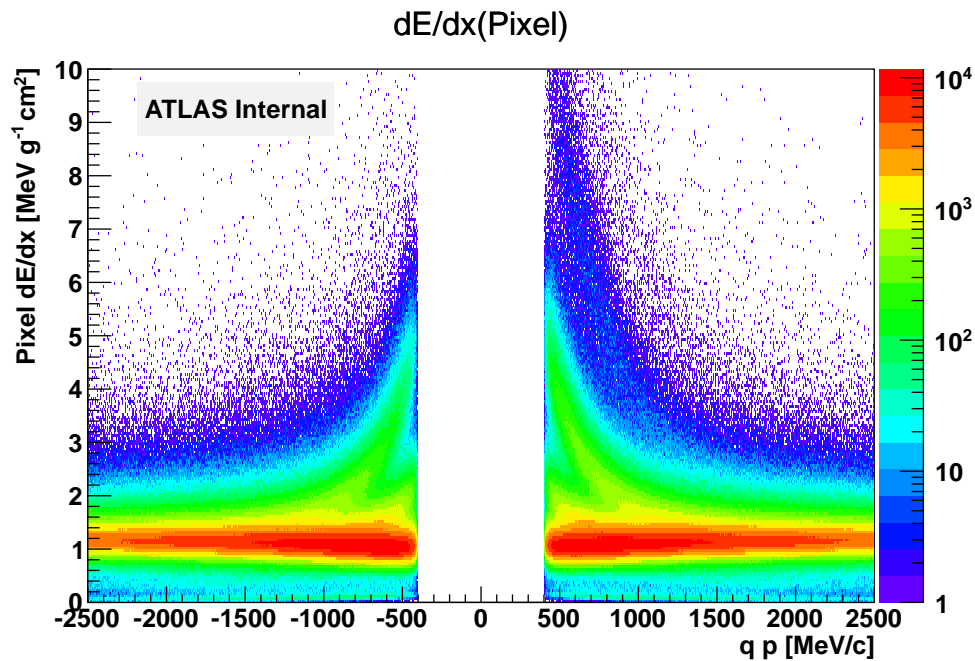


**Figure 6.3: Pixel  $dE/dx$  extracted for data taken in 2011. At low momenta, the proton bands are visible for both positive and negative tracks.**

Figure 6.3 shows the  $dE/dx$  calculated by the Pixel in one of the runs in 2011. Particle bands are visible, these are the less resolution Bethe-Bloch curves. The representation of  $dE/dx$  with  $qp$  is useful to identify the different particles, by looking at the different ionization energy of the observed bands.

In this figure, the proton, kaon and pion bands are quite visible. The lowest  $dE/dx$  band both for positive and negative tracks corresponds to pions, when one looks at the lower momentum region. The next two bands at low momentum are kaons and protons, respectively. There is a positive deuteron band that comes from nuclear interactions, while the negative deuteron originates in fragmentation, therefore the negative one is



unstable and less represented. Protons and deuterons are more visible in secondary vertex tracks, because they originate in interactions in the material (beam pipe wall).

The plot shows that for momentum greater than 800 MeV/ $c$ , all bands converge to the same  $dE/dx$  band, making the separation very difficult.

### 6.3.1 SCT Data Acquisition, Hits and Timing

Each of the 4088 SCT modules are read-out at a rate of 40 MHz. First, the analogue signal is compared to a 1 fC threshold at each time interval and for every channel. If the signal is above (below) threshold, a one (zero) is stored in the pipeline.

The pipeline is a 132 deep binary FIFO for each of the 128 channels. This is represented in Figure 6.4 [110].

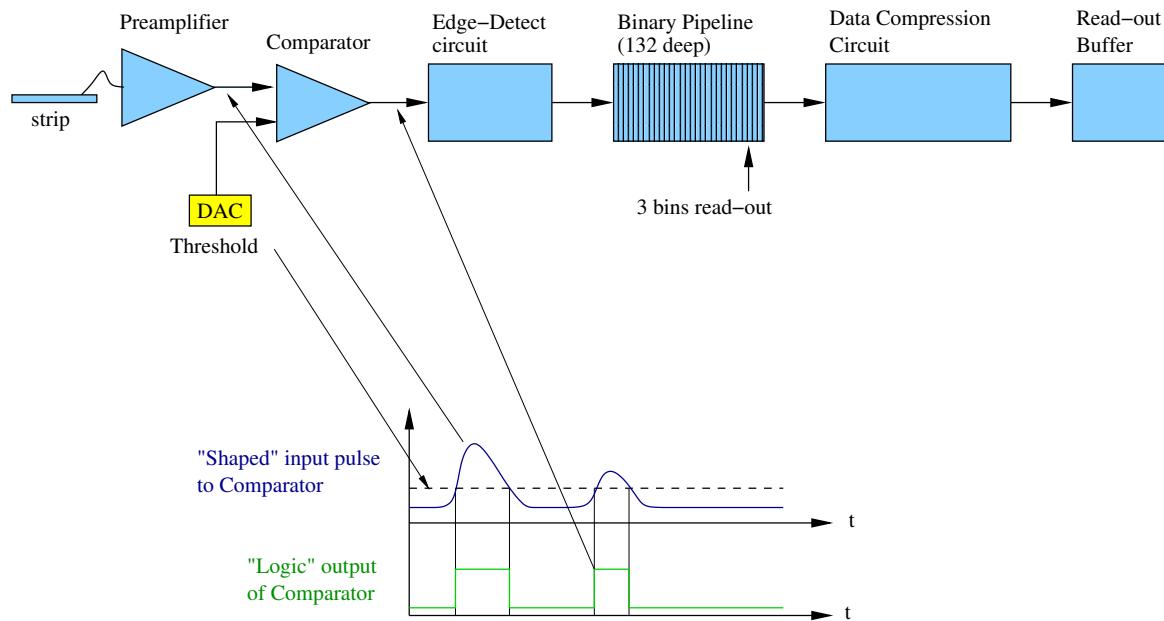


Figure 6.4: Functionality of the ABCD3TA chip.

The arrival of the Level 1 trigger from the ATLAS trigger system drives the sampling of three pipeline bins. The SCT timing is optimized to ensure that the trigger is centred at the second bin, resulting in a 01x occupancy pattern in the three bins.

The ABCD3TA chip can be configured depending on the running conditions, for optimal efficiency:

- XXX mode for cosmic rays and 75 ns bunch spacing. This was the case for the 2010 runs.
- X1X mode is used for 50 ns bunch spacing, in the 2011 and 2012 runs.
- 01X mode is designed to be used in runs with 25 ns bunch spacing. This mode will be the default for operation after 2015.

“Timing-in” the SCT involves setting delays in order to meet these requirements:

- The Level 1 trigger arrives at the module when the three bins are at the end of the pipeline.

- The clock transmitted to the front-end electronics has the correct phase relative to the passing of the particles originating in the collisions.
- The Level 1 trigger is received in the right 25 ns time-bin and the data from the ATLAS sub-systems are merged into the right events.

There are two timing adjustments available, a coarse one with 25 ns step size and a fine one with 280 ps steps [38].

### 6.3.2 SCT $dE/dx$ Calculation with the Time-over-Threshold Method

As shown in Figure 6.5, when the pulse signal is larger, it results in more time-bins above threshold, that is the definition of Time-over-Threshold. As a first approximation, weights  $w^i$  are associated to the number of time-bins for each channel and summed over all strips hit with charge, for all SCT hits associated with a track.

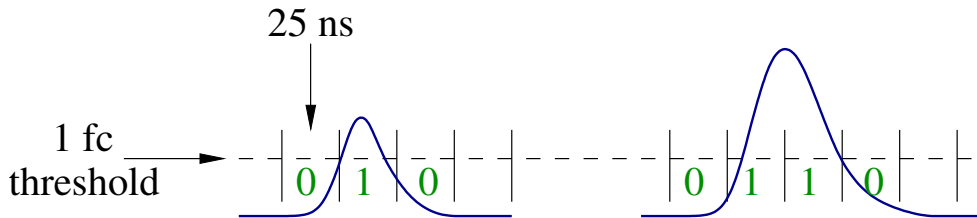


Figure 6.5: Time-over-Threshold for two different pulse sizes.

The obvious choice for assigning weights to the SCT time-bins in XXX read-out mode is the following:

- Time-bins 101 (illegal time-bin) and 000:  $w^i = 0$ .
- Time-bins 001, 010 and 100:  $w^i = 1$ .
- Time-bins 011, 110:  $w^i = 2$ .
- Time-bin 111:  $w^i = 3$ .

Then, the SCT energy loss,  $dE/dx_{\text{SCT}}$ , can be approximated as the sum of weights of all the strips hits on track:

$$dE/dx_{\text{SCT}} = \sum_{\text{Track.hits}} \sum_{\text{Hit.strips}} w_{\text{strip}}^i$$

This is correct for tracks that pass perpendicular to the module, which is typically not the case. Therefore, a path correction that takes into account the incident angle of the particles is needed:

$$dE/dx_{\text{SCT}} = \sum_{\text{Track.hits}} \sum_{\text{Hit.strips}} w_{\text{strip}}^i \cos \alpha$$

The angle  $\alpha$  is the incident angle on the module. The information available in the SCT Ntuple are two local angles, one along the strips and another across the strips,  $\theta_0^{\text{local}}$  and  $\phi_0^{\text{local}}$ .

Redefining the two local angles between  $-\pi/2$  and  $\pi/2$ , leads to the local angles  $\theta'$  and  $\phi'$ :

$$\theta' = \begin{cases} \theta_0^{\text{local}} - \pi & \text{if } \theta_0^{\text{local}} > \pi/2 \\ \theta_0^{\text{local}} + \pi & \text{if } \theta_0^{\text{local}} < \pi/2 \end{cases} \quad (6.2)$$

$$\phi' = \begin{cases} \phi_0^{\text{local}} - \pi & \text{if } \phi_0^{\text{local}} > \pi/2 \\ \phi_0^{\text{local}} + \pi & \text{if } \phi_0^{\text{local}} < \pi/2 \end{cases} \quad (6.3)$$

Then, the angle of the particle trajectory with the silicon surface can be defined as

$$\alpha = \tan^{-1} \left( \sqrt{\tan^2 \theta' + \tan^2 \phi'} \right) \quad (6.4)$$

Finally, the previous  $dE/dx$  formula has to be normalized with respect to the number of hits on the track, leading to the final  $dE/dx$  formula for the SCT (note it is measured in arbitrary units):

$$dE/dx_{\text{SCT}} = \frac{\sum_{\text{Track\_hits}} \sum_{\text{Hit\_strips}} w_{\text{strip}}^i \cos \alpha}{\text{Track\_hits}} \quad [\text{a.u.}] \quad (6.5)$$

With this calculation of the energy loss in the SCT, it is possible to identify the bands corresponding to different particle species.

Figure 6.6 shows the  $dE/dx$  distribution for the SCT in the whole 2010 dataset. The barrel plot shows the calculated  $dE/dx$  for tracks that do not leave hits in the endcap, while the endcaps plots correspond to tracks that have hits in one of the endcaps.

The band separation for tracks that only hit the barrel is more evident than in the tracks that hit the endcaps. Tracks with low total momentum normally do not leave hits in the endcap.

As a result, the endcap  $dE/dx$  data appears at higher momentum than the barrel  $dE/dx$ , around 150 MeV/c for the barrel and around 250 MeV/c for each of the two endcaps. This is primarily caused by the cut on the transverse momentum and the minimum number of hits in the SCT, what makes the minimum momentum shown in the plots greater than for the barrel tracks.

No primary/secondary vertex separation is done for these plots. Note that the Y axis is different for the plot showing all regions and the rest.

## 6.4 Particle Identification

The goal of this part of the study is to evaluate if there is any particle discriminating power in the  $dE/dx$  calculated with the SCT time-bin information.

The Monte Carlo simulations of SCT Ntuples do not include the realistic time-bin information. As a result, it is not possible to use truth information from Monte Carlo simulations to evaluate the performance of the particle identification using the  $dE/dx$  calculated in the SCT to identify protons, kaons and pions.

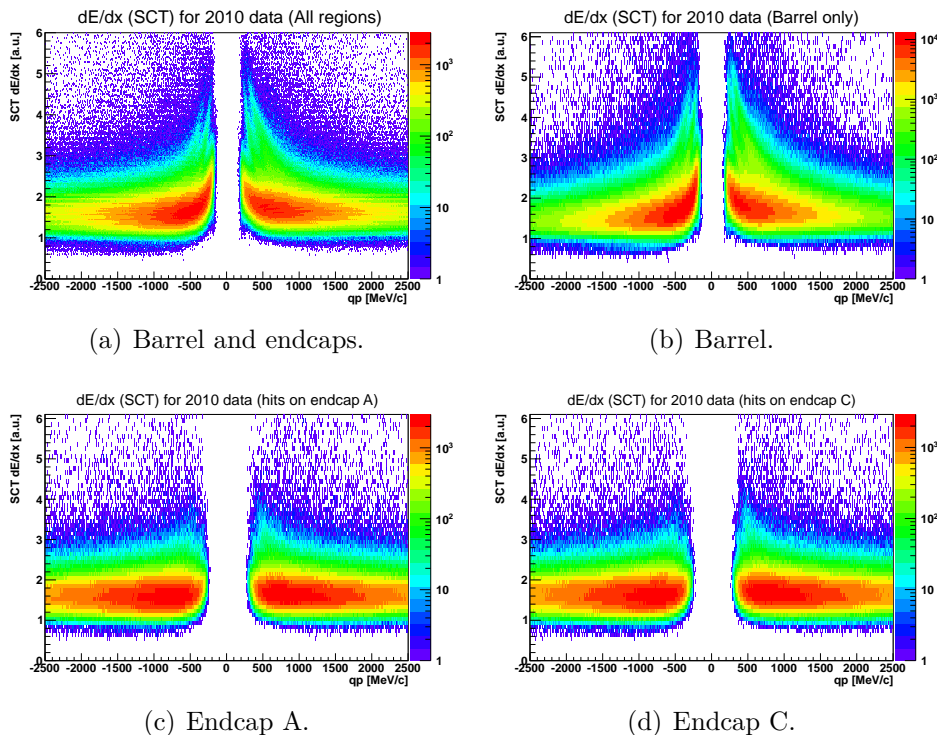


**Figure 6.6:**  $dE/dx$  distributions vs  $pq$  in 2010.

After April 12<sup>th</sup>, 2011 (run 179579, SCT Ntuple tag f359), the SCT Ntuples contain a vector of Pixel likelihoods for pions, kaons and protons. Therefore, with 2011 runs after that date it is possible to perform efficiency-mistag rate studies, which are shown in the next section.

The unavailability of the PID information for the Pixel in 2010 data forced the use of a different approach. A geometrical cut is used on the Pixel  $dE/dx$  to try separate the protons.

This geometrical cut is applied with the following formulas on the  $dE/dx$  calculated by the Pixel detector:

$$\left. \begin{aligned} p[\text{GeV}/c] &\geq 0.3 \\ dE/dx_{\text{Pixel}} &\geq 1.8 \\ 1.5dE/dx_{\text{Pixel}} &\leq -6.6(p[\text{GeV}/c] - 1.5) \\ 0.9dE/dx_{\text{Pixel}} &\geq -6.5(p[\text{GeV}/c] - 0.9) \end{aligned} \right\} \Rightarrow \text{Tag as proton} \quad (6.6)$$

or

$$\left. \begin{aligned} 0.3 &\leq p[\text{GeV}/c] \leq 0.55 \\ 4.0 &\leq dE/dx_{\text{Pixel}} \leq 8.0 \end{aligned} \right\} \Rightarrow \text{Tag as proton} \quad (6.7)$$

Particle identification and resolution of the  $dE/dx$  reconstruction with SCT data taken during 2010 are detailed in [111].

The study to find the geometrical cut for the Pixel  $dE/dx$  is not part of this thesis work, but it is presented here because it was used in some of the studies relevant to this thesis. It is used in the long term stability analysis, presented in section 6.5.

### 6.4.1 Particle Identification with 2011-2012 Data

The lack of Monte Carlo simulated Ntuples with full time-bin information and truth information limits the scope of the analysis. A way to overcome this limitation is the use of the Pixel likelihood. A Particle Identification (PID) study with 2011 and 2012 data from the SCT was done by extracting pure  $i = \pi/K/p$  from the SCT data by using the Pixel  $dE/dx$  likelihood stored in the SCT Ntuple. The likelihoods calculated by the Pixel for each particle type,  $P_{\pi}^{\text{Pixel}}$ ,  $P_K^{\text{Pixel}}$ ,  $P_p^{\text{Pixel}}$ , are first normalized:

$$P_i^{\text{norm,Pixel}} = \frac{P_i^{\text{Pixel}}}{P_{\pi}^{\text{Pixel}} + P_K^{\text{Pixel}} + P_p^{\text{Pixel}}} \quad (6.8)$$

Tracks that have normalized Pixel likelihood  $P_{p/K/\pi}^{\text{norm,Pixel}} > 0.9$  are considered correctly identified, so we call them “true particles”. The SCT  $dE/dx$  is calculated for these tracks to extract the distributions for each particle type in different low momenta regions. Unless specified, there are no cuts on secondary or primary vertices, and barrel or endcap tracks.

Figure 6.7 shows the various distributions of both the Pixel and SCT  $dE/dx$  of each particle species. This plot is generated with data taken during 2011.

Tracks in 2010 were reconstructed only for those with momentum greater than 300 MeV/c, whereas in 2011 and 2012 the minimum track momentum was 400 MeV/c. This means that for the 2011 and 2012 datasets, there is less separation between bands. The band separation can be seen when plotting the  $dE/dx$  for each of the particle species in each momentum slice. The resolution is better if the distributions are more separated.

Distributions of the individual particle species for data recorded in 2011 are shown in Figures 6.9(a) and 6.9(b), for positive and negative tracks respectively. The vertical axis is the fraction of tracks for each momentum range. Only primary vertex tracks have been selected. The fraction of secondary vertex tracks is typically 10% of the total tracks for pions and kaons, and over 20% for protons.

For low momenta and positive protons, nearly 50% of the tracks originate from secondary vertices. Figure 6.8 shows the different distributions of positive tracks for pions, kaons and protons for 2011 data. The plot corresponding to the proton band shows that the secondary vertex tracks represent almost 50% of all the proton tracks. The secondary vertex tracks of pions and kaons are much less abundant than the primary vertex tracks.

A sample of the secondary vertex tracks in 2011 is shown in Figure 6.10(a), for positive tracks, and Figure 6.10(b), for negative tracks. The plots for positive tracks show that the kaon band is mis-identified and also the proton band is slightly more separated for higher momenta tracks.

The same plots using 2012 data are shown in Figures 6.11(a) and 6.11(b) positive and negative tracks respectively. Only the primary vertex tracks are shown.

The plots only show a representative sample of the momenta ranges for both positive and negative tracks, up to 700 MeV/c, in order to illustrate the loss of resolution with increasing momentum. Although the  $dE/dx$  has been calculated for tracks up to

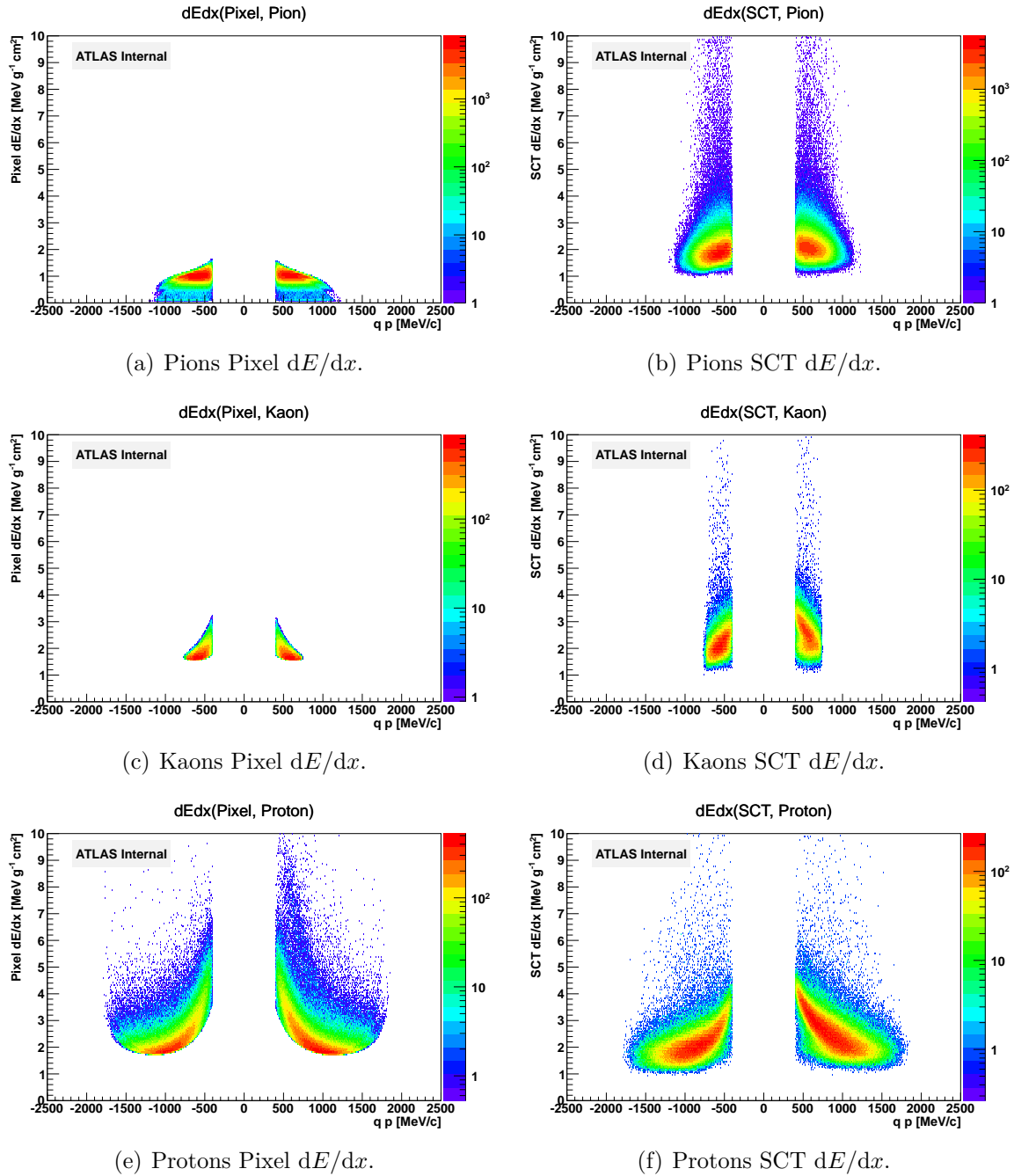
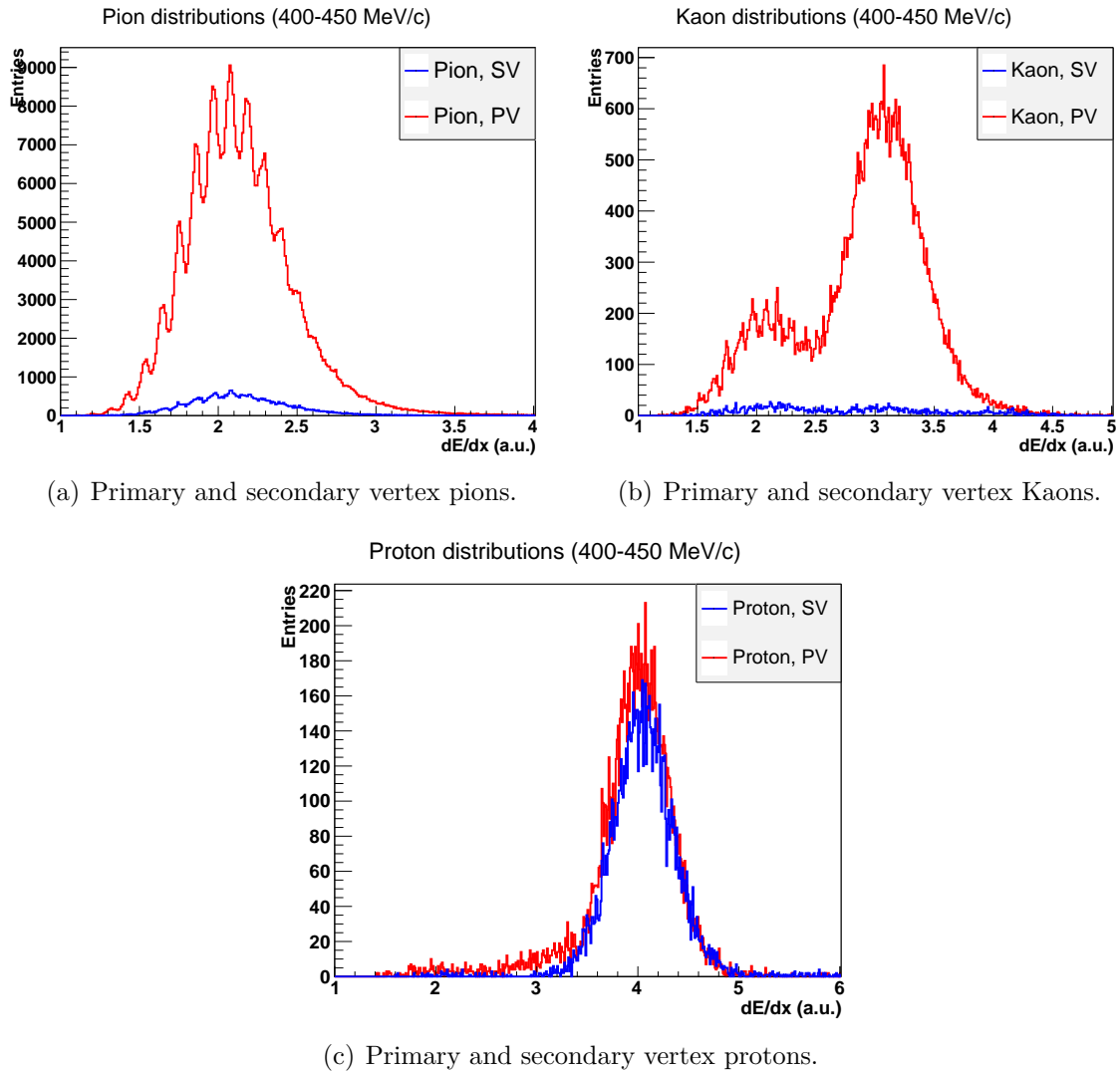


Figure 6.7: Pixel and SCT  $dE/dx$  distributions vs  $pq$  for the different particle species as tagged by the Pixel ( $P_i^{\text{norm,Pixel}} > 0.9$ ). Data taken in 2011.

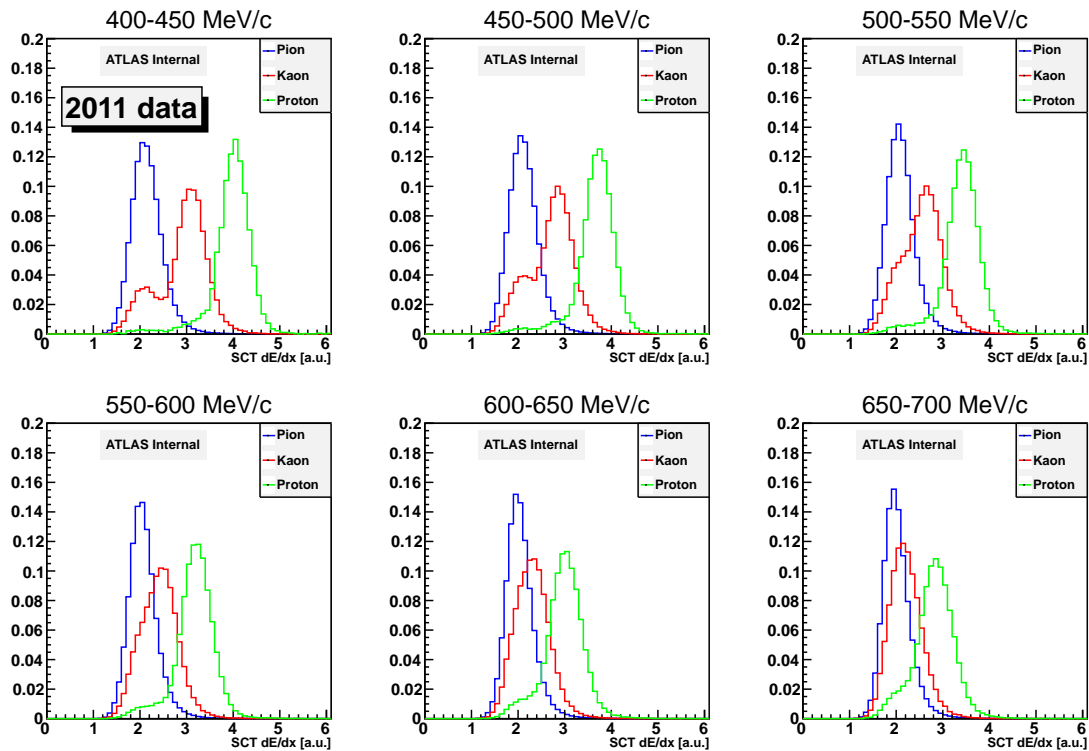
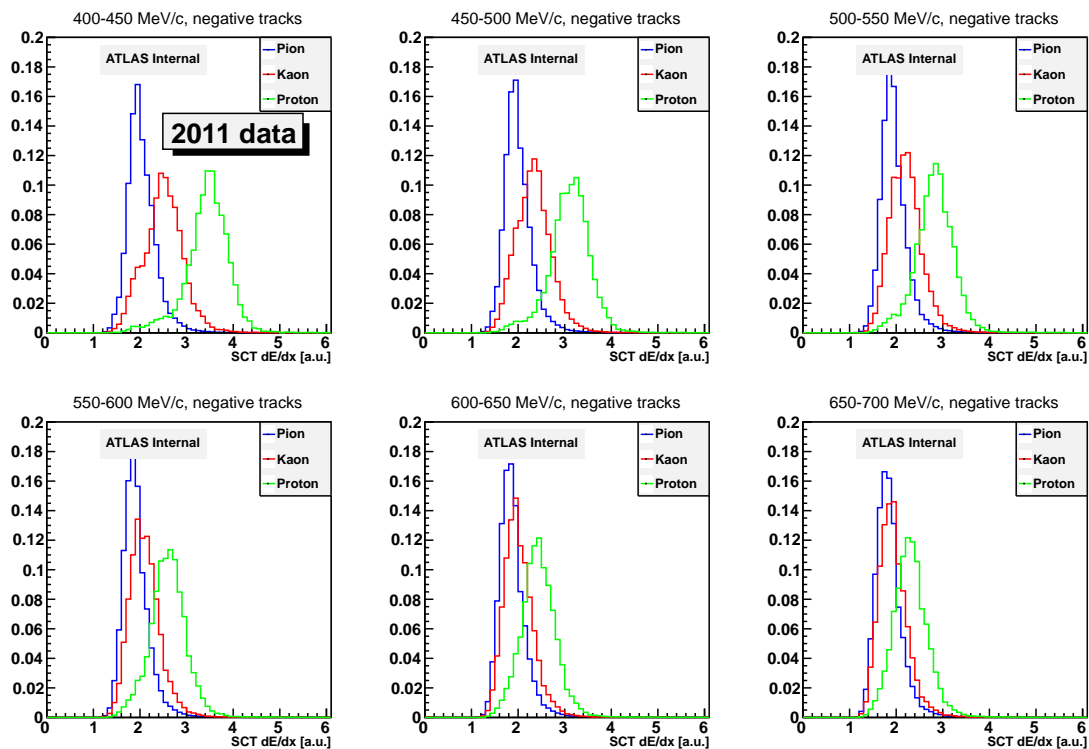


**Figure 6.8:**  $dE/dx$  distributions for positive pions, kaons and protons at low momenta, showing the differences in the rates of appearance for each particle species originating in primary and secondary vertices. The secondary vertex protons represent almost half the total number of protons in the sample for momentum in the (400, 450) MeV range.

2.5 GeV/ $c$ , such high momentum does not allow any particle identification study due to the lack of band separation at high momentum.

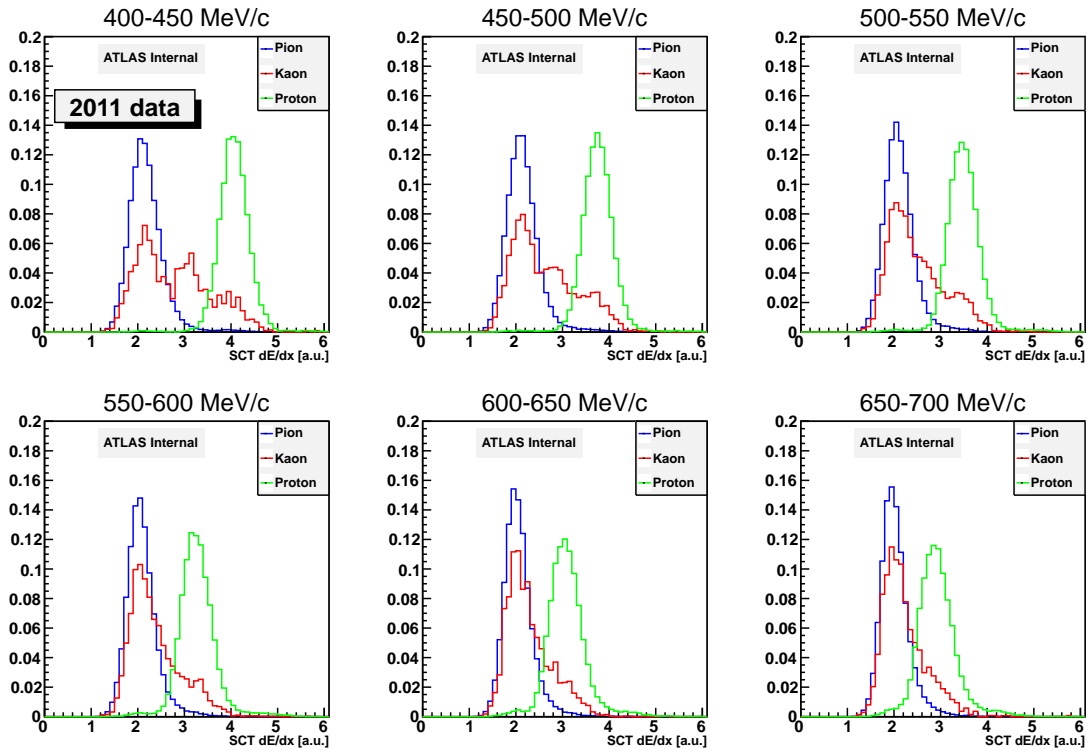
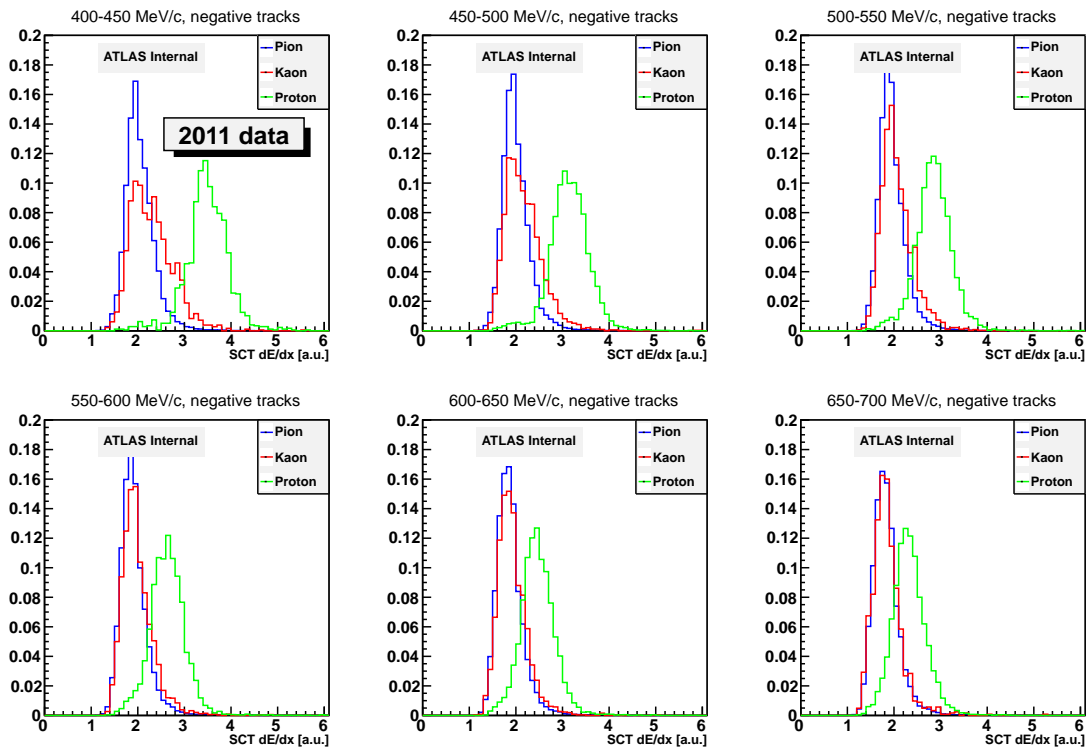
The positive tracks have better resolution for low momentum ( $< 550$  MeV/ $c$ ) in both periods and worse resolution for higher momentum. Negative tracks, on the contrary, show low resolution already at lower momentum, when compared to the positive tracks. The reason for this lower resolution of the negative tracks is the tilt angle of the SCT barrel modules, which is around  $11^\circ$ .

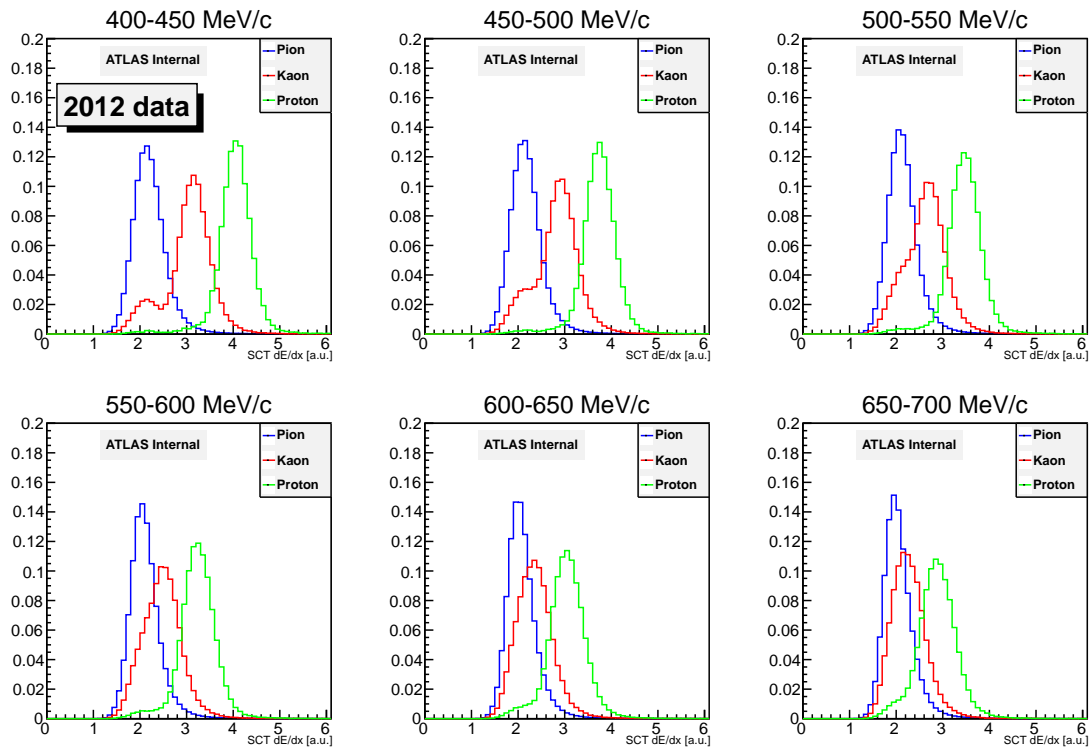
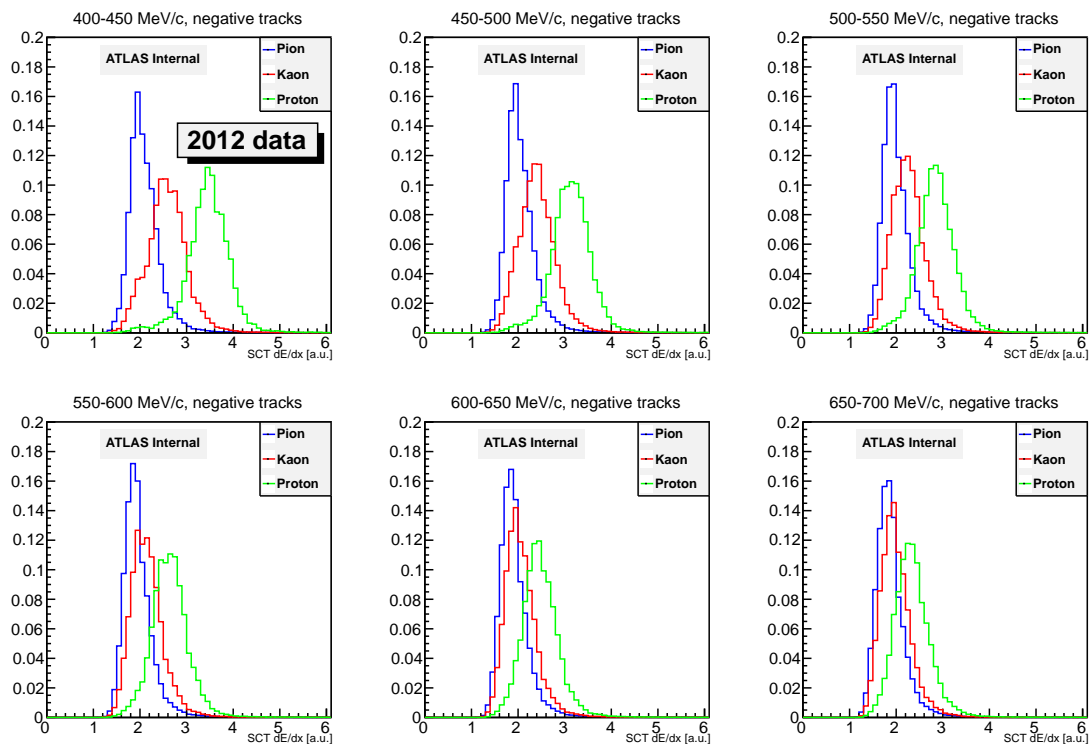
A negative track hits the modules in the barrel at a greater incidence angle than a positive track with the same momentum. The SCT  $dE/dx$  calculation relies on the cluster size, and a negative track will leave smaller clusters for the same momentum as a positive track. Therefore, the calculation of the charge deposited by a negative track will result in lower  $dE/dx$  values than in the case of a positive track.


 (a) SCT  $dE/dx$  distributions for each particle for  $q > 0$  and 2011 data.

 (b) SCT  $dE/dx$  distributions for each particle for  $q < 0$  and 2011 data.

**Figure 6.9: SCT  $dE/dx$  distributions for 2011 data, primary vertex tracks only.**



(a) SCT  $dE/dx$  distributions for each particle for  $q > 0$  and 2011 data.(b) SCT  $dE/dx$  distributions for each particle for  $q < 0$  and 2011 data.Figure 6.10: SCT  $dE/dx$  distributions for 2011 data, secondary vertex tracks only.


 (a) SCT  $dE/dx$  distributions for each particle for  $q > 0$  and 2012 data.

 (b) SCT  $dE/dx$  distributions for each particle for  $q < 0$  and 2012 data.

**Figure 6.11: SCT  $dE/dx$  distributions for 2012 data, primary vertex tracks only.**

Although it is not shown in these plots, there is no kaon band for particle momentum above 750 MeV/ $c$  in positive tracks and 800 MeV/ $c$  in negative tracks. This occurs when the Pixel  $dE/dx$  calculation is such that it is not possible to discriminate between pions and kaons. The Pixel assigns a negative likelihood to them.

## 6.4.2 Efficiency and Mistag Rate

The SCT  $dE/dx$  distributions of the 3 particle species for positive tracks are clearly separated at low momentum. Protons can be identified in the momentum interval (400, 550) MeV/ $c$ . Both data periods have similar distribution of the particles species.

The SCT  $dE/dx$  likelihood,  $P_i^{\text{SCT}}$ , is defined by Gaussian fitting near the first peak each of the SCT  $dE/dx$  particle distribution from Figures 6.9 and 6.11, in each momentum slice. The fit is done after identifying the particle species using the Pixel information. The results are the mean  $(dE/dx)_i$  and  $\sigma_{dE/dx_i}$ , with  $i = \pi/K/p$ :

$$P_i^{\text{SCT}} = \frac{1}{\sqrt{2\pi}\sigma_{dE/dx_i}} \exp\left(-\frac{(dE/dx_{\text{SCT}} - dE/dx_i)^2}{2\sigma_{dE/dx_i}^2}\right) \quad (6.9)$$

The same normalization as in the Pixel likelihood is also applied to the SCT likelihood:

$$P_i^{\text{norm,SCT}} = \frac{P_i^{\text{SCT}}}{P_p^{\text{SCT}} + P_K^{\text{SCT}} + P_\pi^{\text{SCT}}} \quad (6.10)$$

Since the SCT Particle Identification capability is being compared to that of the Pixel, the tagging efficiency is defined as the fraction of tracks that the Pixel and the SCT would tag in the same way. For protons, the tagging efficiency is

$$\varepsilon_p = \frac{N(\text{Pixel} = p, \text{SCT} = p)}{N(\text{Pixel} = p)} \quad (6.11)$$

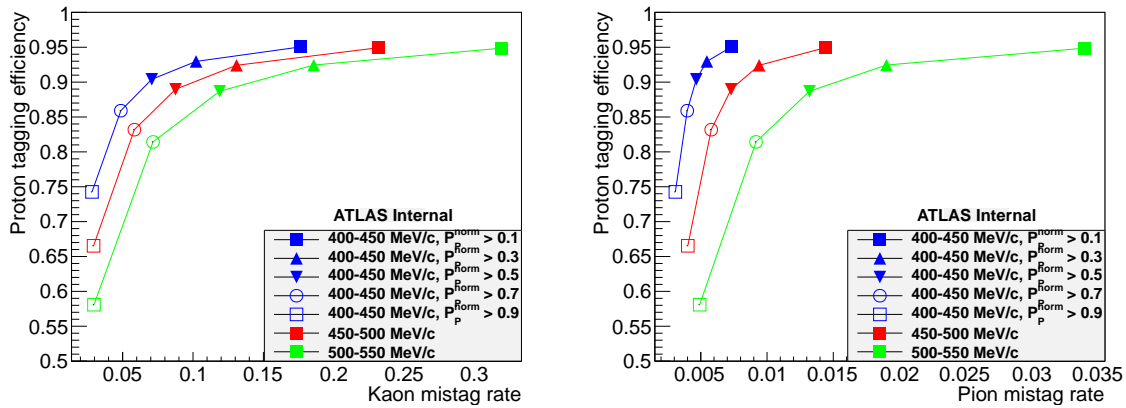
The mistag rate is calculated under the assumption that the Pixel tagging is true for pions and kaons while the SCT would tag as proton:

$$r_p^\pi = \frac{N(\text{Pixel} = \pi, \text{SCT} = p)}{N(\text{Pixel} = \pi)} \quad r_p^K = \frac{N(\text{Pixel} = K, \text{SCT} = p)}{N(\text{Pixel} = K)} \quad (6.12)$$

Where  $N(\text{Pixel} = i)$  is the number of tracks considered as true  $i$  particles by the Pixel ( $P_i^{\text{norm,PIX}} > 0.9$ ) and  $N(\text{Pixel} = i, \text{SCT} = j)$  is the number of tracks considered true  $i$  particles by the Pixel and tagged as  $j$  by the SCT.

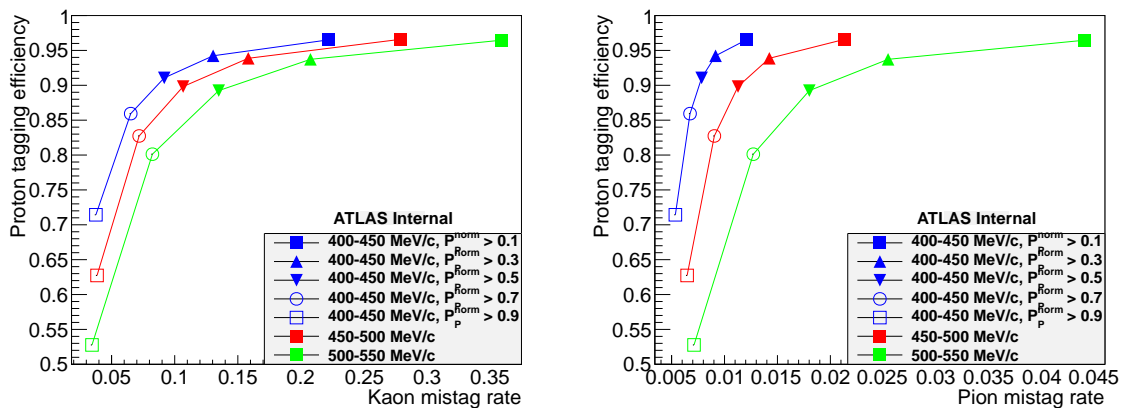
With these definitions, the proton tagging efficiency and mistag rate for pions and kaons can be checked, using five predefined cut values on the SCT normalized likelihood,  $P_p^{\text{norm,SCT}}$ . These cut values are 0.1, 0.3, 0.5, 0.7 and 0.9. They are only applied to the SCT likelihood, as the Pixel likelihood is used as a means to assign ‘‘truth’’ information to the tracks.

Figures 6.12 and 6.13 show the tagging efficiency results for low momentum,  $400 < p < 550$  MeV/ $c$ , both with 2011 and 2012 data. The results show that the SCT has some independent particle discriminating power, with a proton tagging efficiency greater than 95% while maintaining a pion mistag rate lower than 5% and a kaon mistag rate lower than 40%.



(a) Proton tagging efficiency vs kaon mistag rate. (b) Proton tagging efficiency vs pion mistag rate.

**Figure 6.12:** Proton tagging efficiency with respect to the mistag rate for kaon and pion as a function of the cut on  $P_p^{\text{norm,SCT}}$ , 2011 data. Track momentum in the interval (400, 550) MeV/c, with three slices, and for positive particles only.



(a) Proton tagging efficiency vs kaon mistag rate. (b) Proton tagging efficiency vs pion mistag rate.

**Figure 6.13:** Proton tagging efficiency with respect to the mistag rate for kaon and pion as a function of the cut on  $P_p^{\text{norm,SCT}}$ , 2012 data. Track momentum in the interval (400, 550) MeV/c, with three slices, and for positive particles only.

The top (blue) line corresponds to  $400 < p < 450$  MeV/c, the middle (red) line to  $450 < p < 500$  MeV/c and the bottom (green) line to  $500 < p < 550$  MeV/c. The filled squares are the cut  $P_p^{\text{norm}} > 0.1$ , upwards triangles are  $P_p^{\text{norm}} > 0.3$ , downwards triangles are  $P_p^{\text{norm}} > 0.5$ , hollow circles are  $P_p^{\text{norm}} > 0.7$  and hollow squares are  $P_p^{\text{norm}} > 0.9$ .

For the 2011 data, the kaon mistag rate is lower than 30% and the pion mistag rate stays below 4%, with a proton tagging efficiency around 95%.

During the same period, for a kaon mistag rate less than 20%, a tagging efficiency greater than 90% is possible, whereas for a kaon mistag rate lower than 15%, the

efficiency is above 95%.

In 2012 data, the efficiency is slightly higher, as well as the mistag rates. For a proton tagging efficiency of around 96%, the kaon mistag rate is lower than 40% and the pion mistag rate is below 5%.

During this period, the tagging efficiency is close to 94% with kaon mistag rates under 22% and pion mistag rates under 3%. For a tagging efficiency around 90%, the mistag rates stay under 15% and 2%, for kaons and pions respectively.

When comparing the two sets of plots in Figures 6.12 and 6.13, one can observe that the proton tagging efficiency does not degrade over time. The difference between the two periods is likely to be related to the fit values that are derived from the Pixel “truth” particle information and are slightly different for each of the two periods.

## 6.5 Long-term Stability

Because the SCT was not designed to do energy measurements, its PID capability is limited. However, a very useful study is tracking the radiation damage of the silicon tracker over time.

As it was described in section 2.3, the silicon charge collection efficiency drops with accumulated radiation. Due to the lower charge collected, the Time-over-Threshold is inevitably reduced. Hence, the average time-bin size will drop as well.

One way to track the evolution of the charge collection efficiency is to study the change over time of the  $dE/dx$ . For this purpose, the mean  $dE/dx$  of positive protons is tracked in the (500, 550) MeV/ $c$  range. The expected effect is a reduction of the mean value over time when radiation damage effects are present.

This study involves several components. First, the protons have to be identified. The use of Pixel likelihoods is not possible for the 2010 runs because they were not calculated. The Pixel  $dE/dx$ , however, is present in the data. The geometrical cut described in section 6.4 can be applied to the Pixel  $dE/dx$  to separate the protons.

By applying that geometrical cut to the 2010-2012 period it is possible to get consistent results during the whole period. However, it is necessary to check for differences between this geometrical cut and the actual Pixel likelihood cut that was described in section 6.4.1.

Calculation of the mean  $dE/dx$  is done by Gaussian fitting the  $dE/dx$  distribution for the (500, 550) MeV/ $c$  range and extracting the value of the mean parameter.

Therefore, the first part of the study was to see the actual proton mean  $dE/dx$  evolution with time. Figure 6.14 shows this evolution in the whole 2010-2012 period, for the two aforementioned methods of extracting the proton band. The geometrical cut is very close to the Pixel likelihood cut and the trends are consistent with each other.

It is worth noting that, considering that the goal of this study is to track the radiation damage over time, the result shown in Figure 6.14 is initially confusing. The first point is much higher than the second one, then the mean  $dE/dx$  ramps up with time. There seems to be no evidence of radiation damage, especially if the first two points are ignored. In addition, an increase in the collected charge is not something to expect.

From previous studies [112], it is known that the timing of the SCT read-out is not stable with time. The average time-bin size (number of bins over threshold) tends to

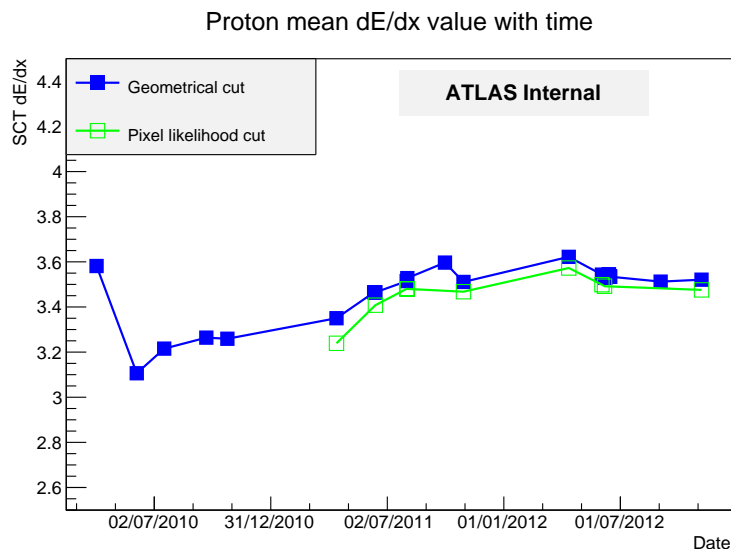


**Figure 6.14:** Time evolution of the proton (positive tracks) mean  $dE/dx$  for track momentum in the (500, 550) MeV/ $c$  range, extracting the protons with the geometrical cut and with the Pixel likelihood for 2011-2012.

increase with time. This is caused by timing drifts over time (refer to section 6.3.1 for a brief review on SCT timing).

A particle traversing one or more strips deposits charge that is collected and a signal pulse is generated. When the timing setting is well adjusted with respect to the Level 1 trigger, a pulse of width around 20 ns is most likely to fall within one 25 ns time-bin. However, small drifts, of a few nanoseconds, on the timing would cause this same pulse to fall in two time-bins, hence increasing the average measured time-bin size. Even smaller pulses might be above threshold during two time-bins if the drift is large.

To prevent this from happening, timing scans are performed in the detector in order to calibrate the SCT timing. The goal is to have 01x patterns on the hits time-bins, as was mentioned in section 6.3.1. Next, the effect of the timing adjustment in the  $dE/dx$  calculation on the SCT is studied.

This part of the study includes a mean time-bin size calculation, for the momentum range of interest. The dates when timing scans were performed are also known:

- 10/4/2010: coarse timing scan. It took place during run 152777, between the first and the second points in the plots.
- 15/4/2011. It took place during run 179710, one of the runs selected for the  $dE/dx$  study.
- 8/9/2011. During run 188921.
- 4/4/2012. Run 200804.
- 1/5/2012. It took place during run 202660.
- 15/11/2012. Run 214553.

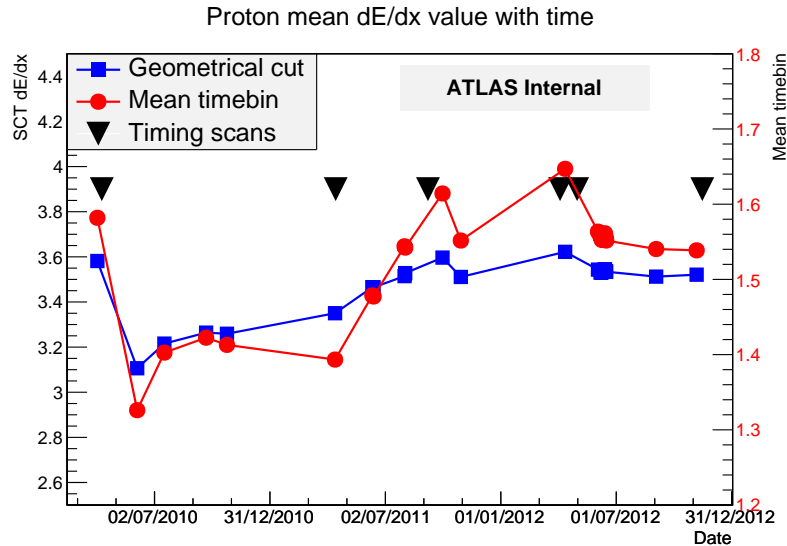


Figure 6.15: Evolution of the proton mean  $dE/dx$  with time, showing the effect of the timing misadjustments and the timing scans dates.

The first scan resulted in a rather large adjustment of the timing. As a result, it is not surprising to see the plot in Figure 6.15, which shows a large decrease of the mean time-bin size for the second run of the period. Note that the left Y axis scale corresponds to the calculated SCT  $dE/dx$  while the right Y axis scale belongs to the mean time-bin size.

This figure shows the mean time-bin size, together with the mean  $dE/dx$  of the proton for (500, 550) MeV/c and also the dates when timing scans were performed.

In addition, the plot also shows that there is some correlation between the mean time-bin size and the calculated  $dE/dx$ . It might be possible to exploit this correlation, shown in Figure 6.16.

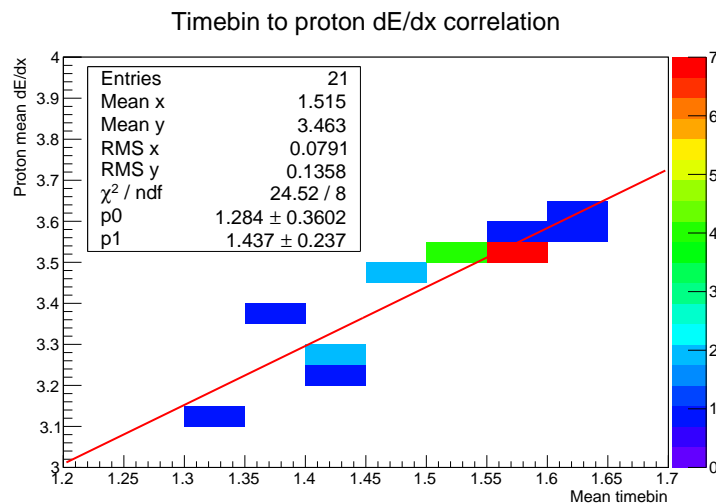
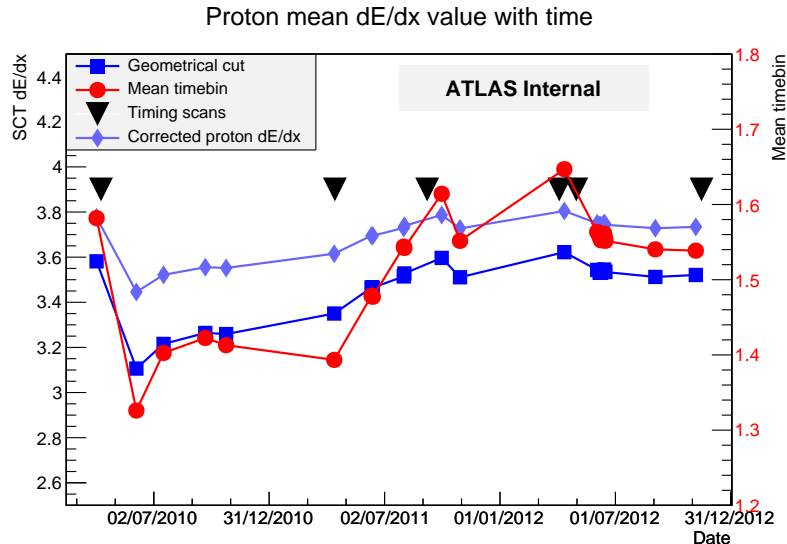


Figure 6.16: Correlation between the mean time-bin size and the calculated mean proton  $dE/dx$ .

Although the statistics are very low, the correlation is quite clear. A linear fit of the 2010 runs, the first five points, gives the following relation:

$$p_0 = 1.284 \pm 0.3602 \quad p_1 = 1.437 \pm 0.237$$



**Figure 6.17: Evolution of the proton mean  $dE/dx$  with time, including a correction for the 2010 runs.**

It is possible to use this relationship between the mean time-bin and the calculated  $dE/dx$  to correct for the variations. Figure 6.17 contains the final correction to the  $dE/dx$  evolution with time. As before, note that the left Y axis scale corresponds to the calculated SCT  $dE/dx$ , both corrected and not corrected versions, while the right Y axis scale belongs to the mean time-bin size.

The corrected proton  $dE/dx$  in this plot shows a small effect from the time-bin size variation over time, although it is not possible to completely eliminate it. In addition, considering the 2011-2012 period is a bit more stable over time, one can say that there is not just yet any evidence of radiation damage that would show up as a reduced  $dE/dx$  due to a lower charge collection.

The overall variation of the calculated  $dE/dx$  is less than 17% in the uncorrected numbers, whereas it is less than 10% in the corrected version. If the first run is ignored, these variations are even lower. The trend since the end of the 2011 run shows a very small variation of around 2%.

## 6.6 Discussion

This chapter described the results obtained with a Time-over-Threshold method for calculating the deposited charge by particles traversing the SCT, thus reconstructing the energy loss,  $dE/dx$ , based on the time-bin information and the number of affected strips, both available in the SCT Ntuples. The results obtained have been compared to the more precise values provided by the Pixel detector and the performance using efficiency vs mistag rate of particle tagging was analysed.



The lack of Monte Carlo simulations for SCT Ntuples that include both truth information and charge simulation obliged the study to extract “truth information” from the  $dE/dx$  calculation performed in the Pixel detector. A possible follow-up for this study is the generation of Monte Carlo simulations with all these characteristics in order to have a proper characterization of the SCT  $dE/dx$  calculation.

The results are encouraging although the SCT read-out has less resolution than the Pixel one. It is also important to note that the SCT was never designed for this purpose, so this result was not expected from the beginning. The ability of this method to separate protons from light particles, such as pions, is shown in the efficiency greater than 90% for low momentum, with a mistag rate below 10%, presented in section 6.4.2.

A possible use of this kind of calculation is to perform long term radiation monitoring by analysing the  $dE/dx$  variations over time, with increasing luminosity.

It was possible to extract the energy loss despite the fact that the SCT was not designed with that feature in mind. The digitization of the particle hits causes a great loss of information, what reduces the resolution, but the available information allows for some  $dE/dx$  calculation.

It is necessary to point out that, in the future, this calculation will not be available for day to day data taking. The 13 and 14 TeV centre-of-mass energy collisions after the first Long Shut-down will have a 25 ns bunch spacing and the SCT will run in 01X mode, with an additional compression that causes the complete loss of the individual time-bins information.

If this analysis is to be used in the future, special runs will need to be used, with the appropriate timing and compression settings so the time-bin information can be recovered from the data.



# Chapter 7

## Conclusions and Future Work

This thesis presents two main topics of research. The first one is the ATLAS Inner Tracker Phase-II Upgrade, focused on the silicon strips tracker. The study shows the results of tests performed on prototypes that have been built to test the electronics, modules and structures defined for the strips tracker that will replace the ATLAS Semiconductor Tracker (SCT) and Transition Radiation Tracker (TRT) sub-systems with an all-silicon tracker when the High Luminosity LHC is deployed.

The results shown in chapter 5 prove that the structures to be built for the upgrade are feasible. The noise results of a full-size stave with twelve modules, and based on the ABCn25 chip, are as good as the noise results for the individual modules. The noise pick-up is not affected by the read-out of the modules on a 1.2 metre long bus tape.

In addition, concepts such as high voltage multiplexing and the VersatileLink have been tested together with stavelets in order to assess their influence on the stavelet performance. These devices cause no interference with the modules read-out and they can be used safely with the strips tracker devices.

Furthermore, a single module has been read-out at the expected working temperature setting of the upgraded tracker,  $-20^{\circ}\text{C}$ , using a commercial chiller unit. The tracker will be cooled using a recirculating  $\text{CO}_2$  cooling system. Blow-off systems are being tested at CERN and RAL to perform initial tests with staves.

The future work regarding this topic will consist in testing the next staves that are being assembled. A serially powered stave with up to 12 modules on one side will be tested and the results compared to the DC-DC powered stave. The best performing stave, or both, will be populated on the second side, building a double sided object for full tests.

Also, the staves will be tested with  $\text{CO}_2$  cooling systems to check their behaviour at very low temperatures.

In the near future, the ABC130 chip will be used in the strips upgrade modules, building staves with up to 13 modules on each side. The tests will be similar to those presented here.

The second topic of this thesis is an analysis of the energy loss measurement using the ATLAS Semiconductor Tracker information. While the SCT was not designed to perform this kind of task, chapter 6 shows a method to extract a way of calculating the  $dE/dx$ , while with a low resolution. It allows some particle discrimination, compared to the pixel detector, with over 90% proton tagging efficiency. The availability of the time-bin information in SCT Ntuples enables us to perform this calculation.

This method of calculating  $dE/dx$  in the SCT has been studied as a means of tracking radiation damage in the SCT by measuring the average proton  $dE/dx$  over time, which is expected to decrease as the silicon is damaged by the radiation at high luminosities. The timing settings of the SCT have to be considered in order to correct the deviations that cause inaccurate  $dE/dx$  calculations.

Further work on this topic is expected as well. The tracking of the proton mean  $dE/dx$  can only be performed with the right read-out settings after the first Long Shut-down of the LHC. After 2015, the SCT will run in a read-out mode that will make the time-bin information unavailable unless special runs are used. We expect to be able to do this study in the future to try check if this method is appropriate for radiation damage tracking.

# Chapter 8

## Resumen

### 8.1 Introducción

Esta tesis está centrada en la Fase 2 de la actualización del experimento ATLAS en el LHC, con énfasis en el futuro detector de trazas de bandas de silicio. Esta actualización supondrá el reemplazo completo del detector de trazas, para cumplir con los requisitos de granularidad y resistencia a la radiación necesarios tras la actualización del acelerador.

Este nuevo acelerador, llamado LHC de alta luminosidad (*High Luminosity LHC*, HL-LHC), colisionará protones a una energía en el centro de masas de 14 TeV y generará alrededor de 140 interacciones por cada cruce de haces de protones en los detectores.

Además del trabajo relacionado con la actualización de ATLAS, esta tesis también presenta un estudio sobre las prestaciones del actual detector de bandas de silicio de ATLAS.

Este resumen recoge algunos de los resultados más relevantes, para una vista más completa puede consultarse la versión en inglés.

#### 8.1.1 El experimento ATLAS

El experimento ATLAS (*A Toroidal LHC Apparatus*), mostrado en la Figura 8.1, es uno de los dos experimentos de propósito general del Gran Colisionador de Hadrones (*Large Hadron Collider*, LHC), situado en el “Punto de Interacción 1”. Está formado por múltiples capas, que se encargan de detectar diferentes tipos de partículas.

El detector de trazas mide el momento de las partículas cargadas que se originan en las colisiones. Se encuentra en la parte más interna del detector, rodeando el punto de colisión.

Está diseñado para medir el momento de las partículas cargadas con gran resolución y calcular vértices primarios y secundarios. Un imán solenoide que genera un campo magnético de 2 tesla de intensidad lo rodea para deflectar la trayectoria de las partículas.

Tres sub-sistemas componen el detector de trazas: un detector de píxeles, un detector de bandas de silicio (*Semi-Conductor Tracker*, SCT) y un detector de radiación de transición (*Transition Radiation Tracker*, TRT).

Los dos sub-detectores más internos, el de píxeles y el de bandas de silicio, están contruidos con detectores de silicio. Las partículas cargadas que pasan a su través depositan carga eléctrica, la cual puede ser medida.

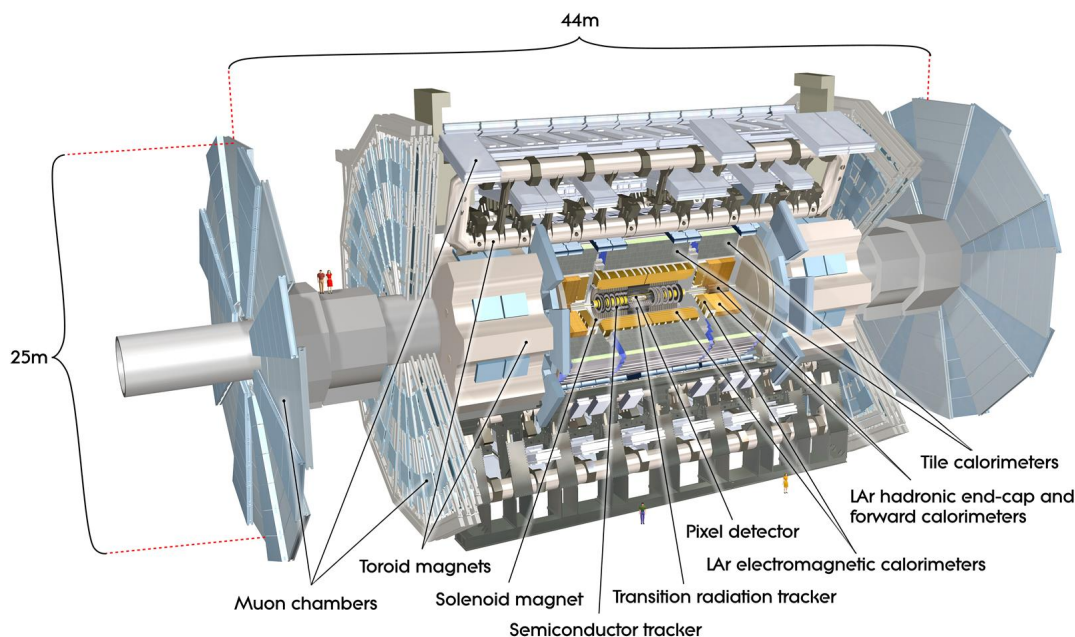


Figure 8.1: Vista del experimento ATLAS.

### 8.1.2 El detector de trazas de semiconductor en ATLAS

El detector de trazas de silicio (*Semiconductor Tracker*, SCT) del experimento ATLAS está formado por 4088 módulos de doble cara, repartidos en cuatro capas cilíndricas (barril) y dos tapas (endcap) con nueve discos cada una.

Los módulos son detectores de bandas de silicio de doble cara, con 768 bandas activas por cada lado, de  $80\ \mu\text{m}$  de ancho cada banda. Los sensores son de sustrato de silicio tipo n con bandas tipo p. Doce chips leen las bandas de cada módulo (seis chips por cada lado), montados sobre un circuito híbrido. Los sensores de cada lado están rotados  $40\ \text{mrad}$  para proporcionar la posición en dos dimensiones del paso de las partículas. Hay un total de 6.3 millones de canales en el detector de bandas de silicio.

Las partículas cargadas que atraviesan el detector depositan carga en el silicio, la cual es recogida por los chips, amplificada y comparada con un umbral. Cuando la carga supera este umbral, se envía a los sistemas que procesan los datos fuera del detector. Los chips utilizados en el SCT se denominan ABCD3TA [30].

## 8.2 Detector de bandas de silicio en ATLAS Fase 2

### 8.2.1 Fase 2 del LHC: HL-LHC

El LHC fue diseñado para ser capaz de entregar una luminosidad integrada de  $400\ \text{fb}^{-1}$ , a lo largo de diez años de operación. Ciertos componentes del acelerador deberán ser reemplazados tras acumular esa cantidad de radiación [44].

Partes de los experimentos también tendrán que sustituirse por otros debido a la radiación. Los detectores de trazas de ATLAS y CMS deberán extraerse para instalar otros nuevos, ya que el silicio de los detectores de píxeles no podrá soportar más

radiación.

El LHC de alta luminosidad (HL-LHC) consiste en un nuevo diseño del acelerador y de parte de los experimentos. Con este nuevo diseño, se pretende alcanzar una luminosidad integrada tras otros diez años de operaciones entre  $2500$  y  $3000 \text{ fb}^{-1}$ , una cantidad de datos que abre nuevos campos de exploración para la física, tanto del Modelo Estándar como más allá del Modelo Estándar.

El HL-LHC mantendría la misma energía por haz de protones, pero multiplicaría por cinco la luminosidad instantánea máxima y casi por seis la luminosidad integrada anual. Un mayor número de protones por paquete y un mayor enfoque del haz serán los mayores cambios que permitan la mayor luminosidad. El incremento del enfoque aumentará la probabilidad de colisión por cruce de paquetes, pasando de un *pile-up* de 27 en el diseño del LHC actual a un *pile-up* medio de 140.

Debido al mayor *pile-up*, los detectores de trazas actuales no podrán ser utilizados sin una pérdida sustancial de su rendimiento. En ATLAS, el detector TRT alcanzaría un 100% de ocupación y los detectores de píxeles y el SCT no podrían resolver trazas cercanas. Se hace necesaria la sustitución del detector de trazas por un nuevo diseño con mayor granularidad y se implementará por completo en silicio.

### 8.2.2 Descripción del detector de bandas

El requisito para el nuevo detector de bandas de silicio en la Fase 2 de ATLAS es que soporte una dosis equivalente de neutrones de 1 MeV de  $1.2 \times 10^{15} \text{ cm}^{-2}$  en las capas más internas, y de  $5 \times 10^{14} \text{ cm}^{-2}$  en las más externas.

Para conseguir sensores que puedan soportar la acumulación de esta dosis, se ha cambiado el tipo de sensor por un sustrato p con implantes tipo n. En este tipo de sustrato, no se produce inversión de tipo dado que ya es de tipo p.

Las dimensiones de los sensores para los módulos del barril son  $97.54 \times 97.54 \text{ mm}^2$ , con cuatro filas de 1280 bandas cada una en los sensores con bandas cortas. En las capas más exteriores, con menor ocupación, se utilizarán sensores con bandas el doble de largas.

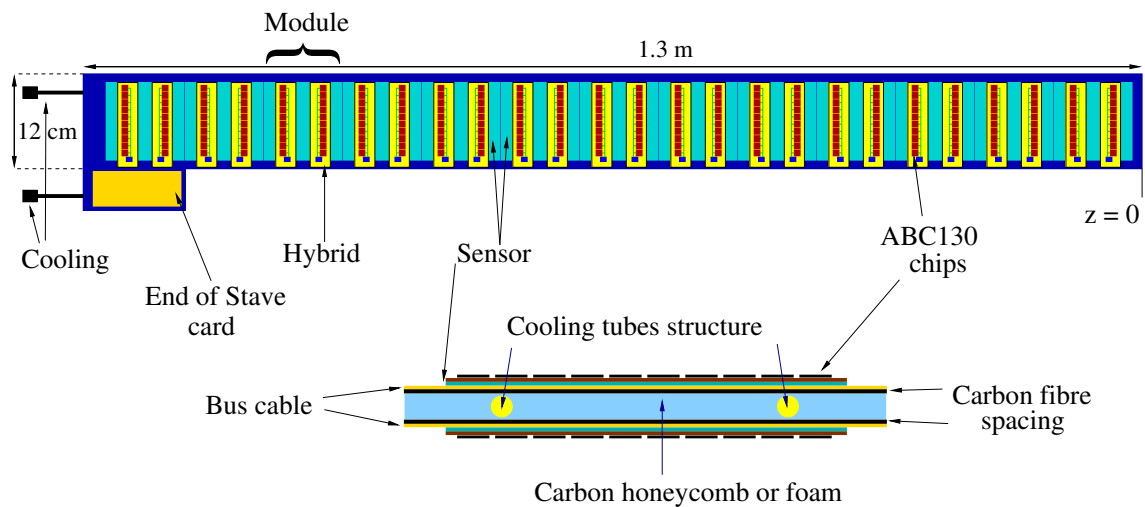


Figure 8.2: Esquema de un stave de barril con 13 módulos.

Los módulos del barril se integrarán en estructuras multi-módulo denominadas

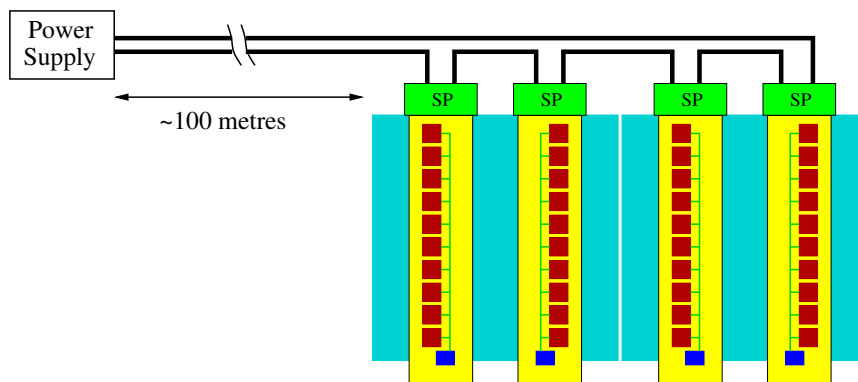
*staves*, conteniendo 26 módulos repartidos en dos lados, para proporcionar resolución en dos dimensiones a través de un estéreo-ángulo de 40 mrad. Se han producido prototipos de los *staves* con un menor número de módulos, llamados *stavelets*, a modo de prueba de concepto de los diseños propuestos. Un esquema del *stave* se muestra en la Figura 8.2, con trece módulos por cada lado.

En el caso de los *endcaps*, los sensores tendrán forma trapezoidal. La estructura circular de las tapas requiere que las bandas formen ángulo entre ellas, de forma que apunten hacia el centro del punto de interacción.

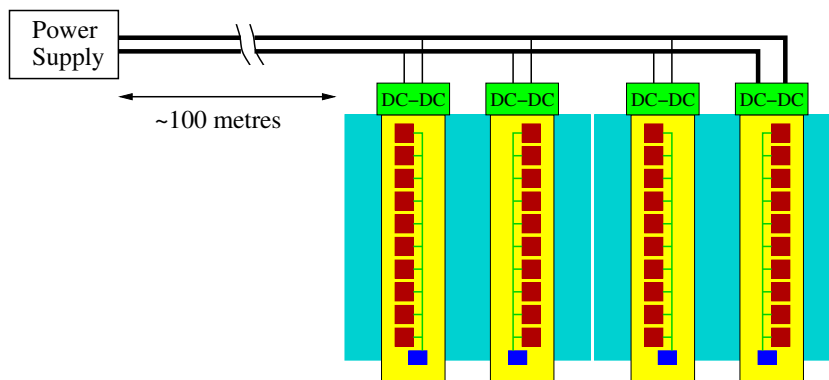
### 8.2.3 Sistemas electrónicos

La lectura de los módulos se realiza a través de una tarjeta que en los primeros prototipos se implementa con búferes LVDS (*Low Voltage Differential Signal*) en una placa denominada EoS (*End of Stave* o *End of Substructure*).

Se han diseñado dos chips de lectura para las bandas, ambos binarios. Un primer chip con 128 canales, ABCn25, en un proceso de 250 nm, ha sido utilizado para construir los módulos que se han probado en el contexto de esta tesis. En el futuro, y previsiblemente para la construcción final del detector de trazas actualizado, se utilizarán chips de 256 canales en un proceso de 130 nm. Este chip se denomina ABC130 y su diseño se finalizó durante 2013 [77].



(a) Alimentación serie de módulos (“cadena de híbridos”).



(b) Alimentación de módulos con conversión DC-DC.

**Figure 8.3: Esquemas alternativos de alimentación de los módulos.**

El consumo de potencia del nuevo detector de trazas será unas 4-5 veces superior al actual SCT. Los módulos del SCT se alimentan con cables independientes por cada



módulo, con fuentes de alimentación que entregan el voltaje requerido por los chips. Las pérdidas producidas en los cables debido a la distancia (100 m) entre las fuentes de alimentación y el detector hacen que se pierda una cantidad no despreciable de energía. Esta falta de eficiencia provoca que se necesite una cantidad de material que afecta al rendimiento del experimento y eleva los costes.

Para alimentar el detector de trazas actualizado se están investigando sistemas de alimentación alternativos, como conversión DC-DC (continua-continua) o alimentación serie. Parte del trabajo de esta tesis consiste en hacer pruebas de rendimiento de elementos funcionando con ambos sistemas de alimentación.

Un ejemplo de alimentación serie se muestra en la Figura 8.3(a), mientras que el equivalente en conversión DC-DC se muestra en la Figura 8.3(b).

Ambas alternativas se basan en reducir la corriente que entregan las fuentes de alimentación, reduciéndose las pérdidas por resistencia de los cables. En la conversión DC-DC la fuente entrega una tensión superior a la necesaria para alimentar los chips, que se reduce a la tensión adecuada en una ubicación próxima a los chips.

#### 8.2.4 Prestaciones del módulo con alimentación serie

El estudio de sistemas para la Fase 2 de ATLAS comienza con la construcción de módulos con un único sensor de bandas de silicio, al cual se pegan dos híbridos con 20 chips cada uno.

El módulo medido en el contexto de esta tesis fue fabricado en la Universidad de Liverpool, con un sensor de grado B (FZ2). El módulo utiliza alimentación serie, en configuración de “cadena de híbridos”, que implica diferentes niveles de tensión continua para ambos híbridos.

En la configuración de “cadena de módulos”, los dos híbridos de un módulo están a la misma tensión de referencia. Se utiliza en estructuras multi-módulo como stavelets o staves.

Los tipos de pruebas que se han llevado a cabo con los módulos individuales y las estructuras multi-módulo son dos.

El primero, para medir el ruido a la entrada del amplificador del chip, en unidades de electrones (*Equivalent Noise Charge*, ENC). Se define como el número de electrones que deben recogerse en el sensor para crear una señal equivalente al ruido del sensor. Se calcula mediante tres barridos del umbral en el comparador del chip inyectando tres cargas de magnitud conocida. Normalmente se utiliza un rango de cargas de entrada en el cual el amplificador se encuentra en su zona lineal.

El segundo se llama ruido de doble disparo (*Double Trigger Noise*, DTN). Se utiliza para estudiar la susceptibilidad del sistema de adquisición de datos a las interferencias electrónicas durante la lectura. Se envían dos disparos espaciados un número de periodos de reloj, variando el espaciado. El segundo evento registra la ocupación del módulo al comenzar la lectura del primer evento.

Se llevaron a cabo pruebas realizadas sobre el módulo disponible en CERN bajo diversas condiciones de funcionamiento, de temperatura y polarización del sensor. Las pruebas se describen en los siguientes apartados, junto a los resultados obtenidos.

##### Variación de temperatura

El objetivo de esta medida es extraer la dependencia del ruido con la temperatura. Se tomaron medidas de ruido con diferentes temperaturas, realizando 20 repeticiones para

cada punto de temperatura.

Las temperaturas de refrigerante con las que se realizó el estudio fueron  $T_{\text{chiller}} = \{12, 18, 24\}^{\circ}\text{C}$ . Se midió la temperatura de los híbridos en cada una de las pruebas, como se muestra en la Tabla 8.1.

$T_{\text{chiller}} [^{\circ}\text{C}]$	12	18	24
$T_{\text{híbrido}} [^{\circ}\text{C}]$	25.9	30.8	35.7

**Table 8.1:** Temperaturas del refrigerante y los híbridos.

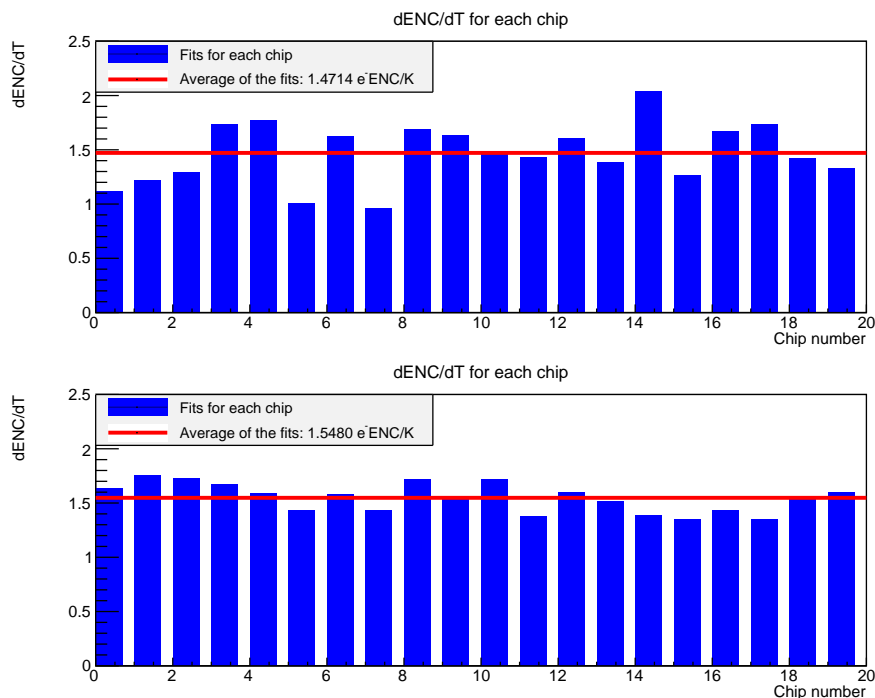


**Figure 8.4:** Ajuste lineal de la variación del ruido con la temperatura para los chips de los dos híbridos.

Para extraer la variación de ruido con la temperatura se tomó la media de las 20 medidas de ruido para cada valor de temperatura de los híbridos y se hizo un ajuste lineal de los tres puntos. Los valores medios obtenidos para los dos híbridos fueron los siguientes:

$$\overline{\Delta\text{ENC}/\Delta T}_{\text{Híbrido } 0} = 1.47 \pm 0.28 e^{-}\text{ENC/K} \quad (8.1)$$

$$\overline{\Delta\text{ENC}/\Delta T}_{\text{Híbrido } 1} = 1.55 \pm 0.13 e^{-}\text{ENC/K} \quad (8.2)$$

Los resultados de esta prueba se pueden ver en la Figura 8.4, que muestra el ajuste lineal de cada chip y la media para los dos híbridos. La dependencia del ruido se estableció en  $1.5 e^{-}\text{ENC/K}$ .

### Variación de polarización del sensor

La desertización de la unión p-n varía en función de esta polarización, y con ella el ruido medido.

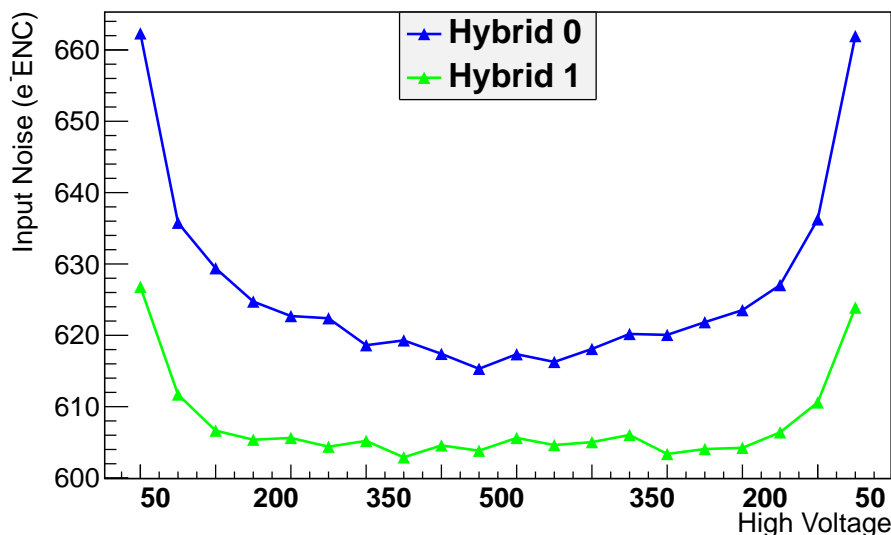


Figure 8.5: Ruido en el módulo serie en función de la polarización del sensor.

Los resultados se muestran en la Figura 8.5, variación entre 50 y 500 V en sentidos creciente y decreciente.

La razón para realizar el barrido en ambos sentidos es la existencia de discrepancias en algunos módulos cuando se reduce el voltaje de polarización del sensor. En ocasiones se observa un aumento del ruido por encima del original en los niveles de alto voltaje probados anteriormente [103]. Este efecto no se observa en este módulo. Sin embargo, en algunos módulos de los stavelets sí, como se podrá ver en la sección siguiente.

### Pruebas a bajas temperaturas

La electrónica que se incluye en el módulo y en sus alrededores debe ser capaz de funcionar a bajas temperaturas. El detector funcionará con refrigeración por debajo de  $-20^{\circ}\text{C}$ , utilizando un sistema con  $\text{CO}_2$ .

El módulo fue probado a temperaturas de  $-6^{\circ}\text{C}$ ,  $-12^{\circ}\text{C}$  y  $-20^{\circ}\text{C}$ . En esta sección se muestra únicamente el resultado para el último valor, por tratarse del más relevante. El refrigerante con base de aceite empleado para estas pruebas permite alcanzar temperaturas alrededor de  $-40^{\circ}\text{C}$ .

Para evitar la formación de hielo en las tuberías y en las inmediaciones del módulo se utilizó aire seco en el contenedor del módulo y revestimientos para las tuberías.

El resultado de las pruebas a bajas temperaturas se muestra en la Figura 8.6. Se puede comprobar que el módulo es capaz de operar a bajas temperaturas. La diferencia de ruido entre la temperatura de funcionamiento usual de  $12^{\circ}\text{C}$  y esta prueba a  $-20^{\circ}\text{C}$  es consistente con la variación de ruido con la temperatura presentada anteriormente.

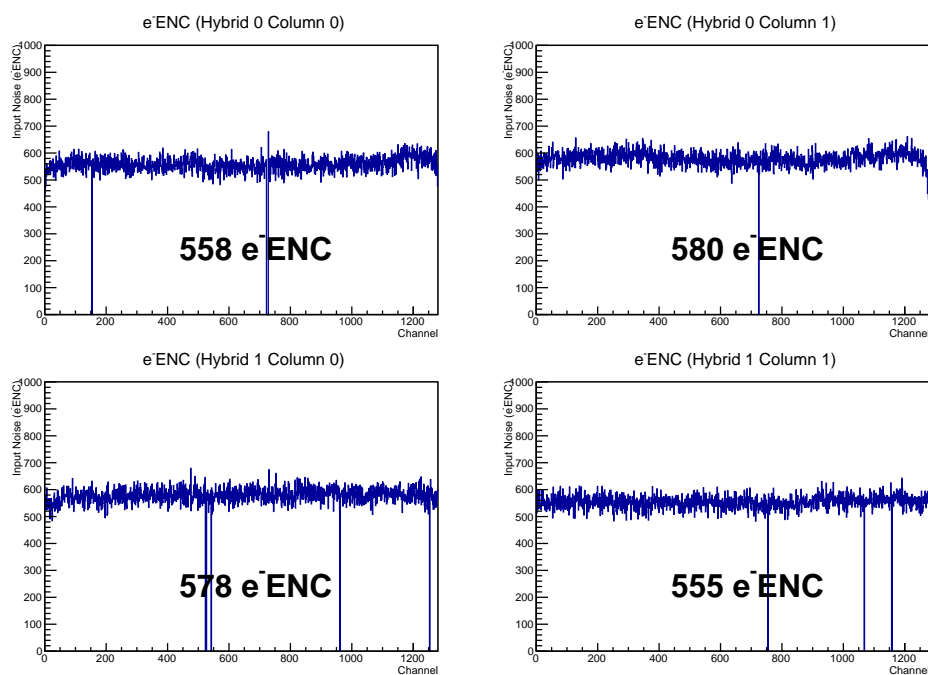


Figure 8.6: Ruido del módulo serie con refrigerante a  $-20^{\circ}\text{C}$ .

### 8.2.5 Prestaciones de estructuras con múltiples módulos

Se han evaluado tres estructuras multi-módulo diferentes en el contexto de esta tesis:

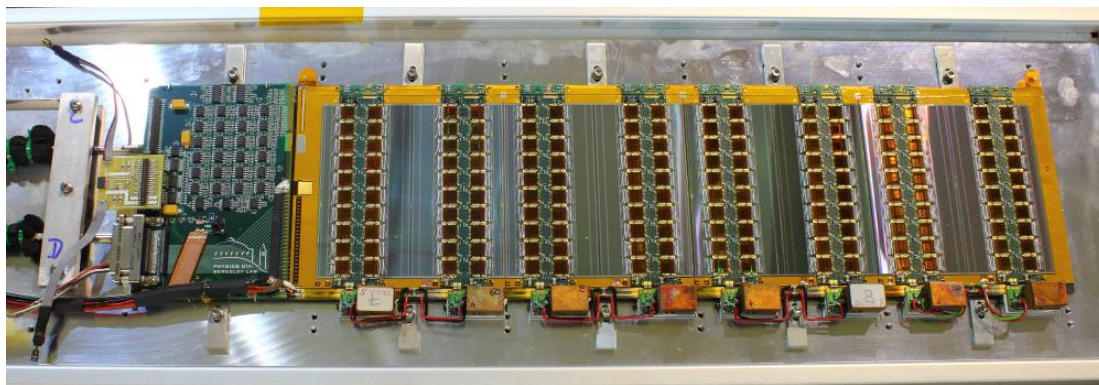
- Un stavelet con cuatro módulos, utilizando alimentación con conversión DC-DC.
- Un stavelet con cuatro módulos, utilizando alimentación serie.
- Un stave, con doce módulos, utilizando alimentación con conversión DC-DC.

Las tres estructuras fueron ensambladas en el Rutherford Appleton Laboratory (RAL), y las dos primeras se recibieron en CERN entre 2012 y 2013. La tercera se probó en RAL durante su construcción. El objetivo de la construcción y evaluación de estructuras de cuatro módulos es determinar los posibles problemas que pueden surgir al alimentar y leer múltiples módulos dispuestos en un bus común.

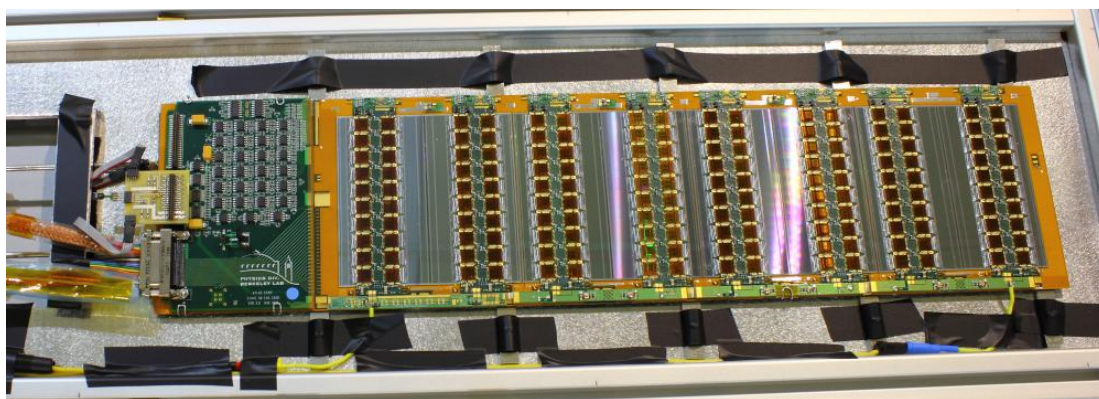
La Figura 8.7(a) muestra una fotografía del stavelet de cuatro módulos con conversión DC-DC. Cada convertidor DC-DC es individual y provee la corriente necesaria para alimentar los veinte chips de un híbrido, proporcionando hasta 5 A de corriente a 2.5 V. La tensión de entrada del convertidor puede ser entre 7 V y 15 V.

Por otro lado, el stavelet de cuatro módulos que emplea alimentación serie se muestra en la Figura 8.7(b). Se trata de un stavelet en “cadena de módulos”, donde los dos híbridos de un módulo están referenciados a la misma tensión. Cada módulo está 2.5 V por encima o por debajo de los vecinos. La corriente de entrada para alimentar el stavelet debe estar entre 9 y 10 A aproximadamente.

Las pruebas de prestaciones de los stavelets de cuatro módulos con conversión DC-DC y con alimentación serie fueron las siguientes:



(a) Stavelet con conversión DC-DC.



(b) Stavelet con alimentación serie.

**Figure 8.7: Los dos stavelets construidos en RAL y probados en CERN.**

### Barrido de polarización de los sensores

Se varió el valor de la tensión de polarización de los sensores, para comprobar la evolución del ruido en uniones antes y después de producirse la desertización. Para ambos stavelets se incrementó la tensión y posteriormente se decrementó.

La Figura 8.8 muestra la evolución del ruido en el stavelet con conversión DC-DC. Primero se incrementó de 75 V a 300 V y posteriormente se disminuyó el voltaje hasta 75 V, en pasos de 25 V.

Algunos sensores presentan un comportamiento anómalo, incrementándose el ruido al volver a una polarización inferior desde una superior. Esto ocurre normalmente con los sensores que utilizan aislamiento de tipo P-stop con concentración elevada ( $10^{13} \text{ cm}^{-3}$ ).

Otro efecto observado en función del tipo de aislamiento es un ruido inicial inferior en los que tienen aislamiento P-spray. El ruido permanece bastante por debajo de  $700 e^-ENC$  a valores de voltaje muy inferiores al voltaje de desertización.

La Figura 8.9 muestra la misma evolución en el stavelet con alimentación serie. De la misma manera que en el stavelet con conversión DC-DC, los módulos con sensores que utilizan aislamiento P-spray parten de un nivel de ruido inferior a baja polarización.

Asimismo, el aumento de ruido al volver a un voltaje inferior es inferior en aislamientos P-stop y P-spray con concentraciones más reducidas que en el caso de los sensores del stavelet con conversión DC-DC.

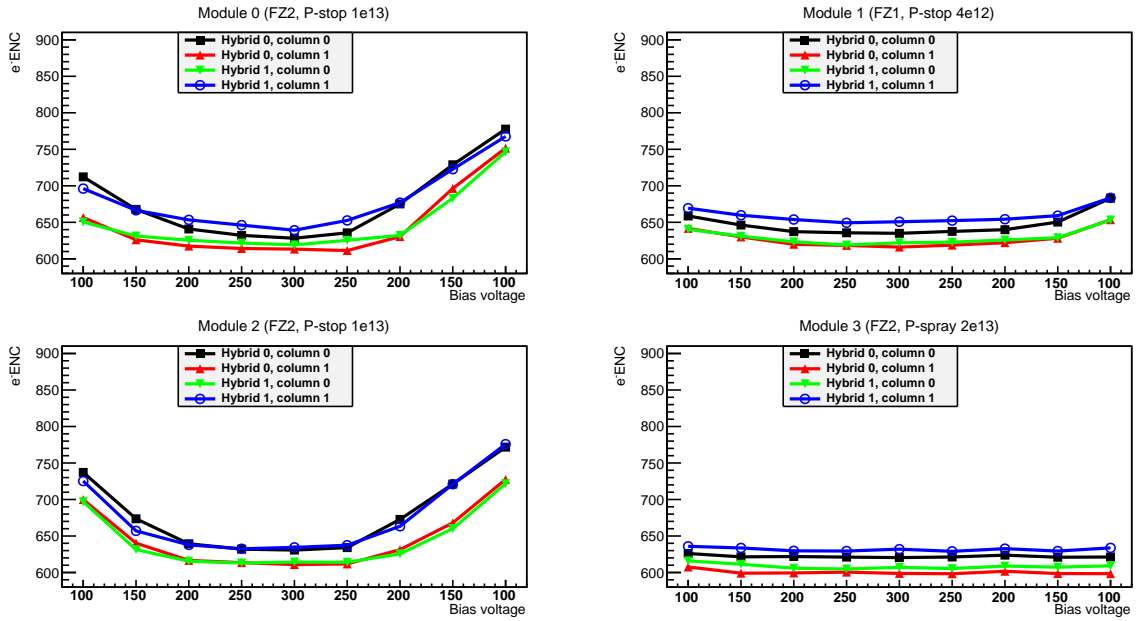


Figure 8.8: Ruido del stavelet DC-DC en función del alto voltaje.

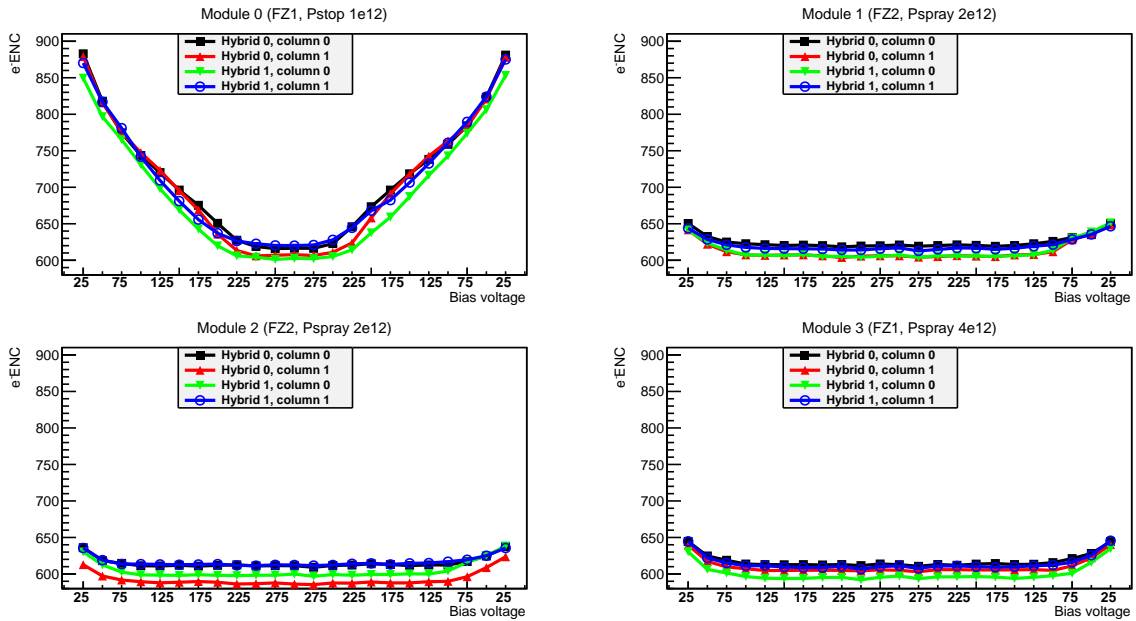


Figure 8.9: Ruido del stavelet serie en función del alto voltaje.

### Variación de la alimentación de los híbridos

Los convertidores DC-DC y los circuitos de alimentación serie admiten un cierto rango de tensiones y corrientes de entrada. Los convertidores DC-DC tienen su punto de máxima eficiencia en 10 V, con un rango entre 7 y 15 V. Por otro lado, la tensión entregada por el circuito de alimentación serie varía en función de la corriente. Para el stavelet con “cadena de módulos” la corriente típica es 9.5 A.

Se han hecho pruebas variando la tensión de entrada de los convertidores DC-DC

entre 10 y 14 V. Cuando aumenta la tensión disminuye la corriente, por lo que se producen menos pérdidas por la resistencia de los cables. Una reducción de la tensión por debajo de los 9 V no es recomendable, debido a la alta corriente cuando la tensión se reduce.

Sin embargo, es conocido que el punto óptimo de funcionamiento de estos convertidores es con una tensión de entrada de 10 V, y que tensiones mayores aumentan el ruido en los módulos.

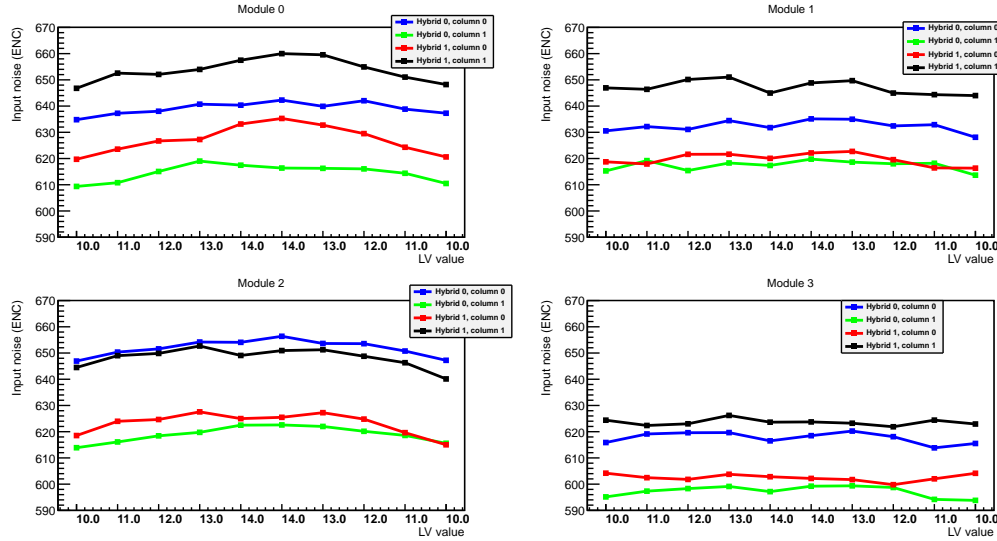


Figure 8.10: Ruido del stavelet DC-DC en función de la tensión de entrada a los convertidores.

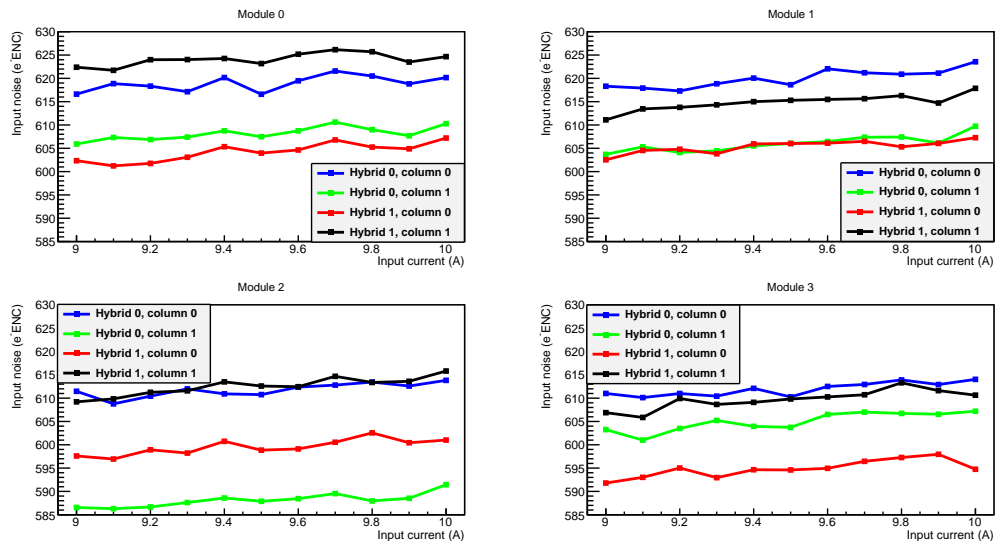


Figure 8.11: Ruido del stavelet con alimentación serie en función de la corriente de entrada.

Los resultados de estas pruebas en el stavelet con conversión DC-DC se muestran en la Figura 8.10. El ruido varía levemente al subir la tensión hacia 14 V en dos de los

módulos, mientras que los otros dos módulos parecen ser inmunes al aumento de ruido de los convertidores al elevar su tensión de entrada.

En el caso del stavelet con alimentación serie, cuando aumenta la corriente de entrada también lo hace la tensión. Esto provoca, en última instancia, un aumento de la temperatura de los híbridos. Como se ha indicado en la sección 8.2.4, esto aumenta el ruido de forma proporcional.

La Figura 8.11 muestra los resultados de ruido frente a la corriente de entrada. El aumento de ruido es el esperado en los cuatro módulos del stavelet. Las variaciones observadas son consistentes con las que se producen al repetir una misma medida bajo las mismas condiciones.

### Multiplexión de líneas de alto voltaje

Con el objetivo de reducir el volumen de cables, se ha diseñado un sistema que multiplexa varias líneas de polarización de los sensores en un único cable, y que se dividen cerca de los módulos.

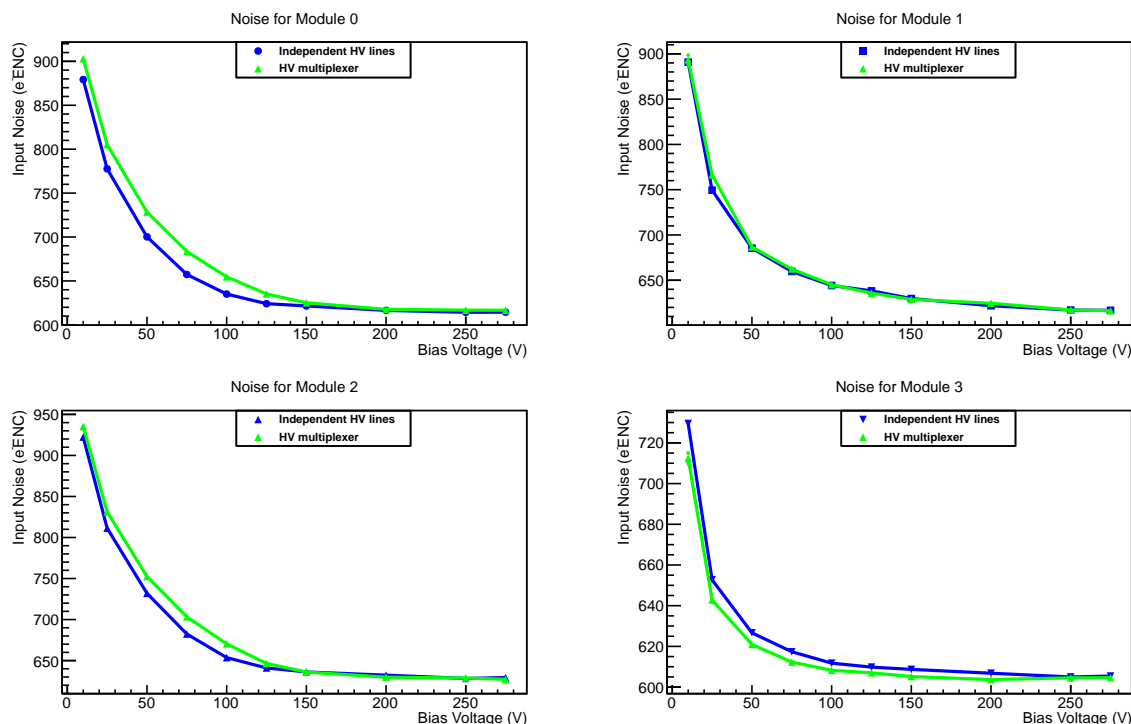


**Figure 8.12:** Comparación de la dependencia del ruido en el stavelet DC-DC en función del alto voltaje, con multiplexor y con líneas independientes.

En un stave sería posible agregar las 13 líneas de un lado, lo que permitiría ahorrar 12 pares de cables por cada stave. El objetivo de estas pruebas es verificar que la multiplexión de líneas de alto voltaje no tiene un efecto negativo en las prestaciones de los stavelets.

Para las pruebas se ha empleado un multiplexor construido en BNL utilizando transistores de carburo de silicio (SiC) que pueden conmutar hasta 500 V [58]. Este multiplexor soporta la desconexión individual de las líneas de alto voltaje, sin embargo no es posible hacer medidas de corriente de fugas individuales.



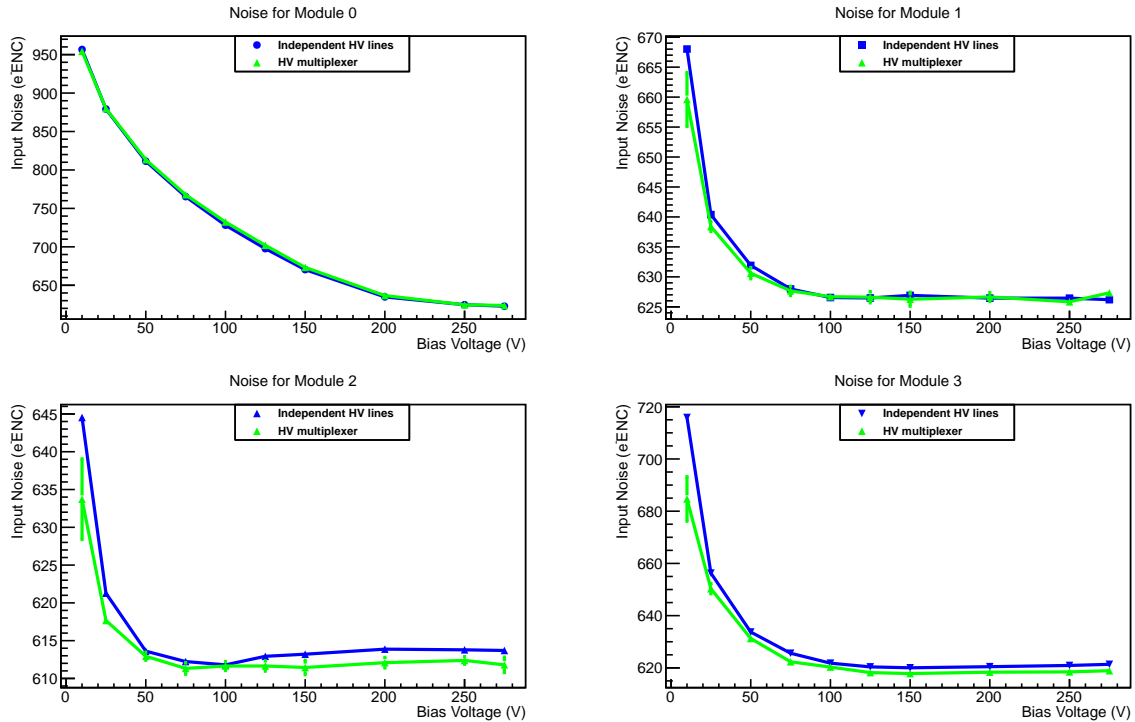


**Figure 8.13:** Comparación de la dependencia del ruido en el stavelet con alimentación serie en función del alto voltaje, con multiplexor y con líneas independientes.

Para tener una funcionalidad completa con multiplexores de alto voltaje, es necesario que los conmutadores sean suficientemente resistentes a la radiación, capaces de conmutar hasta 600 V y que permitan medir la corriente de fugas de los sensores de forma individual.

La Figura 8.12 muestra los resultados obtenidos con el stavelet DC-DC, comparando el ruido con y sin multiplexión. Los resultados del stavelet con alimentación serie se muestran en la Figura 8.13. En ambos casos, se observa una variación despreciable del ruido en los módulos del stavelet. En el stavelet con conversión DC-DC se produce una mezcla entre mayor ruido con el multiplexor y menor ruido, al igual que en el stavelet con alimentación serie. Estas variaciones no representan un aumento sistemático del ruido que pueda atribuirse a un efecto causado por el multiplexor.

Estos resultados permiten asegurar que la multiplexión de líneas de alto voltaje para polarizar los sensores no produce ningún efecto negativo sobre el ruido de los stavelets.

### Interferencia electromagnética

El stavelet con conversión DC-DC se probó junto a un prototipo de *VersatileLink*, el sistema de transmisión óptica que se utilizará en la actualización del detector de trazas para comunicarse con los módulos.

Las pruebas se llevaron a cabo con una temperatura de 12°C en el sistema de refrigeración y una tensión de polarización de los sensores de 250 V. En el momento de realizarse estas pruebas, el sistema de refrigeración no funcionaba correctamente y

reducía su capacidad de enfriamiento tras un tiempo de funcionamiento, por lo que la temperatura no se mantuvo estable durante las pruebas.

La secuencia de pruebas para la medida del ruido ENC fue la siguiente:

- Pruebas 1 y 2: prototipo no colocado en las inmediaciones del stavelet. Medida de la referencia de ruido.
- Prueba 3: prototipo de VersatileLink situado cerca de la tarjeta EoS, con los cables de alimentación colocados a lo largo del stavelet, encendido.
- Prueba 4: igual que el anterior, pero con los cables de alimentación del prototipo pasando desde la tarjeta EoS, como correspondería a la configuración realista en el detector. El prototipo está encendido.
- Prueba 5: prototipo colocado directamente encima de la tarjeta EoS, encendido.
- Prueba 6: VersatileLink colocado sobre un grupo de chips en el módulo M3, encendido.
- Pruebas 7 y 8: prototipo apagado para volver a ver la referencia de ruido.
- Prueba 9: repetición de la prueba 6.

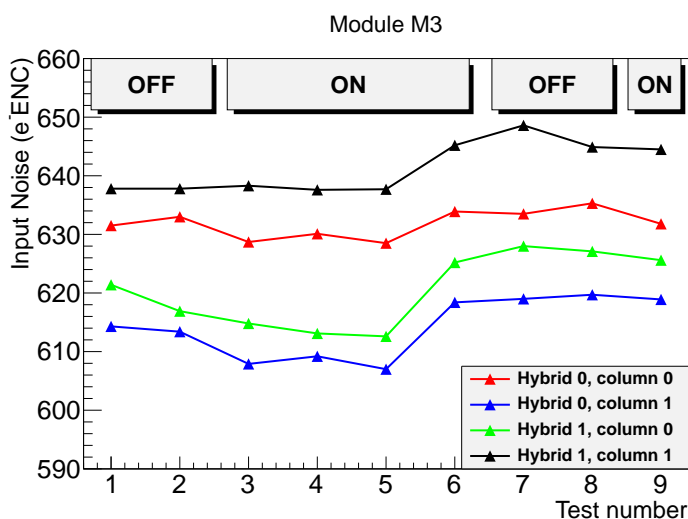


**Figure 8.14: Ruido ENC medido en el módulo M3, con interferencia del prototipo de VersatileLink.**

Por otro lado, la medida de ruido de doble disparo (DTN) se hizo en una secuencia diferente:

1. Sobre el módulo M3, encendido.
2. Sobre el módulo M3, apagado.
3. Sobre la tarjeta EoS (orientado longitudinalmente), encendido.
4. Sobre la tarjeta EoS, apagado.

5. Sobre la tarjeta EoS, apagado.
6. Sobre la tarjeta EoS, encendido.
7. Sobre la tarjeta EoS, girado 90°, encendido.
8. Sobre la tarjeta EoS, girado 90°, apagado.

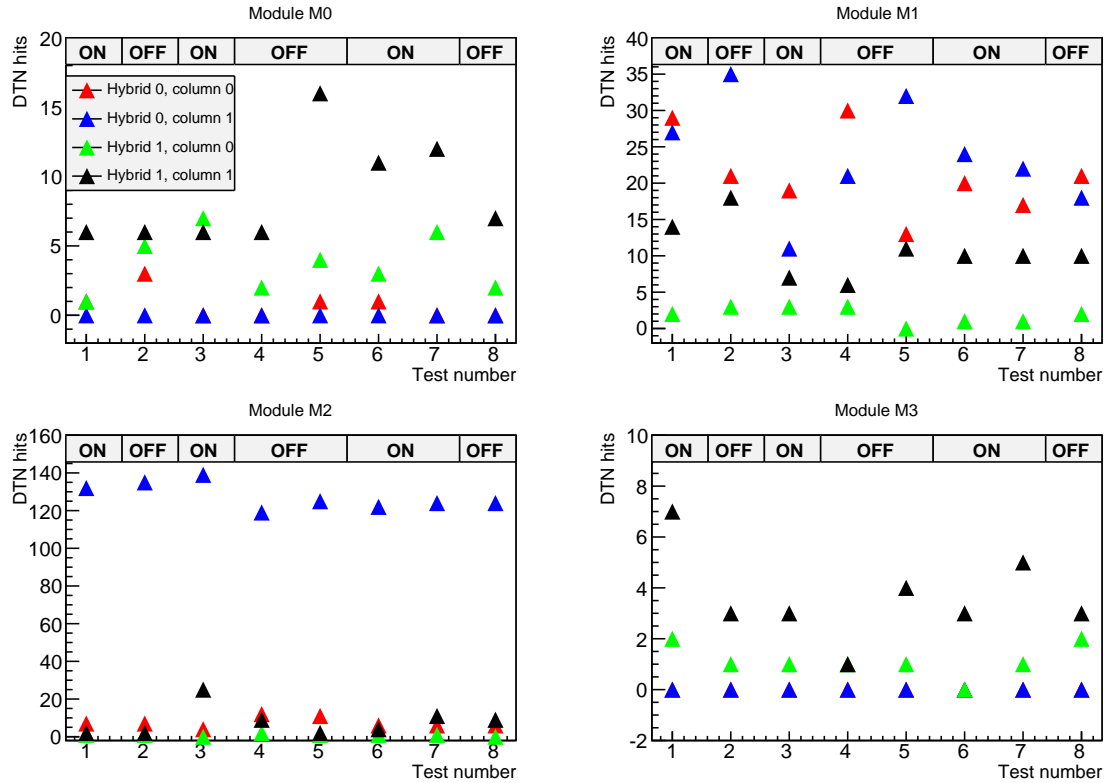


**Figure 8.15: Ruido de doble disparo con umbral a 0.5 fC, con interferencia del prototipo de VersatileLink.**

Para la medida de DTN, se activaron todos los módulos del stavelet.

La disponibilidad del prototipo tuvo lugar cuando únicamente el stavelet con conversión DC-DC se encontraba en el laboratorio, por lo que esta prueba no se pudo repetir en el stavelet con alimentación serie.

Los resultados mostrados en las Figuras 8.14 y 8.15 permiten asegurar que el prototipo no provoca interferencias en el stavelet con conversión DC-DC.

Como se mencionó antes, la temperatura del stavelet en el momento de las pruebas no se mantuvo estable, debido a un malfuncionamiento del refrigerador. El aumento de ruido mostrado en la Figura 8.14 entre la prueba 5 y la 6 sigue a un aumento de la temperatura en los módulos del stavelet.

La evidencia de que no se trata de un aumento de ruido por interferencia del prototipo de VersatileLink se observa en las medidas 7 y 8, durante los cuales el prototipo permaneció apagado y el ruido se mantuvo ligeramente elevado.

En las medidas de ruido ENC se habilitó únicamente el módulo M3 del stavelet, que es el más próximo a la tarjeta de adquisición y es en sus inmediaciones donde se situó el prototipo de VersatileLink.

Los resultados que se pueden ver en la Figura 8.15 muestran que el ruido de doble disparo se mantiene estable en todo el stavelet para los periodos en los que el prototipo de VersatileLink está encendido, con respecto a los periodos en los que está apagado.

El prototipo de VersatileLink probado funciona con en la segunda ventana de transmisión óptica, a una longitud de onda de 1310 nm, la cual no genera señales en el silicio. Por esta razón, no se llevó a cabo ninguna prueba de fugas de luz, al contrario de lo que se hizo con el SCT, dado que los láseres funcionan a 850 nm [40].

### Pruebas individuales y conjuntas de los dos stavelets

Los dos stavelets se probaron de forma independiente, y también alimentados y leídos de forma simultánea y con el mismo sistema de adquisición.

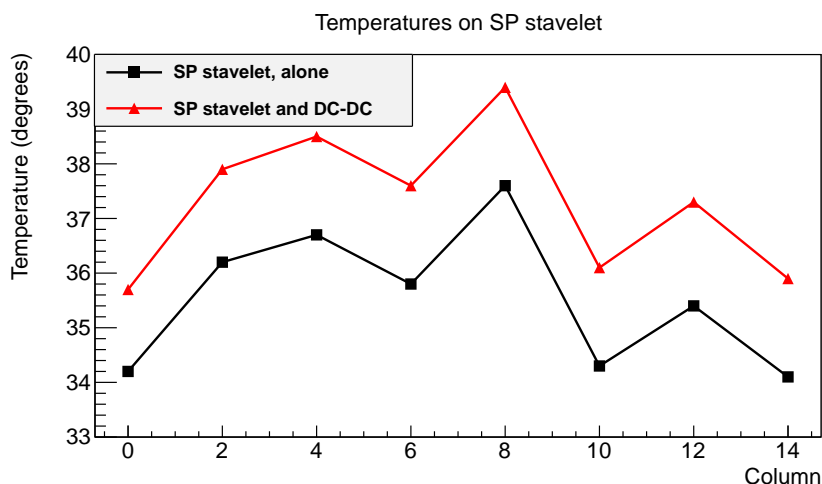


**Figure 8.16: Temperaturas en los híbridos del stavelet serie operado por separado y junto al stavelet DC-DC.**

La tarjeta de adquisición dispone de dos grupos de conectores que pueden emplearse para medir dos stavelets simultáneamente. La conexión del circuito de refrigeración para estas pruebas se hizo en serie, por la falta de disponibilidad de conectores para hacerlo en paralelo. El stavelet con alimentación serie se situó segundo en la línea de refrigeración, lo que provocó que la temperatura de sus módulos fuera superior que en el caso de operarse por separado.

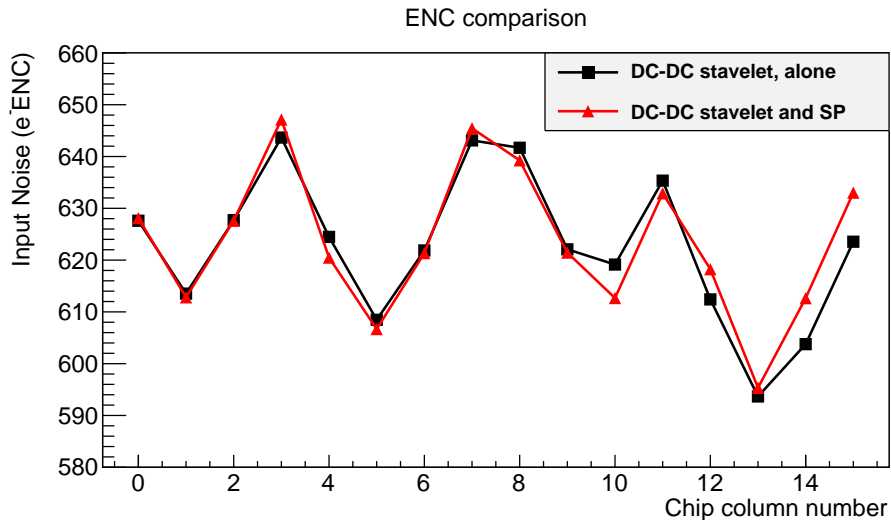
La Figura 8.16 muestra la comparación entre temperaturas del stavelet con alimentación serie operado por separado y después de conectarlo después del stavelet con alimentación DC-DC.

En el stavelet con alimentación DC-DC no se observaron diferencias de temperatura entre la operación por separado y la operación junto al stavelet con alimentación serie.

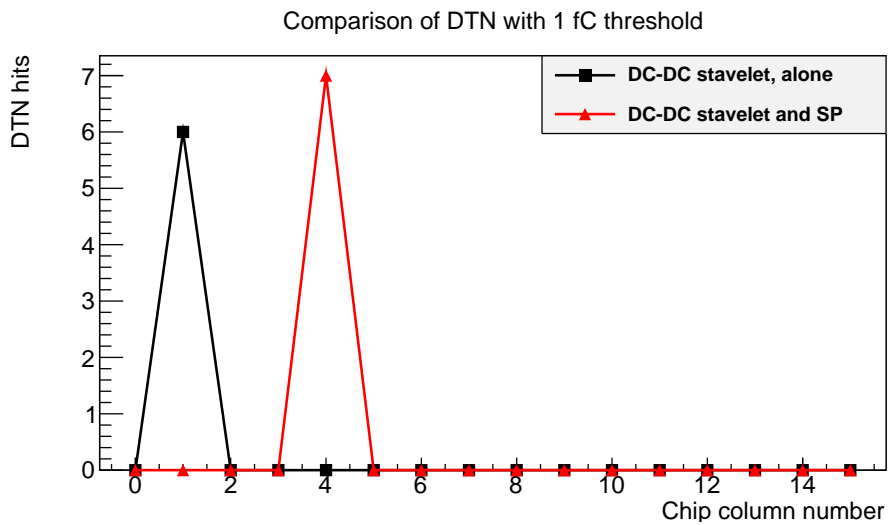
Los resultados de la Figura 8.17 muestran que el stavelet DC-DC no ve mermadas sus prestaciones al ser medido junto al stavelet con alimentación serie.

De la misma manera, la Figura 8.18 muestra que en el stavelet con alimentación serie no se observa aumento del ruido más allá del incremento de temperatura de los híbridos, derivado de la configuración del sistema de refrigeración.

Las únicas precauciones a considerar para probar ambos stavelets de forma simultánea sin que se produzca aumento del ruido es utilizar un apantallado adecuado en las líneas de alimentación de los híbridos, reduciendo el ruido en modo común.

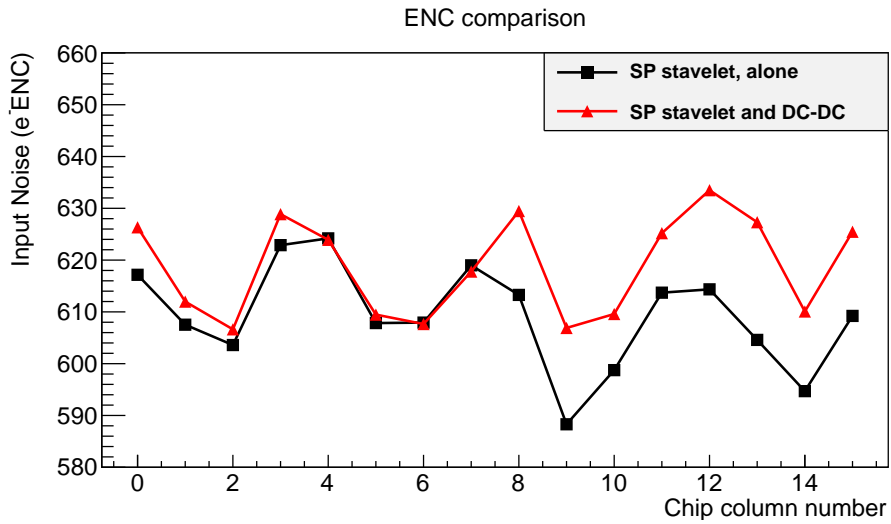


(a) Ruido en el stavelet DC-DC.

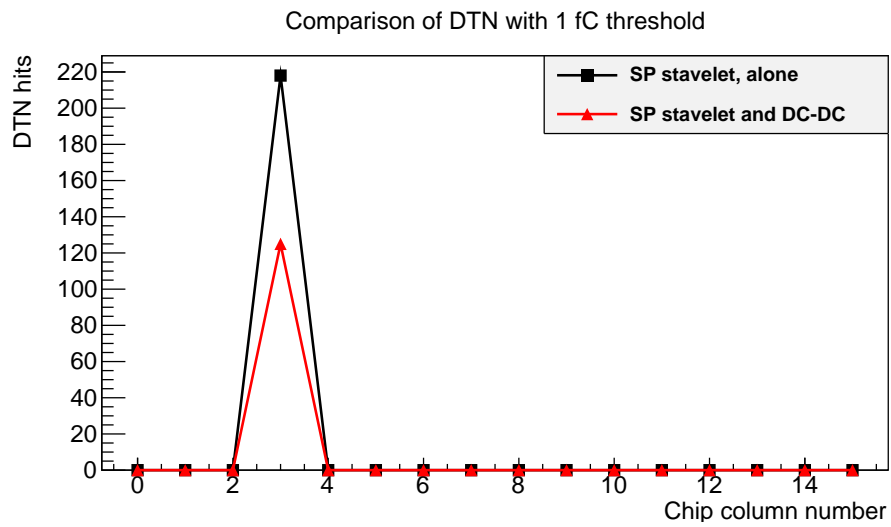


(b) Ruido de doble disparo en el stavelet DC-DC.

Figure 8.17: Diferencias de ruido en el stavelet DC-DC cuando funciona independientemente y cuando funciona junto al stavelet serie.



(a) Ruido en el stavelet serie.



(b) Ruido de doble disparo en el stavelet serie.

Figure 8.18: Diferencias de ruido en el stavelet serie cuando funciona independientemente y cuando funciona junto al stavelet DC-DC.

En particular, el stavelet con alimentación serie es más susceptible al ruido en modo común.

### 8.2.6 Stave de doce módulos con alimentación DC-DC

El primer stave con doce módulos se terminó de construir a finales de 2013 en RAL. Se montaron módulos procedentes de diversos institutos, todos ellos de “grado A”, es decir, de la mejor calidad. Los institutos que contribuyeron con módulos fueron las Universidades de Cambridge (Reino Unido), California Santa Cruz (Estados Unidos), Liverpool (Reino Unido), Friburgo (Alemania) y Glasgow (Reino Unido).

La Figura 8.19 muestra una fotografía del stave completo con los doce módulos montados sobre la estructura. El diseño con doce módulos por cada lado es el que se realizó para los módulos con chips de 250 nanómetros, al contrario del diseño con trece módulos para los chips de 130 nanómetros [58].

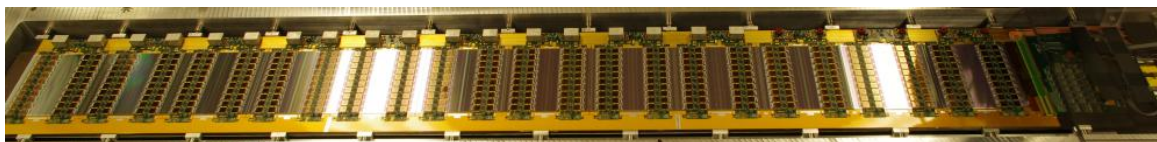


**Figure 8.19:** El stave con alimentación DC-DC, con los doce módulos montados.

Los convertidores DC-DC utilizados con el stave no son los mismos que en el stavelet. Se trata de convertidores en tándem, con una entrada de alimentación y dos salidas, una para cada híbrido de un módulo.

Las pruebas del stave se hicieron por etapas. En lugar de montar todos los módulos de una vez, se montaron en turnos y se probaron en la siguiente secuencia: tres, nueve y doce módulos.

#### Stave con tres módulos

Los tres primeros módulos fueron los más alejados de la tarjeta de lectura (EoS). Se observó que las temperaturas de los convertidores eran demasiado elevadas, concretamente en los inductores de cada convertidor.

Para corregirlo, se sustituyó el apantallado típico, un soporte de plástico envuelto en pintura de cobre, por uno fabricado con cobre estañado. Además, se añadió relleno térmico para incrementar la transferencia de calor hacia el exterior.

También se encontraron problemas con la integridad de las señales, por lo que se corrigieron las terminaciones de los búferes LVDS en la tarjeta EoS.

#### Stave con nueve módulos

Los seis módulos siguientes se ensamblaron de la misma manera que los tres primeros, con la salvedad de utilizar pegamento con mayor conductividad térmica para los convertidores DC-DC. Con ello se consiguió disminuir la temperatura de los convertidores.

Se equiparon los convertidores de los nuevos módulos con sensores de temperatura para comprobar que la refrigeración es correcta. Los sensores se montaron sobre la placa de circuito impreso y dentro de uno de los apantallamientos, junto al inductor,

de forma alterna entre módulos (en el módulo 3 dentro del apantallamiento, el siguiente sobre la placa).

Los problemas de integridad de señal continuaron con estos módulos y hubo que hacer ajustes en las terminaciones.

### Stave con doce módulos

Los tres últimos módulos del stave se ensamblaron de la misma forma que los seis anteriores, incluyendo los convertidores DC-DC.

Las pruebas del stave con tres, nueve y doce módulos se llevaron a cabo con el refrigerante a 13°C, la tensión de polarización de los sensores a 250 V y la humedad se mantuvo por debajo del 10% con nitrógeno.

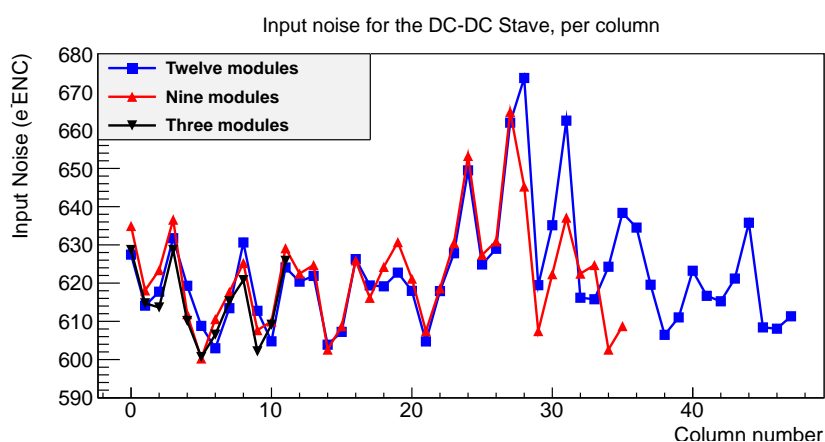


Figure 8.20: Ruido del stave DC-DC con doce módulos.

Los resultados para todas las pruebas llevadas a cabo en cada etapa de ensamblado del stave se presentan en esta sección. El ruido del stave con doce módulos se muestra en la Figura 8.20, incluyéndose las medidas realizadas con tres y nueve módulos.

En los resultados se observa que los niveles de ruido ENC se mantienen estables cuando se incrementa el número de módulos a lo largo del stave.

Dos módulos presentan valores de ruido mayores de lo normal, correspondientes a híbridos que fueron construidos de forma diferente a los demás. Leves defectos en el proceso de fabricación provocan que tengan un ruido mayor de lo que les corresponde.

La temperatura de los híbridos durante las pruebas con tres, nueve y doce módulos se muestra en la Figura 8.21. El leve aumento entre nueve y doce módulos contrasta con el menor ruido medido en algunos híbridos con doce módulos.

El flujo de nitrógeno estaba a una temperatura entre 7 y 15°C inferior en el momento de hacer las pruebas con doce módulos respecto de la temperatura cuando se hicieron las pruebas con nueve módulos, por lo que contribuyó a reducir la temperatura en los chips.

Por otro lado, la medida de ruido de doble disparo se muestra en la Figura 8.22, para los doce módulos.

Con umbrales elevados, 1 fC y 0.75 fC, no se observa ningún incremento en la cuenta de ruido. Para el umbral de 0.5 fC algunos híbridos presentan picos, debidos a algunos canales ruidosos que se pueden encontrar en las cuentas con umbrales más bajos.



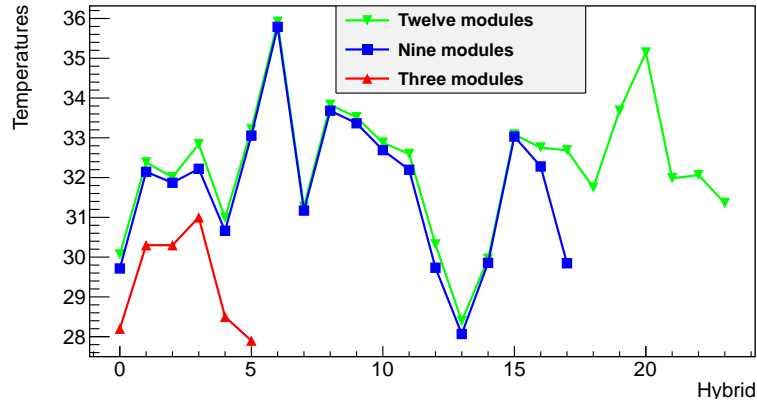
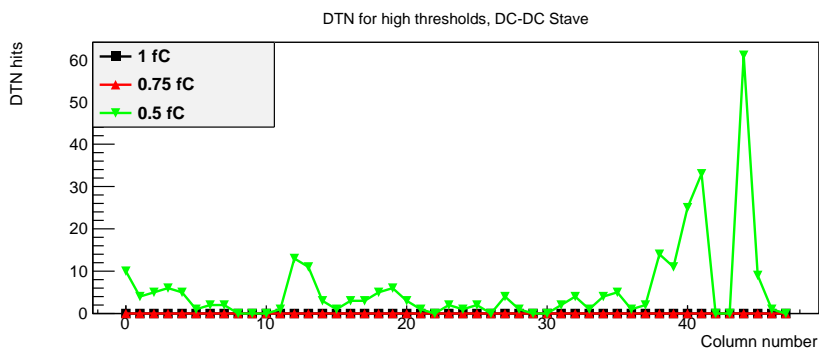
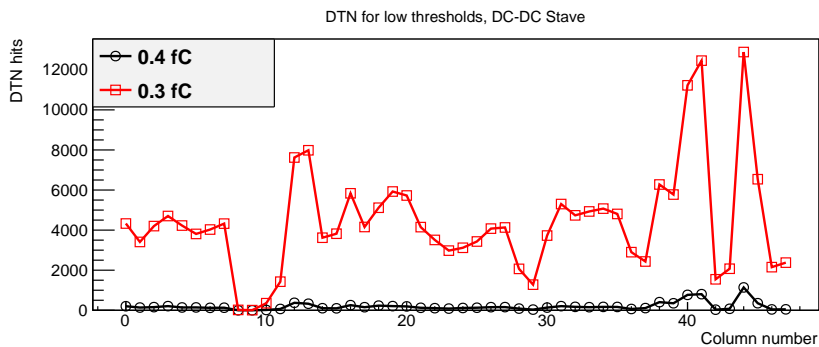


Figure 8.21: Temperaturas medidas en el stave durante las pruebas.



(a) DTN en el stave 250 con doce módulos, umbrales altos.



(b) DTN en el stave 250 con doce módulos, umbrales bajos.

Figure 8.22: Ruido de doble disparo en el stave DC-DC con doce módulos.

Los resultados muestran que las prestaciones de las estructuras multi-módulo con hasta doce módulos son excelentes, por lo que la viabilidad de los staves como estructura para implementar los barriles del detector de bandas de semiconductor está demostrada.

### 8.3 Cálculo del poder de frenada en el SCT

La pérdida de energía es consecuencia del poder de frenada de un material, o  $dE/dx$ , y es un efecto característico del paso de las partículas cargadas a través de un material.

En el silicio, la energía perdida por las partículas genera pares electrón-hueco, que

equivalen a una carga, la cual puede ser medida. Algunos detectores se construyen con el objetivo de medir esta energía, mientras que otros se diseñan únicamente para saber si se ha producido el paso de una partícula por ellos o no (detectores binarios).

### 8.3.1 Introducción

Los dos sub-detectores del detector de trazas basados en silicio, el detector de píxeles y el de bandas de silicio (SCT) del experimento ATLAS no fueron diseñados para realizar medidas de energía, sino que son detectores binarios.

Sin embargo, ambos detectores implementan en sus sistemas de adquisición temporizadores que miden durante cuánto tiempo ha permanecido la señal generada por las partículas por encima de un umbral pre-configurado.

El detector de píxeles dispone de un contador de 8 bits, por lo que puede contar hasta 256 intervalos de 25 ns [109]. Por otra parte, el detector de bandas de silicio usa un contador de 3 bits, lo que reduce la resolución en partículas que depositan mayor cantidad de carga.

### 8.3.2 Selección de eventos y de trazas

Este estudio está basado en los datos recogidos durante las colisiones protón-protón entre 2010 y 2012. Las colisiones en 2010 y 2011 se produjeron a 7 TeV de energía del centro de masas, mientras que las colisiones en 2012 fueron a 8 TeV.

La luminosidad integrada total que se registró en estos conjuntos de datos es  $1.76 \text{ fb}^{-1}$ , con un total de 11 millones de eventos. Los datos están almacenados en Ntuplas del SCT (*SCT Ntuples*), que contienen información de las trazas, tales como el momento, puntos de aproximación al vértice primario y datos provenientes del detector de píxeles.

Los eventos se seleccionan de entre aquellos que tienen lugar durante el estado “Ready” del SCT. Los eventos de interés deben provenir de interacciones protón-protón, para lo cual se exige que cumplan los siguientes requisitos:

- Al menos un vértice primario reconstruido en el evento. De esta manera se pueden descartar eventos que provengan de disparos provocados por rayos cósmicos.
- El vértice primario debe tener al menos cuatro trazas asociadas.
- Al menos una de las trazas que formen parte del evento debe cumplir otra serie de requisitos:
  - Momento transversal  $p_T > 500 \text{ MeV}/c$ .
  - Seis impactos en el SCT.
  - Un impacto en el detector de píxeles.
  - Distancia transversal  $|d_0| < 1.5 \text{ mm}$ .
  - Distancia longitudinal tal que  $|z_0 \sin \theta| < 1.5 \text{ mm}$ .

De esta forma, se buscan eventos que tengan alguna traza de vértice primario con un momento suficientemente elevado.

Para cada evento que pase estos cortes, se seleccionan las trazas para calcular su  $dE/dx$ . Las trazas se seleccionan si cumplen además una serie de requisitos de calidad, que son los siguientes:

- Al menos 8 impactos buenos en la traza. Un impacto que no es “bueno” se denomina *outlier*.
- Momento transversal  $p_T > 100 \text{ MeV}/c$ .
- Momento total de la traza menor que  $2500 \text{ MeV}/c$ .
- $|z_0| < 100 \text{ mm}$ .
- Dos impactos buenos en el detector de píxeles.

De todas las trazas que cumplen con los requisitos se extrae la información sobre intervalos de tiempo sobre umbral de la Ntupla, para aplicar el método que se describe a continuación y calcular su  $dE/dx$ . La Ntupla contiene los datos de intervalos de tiempo sobre umbral de todas las bandas que han generado señal, para todos los impactos de una traza.

### 8.3.3 Reconstrucción de $dE/dx$

En el SCT, el umbral de carga está configurado a 1 fC ( $6242 e^-$ ) y se dispone de tres intervalos de 25 ns en los cuales se registra la carga depositada por las partículas que impactan en los sensores. Se calibra la temporización del detector tal que se registra un patrón 01x. El modo de lectura además varía en función del modo de funcionamiento del LHC.

Para la toma de datos en 2010 se usó un patrón de lectura XXX, para un espaciado de los paquetes de protones de 75 ns. Para los datos en 2011 y 2012 se usó un espaciado de 50 ns con un patrón de lectura X1X.

#### Cálculo de $dE/dx$ en el SCT

La fórmula para calcular el poder de frenada en el SCT es la siguiente (en unidades arbitrarias):

$$dE/dx_{\text{SCT}} = \frac{\sum_{\text{Track\_hits}} \sum_{\text{Hit\_strips}} w_{\text{strip}}^i \cos \alpha}{\text{Track\_hits}} \quad [\text{a.u.}] \quad (8.3)$$

Donde  $w_{\text{strip}}^i$  es el peso asignado según el número de intervalos de 25 ns para cada impacto (por defecto, 1, 2 y 3). El ángulo  $\alpha$  es la proyección de los ángulos locales  $\theta$  y  $\phi$ , redefinidos entre  $-\pi/2$  y  $\pi/2$ :

$$\alpha = \tan^{-1} \left( \sqrt{\tan^2 \theta' + \tan^2 \phi'} \right) \quad (8.4)$$

$$\theta' = \begin{cases} \theta_0^{\text{local}} - \pi & \text{if } \theta_0^{\text{local}} > \pi/2 \\ \theta_0^{\text{local}} + \pi & \text{if } \theta_0^{\text{local}} < \pi/2 \end{cases} \quad (8.5)$$

$$\phi' = \begin{cases} \phi_0^{\text{local}} - \pi & \text{if } \phi_0^{\text{local}} > \pi/2 \\ \phi_0^{\text{local}} + \pi & \text{if } \phi_0^{\text{local}} < \pi/2 \end{cases} \quad (8.6)$$

La Figura 8.23 muestra el resultado de la distribución de la  $dE/dx$  calculada con los datos del SCT para los datos recogidos en 2010.

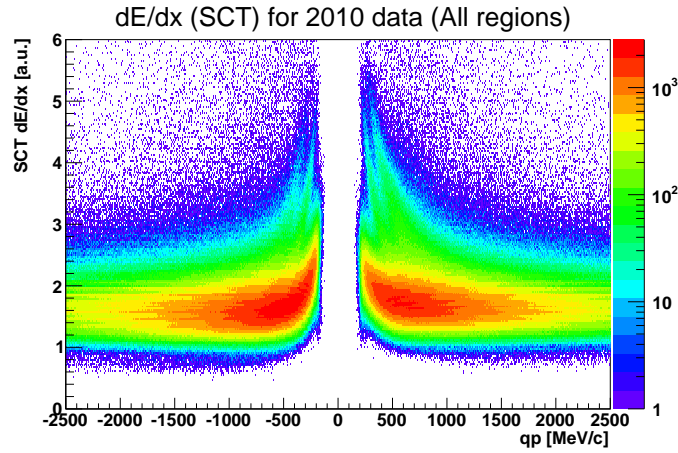


Figure 8.23:  $dE/dx$  calculada en el SCT para datos de 2010.

### 8.3.4 Identificación de partículas

Uno de los objetivos del estudio es evaluar la capacidad de discriminar tipos de partículas mediante el cálculo de  $dE/dx$  en el SCT. Dado que no existen simulaciones Monte Carlo para el SCT con información realista sobre los intervalos de tiempo, no es posible comparar la eficiencia de este cálculo con información de verdad.

Por ello, se hace uso del cálculo existente en el detector de píxeles. La información de identificación aparece en las Ntuplas del SCT desde 2011.

En el detector de píxeles se considera que una partícula está bien identificada (píon, kaón, protón) cuando la verosimilitud normalizada es mayor a 0.9. Esta verosimilitud normalizada se define a partir del vector de verosimilitudes para cada tipo de partícula que está almacenado en la Ntupla:

$$P_i^{\text{norm,Pixel}} = \frac{P_i^{\text{Pixel}}}{P_{\pi}^{\text{Pixel}} + P_K^{\text{Pixel}} + P_p^{\text{Pixel}}} \quad (8.7)$$

Donde  $i = \pi/K/p$ .

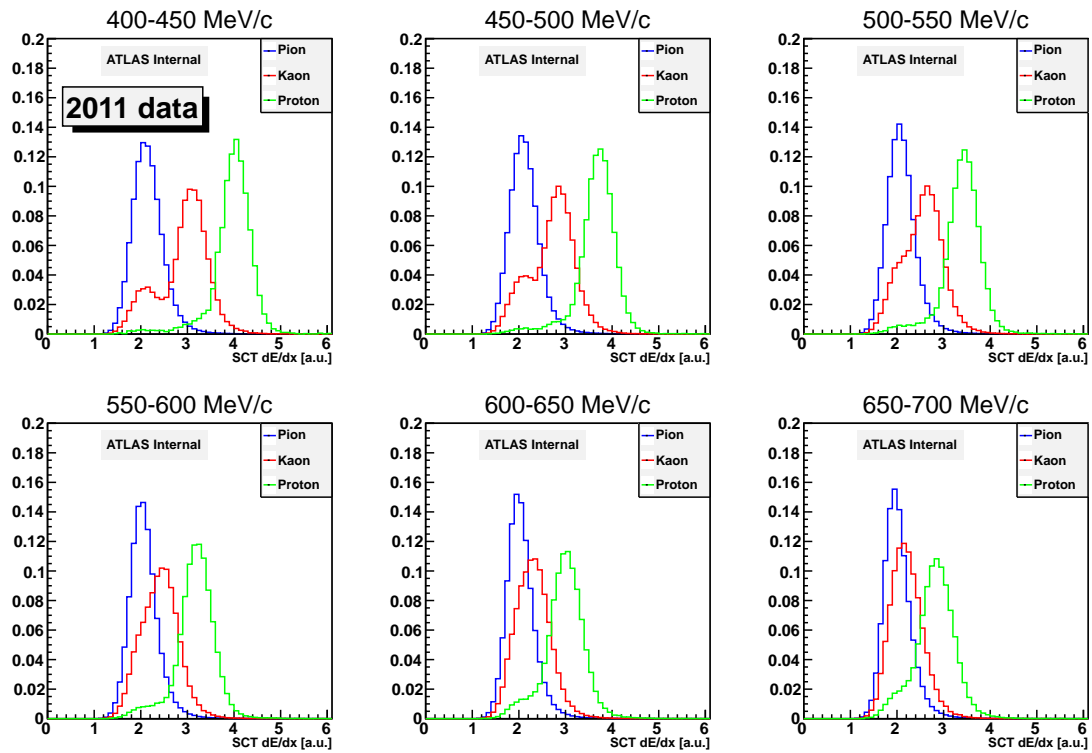
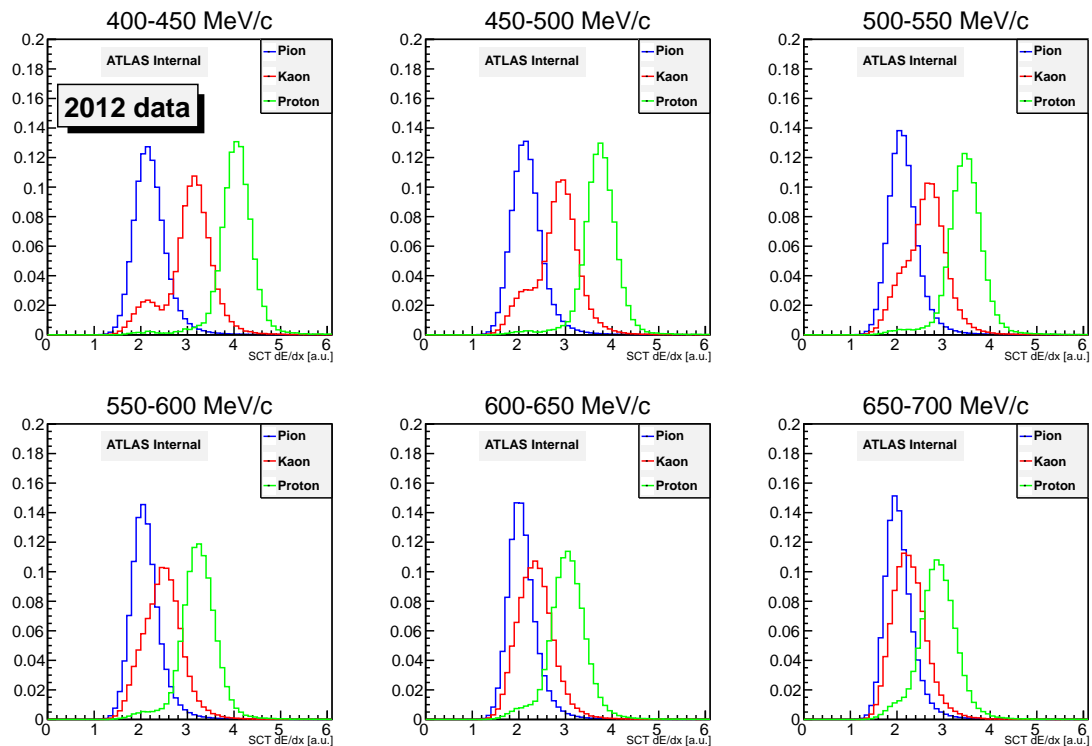
La Figura 8.24 muestra la distribución de  $dE/dx$  calculada en el SCT para trazas positivas, en los años 2011 y 2012.

Se observa en las gráficas que existe cierta capacidad para separar las bandas, por lo que es posible en principio explotar esta separación. Haciendo uso de esta información, se hace un ajuste a una gaussiana de las curvas, de manera que se puede calcular la verosimilitud de una  $dE/dx$  dada para los tres tipos de partículas:

$$P_i^{\text{SCT}} = \frac{1}{\sqrt{2\pi}\sigma_{dE/dx_i}} \exp\left(-\frac{(dE/dx_{\text{SCT}} - dE/dx_i)^2}{2\sigma_{dE/dx_i}^2}\right) \quad (8.8)$$

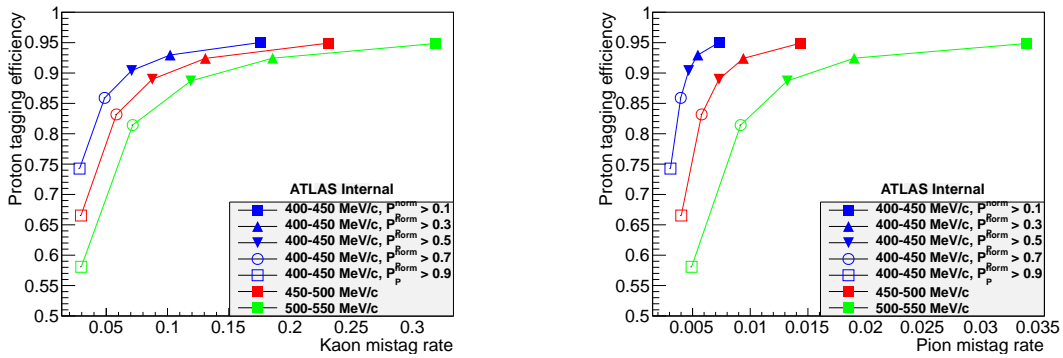
Siendo  $(dE/dx)_i$  y  $\sigma_{dE/dx_i}$  la media y varianza del ajuste para cada tipo de partícula en cada rango de momento, y  $i = \pi/K/p$ .

La verosimilitud de cada tipo de partícula se normaliza de la misma forma en la que se normaliza la calculada por el detector de píxeles y se calculan las tasas de eficiencia y de fallo de etiquetado para protones:

(a)  $dE/dx$  del SCT, datos de 2011.(b)  $dE/dx$  del SCT, datos de 2012.Figure 8.24: Distribuciones de  $dE/dx$  en el SCT para datos de 2011 y 2012, trazas positivas y vértices primarios.

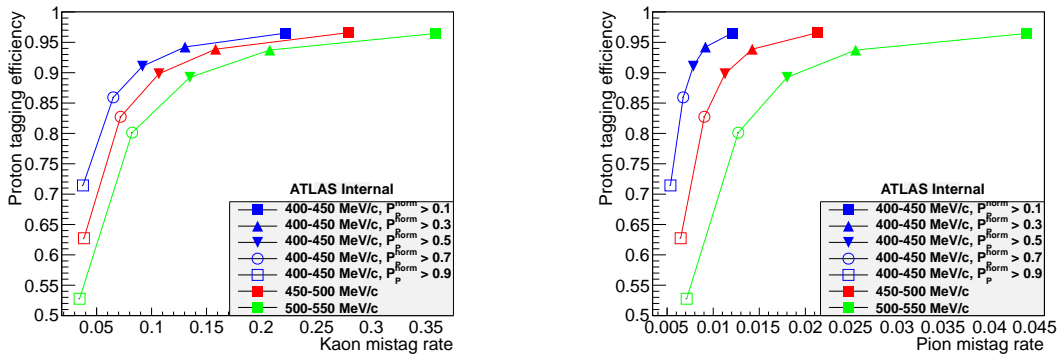
$$r_p^\pi = \frac{N(\text{Pixel} = \pi, \text{SCT} = p)}{N(\text{Pixel} = \pi)} \quad r_p^K = \frac{N(\text{Pixel} = K, \text{SCT} = p)}{N(\text{Pixel} = K)} \quad (8.9)$$

Siendo  $N(\text{Pixel} = i)$  el número de trazas que el detector de píxeles etiquetaría como verdaderos  $i$  (pión, kaón, protón) y  $N(\text{Pixel} = i, \text{SCT} = j)$  es el número de trazas que el detector de píxeles considera verdaderas  $i$  y que el SCT etiquetaría como  $j$ .



(a) Eficiencia de etiquetado de protones frente a tasa de fallos de etiquetado de kaones. (b) Eficiencia de etiquetado de protones frente a tasa de fallos de etiquetado de piones.

**Figure 8.25:** Eficiencia de etiquetado de protones en función del corte de verosimilitud  $P_p^{\text{norm}, \text{SCT}}$ , datos de 2011.



(a) Eficiencia de etiquetado de protones frente a tasa de fallos de etiquetado de kaones. (b) Eficiencia de etiquetado de protones frente a tasa de fallos de etiquetado de piones.

**Figure 8.26:** Eficiencia de etiquetado de protones en función del corte de verosimilitud  $P_p^{\text{norm}, \text{SCT}}$ , datos de 2012.

Con estas definiciones, se hicieron varios cortes de verosimilitud normalizada en el SCT, 0.1, 0.3, 0.5, 0.7 y 0.9. Para estos cortes, se observó la tasa de eficiencia frente al fallo de etiquetado de los protones. Los resultados se muestran en las Figuras 8.25 y 8.26, para los datos de 2011 y 2012, respectivamente.

Se obtiene una eficiencia máxima del 95% con un fallo de etiquetado de piones por protones inferior al 5% y de kaones por protones inferior al 40%, en 2012.

### 8.3.5 Estabilidad a largo plazo

Dado que el SCT no se diseñó para efectuar medidas de energía, la capacidad de hacer identificación de partículas es limitada. Sin embargo, existe una aplicación del cálculo de  $dE/dx$  que resulta interesante desde el punto de vista del rendimiento del detector. Dado que la  $dE/dx$  está directamente relacionada con la carga depositada por las partículas y la carga recogida por los detectores se reduce con el daño por radiación, se puede analizar el valor de  $dE/dx$  a lo largo del tiempo, como forma de monitorizar el daño por radiación en el detector.

Se ha optado por monitorizar la media de  $dE/dx$  calculada en protones positivos con momento entre 500 y 550 MeV/ $c$ . La identificación de protones se ha realizado usando un método de corte geométrico de la  $dE/dx$  calculada por el detector de píxeles, para poder extraer los protones desde el comienzo de las operaciones del detector.

Asimismo, es necesario tener una buena temporización del detector, por lo que se efectuaron correcciones en ciertas fechas señaladas. El intervalo de tiempo medio en el SCT para los protones identificados por el detector de píxeles varía con el tiempo, y afecta al cálculo de  $dE/dx$  efectuado en el SCT. Es posible corregir levemente estas variaciones, pero lo más importante es conocer que estas variaciones existen para poder interpretar correctamente los datos.

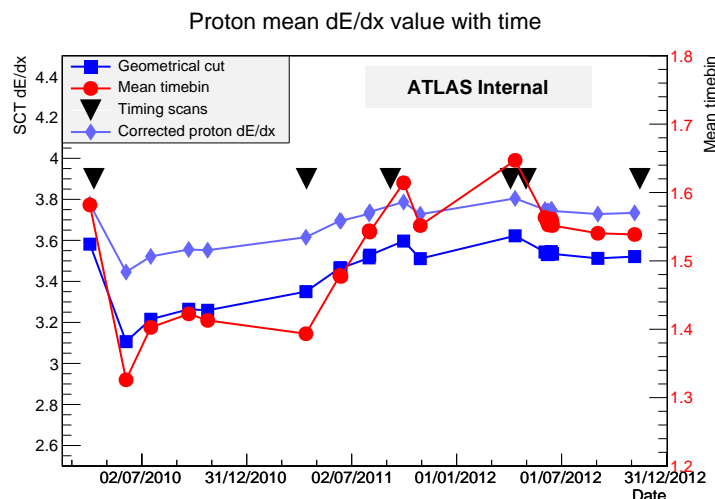


**Figure 8.27: Evolución de la  $dE/dx$  media de protones con el tiempo.**

La Figura 8.27 muestra la evolución de la  $dE/dx$  media de los protones con el tiempo, incluyendo el ajuste del tamaño medio de los intervalos de tiempo. Los incrementos de  $dE/dx$  se deben a leves desajustes de la temporización, que provocan que un pulso pueda ser detectado por encima del umbral durante un intervalo de tiempo más del que le correspondería.

Las variaciones observadas son inferiores al 17% en la gráfica no corregida, mientras que son inferiores al 10% en la versión corregida. La tendencia desde el final de 2011 es de una variación alrededor del 2%.

Dado que el SCT aún no padece los problemas derivados del daño por radiación que reducen la carga recogida por los detectores, no es posible observar variación en ese sentido. Sin embargo, esperamos poder aplicar este método en el futuro para monitorizar el daño por radiación, cuando la luminosidad acumulada sea mucho mayor.

## 8.4 Conclusiones

En esta tesis se ha presentado el trabajo realizado con detectores de bandas de silicio que se han prototipado para la Fase 2 de la actualización del experimento ATLAS. Esta actualización tendrá lugar para que el detector de trazas del experimento sea capaz de funcionar con los requisitos de luminosidad, granularidad y resistencia a la radiación del LHC de alta luminosidad.

Los resultados sobre estructuras multi-módulo son prometedores y permiten verificar que los diseños propuestos para la lectura agregada de módulos y su alimentación son factibles. El aumento en el número de canales de lectura, con el consiguiente incremento en la potencia eléctrica consumida, hace necesario un cambio importante en la forma de alimentar la electrónica en los detectores.

La forma de adquisición de datos también cambiará para reducir el número de líneas de datos que van desde los módulos a la sala en la que se procesa la información. Para ello se agregarán trece módulos en una línea de datos compartida.

En el contexto de esta tesis se han prototipado y evaluado varios componentes, que implementan estas reducciones de líneas. Los resultados muestran que el rendimiento de los módulos no se ve perjudicado por la multiplexación de líneas de alimentación, lectura de los módulos o líneas de alto voltaje.

El primer prototipo de estructura del barril con doce módulos también ha sido medido con éxito.

El trabajo presentado en esta tesis continuará con la evolución de los chips en proceso de 130 nm, y se deberán probar las mismas estructuras con módulos que incluyan este chip.

Asimismo, se ha presentado un segundo tema de investigación, consistente en estudiar la posibilidad de calcular el poder de frenada,  $dE/dx$ , en el detector de bandas de silicio (SCT) del experimento ATLAS. A pesar de que no fue diseñado para realizar esta tarea, es posible realizar un cálculo aproximado de este parámetro. Se ha estudiado la aplicación de este cálculo como forma de hacer identificación de partículas en el SCT y para hacer una monitorización del daño debido a la radiación en los sensores de silicio.



# Acronyms

**ABC** ATLAS Binary Chip

**ALICE** A Large Ion Collider Experiment

**ASIC** Application-Specific Integrated Circuit

**ATLAS** A Toroidal LHC Apparatus

**BCC** Buffer Control Chip

**BSM** Beyond Standard Model

**CERN** Organisation Européenne pour la Recherche Nucléaire (European Organization for Nuclear Research)

**CMS** Compact Muon Solenoid

**DAQ** Data Acquisition

**DTN** Double Trigger Noise

**ENC** Equivalent Noise Charge

**EoS** End of Stave or End of Substructure

**FCal** Forward Calorimeter

**FE** Front-End

**FSI** Frequency Scanning Interferometry

**FZ** Float-Zone

**GaAs** Gallium Arsenide

**GBT** GigaBit Transceiver

**Ge** Germanium

**HCC** Hybrid Control Chip

**HEC** Hadronic Endcap Calorimeter

**HEP** High Energy Physics

**HL-LHC** High Luminosity-Large Hadron Collider

**HSIO** High Speed Input/Output  
**HV** High Voltage  
**IP** Interaction Point  
**LAr** Liquid Argon  
**LEP** Large Electron-Positron collider  
**LHC** Large Hadron Collider  
**LHCb** Large Hadron Collider beauty  
**LHCf** Large Hadron Collider forward  
**LS1** Long Shut-down 1  
**LS2** Long Shut-down 2  
**LS3** Long Shut-down 3  
**LV** Low Voltage  
**LVDS** Low Voltage Differential Signal  
**MIP** Minimum Ionizing Particle  
**NIM** Nuclear Instrumentation Module  
**NO** Noise Occupancy  
**PCA** Point of Closest Approach  
**PID** Particle IDentification  
**SCT** Semi-Conductor Tracker  
**SD** Strobe Delay  
**Si** Silicon  
**SiC** Silicon Carbide  
**SM** Standard Model  
**SP** Serial Powering  
**ToT** Time over Threshold  
**TOTEM** TOTAl Elastic and diffractive cross section Measurement  
**TRT** Transition Radiation Tracker  
**VME** VERSAmodule Eurocard

# Bibliography

- [1] L. Evans and P. Bryant, “LHC Machine,” *Journal of Instrumentation*, vol. 3, no. 08, p. S08001, 2008.
- [2] ATLAS Collaboration, “The ATLAS Experiment at the CERN Large Hadron Collider,” *Journal of Instrumentation*, vol. 3, no. 08, p. S08003, 2008.
- [3] ATLAS Collaboration, “Observation of a new particle in the search for the Standard Model Higgs boson with the ATLAS detector at the LHC,” *Physics Letters B*, vol. 716, no. 1, pp. 1 – 29, 2012.
- [4] ATLAS collaboration, “Performance of the ATLAS Inner Detector Track and Vertex Reconstruction in the High Pile-Up LHC Environment,” Tech. Rep. ATLAS-CONF-2012-042, CERN, Geneva, Mar 2012.
- [5] *ATLAS inner detector: Technical Design Report, 1*. Technical Design Report ATLAS, Geneva: CERN, 1997. ISBN 9290831022.
- [6] P. Wells, “Trackers and the effect of material on impact parameter and momentum resolution.” Excellence in Detectors and Instrumentation Technologies <http://indico.cern.ch/event/96989/contribution/14/material/slides/0.pdf>, February 2011.
- [7] J. Beringer *et al.*, “Review of Particle Physics, 2012-2013. Review of Particle Properties,” *Phys. Rev. D*, vol. 86, no. 1, p. 010001, 2012.
- [8] S. Haywood, “Impact Parameter Resolution in the Presence of Multiple- Scattering,” Tech. Rep. ATL-INDET-94-091. ATL-I-PN-91, CERN, Geneva, Jan 1994.
- [9] ATLAS Collaboration, “The ATLAS Inner Detector commissioning and calibration,” *Eur. Phys. J. C*, vol. 70, pp. 787–821. 34 p, Jun 2010.
- [10] R. L. Gluckstern, “Uncertainties in track momentum and direction, due to multiple scattering and measurement errors,” *Nuclear Instruments and Methods*, vol. 24, no. 0, pp. 381 – 389, 1963.
- [11] Paul Avery, “Applied Fitting Theory I General Least Squares Theory,” *CLEO Note CBX 91-72*, 1991.
- [12] M. Limper, S. Bentvelsen, and A. P. Colijn, *Track and vertex reconstruction in the ATLAS inner detector*. PhD thesis, Amsterdam, The University of Amsterdam, Amsterdam, 2009. Presented on 12 Oct 2009.

- [13] T. G. Cornelissen, P. F. van der Heijden, F. L. Linde, S. C. M. Bentvelsen, and P. M. Kluit, *Track Fitting in the ATLAS Experiment*. PhD thesis, U. Amsterdam, Amsterdam, 2006. Presented on 12 Dec 2006.
- [14] Fruhwirth, R., “Application of Kalman filtering to track and vertex fitting,” *Nuclear Instruments and Methods*, vol. A262, pp. 444–450, 1987.
- [15] Rainer Mankel, “ranger - a Pattern Recognition Algorithm for the HERA-B Main Tracking System - Part I: The HERA-B Pattern Tracker.” HERA B 97-82, Apr 1997.
- [16] P. Billoir and S. Qian, “Fast vertex fitting with a local parametrization of tracks,” *Nuclear Instruments and Methods in Physics Research Section A: Accelerators, Spectrometers, Detectors and Associated Equipment*, vol. 311, no. 1–2, pp. 139 – 150, 1992.
- [17] R. Frühwirth *et al.*, *Data Analysis Techniques for High-Energy Physics; 2nd ed.* Cambridge monographs on particle physics, nuclear physics and cosmology, Cambridge: Cambridge Univ. Press, 2000. ISBN 9780521635486.
- [18] F. Ragusa and L. Rolandi, “Tracking at LHC,” *New Journal of Physics*, vol. 9, no. 9, p. 336, 2007.
- [19] Daniel Kollár and ATLAS Collaboration, “Alignment of the ATLAS inner detector tracking system,” *Journal of Physics: Conference Series*, vol. 219, no. 3, p. 032046, 2010.
- [20] W. R. Leo, *Techniques for Nuclear and Particle Physics Experiments. A How-to Approach*. Springer-Verlag, 1994. ISBN 9783642579202.
- [21] H. Spieler, *Semiconductor Detector Systems*. Oxford Science Publications, 2005. ISBN 9780198527848.
- [22] M. Valentan, M. Regler, and R. Frühwirth, “Generalization of the Gluckstern formulas II: Multiple scattering and non-zero dip angles,” *Nuclear Instruments and Methods in Physics Research Section A: Accelerators, Spectrometers, Detectors and Associated Equipment*, vol. 606, no. 3, pp. 728 – 742, 2009.
- [23] J. C. Bean, *Materials and Technologies for High Speed Devices*. John Wiley & Sons, 1990. ISBN 9780471623076.
- [24] G. Lutz, *Semiconductor Radiation Detectors*. Springer, 2007. ISBN 978-3540716785.
- [25] A. Owens, *Compound Semiconductor Radiation Detectors*. Series in Sensors, Hoboken: CRC Press, 2012. ISBN 9781439873120.
- [26] Kraner, H. W., “Radiation Damage in Silicon Detectors,” *Nuclear Instruments and Methods*, vol. A225, pp. 615–618, 1984.
- [27] D. Pitzl *et al.*, “Type inversion in silicon detectors,” *Nuclear Instruments and Methods in Physics Research Section A: Accelerators, Spectrometers, Detectors and Associated Equipment*, vol. 311, pp. 98–104, Jan. 1992.

- 
- [28] Michael Moll, *Radiation Damage in Silicon Particle Detectors, microscopic defects and macroscopic properties*. PhD thesis, 1999.
- [29] R. Wunstorff *et al.*, “Results on radiation hardness of silicon detectors up to neutron fluences of  $10^{15}$  n/cm<sup>2</sup>,” *Nuclear Instruments and Methods in Physics Research Section A: Accelerators, Spectrometers, Detectors and Associated Equipment*, vol. 315, no. 1–3, pp. 149 – 155, 1992.
- [30] F. Campabadal *et al.*, “Design and performance of the ABCD3TA ASIC for readout of silicon strip detectors in the ATLAS semiconductor tracker,” *Nuclear Instruments and Methods Physics Research Section A: Accelerators, Spectrometers, Detectors and Associated Equipment*, vol. 552, pp. 292–328, 2005.
- [31] A. Ahmad *et al.*, “The silicon microstrip sensors of the ATLAS semiconductor tracker,” *Nuclear Instruments and Methods in Physics Research Section A: Accelerators, Spectrometers, Detectors and Associated Equipment*, vol. 578, no. 1, pp. 98 – 118, 2007.
- [32] C. Jacoboni *et al.*, “A review of some charge transport properties of silicon,” *Solid-State Electronics*, vol. 20, no. 2, pp. 77 – 89, 1977.
- [33] S. McMahon, “Depletion Voltages in the SCT,” tech. rep., SCT Performance Meeting <https://indico.cern.ch/event/145348/contribution/1/1/material/slides/0.pdf>, December 2011.
- [34] A. Abdesselam *et al.*, “The ATLAS semiconductor tracker end-cap module,” *Nuclear Instruments and Methods in Physics Research. Section A: Accelerators, Spectrometers, Detectors, and Associated Equipment*, vol. 575, pp. 353–389, June 2007.
- [35] ATLAS Collaboration, “Operation and performance of the ATLAS semiconductor tracker,” *Journal of Instrumentation*, vol. 9, no. 08, p. P08009, 2014.
- [36] A. Chilingarov, “Generation current temperature scaling,” Tech. Rep. PH-EP-Tech-Note-2013-002, CERN, Geneva, Jan 2013.
- [37] B. Demirkoz, *Construction and Performance of the ATLAS SCT Barrels and Cosmic Tests*. PhD thesis, 2007.
- [38] A. Abdesselam *et al.*, “The data acquisition and calibration system for the ATLAS Semiconductor Tracker,” *Journal of Instrumentation*, vol. 3, no. 01, p. P01003, 2008.
- [39] S. Burdin, N. P. Hessey, and C. A. Magrath, “SCT Noise: A detailed investigation into its understanding and a future method for monitoring radiation damage.,” Tech. Rep. ATL-INDET-INT-2010-002, CERN, Geneva, Feb 2010.
- [40] P. W. Phillips, “Functional testing of the ATLAS SCT barrels,” *Nuclear Instruments and Methods in Physics Research Section A: Accelerators, Spectrometers, Detectors and Associated Equipment*, vol. A570, pp. 230–235, 2007.
-

- [41] P. A. Coe, D. F. Howell, and R. B. Nickerson, “Frequency scanning interferometry in ATLAS: remote, multiple, simultaneous and precise distance measurements in a hostile environment,” *Measurement Science and Technology*, vol. 15, no. 11, p. 2175, 2004.
- [42] F. Hubaut, “ATLAS studies on Higgs to diboson states,” Tech. Rep. ATL-PHYS-PROC-2013-108, CERN, Geneva, May 2013.
- [43] H. Zhu, “ATLAS Upgrades Towards the High Luminosity LHC,” *International Workshop: LHC on the March*, Nov 2012.
- [44] L. Rossi and O. Brüning, “High Luminosity Large Hadron Collider A description for the European Strategy Preparatory Group,” Tech. Rep. CERN-ATS-2012-236, CERN, Geneva, Aug 2012.
- [45] T. Flick, “Overview of the Insertable B-Layer (IBL) Project of the ATLAS Experiment at the Large Hadron Collider at CERN,” Tech. Rep. ATL-INDET-PROC-2013-006, CERN, Geneva, Jun 2013.
- [46] S. Welch and J. Dopke, “The ATLAS Pixel nSQP Readout Chain,” Tech. Rep. ATL-INDET-PROC-2012-018, CERN, Geneva, Oct 2012.
- [47] T. Weidberg, D. Robinson, C. García-Argos, M. Jones, and M. Goodrick, “Light-ABLE/TX Review.” Meeting <https://indico.cern.ch/event/246631/>, April 2013. University of Oxford.
- [48] A. R. Weidberg, “VCSEL Reliability in ATLAS and development of robust arrays,” Tech. Rep. ATL-COM-ELEC-2011-003, CERN, Geneva, Oct 2011.
- [49] 36th International Conference for High Energy Physics, *LHC Status and Future Upgrade Plans*, 2012.
- [50] LHC Performance Workshop - Chamonix, *Performance potential of the injectors after LS1*, 2012.
- [51] “Letter of Intent for the Phase-I Upgrade of the ATLAS Experiment,” Tech. Rep. CERN-LHCC-2011-012. LHCC-I-020, CERN, Geneva, Nov 2011.
- [52] A. Dominguez, “CMS Technical Design Report for the Pixel Detector Upgrade,” Tech. Rep. CERN-LHCC-2012-016. CMS-TDR-11, CERN, Geneva, Sep 2012.
- [53] P. Klabbbers *et al.*, “CMS Calorimeter Trigger Phase I upgrade,” *Journal of Instrumentation*, vol. 7, no. 01, p. C01046, 2012.
- [54] The CMS Collaboration, “Technical Proposal for the Upgrade of the CMS detector through 2020,” Tech. Rep. CERN-LHCC-2011-006. LHCC-P-004, CERN, Geneva, Jun 2011.
- [55] P. Campana, “The LHCb Upgrade,” in *XL International Meeting on Fundamental Physics*, 2012.
- [56] W. Riegler, “ALICE LS1 Activities, LS2 Upgrade: Items related to the LHC,” tech. rep., HL-LHC WP8, 1st Workshop Collider-Experiment Interface, Geneva, Nov 2012.

- [57] “Physics Briefing Book, Input for the Strategy Group to draft the update of the European Strategy for Particle Physics.” CERN-ESG-005, 2013.
- [58] ATLAS Collaboration, “Letter of Intent for the Phase-II Upgrade of the ATLAS Experiment,” Tech. Rep. CERN-LHCC-2012-022. LHCC-I-023, CERN, Geneva, Dec 2012. Draft version for comments.
- [59] P. Allport, “Experimental Challenges for the HL-LHC,” in *XL International Meeting on Fundamental Physics*, 2012.
- [60] A. Clark *et al.*, “ATLAS Phase II Letter of Intent: Backup Document: Final Report: Phase-2 Tracker Upgrade Layout Task Force,” Tech. Rep. ATL-COM-UPGRADE-2012-021, CERN, Geneva, Aug 2012.
- [61] A. Blue, “Plans for 130nm: Production Rate/QA,” tech. rep., ATLAS Upgrade Week, May 2013.
- [62] A. Clark *et al.*, “Development of a silicon-microstrip super module prototype for the high luminosity LHC,” *Nuclear Instruments and Methods in Physics Research Section A: Accelerators, Spectrometers, Detectors and Associated Equipment*, vol. 699, no. 0, pp. 97 – 101, 2013.
- [63] V. Benítez, M. Ullán, and C. Lacasta, “Petalet prototype,” tech. rep., ATLAS Upgrade Week, November 2011.
- [64] M. Lozano *et al.*, “Comparison of radiation hardness of P-in-N, N-in-N, and N-in-P silicon pad detectors,” *Nuclear Science, IEEE Transactions on*, vol. 52, no. 5, pp. 1468–1473, 2005.
- [65] P. S. Miyagawa and I. Dawson, “Radiation background studies for the Phase II inner tracker upgrade,” Tech. Rep. ATL-UPGRADE-PUB-2013-012, CERN, Geneva, Feb 2013.
- [66] A. Affolder, “Silicon Strip Detectors for the ATLAS HL-LHC Upgrade,” Tech. Rep. ATL-UPGRADE-PROC-2011-005, CERN, Geneva, Sep 2011.
- [67] Y. Unno *et al.*, “Development of n-on-p silicon sensors for very high radiation environments,” *Nuclear Instruments and Methods*, vol. A636, pp. S24–S30, 2011.
- [68] Unno, Y., “Supply of Silicon Microstrip Sensors of ATLAS07 Specification. Version 4.6,” tech. rep., ATLAS SCT Collaboration, 2007.
- [69] P. J. Dervan, “Silicon strip detectors for the ATLAS HL-LHC upgrade,” *Journal of Instrumentation*, vol. 7, p. C03019, 2012.
- [70] G. Casse *et al.*, “Comparison of charge collection efficiency of segmented silicon detectors made with FZ and MCz p-type silicon substrates,” *Nuclear Instruments and Methods A*, vol. 591, no. 1, pp. 178–180, 2008.
- [71] Unno, Y., “Supply of Silicon Microstrip Sensors of ATLAS12 Specification. Version 1.3,” tech. rep., ATLAS SCT Collaboration, 2012.

- [72] K. Hara and Y. Ikegami, “Silicon Strip Detectors for ATLAS at the HL-LHC Upgrade,” Tech. Rep. ATL-UPGRADE-PROC-2012-005, CERN, Geneva, Oct 2012.
- [73] N. P. Hessey, “Building a Stereo-angle into strip-sensors for the ATLAS-Upgrade Inner-Tracker Endcaps,” Tech. Rep. ATL-UPGRADE-PUB-2013-002, CERN, Geneva, Feb 2013.
- [74] V. H. B. Casma, “Design and fabrication of Endcap prototype sensors (petalet) for the ATLAS Upgrade,” tech. rep., 20th RD50 Workshop, Bari, May 2012.
- [75] R. Mori, “Report on petalet modules (250nm) ,” tech. rep., ATLAS Upgrade Week, May 2013.
- [76] W. Dabrowski *et al.*, “Design and performance of the ABCN-25 readout chip for ATLAS inner detector upgrade,” p. 8 p, 2010.
- [77] T. Affolder *et al.*, “System Electronics for the ATLAS Upgraded Strip Detector,” Tech. Rep. ATL-UPGRADE-PUB-2013-011, CERN, Geneva, Feb 2013.
- [78] L. Gonella *et al.*, “Total Ionizing Dose effects in 130-nm commercial CMOS technologies for HEP experiments,” *Nuclear Instruments and Methods in Physics Research Section A: Accelerators, Spectrometers, Detectors and Associated Equipment*, vol. 582, no. 3, pp. 750 – 754, 2007.
- [79] ATLAS Collaboration, “ABC130 Specifications.” <https://indico.cern.ch/event/227566/material/0/0.pdf>, 2013.
- [80] C. Soós *et al.*, “The Versatile Transceiver: towards production readiness,” *Journal of Instrumentation*, vol. 8, no. 03, p. C03004, 2013.
- [81] Topical Workshop on Electronics for Particle Physics, *ATLAS SCT power supply system*, 2007.
- [82] M. Weber, “Power distribution for SLHC trackers: Challenges and solutions,” *Nuclear Instruments and Methods in Physics Research Section A: Accelerators, Spectrometers, Detectors and Associated Equipment*, vol. 592, no. 1–2, pp. 44 – 55, 2008.
- [83] Topical Workshop on Electronics for Particle Physics, *Performance and Comparison of Custom Serial Powering Regulators and Architectures for SLHC Silicon Trackers*, 2009.
- [84] Topical Workshop on Electronics for Particle Physics, *Serial Powering of Silicon Strip Modules for the ATLAS Tracker Upgrade*, 2008.
- [85] A. Affolder *et al.*, “DC-DC converters with reduced mass for trackers at the HL-LHC,” *Journal of Instrumentation*, vol. 6, no. 11, p. C11035, 2011.
- [86] F. Faccio *et al.*, “Development of custom radiation-tolerant DCDC converter ASICs,” *Journal of Instrumentation*, vol. 5, no. 11, p. C11016, 2010.
- [87] P. Phillips, “Strip Tracker Powering Overview,” tech. rep., ITk Subcommittee. <https://indico.cern.ch/event/142815/>, July 2011.



- 
- [88] M. Weber, G. Villani, M. Tyndel, and R. Apsimon, “Serial powering of silicon strip detectors at SLHC,” *Nuclear Instruments and Methods in Physics Research Section A: Accelerators, Spectrometers, Detectors and Associated Equipment*, vol. 579, no. 2, pp. 844 – 847, 2007.
- [89] A. Lebedev, V. Kozlovski, N. Strokan, D. Davydov, A. Ivanov, A. Strel’chuk, and R. Yakimova, “Radiation hardness of wide-gap semiconductors (using the example of silicon carbide),” *Semiconductors*, vol. 36, no. 11, pp. 1270–1275, 2002.
- [90] S. Díez, C. H. Haber, R. Witharm, A. A. Affolder, *et al.*, “A double-sided, shieldless stave prototype for the ATLAS Upgrade strip tracker for the High Luminosity LHC,” *Journal of Instrumentation*, vol. 9, no. 03, p. P03012, 2014.
- [91] J. Matheson, “Progress and advances in Serial Powering of silicon modules for the ATLAS Tracker Upgrade,” *Journal of Instrumentation*, vol. 6, no. 01, p. C01019, 2011.
- [92] P. W. Phillips, “ATLAS strip tracker stavelets,” *Journal of Instrumentation*, vol. 7, no. 02, p. C02028, 2012.
- [93] “ROOT, a framework for data analysis.” <http://root.cern.ch>.
- [94] E. Villani, “Progress and Advances in Serial Powering of Silicon Modules for the ATLAS Tracker Upgrade,” *Nuclear Physics B - Proceedings Supplements*, vol. 215, no. 1, pp. 238 – 241, 2011.
- [95] E. Górnicki, S. Koperny, and P. Malecki, “SCTHV VME Model 203 User’s Manual.” <http://www.ifj.edu.pl/publ/reports/2004/1947.pdf>, 2004.
- [96] Hommels, B. and Sigurdsson, S., “Temperature Interlock.” <http://www.hep.phy.cam.ac.uk/~hommels/interlock/>.
- [97] B. M. Demirköz, *Construction and Performance of the ATLAS SCT Barrels and Cosmic Tests*. PhD thesis, University of Oxford, 2007.
- [98] C. Friedrich *et al.*, “SCT Upgrade DAQ Documentation Twiki.” <https://twiki.cern.ch/twiki/bin/viewauth/Atlas/SCTUpDAQDown>.
- [99] C. García-Argos, “DC-DC Stavelet Studies in CERN B180,” tech. rep., ATLAS Upgrade Week, March 2012.
- [100] Simon Jan Marie Peeters, *The ATLAS SemiConductor TRacker Endcap*. PhD Thesis, 2003.
- [101] J. Kaplon and W. Dabrowski, “Fast CMOS binary front end for silicon strip detectors at LHC experiments,” *Nuclear Science, IEEE Transactions on*, vol. 52, pp. 2713–2720, Dec 2005.
- [102] T. Dilger *et al.*, “Report on Hybrids,” tech. rep., Petalet Meeting <https://indico.cern.ch/event/255266/>, June 2013.
-

- [103] S. Wonsak, “Entwicklung und Untersuchung von Silizium-Streifendetektor-Modulen für das Upgrade des ATLAS-Experiments,” Diplomarbeit (Diploma Dissertation), 2012.
- [104] P. Moreira *et al.*, “The GBT-SerDes ASIC prototype,” *Journal of Instrumentation*, vol. 5, no. 11, p. C11022, 2010.
- [105] C. García-Argos, T. Huffman, J. Troska, and S. Wonsak, “Measurement of the potential electromagnetic interaction of the Versatile Link with the Strips Upgrade Stavelet,” Tech. Rep. ATL-COM-UPGRADE-2012-014, CERN, Geneva, Jun 2012.
- [106] P. Phillips and A. Greenall, “DC-DC for ABCN-25,” tech. rep., ATLAS Upgrade Week, May 2013.
- [107] P. Phillips and C. García-Argos, “DC-DC Stave Status and Results: A Story of Nine Modules on a Very Long Bus,” tech. rep., ATLAS Upgrade Week, November 2013.
- [108] I. Perić *et al.*, “The FEI3 readout chip for the ATLAS pixel detector,” *Nuclear Instruments and Methods in Physics Research Section A: Accelerators, Spectrometers, Detectors and Associated Equipment*, vol. 565, no. 1, pp. 178 – 187, 2006.
- [109] ATLAS Collaboration, “dE/dx measurement in the ATLAS Pixel Detector and its use for particle identification,” Tech. Rep. ATLAS-CONF-2011-016, CERN, Geneva, Mar 2011.
- [110] D. Robinson, “The ATLAS Semi-Conductor Tracker Operation and Performance,” Tech. Rep. ATL-INDET-PROC-2012-002, CERN, Geneva, Jan 2012.
- [111] C. García-Argos, S. J. McMahon, M. Stanescu, and T. Mitani, “dE/dx measurement in the ATLAS SCT detector and its potential for particle identification and performance tracking,” Tech. Rep. ATL-COM-INDET-2013-026, CERN, Geneva, Jun 2013.
- [112] S. Yacoob, N. Barlow, D. Damiani, and D. Robinson, “SCT Timing Study.” SCT Performance Meeting <https://indico.cern.ch/event/173670/>, March 2012.